

Dissertation

Multispectral and Multimodal Three-dimensional Optical Coherence Tomography

Submitted in partial fulfilment of the requirements for the degree of
Doctor of Philosophy

by

Aneesh Alex

School of Optometry and Vision Sciences
Cardiff University
United Kingdom

September 2010



UMI Number: U517673

All rights reserved

INFORMATION TO ALL USERS

The quality of this reproduction is dependent upon the quality of the copy submitted.

In the unlikely event that the author did not send a complete manuscript and there are missing pages, these will be noted. Also, if material had to be removed, a note will indicate the deletion.



UMI U517673

Published by ProQuest LLC 2013. Copyright in the Dissertation held by the Author.
Microform Edition © ProQuest LLC.


All rights reserved. This work is protected against
unauthorized copying under Title 17, United States Code.



ProQuest LLC
789 East Eisenhower Parkway
P.O. Box 1346
Ann Arbor, MI 48106-1346

DECLARATION

This work has not previously been accepted in substance for any degree and is not concurrently submitted in candidature for any degree.

Signed 

Date 11/05/2011

STATEMENT 1

This thesis is being submitted in partial fulfilment of the requirements for the degree of PhD.

Signed 

Date 11/05/2011

STATEMENT 2

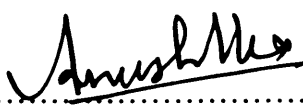
This thesis is the result of my own independent work/investigation, except where otherwise stated. Other sources are acknowledged by explicit references.

Signed 

Date 11/05/2011

STATEMENT 3

I hereby give consent for my thesis, if accepted, to be available for photocopying and for inter-library loan, and for the title and summary to be made available to outside organisations.

Signed 

Date 11/05/2011

Dedicated to

Daddy, Mummy, Anu and Aski

Acknowledgments

First and foremost, I owe my deepest gratitude to **Prof. Wolfgang Drexler**, Head of Centre for Medical Physics and Biomedical Engineering, Medical University Vienna for his consistent supervision, patient guidance and astute suggestions during the entire period of my PhD. I have great pleasure to express my sincere gratefulness to **Dr. Boris Považay**, Centre for Medical Physics and Biomedical Engineering, Medical University Vienna for his firm support and guidance during this period. His valuable contributions helped me a lot for carrying out my work fruitfully. I place on record my profound obligation to **Dr. Bernd Hofer**, Centre for Medical Physics and Biomedical Engineering, Medical University Vienna for his helpful suggestions and technical support for the progress of my work.

I am grateful to all my collaborators for their helpful suggestions and co-operation, which helped to successfully complete my PhD. I would like to express my appreciation towards **Mr. Bob Bonwick**, **Dr. Catherine Kendall** and **Prof. Nicholas Stone**, Biophotonics Research Group, Gloucestershire Royal Hospital, Gloucester. I am also thankful to **Dr. Edward Zhang**, **Dr. Jan Laufer** and **Prof. Paul Beard**, Photoacoustic Imaging and Optical Ultrasound Sensing Research Group, University College London.

I am greatly indebted to all the members of the Biomedical Imaging Group, Cardiff University for their encouragement and full-handed co-operation given throughout these years. I would like to thank **Alex Tumlinson**, **Angelika Unterhuber**, **Boris Hermann**, **Cristiano Torti**, **James Fergusson**, **Ling Wang**, **Sara Rey**, **Vedran Kajić** and **Yaiza Garcia Sanchez** for their kind support and fellowship.

I feel honoured to have pursued my doctoral studies at School of Optometry and Vision Sciences, Cardiff University. I would like to express my heartfelt thanks to all the academic and supporting staff of this School for their helping hands and support at all times.

It is my immense pleasure to thank all my friends and relatives in Cardiff, who made my stay here an unforgettable experience.

Above all, I thank almighty God for steering me to successfully complete my doctoral studies with great satisfaction and hope.

Abstract

The growing demand for non-invasive *in vivo* biomedical imaging modalities that can deliver micro-morphological and functional information of the human body, with a resolution comparable to that of histology, has led to rapid advancements in the field of imaging technology over the past few decades. Optical coherence tomography (OCT) is one of the non-invasive biomedical imaging modalities capable of providing three dimensional images with micrometre-scale resolution in real-time. To date, OCT has had the largest clinical impact in ophthalmology. Its high sensitivity is based on optical scattering and the penetration depth of 1 – 2 mm extends the scope of this ultrafast *in vivo* imaging technique onto diverse biomedical applications. The resolution, imaging speed and sensitivity of OCT has significantly improved over the past two decades with the development of ultra-broadband light sources, fibre-optic technology, computational power and frequency domain techniques.

During the course of this dissertation, a spectral-domain OCT system operating at 1300 nm wavelength region, capable of acquiring 47,000 A-lines/s, was designed and developed. Its axial and transverse resolutions were measured to be $\sim 6 \mu\text{m}$ and $\sim 15 \mu\text{m}$ respectively. It was compared with similar OCT systems operating at 800 nm and 1060 nm wavelength regions in terms of axial and transverse resolutions, signal-to-noise ratio (SNR) and depth-dependent SNR roll-off. OCT images of human skin were obtained *in vivo* using the three OCT systems, in order to find the optimal wavelength region for dermal imaging. 800 nm OCT system provided better image contrast over other two wavelength regions, whereas 1300 nm wavelength region was needed to obtain information from deeper dermal layers. To determine the effect of melanin pigmentation on OCT, images were taken from subjects with different ethnic origins. Interestingly, melanin pigmentation was found to have little effect on penetration depth in OCT.

In vitro tumour samples, comprising samples with different degrees of dysplasia, were imaged at 800 nm, 1060 nm and 1300 nm wavelength regions to determine the capability of OCT to diagnose microstructural changes occurring during tumour progression. Moreover, this study helped to demonstrate the advantages and limitations of each wavelength region in tumour diagnosis. 800 nm OCT system was capable to detect the malignant changes with higher contrast than other wavelength regions. However, higher wavelength regions were required to penetrate deeper in densely scattering tumour samples at advanced stages. OCT

system operating at 1060 nm was combined with a photoacoustic imaging (PAT) system to obtain complementary information from biological tissues. This multimodal OCT/PAT system demonstrated its potential to deliver microstructural information based on optical scattering and vascular information based on optical absorption in living mice and human skin. Thus, the work described in this dissertation has attempted to demonstrate the capabilities of OCT in revealing 3-D micro-morphological information of various scattering biological tissues and the results indicate OCT as a promising imaging modality that can have profound applications in several areas of clinical diagnostic imaging.

Table of Contents

Chapter 1	1
<i>In vivo</i> biomedical imaging modalities and oncology	1
1.1 Introduction to biomedical imaging	1
1.2 Biomedical imaging modalities	1
1.2.1 X-ray computed tomography	2
1.2.2 Magnetic resonance imaging	3
1.2.3 Nuclear medicine imaging	6
1.2.4 Ultrasound imaging.....	8
1.2.5 Optical imaging modalities	10
1.2.6 Other emerging imaging modalities.....	16
1.3 Multimodal imaging systems	17
1.4 Role of biomedical imaging in cancer management.....	18
1.4.1 What is cancer?	18
1.4.2 Biomedical imaging modalities in oncology	19
1.4.3 Potential role of OCT in cancer diagnosis	22
1.5 Aim of the study.....	23
1.6 Overview of Chapters	24
Chapter 2	25
Spectral domain OCT	25
2.1 Introduction to OCT.....	25
2.2 Principle of OCT	25
2.2.1 Low coherence interferometry.....	27
2.3 Theory of OCT.....	31
2.3.1 Frequency domain low coherence interferometry	35
2.3.2 Time domain low coherence interferometry	38

2.4 Key parameters of OCT	39
2.4.1 Centre wavelength of the light source	39
2.4.2 Axial and transverse resolutions	40
2.4.3 Detection sensitivity.....	42
2.5 SD-OCT system at 1300 nm	46
2.5.1 Components of the system	46
2.5.2 Implementation of the SD-OCT system	50
2.5.3 Characterization of the SD-OCT system	52
2.5.3.1 Axial and transverse resolutions	52
2.5.3.2 Axial and transverse scaling	53
2.5.3.3 Detection sensitivity.....	54
2.5.4 Comparison with other SD-OCT systems	55
Chapter 3	58
Multispectral <i>in vivo</i> three dimensional OCT of human skin.....	58
3.1 Introduction.....	58
3.1.1 OCT in dermatology	58
3.1.2 Anatomy of the human skin.....	60
3.2 Motivation: Multi-spectral OCT of human skin	63
3.3 Multispectral imaging of human skin	64
3.3.1 Subjects	64
3.3.2 Imaging systems.....	64
3.3.3 OCT image analysis.....	65
3.3.4 Results.....	65
3.3.5 Limitations of this study	82
3.4 Effect of the bandwidth of the light source in dermal OCT	82
3.5 Quantum-dot vs. amplified spontaneous emission SLD for OCT at 1 μm	83
3.6 Comparison of dermal imaging modalities.....	84

3.7 Conclusions and Outlook.....	88
Chapter 4	90
<i>In vitro</i> tumour study in gastrointestinal tissues using 3-D OCT at multiple wavelengths	90
4.1 Introduction.....	90
4.1.1 Anatomy of the oesophagus and the colon	90
4.1.2 Tumour classification of the oesophagus and the colon	92
4.1.3 Motivation: <i>In vitro</i> gastrointestinal tumour imaging using multispectral OCT	97
4.2 Materials and methods	98
4.2.1 Specimens	98
4.2.2 OCT imaging	99
4.2.3 Tissue marking and fixing	99
4.2.4 Histology.....	100
4.2.5 OCT tumour data analysis	101
4.3 Results.....	101
4.3.1 Oesophageal specimens	101
4.3.2 Colonic specimens	106
4.3.3 Other specimens.....	115
4.4 Discussion	119
4.5 Conclusions.....	123
Chapter 5	124
Multimodal optical coherence/photoacoustic tomography	124
5.1 Introduction to photoacoustic imaging	124
5.1.1 Optical ultrasound detection	127
5.2 Motivation for this study: OCT/PAT multimodal imaging	128
5.3 Materials and methods	129
5.3.1 Subjects	129

5.3.2 OCT/PAM imaging system.....	129
5.3.3 Calibration target	131
5.4 Results and Discussions	132
5.5 Conclusions.....	136
Chapter 6	138
Summary & Outlook	138
6.1 Summary	138
6.1.1 Design and development of 1300 nm SD-OCT system.....	138
6.1.2 Optimal wavelength region for dermal OCT	138
6.1.3 <i>In vitro</i> tumour study using multispectral OCT	139
6.1.4 Multimodal OCT/PAT imaging approach	140
6.2 Future prospects of this research.....	140
6.2.1 Pharmacological applications	140
6.2.2 Dermal diagnostic applications.....	142
6.2.3 Gastrointestinal endoscopic applications.....	143
6.2.4 Potential applications of multimodal OCT/PAT approach in dermatology.....	143
Bibliography	145

Chapter 1

In vivo biomedical imaging modalities and oncology

1.1 Introduction to biomedical imaging

More than a century has passed since Roentgen's discovery of the "mysterious rays" that launched the modern field of biomedical imaging (Roentgen, 1896). The advancements in science and technology have led to the emergence of new biomedical imaging modalities capable of revealing micro-morphological details of the human body. These innovations are providing investigators with powerful new approaches for probing the mechanisms of health and disease. All the biomedical imaging modalities utilize different kinds of energy resources to interact with the human body in one way or another and these interactions are analysed to retrieve structural or functional information of the human body. Except ultrasound imaging, most of the clinical imaging systems are based on the interactions of electromagnetic radiation with the biological tissues and fluids [Figure 1.1]. These novel imaging modalities offer an extraordinary potential to promote health, to improve the treatment of disease and to accelerate the pace of scientific inquiry in medical science (Ehman et al., 2007; Fass, 2008).

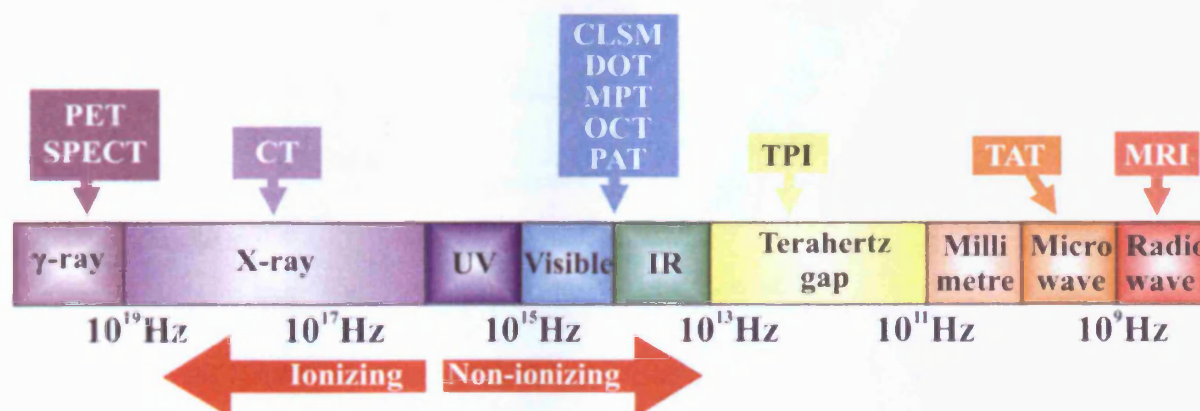


Figure 1.1: Different frequency regions employed by various biomedical imaging modalities. PET – Positron emission tomography, SPECT – Single photon emission computed tomography, CT – Computed tomography, CLSM – Confocal laser scanning microscopy, DOT – Diffuse optical tomography, MPT – Multiphoton tomography, OCT – Optical coherence tomography, PAT – Photoacoustic tomography, TPI – Terahertz pulse imaging, TAT – Thermoacoustic tomography and MRI – Magnetic resonance imaging.

1.2 Biomedical imaging modalities

Biomedical imaging modalities may generally be categorised as anatomical-based and functional-based depending on their purpose. Anatomical imaging modalities retrieve

structural information of the imaging volume, whereas functional imaging modalities provide physiological and metabolic information concerning the target tissue. Some of these imaging modalities serve both these purposes simultaneously. The rapid progress in the fields of medical physics, sensor technology and computational modelling led to the evolution of many novel imaging techniques during the past few decades.

1.2.1 X-ray computed tomography

Medical imaging has gone through a revolution since the advent of x-ray computed tomography (CT) imaging in 1972 (Hounsfield, 1973). It was the first non-invasive radiological method allowing generation of tomographic images of all parts of the body without superposition of neighbouring structures. In the first generation CT scanners, a narrow fan-beam of x-rays passed through the patient was picked up by a row of detectors on the other side. The source and detectors were placed on opposite sides of a ring that rotated around the patient (Garvey and Hanlon, 2002). A series of x-ray attenuation projections were recorded at fixed angles of rotation and a tomogram was reconstructed using inverse Radon transform (Deans, 1992).

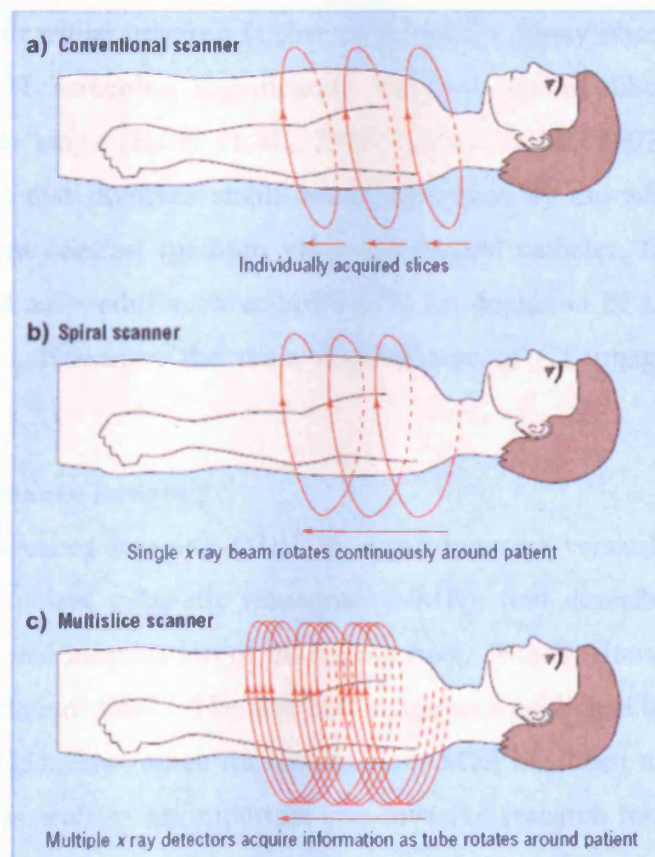


Figure 1.2: Different types of CT scanning procedures. (a) Axial CT, (b) Spiral CT and (c) Multi-slice CT (Garvey and Hanlon, 2002).

In axial CT, commonly used in examination of heads for cerebral infarcts or haemorrhage, the patient table is stationary during a rotation of the x-ray apparatus, after which the table is moved along for the next slice, as shown in figure 1.2. This technique has many limitations such as slow scan rate, motion artifacts due to movement or respiration and poor dynamic contrast. In order to achieve shorter scan times, an alternative concept known as electron beam CT (EBCT) was developed in 1980's. In EBCT, an electron beam is swept across one of the four semi-circular targets, which enclose the patient. This technique was capable of providing extremely high temporal resolution as image acquisition was devoid of any mechanical movements. The incorporation of slip ring technology into the design of CT scanners led to the introduction of spiral or helical CT in 1989 (Kalender, 2006). In spiral CT, the table moves at a constant speed through the gantry as the x-ray source and detectors rotate, producing a spiral scan that allows rapid volumetric data acquisition over a large part of the body. The development of multi-slice CT scanners helped to reduce the scanning times further. A multi-slice CT scanner can be considered as a turbocharged spiral scanner with multiple rows of x-ray detectors for acquiring information. Recently, dual-source CT systems with two x-ray units and two detectors mounted orthogonally in the gantry have yielded impressive results in cardiac imaging (Leber et al., 2007). Many observational studies have demonstrated that CT screening significantly increases the likelihood of detecting lung cancers at an earlier stage (Bach et al., 2003; Fasola et al., 2007). CT enteroclysis, a diagnostic procedure that involves small bowel distension by the administration of a high volume of fluorescent contrast medium via a nasojejunal catheter, followed by CT image acquisition, provided an overall accuracy of 84.7% for depiction of small-bowel neoplasms (Pilleul et al., 2006). However, the main disadvantage of CT imaging is its risk due to radiation exposure.

1.2.2 Magnetic resonance imaging

Magnetic resonance imaging (MRI) is a non-invasive versatile biomedical imaging modality based on nuclear magnetic resonance (NMR), first described in 1946, to obtain structural and functional information of the human body (Bloch, Hansen and Packard, 1946; Purcell, Torrey and Pound, 1946). The first MR image was published by Paul C. Lauterbur in 1973 (Lauterbur, 1973). Ever since its introduction, MRI has been a method-of-choice for diagnostic imaging as well as an important non-invasive research tool for both human and animal studies.

MRI maps the spatial distribution of MR active nuclei, i.e. nuclei with non-zero spin, present in the biological tissues to form an MR image. When kept in an external magnetic field, MR active nuclei align their axis of rotation with the magnetic field. Hydrogen (^1H), Phosphorous (^{31}P), Carbon (^{13}C), Fluorine (^{19}F) and Nitrogen (^{15}N) are some of the MR active nuclei in biological tissues. Hydrogen nucleus is the most frequently used nucleus for clinical MRI due to its high gyromagnetic ratio, natural abundance and concentration in biological tissues in the form of water and fat. Hydrogen nuclei possess two energy states in the presence of a static magnetic field due to Zeeman effect. In thermal equilibrium, the number of protons in lower energy state is slightly greater than the number of protons in higher energy state. The protons in the lower energy state align parallel to the magnetic field and vice versa. This produces a net magnetization vector that is used in clinical MRI. In addition to the natural spin of the nuclei, an external magnetic field induces a secondary spin of the nuclear magnetic moments around the field, known as precession. When exposed to the same field strength, MR-active nuclei of different elements will precess at different frequencies depending on their gyromagnetic ratio. Energy of hydrogen nuclei at its precession frequency at all field strengths are related to the radio frequency (RF) band of the electromagnetic spectrum. Hence, upon a RF pulse excitation, some of the low energy nuclei absorb this energy to become high energy nuclei. As a result of this resonant absorption, the nuclear magnetization vector (NMV) deviates from the magnetic field direction and precesses in a transverse plane perpendicular to the field. The voltage induced as a result of the precession of coherent NMV along the transverse plane is detected using a receiver coil, which constitutes the MR signal. When the RF pulse is switched off, the NMV tries to realign with the external magnetic field. For this, the nuclei have to give up the absorbed RF energy. This relaxation of nuclei results in the recovery of magnetization along the field direction (T1 recovery) and the decay of transverse magnetization (T2 decay). T1 recovery is caused by the nuclei giving up their energy to the surrounding lattice, known as spin-lattice relaxation, whereas T2 decay is caused by the nuclei exchanging energy with its neighbouring nuclei, which is termed as spin-spin relaxation (Westbrook, Roth and Talbot, 2005).

The intrinsic contrast parameters in MRI are T1 recovery time, T2 decay time, proton density, flow and apparent diffusion coefficient. T1 recovery time and T2 decay time vary depending on tissues, which gives MRI its tremendous soft tissue contrast. The two extremes of contrast in MRI are fat and water. Fat appears brighter in T1 weighted images due to its shorter T1 recovery time, whereas water appears brighter in T2 weighted images due to its

that produces changes in the intensity of the MR signal, which enables the demarcation of the active period and the rest period is the blood oxygenation level dependent (BOLD) effect (Ogawa et al., 1990). This exploits differences in magnetic susceptibility of oxyhaemoglobin and deoxyhaemoglobin as a result of increased cerebral blood flow and no increase in local oxygen consumption that occurs during stimulation. MR spectroscopy (MRS) produces a spectrum as opposed to an MR image (Cox, 1996). This provides functional information regarding the chemical composition of the target tissue. MRS is particularly useful in stroke and tumour imaging especially in brain, breast and prostate (Jansen et al., 2006; Kwock et al., 2006). Currently, MRI systems for whole body imaging using multiple coil elements and MR microscopy (MRM) systems for imaging with extremely fine resolutions are active areas of research (Hu and Norris, 2004; Querleux, 2004; Bittoun, Querleux and Darrasse, 2006).

1.2.3 Nuclear medicine imaging

Radionuclide imaging is a valuable tool for molecular imaging because of the striking sensitivity of this technique. It is mainly used to probe the physiology and biochemistry of normal and malignant tissues. The first application of the radioactive tracer principle was made in 1911 by Hevesy using naturally occurring radioactive tracers (Levi, 1976). Thyroid was the first organ to be studied using nuclear medicine technique, following the discovery of short-lived isotopes by Fermi in 1934 (Wagner, 2006). The three inherent advantages of radiotracers are their high specificity, high sensitivity and minimal amount requirement of labelled materials as compared to other imaging modalities. In contrast to other imaging modalities, the quantity of naturally occurring background activity in biological organisms is very low in the case of radionuclide imaging. These radionuclides are incorporated into compounds normally used by human body such as glucose, fatty acids or antibodies and are injected as radiopharmaceuticals to visualize the active processes (Blankenberg and Strauss, 2002). The quality of the acquired image will depend on several basic factors such as resolution of the detecting system, the radiopharmaceutical used and the degree of uptake by the target organ or tissue. The efficiency of radionuclide imaging has been tremendously improved with the development of a wide variety of receptor-based radiopharmaceuticals with different decay times and by employing highly sophisticated image acquisition systems (Mettler and Guiberteau, 2005).

Single photon emission computed tomography (SPECT) is a radionuclide imaging method, which makes use of radiopharmaceuticals labelled with a single photon emitter, i.e., a radio-isotope that emits one gamma (γ) photon for each radioactive decay event (Wernick

and Aarsvold, 2004). In its simplest form, SPECT is accomplished by using a conventional γ detector head and a parallel hybrid collimator fitted to a rotating gantry. The collimator is used to select only the photons travelling in a particular direction and those photons are detected using a γ camera. Advanced systems use multiple camera heads for improving the imaging speed. The data used to produce diagnostic SPECT images are usually acquired as a series of multiple planar images collected at discrete angular intervals or in continuous acquisition as the detector head moves around the patient. The acquired data is combined and manipulated by using mathematical back projection algorithms to reconstruct a three dimensional (3-D) image of the organ scanned. SPECT has been successfully employed for obtaining valuable functional and perfusion information about several organ systems such as cerebrovascular system, cardiovascular system, skeletal system and respiratory system (Kim et al., 1990; Hirano et al., 1995).

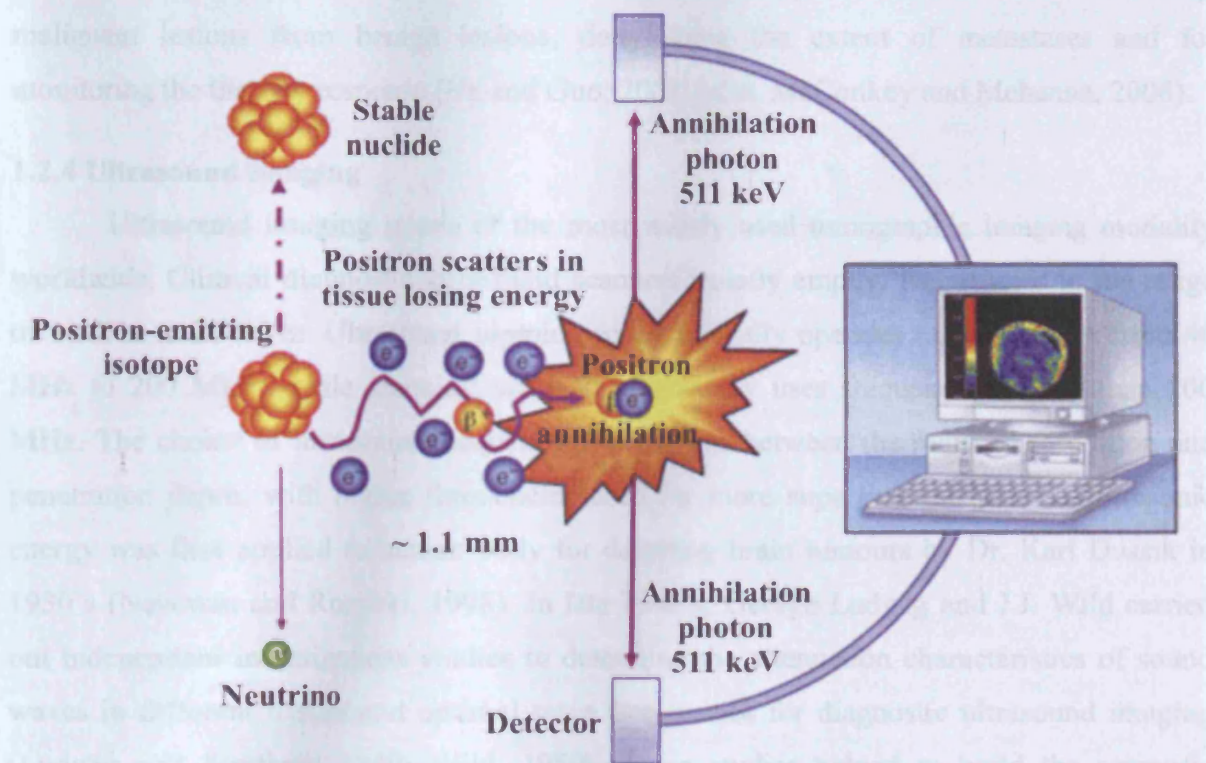


Figure 1.4: Principle of Positron emission tomography

Positron emission tomography (PET) is another radionuclide imaging modality that detects the rate of biological processes *in vivo*, by measuring concentration of radio-labelled positron emitting tracers (Muehllehner and Karp, 2006). In PET, a short-lived positron-emitting radionuclide which has been chemically incorporated into a biologically active

molecule is injected into the body. This active molecule will be concentrated at the region of interest, where it decays by emitting a positron. This positron will annihilate with an electron after travelling a short distance from the site of origin, producing a pair of γ photons that are emitted in opposite directions, as shown in figure 1.4. These photons are detected using scintillation detectors of the PET scanner and permits localization of the reaction. State-of-the-art PET scanners are multi-detector full ring systems that axially surround the patient. Although PET is limited by the short-lived isotopes and expensive instrumentation, it offers better spatial resolutions and contrast over SPECT (Knesaurek and Machac, 2006). The most commonly used positron-emitting radiopharmaceutical in clinical imaging is ^{18}F -Fluorodeoxyglucose (^{18}F -FDG). Many tumour cells use large amounts of glucose as an energy source and this allows ^{18}F -FDG to be trapped within the cell in proportion to the rate of glucose metabolism. This feature makes ^{18}F -FDG PET an ideal imaging technique for diagnosing malignant tumours. It can be used for several applications such as differentiating malignant lesions from benign lesions, determining the extent of metastases and for monitoring the therapy response (He and Guo, 2008; Isles, McConkey and Mehanna, 2008).

1.2.4 Ultrasound imaging

Ultrasound imaging is one of the most widely used tomographic imaging modality worldwide. Clinical diagnostic ultrasound scanners usually employ frequencies in the range of 1 MHz to 20 MHz. Ultrasound biomicroscopy typically operates at frequencies from 40 MHz to 200 MHz, while scanning acoustic microscopy uses frequencies higher than 200 MHz. The choice of ultrasound frequency is a balance between the required resolution and penetration depth, with higher frequencies used for more superficial structures. Ultrasonic energy was first applied to human body for detecting brain tumours by Dr. Karl Dussik in 1930's (Newman and Rozycki, 1998). In late 1940's, George Ludwig and J.J. Wild carried out independent investigations studies to determine the attenuation characteristics of sound waves in different tissues and optimal wave frequencies for diagnostic ultrasound imaging (Ludwig and Struthers, 1949; Wild, 1950). These studies helped to build the scientific foundation for the clinical use of ultrasound.

Ultrasound imaging uses a pulse-echo technique to synthesize gray-scale or colour-coded tomographic images of tissues based on their mechanical interactions with short ultrasonic pulses. Generation of ultrasound pulses and detection of echoes is accomplished with the help of a transducer, which also directs the ultrasound pulse along a linear path through the patient. Along any given beam path, the depth of an echo-producing structure is

determined from the time delay between the pulse emission and its echo return. Subsequently, the amplitude of the echo is encoded usually as a gray-scale value. There are four different modes in ultrasound imaging. In A-mode (Amplitude modulation) scan, a single transducer is used to scan a line through the body, whose echoes are plotted on the display device as a function of depth. In B-mode (Brightness modulation) scan, a linear array of transducers is used to obtain images of a cross-sectional plane and a two-dimensional tomographic image of the plane is displayed. In M-mode (Motion modulation) scan, a rapid series of B-scans are performed in a sequence to detect the motion of portion being imaged. In Doppler mode scan, it makes use of Doppler effect to assess whether the imaging structures are moving towards or away from the probe and measure the relative velocity of the moving particles within the imaging volume. The colour-coded Doppler information displayed along with the B-scan images has found major applications in microcirculation studies (Hadani et al., 1999).

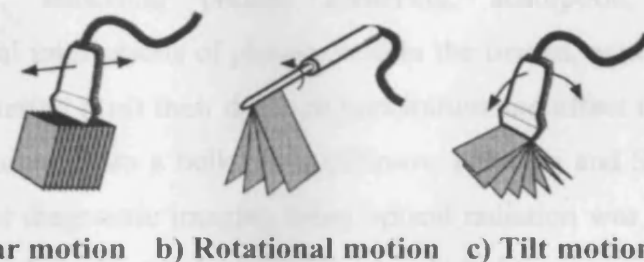


Figure 1.5: Different types of probe motion used in 3-D ultrasound imaging (Harvey et al., 2002)

The transducer array can be moved mechanically over the sample to record a series of B-scans and these two-dimensional images can be used to reconstruct a three-dimensional image. A linear, tilting or rotational motion of the transducer array can be used to produce a three-dimensional image of the sample as shown in figure 1.5. Two dimensional (2-D) arrays have also been developed to acquire volumetric images in real-time without moving the probe. Digital technology has revolutionized all stages of ultrasound systems. Digital beam forming has allowed the development of faster techniques, which may be used to improve image quality, field of view and frame rate. Digital control of transducer array can be used to steer the ultrasound beam and this allows dynamic changes in both focussing and aperture, while receiving ultrasound echoes. This provides higher spatial resolution and improves image contrast by reducing artifacts (Fenster and Downey, 2000).

Technological advances in harmonic imaging, non-linear signal processing, two-dimensional matrix array transducers and computational power have resulted in novel ultrasound imaging modes, such as those which exploit the non-linear behaviour of tissue and employ microbubbles as contrast agents. Microbubbles are safe and effective vascular echo enhancers, which have extended the versatility of ultrasound imaging. They allow imaging of microcirculation as well as provide functional data. Ultrasound also has a unique potential as tissue-specific and targeted therapeutic agents. High intensity focused ultrasound (HIFU) is a recently developed therapeutic technique, in which a highly focused ultrasound beam is used to destroy a defined volume of tissue by inducing a rapid rise in temperature to greater than 50°C. This is used to treat malignant tumours of liver, kidney, prostate etc. (Harvey et al., 2002).

1.2.5 Optical imaging modalities

Optical imaging modalities are based on physical principles of wavelength-dependent light-tissue interactions, including photon scattering, absorption, reflectance and fluorescence. The physical interactions of photons within the tissues, namely, intrinsic tissue absorption and light scattering limit their depth of penetration and affect the spatio-temporal resolution of images obtained from a bulk tissue (Efimov, Nikolski and Salama, 2004). The first significant attempt at diagnostic imaging using optical radiation was made by Cutler in 1929, who transilluminated the female breast with a bright light source in a darkened room (Cutler, 1929). The main advantages of optical imaging modalities are the use of non-ionizing radiation for imaging, the potential to differentiate between soft tissues depending on the light-tissue interactions and the capability to obtain functional information from these interactions. Various optical imaging modalities use different methods such as collimated detection, polarization discrimination, coherence gating, heterodyne detection and non-linear techniques to extract information needed to reconstruct the image (Hebden, Arridge and Delphy, 1997).

1.2.5.1 Fluorescence molecular tomography

In fluorescence molecular tomography (FMT), an external light of appropriate wavelength is used to excite a target fluorescent molecule, followed almost immediately by emission of longer wavelength light, as shown in figure 1.6. Targets for fluorescence imaging may be endogenous molecules like collagen or haemoglobin, fluorescent proteins like green fluorescent protein and related molecules, or optical contrast agents with fluorescent molecules. Several fluorescent proteins emitting in far-red and near-infrared regions have

been developed to reduce autofluorescence and to improve detection sensitivity owing to reduced absorption in this spectral region (Wang et al., 2004). Fluorescence molecular tomography is a fluorescence-mediated tomographic imaging approach used for three dimensional quantitative imaging, mainly used for mapping tumour targets (Montet et al., 2005; Ntziachristos, 2006). Fluorescence lifetime imaging (FLI) is another powerful tool for producing images based on the differences in the exponential decay rate of fluorescence from a fluorescent sample. Due to the potential of accessing intensity-independent lifetime information from sub-cellular volumes and due to a broad availability of lifetime probes, FLI has gained popularity in cellular biology, biophysics and biomedical sciences. Unlike fluorescence imaging, bioluminescence imaging (BLI) relies on activity of enzymes such as luciferase that oxidise unique substrates to produce light (Luker and Luker, 2008). *In vivo* BLI has been successfully employed to study tumour progression with high sensitivity and accuracy (Thorne and Contag, 2005). Recently, these technologies have been adapted to flexible fibre probes that can be used with endoscopic methods to obtain images of sites that were previously inaccessible.

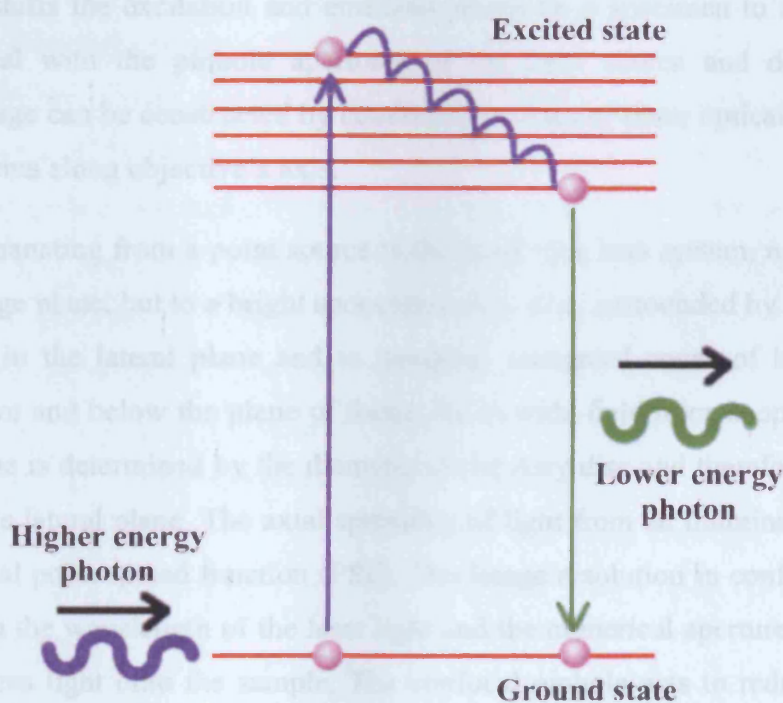


Figure 1.6: Fluorescence emission

1.2.5.2 Confocal laser scanning microscopy

Confocal laser scanning microscopy (CLSM) is a type of non-invasive high-resolution microscopy that overcomes the limitations of conventional wide-field microscopy and

as well as any fluorescent light is recollected from the focal spot by the objective. A beam splitter is used to direct some portion of the recollected light onto the detector. In fluorescence mode operation, a filter for selectively passing fluorescent wavelengths is used. The light intensity is measured by the detector after passing through a second aperture positioned in front of the detector, as shown in figure 1.7. The detector aperture obstructs the light that is not coming from the focal point. Optical sectioning or optical sectional plane is achieved by raster scanning the focussed laser light across the specimen plane. The optical sectioning thickness depends on the pinhole aperture. Refocusing the objective lens shifts the excitation and emission points on a specimen to a new focal plane, which become confocal with the pinhole apertures of the light source and detector. A three-dimensional image can be constructed by combining a series of these optical sections taken at fixed increments along objective's axis.

Light emanating from a point source is focussed by a lens system, not to a single point in the image plane, but to a bright spot called Airy disc, surrounded by a series of bright and dark rings in the lateral plane and to complex, elongated cones of light in the axial dimension, above and below the plane of focus. As in wide-field microscopy, the resolution at the focal plane is determined by the diameter of the Airy disc and therefore is optically limited along the lateral plane. The axial spreading of light from an illuminated point source is called the axial point spread function (PSF). The image resolution in confocal microscopy depends on both the wavelength of the laser light and the numerical aperture of the objective lens used to focus light onto the sample. The confocal pinhole acts to reduce the effect of diffraction on image formation. Eliminating outer rings increases overall resolution. However, there is a trade-off between decreased pinhole size and increased detection efficiency. The elucidation of sample depth information is always less than lateral resolution due to the blurring effect of the axial PSF. New generation CLSM systems use single mode optical pathways as both the laser light delivery vehicle and the confocal aperture (Johnson, 1992).

2005). Along with endoscopic applications, CLSM has been used for *in vivo* imaging studies in several fields such as neurobiology, ophthalmology and dermatology (Kasparov, Teschemacher and Paton, 2002; Drezek et al., 2003; Tervo and Moilanen, 2003).

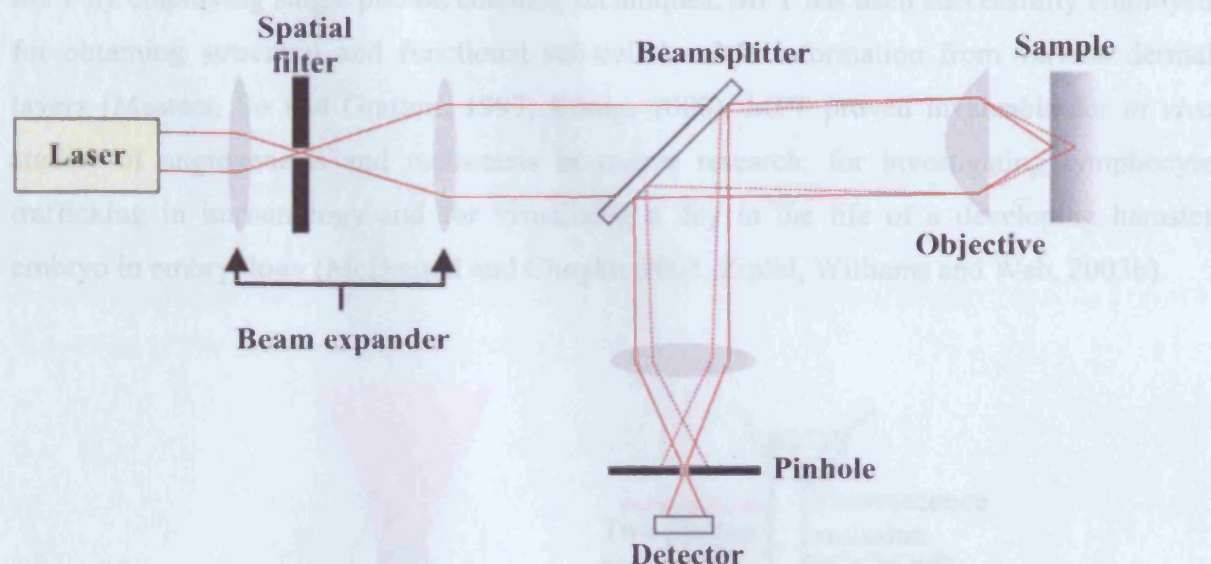


Figure 1.7: Schematic of a confocal imaging system

1.2.5.3 Multiphoton tomography

Maria Göppert-Mayer first predicted the possibility of multiphoton excitation in her doctoral dissertation in 1931 (Göppert-Mayer, 1931). However, experimental verification of multiphoton process was not realized until 1961, when Kaiser and Garret first observed two-photon excitation of $\text{CaF}_2:\text{Eu}^{2+}$ fluorescence (Kaiser and Garrett, 1961). The utilization of non-linear optical processes to provide image contrast for microscopic studies was reported by Hellwarth and Christensen (Hellwarth and Christensen, 1974). In 1990, Denk *et al* used the two-photon excitation principle to obtain images of biological specimens (Denk, Strickler and Webb, 1990). This was soon followed by applications of other non-linear optical mechanisms in biological imaging such as second and third harmonic generation, sum frequencies generation and coherent anti-Stokes Raman scattering (CARS) (Barad et al., 1997; Campagnola et al., 1999).

Multiphoton tomography (MPT) is a form of laser-scanning microscopy that uses localized non-linear excitation to excite fluorescence only within a thin raster-scanned plane, as shown in figure 1.8. Nonlinear excitation through multiphoton absorption in the near-infrared region brings about a range of advantages in scanning fluorescence microscopy such as inherent three-dimensional imaging without a confocal pinhole, reduced total

photobleaching, imaging of ultraviolet dyes with non-ultraviolet optical components and deeper penetration into scattering specimens. A variety of endogenous fluorophores can be imaged via multiphoton excitation. In principle, single molecule detection is possible using MPT by employing single photon counting techniques. MPT has been successfully employed for obtaining structural and functional sub-cellular 3-D information from various dermal layers (Masters, So and Gratton, 1997; König, 2008). MPT proved invaluable for *in vivo* studies of angiogenesis and metastasis in cancer research; for investigating lymphocyte trafficking in immunology and for visualizing a day in the life of a developing hamster embryo in embryology (McDonald and Choyke, 2003; Zipfel, Williams and Web, 2003b).

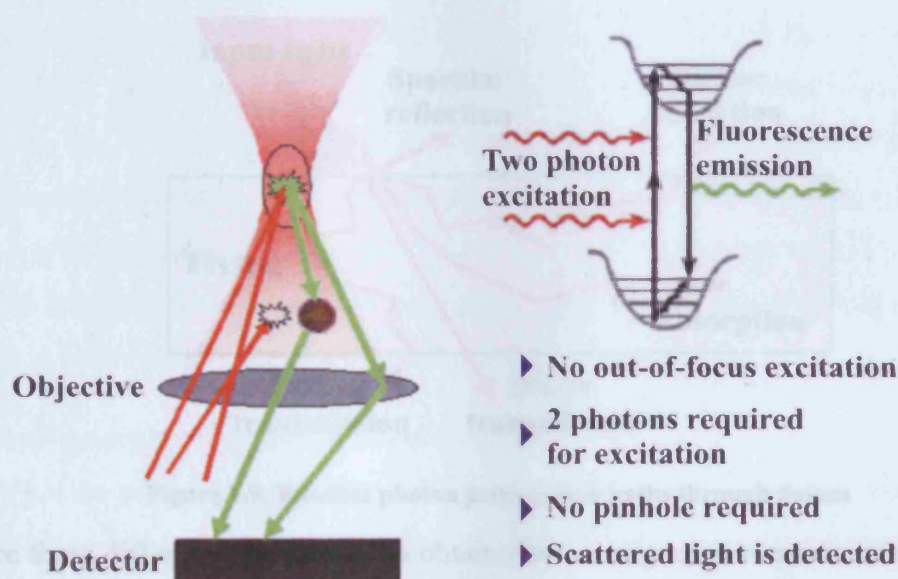


Figure 1.8: Schematic showing fluorescence emission using two-photon excitation

Although two-photon excited fluorescence is usually the primary signal source for MPT, some non-linear optical imaging systems utilize three-photon excited fluorescence signal, second-harmonic signal or third-harmonic signal captured from the specimen for image reconstruction purposes. In harmonic generation, multiple photons interact with tissue structures with less absorption, producing radiation in multiples of excitation frequency depending on the order of non-linear interaction. It can be used for high-resolution imaging of physiology, morphology and inter-cellular interactions in intact tissues or living animals (Müller et al., 1998; Zipfel et al., 2003a). Coherent anti-Stokes Raman scattering (CARS) microscopy is another complex non-linear imaging technique with 3-D sectioning capability.

It derives contrast directly from Raman-active vibrational modes within the molecules and requires two synchronized pulsed lasers operating at different wavelengths. CARS can achieve label-free chemical imaging enabling the analysis of spatial organization of biological structures with molecular details (Evans et al., 2005; Cheng, 2007).

1.2.5.4 Diffuse optical tomography

Diffuse optical tomography (DOT) is a non-invasive medical imaging modality in which tissue is illuminated by near-infrared light from an array of sources and the emerging multiply-scattered light is observed using an array of detectors (Boas et al., 2001). A computational model for the propagation of scattered light is used to infer localized optical properties of the illuminated tissue [Figure 1.9].

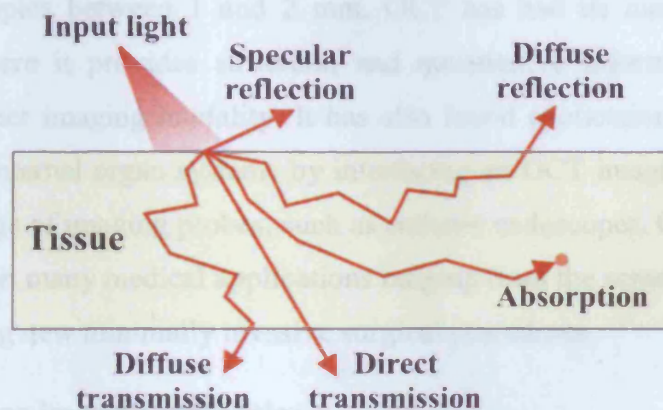


Figure 1.9: Possible photon propagation paths through tissues

There are three different approaches to obtain photon migration measurements: illumination by pico-second pulses of light, continuous wave illumination and RF amplitude modulated illumination. In DOT, sources and detectors are usually arranged in transmissive, reflective or annular geometries. The three primary absorbers at this wavelength region present in the tissues are water, oxyhaemoglobin and deoxyhaemoglobin. In addition to the measurement of optical absorption and scattering coefficients of tissue, functional and metabolic properties such as concentration of oxygenated and de-oxygenated haemoglobin can also be determined by DOT using multi-wavelength illumination or fluorescent dyes. Currently, the most important application of DOT is in detection of breast tumours and for functional imaging of brain. The greater amount of blood supply in tumours compared to the surrounding tissues provides optical absorption inhomogeneities for the diffuse optical signal that can play a crucial role in cancer detection (Choe, 2009). Recently, DOT has been successfully used to

distinct neurological responses of somatosensory cortex to different types of stimuli (Becerra et al., 2009).

1.2.5.5 Optical coherence tomography

Optical coherence tomography (OCT) is a promising optical imaging modality for biomedical research and clinical medicine, based on low-coherence interferometry. OCT performs high resolution, cross-sectional tomographic imaging in materials and biological tissues by measuring the echo-time delay and the magnitude of back reflected or backscattered light (Huang et al., 1991). Its main advantage is that it can perform “optical biopsy”, imaging tissue structure *in situ* and in real time non-invasively with high axial and transverse resolutions. In tissues other than eye, optical scattering limits the penetration depth of light in the samples between 1 and 2 mm. OCT has had its most clinical success in ophthalmology, where it provides structural and quantitative information that cannot be obtained by any other imaging modality. It has also found applications in cancer diagnosis and in imaging of internal organ systems by interfacing an OCT imaging system via optical fibres to a wide range of imaging probes, such as catheter endoscopes. OCT promises to have a powerful impact on many medical applications ranging from the screening and diagnosis of neoplasia to enabling new minimally invasive surgical procedures.

1.2.6 Other emerging imaging modalities

With the advancement of technology, several novel non-invasive imaging modalities have been investigated over the past few decades. Thermoacoustic tomography (TAT) and photoacoustic tomography (PAT) are emerging imaging modalities based on the measurement of ultrasonic waves induced by electromagnetic pulses (Kruger, Reinecke and Kruger, 1999; Kolkman et al., 2003; Ku et al., 2005). TAT employs electromagnetic radiation in RF or microwave bands, while PAT uses visible or near-infrared light. These techniques can reveal dielectric and optical properties of tissues respectively, which are related to its physiological and pathological condition. They are non-ionizing imaging techniques, combining the high contrast in absorption of electromagnetic radiation between healthy and abnormal tissue with the high resolution of ultrasound. Terahertz pulse imaging (TPI) is another non-invasive imaging modality employing radiation in the frequency range, 0.1 – 10 THz, a comparatively unexplored region of the electromagnetic spectrum. These wavelengths are significantly larger than the scattering structures in tissues and hence the scattering effects are negligible for this wavelength region. TPI has demonstrated its potential to obtain

structural and functional information from tissues and to distinguish malignant tissues from normal ones (Woodward et al., 2003).

1.3 Multimodal imaging systems

Recently, there has been a growing interest in the development of multimodal imaging systems, as this kind of imaging approach facilitates simultaneous acquisition of anatomical and functional information from the human body (Papathanassiou and Liehn, 2008). Imaging techniques such as PET and SPECT give insight into metabolic and functional changes associated with a pathological process, whereas imaging techniques such as CT, MRI, ultrasound imaging and OCT reveals anatomical changes due to a disease. Anatomical information alone is not always sufficient in diagnosing a disease, since functional changes usually precede structural changes in most cases and even in later stages, functional information helps to evaluate the pathological condition. On the other hand, functional imaging techniques lack specificity due to their limited spatial resolutions. Therefore, the addition of anatomical information can improve their effectiveness in disease management. Thus, multimodal imaging systems can have profound impact in the field of biomedical imaging.

The association of PET with CT has been a major breakthrough in cancer imaging. This represented the first widespread clinical application of a multimodal imaging system being used for acquisition of images generated by different principles in a single session (Beyer et al., 2000). Since 2003, majority of clinical PET devices implemented have been associated with a CT scanner. PET/CT had a huge impact in many fields of oncology imaging such as staging, monitoring therapy and recurrence detection (Townsend, 2001; Schoder, Larson and Yeung, 2004). Similarly, SPECT was combined with CT leading to a better localization of radioactive tracers and the clinical benefits of such a combination have been demonstrated across a wide spectrum of applications. SPECT/CT systems have found prominent applications in various medical fields such as cardiology, oncology and infectious disease imaging (Chowdhury and Scarsbrook, 2008; Seo, Mari and Hasegawa, 2008). Combination of PET and MRI principles represent another promising multimodal approach with huge potential in clinical imaging applications. *In vivo* studies performed using PET/MRI multimodal system has demonstrated capability in detecting tumour cell proliferation, tumour necrosis and inflammation. Combining fMRI and MRS with PET paves the way for a new perspective in medical imaging (Judenhofer et al., 2008).

Various optical imaging modalities yielding complementary contrasts have been combined to obtain microstructural and functional information of biological tissues simultaneously. Anatomical optical imaging modalities such as OCT, DOT, MPT and CLSM were combined with functional imaging techniques such as Raman spectroscopy (RS), PAT and fluorescence imaging to improve the sensitivity and specificity of the imaging application. Multimodal RS/CSLM and RS/OCT systems have been implemented to analyse the chemical composition of target tissues, along with microstructural information (Caspers, Lucassen and Puppels, 2003; Patil et al., 2008). Concurrent studies using combined OCT/Laser induced fluorescence spectroscopy systems have demonstrated capability in identifying and characterizing plant tissue, mouse colon tissues and atherosclerotic plaques (Barton, Guzman and Tumlinson, 2004; Tumlinson et al., 2004; Ryu et al., 2008). Recently, multimodal OCT/MPT and OCT/PAT systems have also been implemented to obtain complementary micro-morphological and vascular information from biological tissues *in vivo* (Jiao et al., 2009; König et al., 2009; Li et al., 2009).

1.4 Role of biomedical imaging in cancer management

1.4.1 What is cancer?

The essential characteristic of a cancer cell is a change in its gene expression that confers a growth advantage over normal cellular neighbours. This acquired property of uncontrolled growth is the hallmark of the broad spectrum of diseases, collectively known as cancers. Despite major differences in biological properties, diversity in types of originating tissue and distinct mechanisms for subverting growth control, all cancers are initiated by a basic underlying gene mutation. This is followed by further genetic changes that allow cancer cells to invade into local tissues and eventually metastasize to distant sites, as shown in figure 1.10. Thus, cancer is a genetic disease where mutations in DNA lead to changes in its gene expression, which consequently alters the properties of a cell.

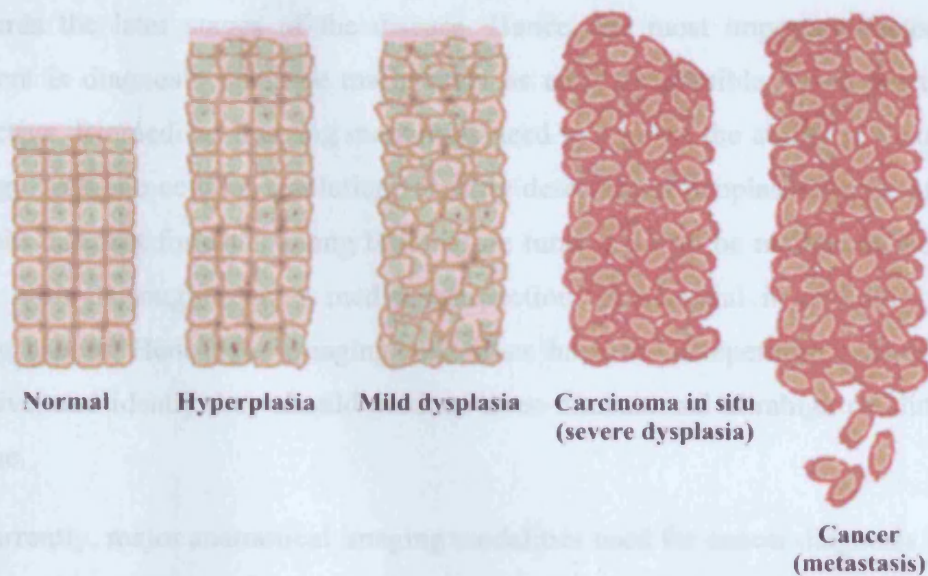


Figure 1.10: Different stages of tumour progression (Bishop and Bishop, 1999)

Cancer is generally classified according to its location and histology. The most common forms of malignancy are those derived from epithelial surfaces or glandular organs, termed as carcinoma. They include adenocarcinoma, squamous cell carcinoma and transitional cell carcinoma. Other major types of cancers are leukaemia, lymphoma, sarcoma, myeloma and germ cell tumours. The processes following the diagnosis of a malignancy are its typing, grading and staging based on its histogenesis, aggressiveness and extent of spread (Bishop and Bishop, 1999).

1.4.2 Biomedical imaging modalities in oncology

Histological examination of the cancerous cells obtained through biopsy is still the gold standard in cancer diagnosis. With the advent of modern techniques, biomedical imaging modalities are playing an ever important role in all phases of disease management (Fass, 2008). Non-invasive biomedical imaging offers several advantages such as real-time monitoring of infected regions and accessibility to areas of interest without tissue destruction. These imaging modalities can function over wide ranges of size and time scales involved in biological and pathological processes. The current role of biomedical imaging in cancer management is based on screening and symptomatic disease management.

In 2008, International Agency for Research on Cancer, which is a part of the World Health Organization, submitted a report predicting that the annual cancer incidence rate could further increase by 60% to 21.4 million cases by 2030 (Ferlay et al., 2008). The high mortality associated with cancer is due to the fact that in most of the cases they are diagnosed

of tremendous potential in diagnosing and screening of epithelial cancers.

Imaging modality	Primary contrast mechanism	Resolution (highest)	Penetration depth (max)
CT	X-ray attenuation	~ 1 mm	Entire body
MRI	Proton density	~ 1 mm	Entire body
PET	Exogenous Positron emitters	7 – 12 mm	Entire body
SPECT	Exogenous γ-photon emitters	14 – 19 mm	Entire body
Ultrasound @ 1MHz @ 20 MHz	Acoustic impedance	~ 150 μm ~ 80 μm	30 – 150 mm ~ 1 cm
FMT	Fluorescent markers	~ 500 μm	~ 0.5 – 1 cm
CLSM	Scattering (reflectance-mode) Fluorescence (fluorescence-mode)	$\leq 1 \mu$m	~ 0.5 – 1 mm
MPT	Non-linear optical excitation	$\leq 1 \mu$m	~ 0.5 – 1 mm
OCT	Optical scattering	1 – 10 μm	1 – 2 mm
DOT	Optical scattering and absorption	~ 10 mm	~ 1 – 2 cm
PAT @ 5 MHz @ 50 MHz	Optical absorption	~ 300 μm ~ 15 μm	~ 3 – 5 cm ~ 1 – 2 cm
TAT @ 1 MHz @ 12 MHz	Optical absorption	~ 3 mm ~ 125 μm	~ 5 – 10 cm ~ 1 – 2 cm

Table 1.1: Comparison of the primary contrast mechanism and penetration depth of various imaging modalities

The past two decades have seen a rapid increase in the number of research studies using fluorescence imaging, CLSM, OCT and MPT in an attempt to unveil their potential in oncology. Further studies are needed to determine the clinical viability of these techniques.

1.5 Aim of the study

The purpose of this study is to identify the optimal wavelength region for OCT to detect microstructural features associated with various pathological conditions in scattering tissues. Due to the reduced scattering of light and lower water absorption in the near-infrared wavelength region, broadband light sources emitting in 700 nm - 1300 nm range are usually employed for OCT investigations. During the course of this study, a frequency domain OCT system operating at 1300 nm wavelength region will be designed and developed for non-invasive *in vivo* dermal imaging applications. This 1300 nm OCT system will be compared with similar systems operating at 800 nm and 1060 nm wavelength regions in terms of imaging speed, signal-to-noise ratio (SNR) and SNR degradation with depth. All three OCT systems will be used to obtain *in vivo* images of human skin from identical locations. Images obtained using these three systems will be compared in terms of spatial resolutions, penetration depth and image contrast to find the optimal wavelength region for dermal OCT. Subsequently, images of tumour samples at different stages of tumour progression will be obtained *in vitro* using these three OCT systems, in order to identify the potential of OCT to delineate micro-morphological abnormalities associated with different tumour stages. Moreover, the *in vitro* tumour study will help to determine the advantages and limitations of each of these wavelength regions in detecting malignant changes. Finally, a multimodal OCT/PAT system will be employed to obtain images of mice and human skin *in vivo*. This imaging approach will help to demonstrate the potential of the OCT/PAT imaging system for simultaneous acquisition of complementary structural and functional information, which can be of significant value in dermatological studies.

1.6 Overview of Chapters

Following the discussion of different biomedical imaging modalities in the first chapter, the principle of OCT and its key parameters are discussed in the first part of the second chapter. The design and development of the 1300 nm frequency domain OCT system and comparison of its specifications with similar OCT systems, functioning at 800 nm and 1060 nm, is discussed in the second part of the second chapter. In the third chapter, multi-spectral *in vivo* imaging of the human skin using OCT is described. This chapter compares dermal images of similar locations obtained using the three OCT systems in terms of resolution, penetration depth and contrast. The first section of the fourth chapter is dedicated for discussing the typical histology of the tumour specimens and the procedures followed during the *in vitro* tumour study. In the following section of this chapter, OCT images of different stages of tumour obtained at multiple wavelengths will be analysed and interpreted. Fifth chapter provides basic background information on PAT and describes the multimodal OCT/PAT study. Preliminary results of the *in vivo* dermal imaging study performed using this multimodal system are included in this chapter. The final chapter summarizes the research studies carried out during the course of this dissertation and elucidates its future prospects.

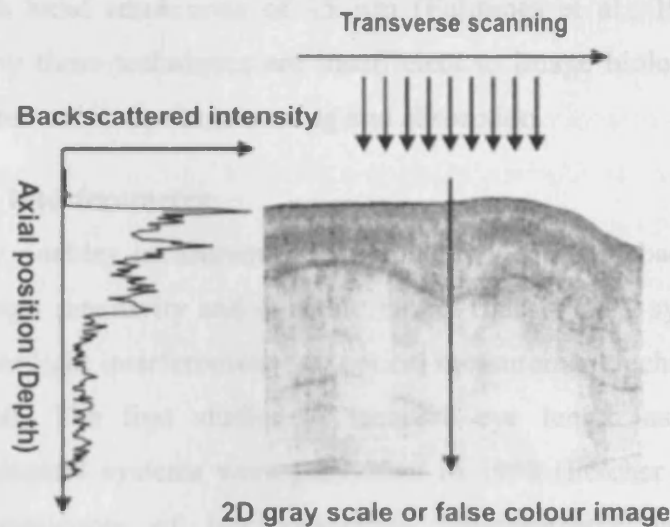


Figure 2.1: Basic principle of OCT: a 2D cross-sectional OCT image

OCT images are essentially a two-dimensional or three-dimensional data set which represents the optical backscattering from a cross-sectional plane or volume. OCT images are displayed using gray scale or false-colour scale, where varying amounts of backscattered or back reflected light are displayed as different colours on a rainbow colour or gray scale. The light signals detected in OCT imaging are extremely weak, typically ranging from 10^{-10} to 10^{-5} of the incident light. It is convenient to use a logarithmic scale to display OCT images, since the signal varies over 4 to 5 orders of magnitude. Logarithmic scale expands the dynamic range, however compresses the relative variations in OCT signals.

The principal difference between ultrasound and optical imaging is the fact that the characteristic distances and time scales for light and sound propagation are significantly different. The echo time delays associated with light are extremely rapid, when compared to ultrasound, and hence direct electronic detection is extremely challenging on this time scale. Thus, OCT measurements of echo time delay require optical gating and correlation techniques. The concept of using high speed optical echoes to perform imaging in scattering systems was first proposed by Michel Duguay in 1971 (Duguay and Mattick, 1971). Duguay demonstrated an ultrafast optical shutter using Kerr effect to photograph pulses of light in flight. He postulated that a high speed shutter could be used to gate out unwanted scattered light and detect echoes of light from the internal structure of tissue. An alternate approach for high speed gating is to use non-linear processes such as harmonic generation or parametric conversion. Optical ranging measurements have been demonstrated in biological tissues using femtosecond pulses and non-linear intensity autocorrelation to measure structures such

as eye and skin with axial resolutions of $15\ \mu\text{m}$ (Fujimoto et al., 1986). However, the sensitivities offered by these techniques are insufficient to image biological tissues, which have strong optical attenuation due to scattering and absorption.

2.2.1 Low coherence interferometry

Interferometry enables measurement of echo time delay of backscattered or back reflected light with high sensitivity and dynamic range. Classic OCT systems are based on low coherence or white light interferometry, an optical measurement technique first described by Sir Isaac Newton. The first studies to measure eye length using low coherence interferometry in biological systems were performed in 1988 (Fercher et al., 1988). Since then, different embodiments of low coherence interferometry versions have been demonstrated for non-invasive high precision and resolution optical biometry. Interferometric detection is sensitive to field rather than its intensity and is analogous to optical heterodyne detection. Three different types of interferometric detection can be used in OCT systems.

2.2.1.1 Time domain detection

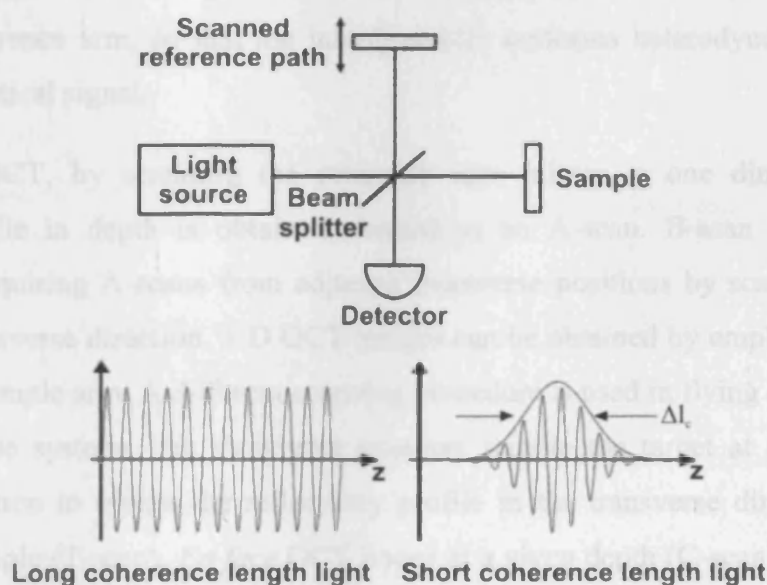


Figure 2.2: Principle of time domain OCT

Time domain OCT (TD-OCT) systems use an interferometer with low coherence light source and a scanning reference arm. This technique in which interference signal is measured as a function of time and echoes are measured sequentially is known as time domain

detection. Figure 2.2 shows a schematic diagram of a Michelson interferometer. The light source is directed onto a beam splitter to produce a reference beam and a measurement or sample beam. The reference beam $E_r(t)$, is reflected from a reference mirror that is being scanned over a calibrated path delay, while the sample beam $E_s(t)$, is backscattered from the biological specimen or tissue being imaged. These beams interfere and the detector measures the intensity proportional to the square of the electromagnetic field. If the lengths of the two arms of the interferometer are l_r and l_s , then the output intensity from the interferometer will oscillate as a function of $\Delta l = l_r - l_s$.

Interference is observed for a wide range of relative path lengths of the reference and sample arms using a monochromatic light source (long coherence length). Instead, when a low coherence light is used (broadband source), interference is observed only when the path lengths of the reference and sample arms are matched to within the coherence length of the light. The coherence length of the light determines the axial resolution with which optical echoes, and hence distance, can be measured in OCT. The magnitude and echo time delay of backscattered light can be measured by scanning the reference mirror position and demodulating the interference signal. Moreover, scanning the reference mirror Doppler shifts light in the reference arm, so that the interferometer performs heterodyne detection of the backscattered optical signal.

In TD-OCT, by scanning the reference arm mirror, a one dimensional sample reflectivity profile in depth is obtained, termed as an A-scan. B-scan OCT images are generated by acquiring A-scans from adjacent transverse positions by scanning the sample beam in the transverse direction. 3-D OCT images can be obtained by employing a dual-axis scanner in the sample arm. A different scanning procedure is used in flying spot *en-face* OCT systems. In those systems, the transverse scanners sample the target at a fast rate in the transverse direction to obtain the reflectivity profile in the transverse direction at a given depth of the sample (T-scan). *En face* OCT image at a given depth (C-scan) is made from T-scans performed along a transverse plane. To form a 3-D image, C-scans are obtained from successive axial positions of the sample by step-wise or continuous motion of the reference arm (Podoleanu et al., 1996; Podoleanu, Dobre and Jackson, 1998; Rosa, Rogers and Podoleanu, 2005).

2.2.1.2 Frequency domain detection

In OCT imaging, it is also possible to detect signals in frequency domain by measuring the interference spectrum (Fercher et al., 1995; Häusler et al., 1996). Echo signals or A-scans are measured by inverse Fourier transforming the spectrum at the interferometer output. Frequency domain OCT (FD-OCT) has powerful sensitivity ($\sim -100\text{dB}$) and speed advantage compared with TD-OCT, since FD-OCT essentially measure all the echoes of light in depth simultaneously. This makes FD-OCT is more efficient than TD-OCT systems, which results in higher speed with same sensitivity or higher sensitivity at lower speed. There are two types of frequency domain detection techniques in OCT, spectral domain OCT (SD-OCT) and swept source OCT (SS-OCT).

2.2.1.2.1 Spectral domain OCT

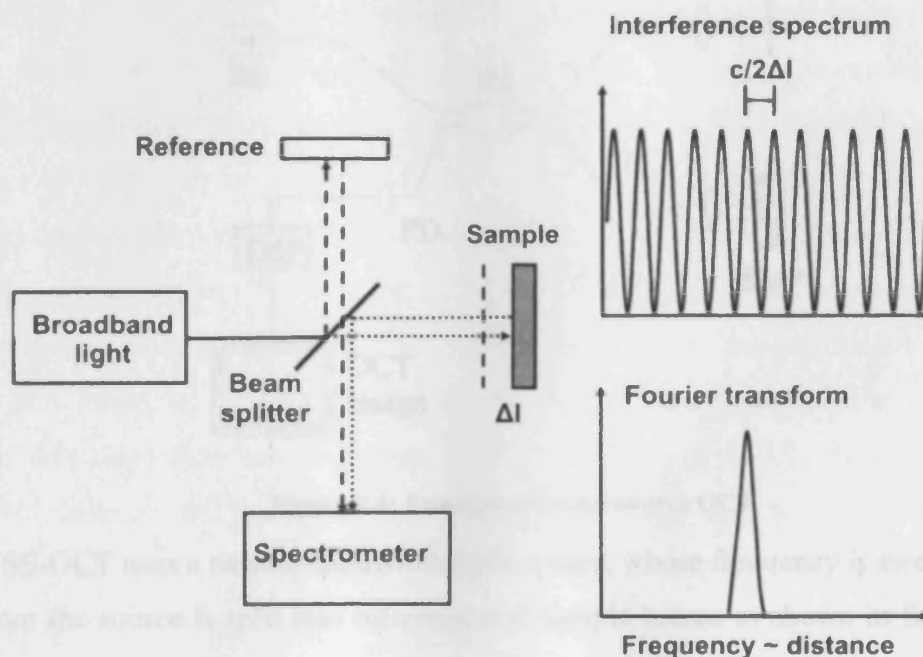


Figure 2.3: Principle of spectrometer-based frequency domain OCT

SD-OCT uses a broadband light source and detects the interference spectrum from the interferometer using a spectrometer equipped with a line scan camera (Fercher et al., 1995; Wojtkowski et al., 2002). The output from the light source is divided into two parts, reference and sample beams. The reference arm of the interferometer is stationary. The interference of reference and sample beams leads to a spectral modulation of the output spectrum and the periodicity of this modulation can be measured using a spectrometer [Figure 2.3]. The

periodicity of this modulation is inversely related to the echo time delay. Hence, echo delays from different depths will produce different frequency modulations. The echo delays can be measured by rescaling the spectrometer output from wavelength to frequency and then inverse Fourier transforming the output signal. This results in an A-scan measurement of the magnitude and echo delay of light from tissue. SD-OCT allows an increase in the imaging speed by around 50 times, compared to TD-OCT systems (Leitgeb et al., 2003; Cense et al., 2004). For a given acquisition time, high speed imaging helps to increase the number of A-scans or transverse pixels per B-scan to yield high-definition cross-sectional images, as well as to obtain higher number of B-scans from a volume to yield densely sampled three-dimensional information. High speed imaging also helps in reducing motion artifacts.

2.2.1.2.2 Swept source OCT

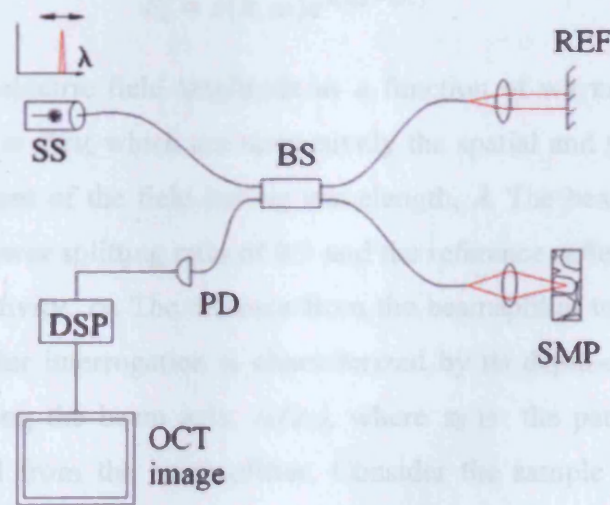


Figure 2.4: Principle of swept source OCT

SS-OCT uses a narrow bandwidth light source, whose frequency is swept in time. The light from the source is split into reference and sample beams as shown in figure 2.4. As in SD-OCT, the reference arm is stationary. The reference and sample beams will have a frequency offset determined by path length difference, since the frequency of light is swept as a function of time. When these beams interfere, a modulation or beat in intensity corresponding to the frequency offset is produced. Hence different echo delays will have different frequency modulations. The echo delays can be measured by digitizing the photodetector signal over a single frequency sweep as a function of time and then inverse Fourier transforming the beat frequency signal. This provides an A-scan measurement of the magnitude and echo delay of light from tissue. SS-OCT also facilitates a significant increase

in imaging speed and improves the detection sensitivity, when compared to TD-OCT (Fercher et al., 1995; Chinn, Swanson and Fujimoto, 1997).

2.3 Theory of OCT

The theoretical description of OCT in this section has been mainly followed from the second chapter of the book, optical coherence tomography: technology and applications (Izatt and Choma, 2008). The main difference between OCT and other forms of optical microscopy is that the predominant axial component of image formation derives from a ranging measurement performed using low coherence interferometry. Consider the Michelson interferometer illustrated in figure 2.5. The interferometer is illuminated by a polychromatic plane wave, whose electric field can be expressed as:

$$E_i = s(k, \omega)e^{i(kz - \omega t)} \quad \dots (2.1)$$

where $s(k, \omega)$ is the electric field amplitude as a function of wavenumber, $k = 2\pi/\lambda$ and angular frequency, $\omega = 2\pi\nu$, which are respectively the spatial and temporal frequencies of each spectral component of the field having wavelength, λ . The beamsplitter is assumed to have an achromatic power splitting ratio of 0.5 and the reference reflector is assumed to have an electric field reflectivity, r_R . The distance from the beamsplitter to the reference reflector is z_R . The sample under interrogation is characterized by its depth-dependent electric field reflectivity profile along the beam axis, $r_S(z_S)$, where z_S is the pathlength variable in the sample arm measured from the beamsplitter. Consider the sample to be consisting of N discrete, real delta function reflections of the form, $r_S(z_S) = \sum_{n=1}^N r_{Sn} \delta(z_S - z_{Sn})$, each reflection characterized by its electric field reflectivity, r_{S1} , r_{S2} etc. corresponding to pathlengths, z_{S1} , z_{S2} etc. The power reflectivity of the sample from different axial positions, $R_S(z_S)$, is given by the square of the magnitude of its electric field reflectivity, $r_S(z_S)$. The reconstruction of the function, $r_S(z_S)$, from the non-invasive interferometric measurements is the goal of low coherence interferometry in OCT.

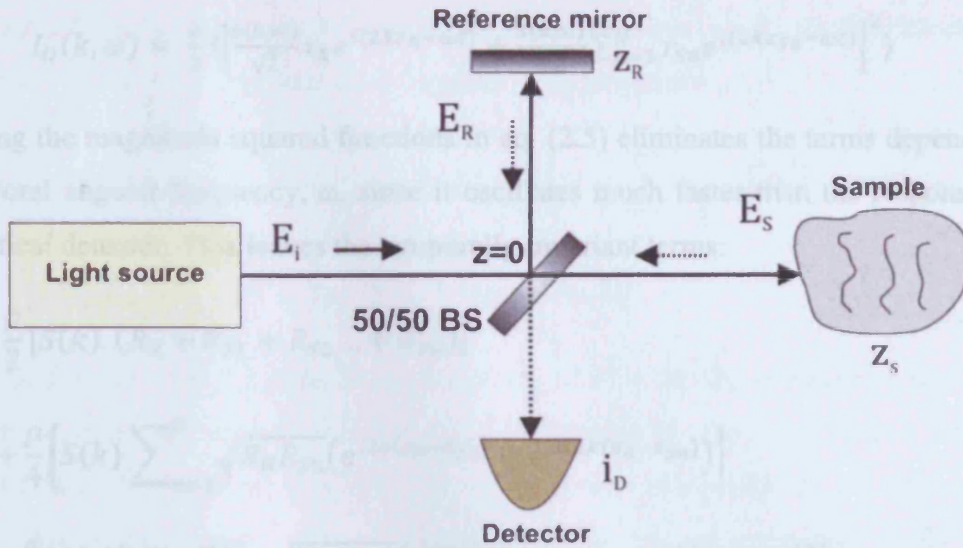


Figure 2.5: Schematic of a Michelson interferometer used in OCT

The electric field returning from the sample arm after passing through the beamsplitter is, $E_S = E_i/\sqrt{2} [r_S(z_S) \otimes e^{i2kz_S}]$, where \otimes represents convolution and the factor of 2 in the exponential kernel accounts for the round-trip pathlength to each sample reflection. For most of the biological tissues imaged with OCT, sample reflectivities are typically small in the order of 10^{-4} to 10^{-5} , thus the returned reference field typically dominates the reflected sample field in terms of signal intensity. The fields incident on the beamsplitter after returning from the reference and sample arms are given by:

$$E_R = \frac{E_i}{\sqrt{2}} r_R e^{i2kz_R} \quad \dots (2.2)$$

$$E_S = \frac{E_i}{\sqrt{2}} \sum_{n=1}^N r_{Sn} e^{i2kz_{Sn}} \quad \dots (2.3)$$

These returning fields are halved in power upon passing through the beamsplitter again and interfere at the square law detector, which generates a photocurrent proportional to the square of the sum of the fields incident upon it. The photocurrent,

$$I_D(k, \omega) = \frac{\rho}{2} \langle |E_R + E_S|^2 \rangle = \frac{\rho}{2} \langle (E_R + E_S)(E_R + E_S)^* \rangle \quad \dots (2.4)$$

Where ρ is the responsivity of the detector, the division by 2 accounts for a second pass of each field through the beamsplitter and the angular brackets denote integration over the response time of the detector. Arbitrarily setting $z = 0$ at the surface of the beamsplitter and expanding for the photocurrent gives:

$$I_D(k, \omega) = \frac{\rho}{2} \left\langle \left| \frac{s(k, \omega)}{\sqrt{2}} r_R e^{i(2kz_R - \omega t)} + \frac{s(k, \omega)}{\sqrt{2}} \sum_{n=1}^N r_{S_n} e^{i(2kz_{S_n} - \omega t)} \right|^2 \right\rangle \quad \dots (2.5)$$

Expanding the magnitude squared functions in eq. (2.5) eliminates the terms dependent upon the temporal angular frequency, ω , since it oscillates much faster than the response time of any practical detector. This leaves the temporally invariant terms:

$$\begin{aligned} I_D(k) &= \frac{\rho}{2} [S(k) \cdot (R_R + R_{S_1} + R_{S_2} \dots + R_{S_N})] \\ &+ \frac{\rho}{4} \left[S(k) \sum_{n=1}^N \sqrt{R_R R_{S_n}} (e^{i2k(z_R - z_{S_n})} + e^{-i2k(z_R - z_{S_n})}) \right] \\ &+ \frac{\rho}{4} [S(k) [S(k) \sum_{n=1}^N \sqrt{R_{S_n} R_{S_m}} (e^{i2k(z_{S_n} - z_{S_m})} + e^{-i2k(z_{S_n} - z_{S_m})})]] \quad \dots (2.6) \end{aligned}$$

where $S(k) = \langle |s(k, \omega)|^2 \rangle$ is substituted, which encodes the power spectral dependence of the light source. A Gaussian-shaped light source spectrum is convenient to use in modelling OCT, because it approximates the shape of the spectrum of actual light sources and also has useful Fourier transform properties. The axial resolution in OCT imaging is determined by the coherence length of the light source. The coherence length is the spatial width of the field autocorrelation measured by the interferometer. The envelope of the field correlation is equivalent to the Fourier transform of the power spectrum. Thus the coherence length is an explicit function of the light source bandwidth. The normalized Gaussian function, $S(k)$, characterized by central wavenumber, k_0 and spectral bandwidth, Δk , can be represented as $\frac{1}{\Delta k \sqrt{\pi}} e^{-\left[\frac{(k-k_0)}{\Delta k}\right]^2}$ and its inverse Fourier transform, $\gamma(z) = e^{-z^2 \Delta k^2}$, represents the envelope of the field correlation known as coherence function, which is also a Gaussian.

$$\gamma(z) = e^{-z^2 \Delta k^2} \xleftrightarrow{\mathcal{F}} S(k) = \frac{1}{\Delta k \sqrt{\pi}} e^{-\left[\frac{(k-k_0)}{\Delta k}\right]^2} \quad \dots (2.7)$$

This coherence function is commonly characterized by its full width at half maximum (FWHM) value, which is used to define coherence length, l_c , of a Gaussian light source. Hence coherence length of a light source with spectral bandwidth, Δk , can be determined as:

$$l_c = \frac{2\sqrt{\ln(2)}}{\Delta k} = \frac{2\ln(2)}{\pi} \frac{\lambda_0^2}{\Delta \lambda} \quad \dots (2.8)$$

where $\lambda_0 = 2\pi/k_0$, is the centre wavelength of the light source and $\Delta \lambda$ is its wavelength bandwidth.

Using Euler's rule to simplify eq. (2.6) generates a real result for the detector current as a function of wavenumber, known as 'spectral interferogram'.

$$I_D(k) = \frac{\rho}{4} [S(k) \cdot (R_R + R_{S1} + R_{S2} \dots + R_{SN})] + \frac{\rho}{2} \left[S(k) \sum_{n=1}^N \sqrt{R_R R_{Sn}} \cos[2k(z_R - z_{Sn})] \right] + \frac{\rho}{4} [S(k) \sum_{n \neq m=1}^N \sqrt{R_{Sn} R_{Sm}} \cos[2k(z_{Sn} - z_{Sm})]] \quad \dots (2.9)$$

The first term on the right hand side of eq. (2.9) is the DC component representing a pathlength-independent offset to detector current, scaled by the light source wavenumber spectrum and with amplitude proportional to the power reflectivity of the reference mirror plus the sum of the sample reflectivities. This is the largest component if the reference reflectivity dominates the sample reflectivity. The middle term is the cross-correlation component for each sample reflector, which depends upon both the light source wavenumber and the pathlength difference between the reference arm length and the respective sample reflector path lengths. This is the desired component of the OCT imaging. The last term on the right hand side of the equation is the autocorrelation component representing interference occurring between different sample reflectors and appears as artifacts in typical OCT images. The primary tool for reducing autocorrelation artifacts is the selection of proper reference reflectivity so that the autocorrelation terms are small compared to the DC and interferometric terms.

For a single reflector in the sample, only DC and a single interferometric term will be present and the source spectrum is modulated by a simple cosinusoid, whose period is proportional to the distance between the sample and the reference reflectors as shown in figure 2.6. Also, the amplitude of the spectral modulation will be proportional to the amplitude reflectivity of the sample reflector. For the case of multiple reflectors, the spectral interferogram is modulated by multiple cosinusoids, each having a frequency and amplitude characteristic of the sample reflector which give rise to it. Then there will be also autocorrelation components modulated according to the pathlength difference between the sample reflectors. These autocorrelation terms are typically small, since the sample reflectivities are small. Also their modulation frequencies will be small as reflections from within the sample tend to be clumped closely together, compared to the distance between the sample and the reference reflector.

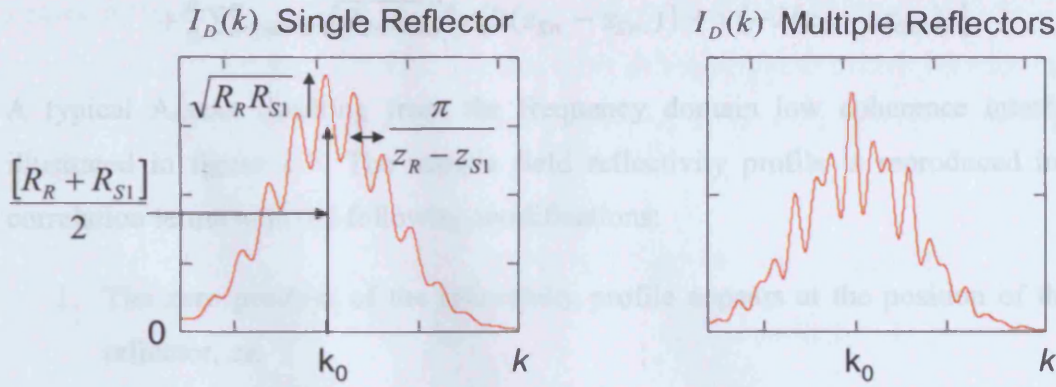


Figure 2.6: Important features of a spectral interferogram. For a single sample reflector of field reflectivity, $r_{S1} = 0.1$, the cross-correlation component with amplitude, $\sqrt{R_R R_{S1}}$ and wavenumber, $\frac{\pi}{z_R - z_{S1}}$ rides over the DC term of amplitude, $(R_R + R_{S1})/2$ (left). For multiple reflectors, cross-correlation component is a superposition of cosinusoids (right) (Izatt and Choma, 2008)

2.3.1 Frequency domain low coherence interferometry

In frequency domain OCT (FD-OCT), the wavenumber-dependent detector current, $I_D(k)$, is captured and processed using Fourier analysis to reconstruct an approximation of the internal sample reflectivity profile. In SD-OCT, a broadband light source is used and all spectral components of $I_D(k)$ are captured simultaneously on a detector array placed at the output of the spectrometer. However in SS-OCT, the spectral components of $I_D(k)$ are captured sequentially by recording the signal using a single photodetector, while synchronously sweeping the wavenumber of a narrowband swept-laser source.

The sample reflectivity profile is estimated from the inverse Fourier transform of $I_D(k)$ and hence taking the inverse Fourier transform of eq. (2.9),

$$\begin{aligned}
 i_D(z) &= \frac{\rho}{8} [\gamma(z)(R_R + R_{S1} + R_{S2} \dots + R_{S_N})] \\
 &+ \frac{\rho}{4} \left[\gamma(z) \otimes \sum_{n=1}^N \sqrt{R_R R_{S_n}} \delta(z \pm 2(z_R - z_{S_n})) \right] \\
 &+ \frac{\rho}{8} [\gamma(z) \otimes \sum_{n \neq m=1}^N \sqrt{R_{S_n} R_{S_m}} \delta(z \pm 2(z_{S_n} - z_{S_m}))] \quad \dots (2.10)
 \end{aligned}$$

Carrying out convolutions by taking advantage of shifting property of the delta function,

$$\begin{aligned}
 i_D(z) &= \frac{\rho}{8} [\gamma(z)(R_R + R_{S1} + R_{S2} \dots + R_{S_N})] \\
 &+ \frac{\rho}{4} \sum_{n=1}^N \sqrt{R_R R_{S_n}} [\gamma(2(z_R - z_{S_n})) + \gamma(-2(z_R - z_{S_n}))]
 \end{aligned}$$

$$+ \frac{\rho}{8} \sum_{n \neq m=1}^N \sqrt{R_{Sn} R_{Sm}} [\gamma(2(z_{Sn} - z_{Sm})) + \gamma(-2(z_{Sn} - z_{Sm}))] \quad \dots (2.11)$$

A typical A-scan resulting from the frequency domain low coherence interferometry is illustrated in figure 2.7. The sample field reflectivity profile is reproduced in the cross-correlation terms with the following modifications:

1. The zero position of the reflectivity profile appears at the position of the reference reflector, z_R .
2. The apparent displacement of each sample reflector from the reference position is doubled, since the interferometer measures the round-trip distance to each reflector.
3. Each reflector appears broadened to width of about a coherence length by convolution with the function, $\gamma(z)$, which is known as the point spread function of the imaging system.
4. The magnitude of detected sample reflectivity, which can be very small, is amplified by the large homodyne gain factor represented by the strong reference reflectivity, $\sqrt{R_R}$.

All of these modifications can be dealt with through proper interpretation of data. There are a number of additional modifications to the sample field reflectivity profile termed as artifacts. As it can be seen from eq. (2.11), a mirror image of the blurred version of $\sqrt{R_S(z_S)}$ appears on the opposite side of the zero pathlength delay. This is known as the complex conjugate artifact. This is due to the fact that since the detected interferometric spectrum is real, its inverse Fourier transform must be Hermitian symmetric, i.e., its positive and negative distances are complex conjugates of each other and are identical. This artifact can be avoided by keeping the sample entirely to one side of the zero delay. Additional image artifacts arise from the DC and autocorrelation terms in eq. (2.11). The DC term gives rise to a large artifact signal centred at zero delay. This component can be avoided by recording the amplitude of the spectral interferometric signal with the reference mirror without any sample and then subtracting this signal component from subsequent spectral interferometric signals acquired. The autocorrelation terms give rise to artificial signals at and near zero delay, since the distance between reflectors in a sample is typically much smaller than the distance between the sample reflectors and the reference mirror. The best method to eliminate autocorrelation signals is to ensure that the reference reflectivity is sufficient so that the amplitude of the autocorrelation terms is very small compared to cross-correlation terms. The DC,

should be corrected by multiplying the interferometric data with appropriate phase factors, prior to inverse Fourier transformation.

2.3.2 Time domain low coherence interferometry

In TD-OCT, the wavenumber-dependent detector current, $I_D(k)$, in eq. (2.9) is captured using a single detector, while the reference delay, z_r , is scanned to reconstruct an approximation of the internal sample reflectivity profile. By integrating eq. (2.9) in k -space,

$$I_D(z_R) = \frac{\rho}{4} [S_0(R_R + R_{S1} + R_{S2} \dots + R_{Sn})] + \frac{\rho}{2} [S_0 \sum_{n=1}^N \sqrt{R_R R_{Sn}} e^{-(z_R - z_{Sn})^2 \Delta k^2} \cos(2k_0(z_R - z_{Sn})))] \quad \dots (2.12)$$

where $S_0 = \int_0^\infty S(k)dk$ is the spectrally integrated power emitted by the light source.

The resulting time domain A-scan is shown in figure 2.9. The first term represents the DC offset, which is proportional to the sum of the reference and the sample power reflectivities and the second term is the cross-correlation term containing the sample reflectivity profile. It is modulated by a cosinusoidal carrier wave at a frequency proportional to the centre wavenumber of source, k_0 and the path length difference between reference and sample arms.

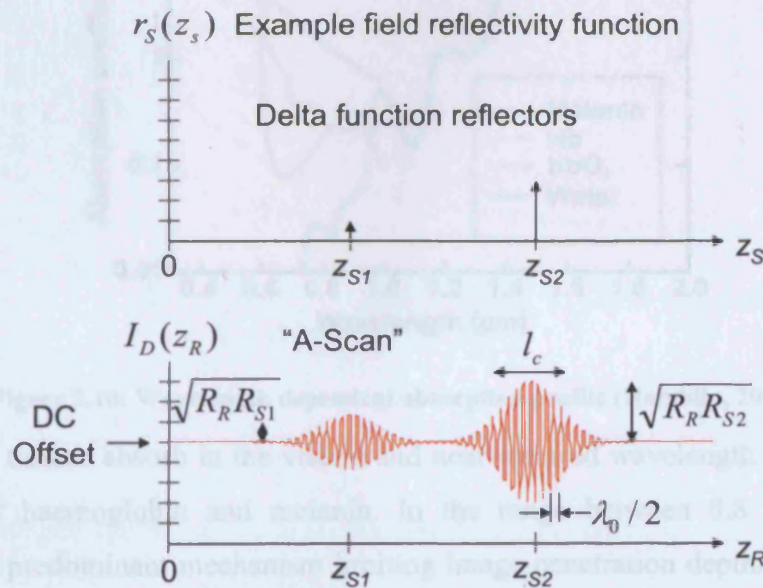


Figure 2.9: Illustration of an example discrete reflector sample field reflectivity function, $r_s(z_s)$ (top) and the A-scan resulting from time domain low coherence interferometry (bottom) (Izatt and Choma, 2008)

2.4 Key parameters of OCT

The performance parameters of an OCT system are mainly determined by its axial resolution, transverse resolution, detection sensitivity and data acquisition specifications such as digital resolution and imaging speed. For medical diagnostic applications, in addition to the visualization of microstructural morphology, factors such as non-contact applicability, adequate penetration to the investigated tissue, sufficient image contrast and extraction of functional or biochemical information have to be considered. For clinical applications, compactness, non-invasiveness, repeatability, imaging speed, flexibility, overall expenditure of the OCT system, user friendliness and possibility of interfacing it with existing diagnostic technologies are also decisive factors.

2.4.1 Centre wavelength of the light source

OCT imaging at different wavelengths can be used to measure scattering and absorption properties of various pigments and structures, as well as to enhance tissue contrast and penetration. The difference in tissue scattering and absorption provides the structural contrast for OCT. Scattering and absorption properties of a tissue are dependent on the tissue composition as well as on the physiological state of certain chromophores.

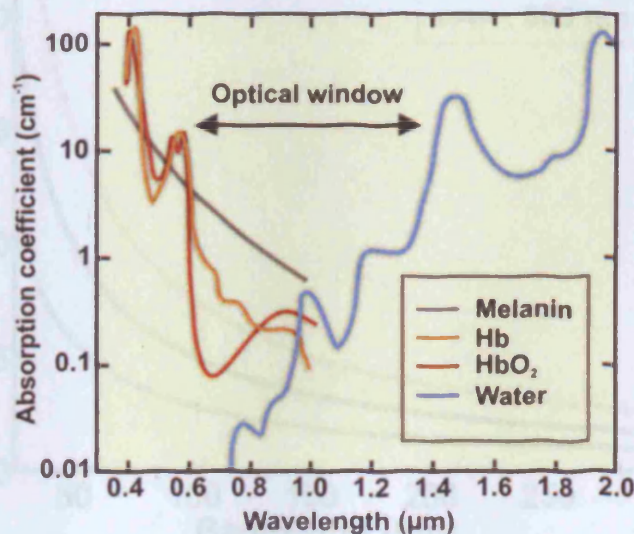


Figure 2.10: Wavelength dependent absorption profile (Hamblin, 2006)

Most biological tissues absorb in the visible and near-infrared wavelength region because of the presence of haemoglobin and melanin. In the range between 0.8 μm and 1.8 μm , scattering is the predominant mechanism limiting image penetration depth. The scattering of light within a biological tissue is scaled as, $1/\lambda_c^k$, where λ_c is the centre wavelength of the light source and the coefficient, k , is dependent on the size, shape and relative refractive

index of the scattering particles (Schmitt, 1999). Thus, the penetration depth can be increased by using longer wavelengths. However, since water constitutes 50% to 90% of its content in most tissues, water absorption becomes a major problem for wavelengths greater than 1.8 μm . The wavelength-dependent absorption coefficients for the major absorbing components of biological tissues are shown in figure 2.10 (Hamblin, 2006).

2.4.2 Axial and transverse resolutions

In contrast to standard microscopy, OCT can achieve fine axial resolution independent of beam focussing and spot size. Its axial resolution is mainly governed by the coherence length of the light source, which in turn is proportional to the spatial width of its field autocorrelation measured by the interferometer. Moreover, the envelope of the field autocorrelation is related to the Fourier transform of its power spectrum. Hence, the coherence length or axial resolution is inversely proportional to the spectral bandwidth of the light source.

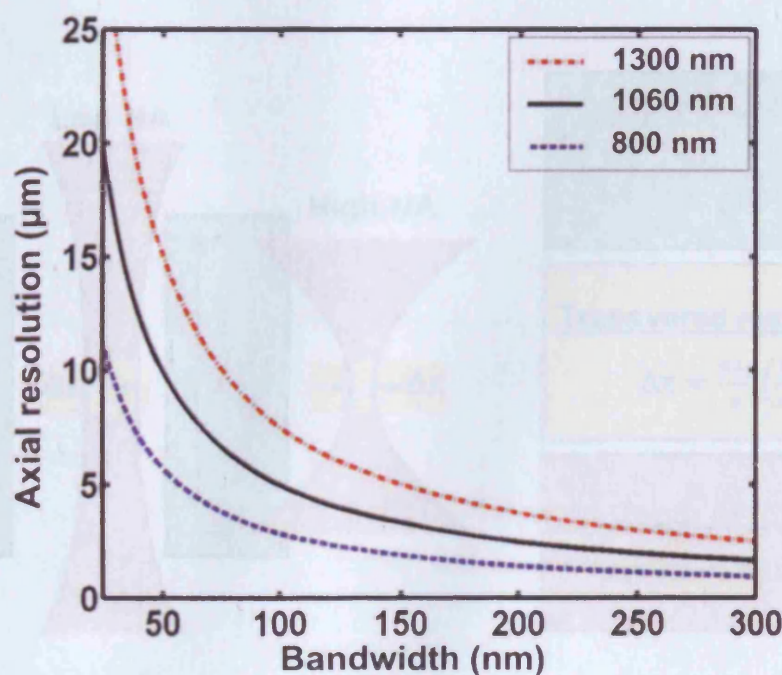


Figure 2.11: Axial resolution versus light source bandwidth for different centre wavelengths (Fujimoto and Drexler, 2008)

For a Gaussian-shaped spectrum, the axial resolution in free space is,

$$\Delta Z = \frac{2 \ln(2) \lambda_0^2}{\pi \Delta \lambda} \quad \dots (2.13)$$

where Δz and $\Delta\lambda$ are FWHM of the autocorrelation function and power spectrum respectively and λ_0 is the centre wavelength of the source. Hence broadband light sources are used in OCT to achieve high axial resolution. Figure 2.11 shows a plot of axial resolution versus bandwidth for light sources with different centre wavelengths.

The transverse resolution in OCT is the same as in optical microscopy and is determined by the diffraction-limited spot size of the focussed optical beam. The transverse spot size of a Gaussian beam is defined as radius at which intensity reduces to $1/e^2$ times its central value. It is inversely proportional to the numerical aperture of the objective lens. The transverse resolution is given by,

$$\Delta x = \frac{4\lambda_0}{\pi} \left(\frac{f}{d} \right) = 1.22 \frac{\lambda_0}{2NA_{obj}} \quad \dots (2.14)$$

where d is the spot size on the objective lens, f is focal length of the objective lens and NA_{obj} is its numerical aperture.

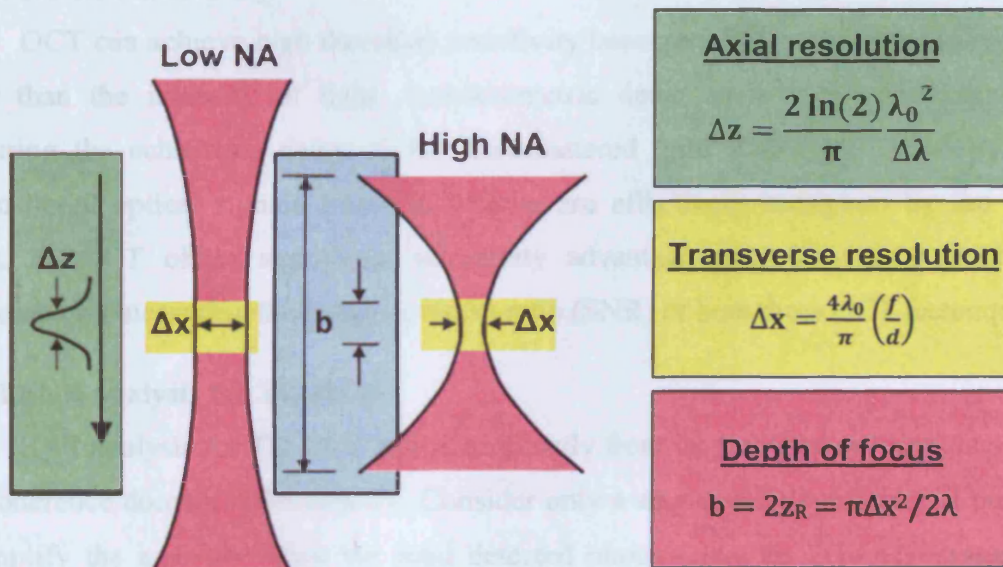


Figure 2.12: Transverse resolution limits in OCT (Drexler et al., 2008)

The transverse resolution is also related to the depth of the field, quantified by the confocal parameter, $b = 2z_R = \pi \Delta x^2 / 2\lambda$, where z_R is the Rayleigh range. Rayleigh range is the distance from the focus at which beam spot size increases by a factor of $\sqrt{2}$. Thus, high transverse resolution OCT imaging can be achieved by focussing with a high numerical

aperture objective lens at the expense of the reduced depth of field as shown in figure 2.12. To overcome this depth of field limitation caused by high numerical aperture, C-mode scanning, special imaging lenses (Ding et al., 2002) or dynamic focus tracking (Schmitt, Lee and Yung, 1997) can be used to maintain high transverse resolution throughout the whole penetration depth.

Typically OCT imaging is performed with a low numerical aperture focussing in order to have a large depth of field. Then the confocal parameter, $b > \Delta z$, and low coherence interferometry is used to achieve high axial resolution. It is also possible to perform OCT with a high numerical aperture focussing, in order to achieve fine transverse resolutions. Then, $b < \Delta z$, and the depth of field can be used to differentiate backscattering or back reflected signals from different depths. This mode of operation is known as optical coherence microscopy (OCM). This is useful in imaging scattering systems because coherence gating rejects scattered light in front and behind the focal plane more effectively than confocal gating alone.

2.4.3 Detection sensitivity

OCT can achieve high detection sensitivity because interferometry measures the field rather than the intensity of light. Interferometric detection is a powerful approach for measuring the echo time delay of the backscattered light with high sensitivity. Weakly backscattered optical signals from the sample are effectively multiplied by the reference signal. FD-OCT offers significant sensitivity advantage over TD-OCT, which can be determined by measuring the signal-to-noise ratio (SNR) of both these OCT techniques.

2.4.3.1 SNR analysis for TD-OCT

SNR analysis for TD-OCT followed directly from its predecessor technique of optical low-coherence domain reflectometry. Consider only a single sample reflector at position, z_s , to simplify the analysis. Then the total detected photocurrent in TD-OCT system can be obtained from eq. (2.12) as:

$$I_D(z_R) = \frac{\rho S_{TD-OCT}}{2} [R_R + R_S + 2\sqrt{R_R R_S} e^{-(z_R - z_S)^2 \Delta k^2} \cos(2k_0(z_R - z_S))] \quad \dots (2.15)$$

where $S_{TD-OCT} = S_0/2$ is the instantaneous power incident in the sample and reference arms. The desired OCT signal resides in the third term on the right hand side of eq. (2.15), whose mean-square peak signal power at $z_R = z_S$ is, $\langle I_D \rangle_{TD-OCT}^2 = \frac{\rho^2 (S_{TD-OCT})^2}{2} [R_R R_S]$. The main

noise sources of interest are receiver noise, shot noise and excess photon noise. However, shot noise limited performance has been achieved by the optimal design of OCT systems. Shot noise variance in an optical receiver is given by, $\sigma_{sh}^2 = 2e\bar{I}B$, where e is the electronic charge, \bar{I} is the mean detector photocurrent and B is the electronic detection bandwidth. Assuming that the light intensity backscattered from the sample is much smaller than that reflected from the reference mirror, the mean detector photocurrent, $\bar{I} = \frac{\rho S_{TD-OCT} R_R}{2}$. Let the electronic detection bandwidth, $B = B_{TD-OCT}$, then $\sigma_{TD-OCT}^2 = \rho e S_{TD-OCT} R_R B_{TD-OCT}$. Thus, SNR of a TD-OCT system is given by:

$$SNR_{TD-OCT} = \frac{\langle I_D \rangle_{TD-OCT}^2}{\sigma_{TD-OCT}^2} = \frac{\rho S_{TD-OCT} R_S}{2e B_{TD-OCT}} \quad \dots (2.16)$$

Hence, the SNR of a TD-OCT system in the shot noise limit is proportional to the optical power returning from the sample and inversely proportional to the electronic detection bandwidth.

2.4.3.2 SNR analysis for FD-OCT

To calculate the SNR of a FD-OCT system, the propagation of signal and noise through the spectral sampling and inverse Fourier transform processes has to be analyzed. Assume that there is only a single sample reflector and autocorrelation terms are absent for the simplicity of the analysis. The sampled version of spectral interferogram in a FD-OCT system can be obtained from eq. (2.9) as:

$$I_D(k_m) = \frac{\rho S_{FD-OCT}(k_m)}{2} [R_R + R_S + 2\sqrt{R_R R_S} \cos(2k_m(z_R - z_S))] \quad \dots (2.17)$$

where $S_{FD-OCT}(k_m) = \frac{S(k)|_{k=k_m}}{2}$, is that portion of instantaneous power incident on the sample which corresponds to spectral channel 'm' of the detection system, whether time-multiplexed in SS-OCT or on separate detectors in SD-OCT. In the discrete case, the inverse Fourier transform operation is implemented as an inverse discrete Fourier transform, $i_D(z_m) = \sum_{m=1}^M I_D(k_m) e^{ik_m z_m / M}$, where $z_m = z_R - z_S$. Assume a rectangular source spectrum in which each spectral channel will have equal power in it. Then applying inverse discrete Fourier transform to the peak value of the interferometric term in eq. (2.17) gives,

$$i_D(z_m = 0) = \frac{\rho}{2} \sqrt{R_R R_S} \sum_{m=1}^M S_{FD-OCT}(k_m) = \frac{\rho}{2} \sqrt{R_R R_S} S_{FD-OCT}(k_m) \cdot M \quad \dots (2.18)$$

Thus in FD-OCT the cosinusoidal spectral interference pattern in each separate detection channel from a single reflector adds coherently to give a peak signal power much greater than the signal power in each channel alone. Due to its restricted spectral extent, each detection channel in FD-OCT senses interference over a much longer coherence length than single detection channel in TD-OCT. Thus mean-square peak signal power in FD-OCT is given by,

$$\langle i_D \rangle_{FD-OCT}^2 = \frac{\rho^2(S_{FD-OCT}(k_m))^2}{4} [R_R R_S] \cdot M^2.$$

$I_D(k_m)$ can be generalized to include an additive, uncorrelated Gaussian white noise terms, $\alpha(k_m)$, with standard deviation, $\sigma(k_m)$. The mean of this noise term is zero and its lower limit is set by the shot noise. Since the noise in each spectral channel is uncorrelated, noise variances add incoherently in the inverse Fourier summation to give,

$$\sigma_{FD-OCT}^2(z_m) = \sum_{m=1}^M \sigma_{FD-OCT}^2(k_m) = \rho e [S_{FD-OCT}(k_m)] R_R B_{FD-OCT} \cdot M \quad \dots (2.19)$$

Thus SNR of FD-OCT is given by:

$$SNR_{FD-OCT} = \frac{\langle i_D \rangle_{FD-OCT}^2}{\sigma_{FD-OCT}^2} = \frac{\rho [S_{FD-OCT}(k_m)] R_S}{4e B_{FD-OCT}} \cdot M \quad \dots (2.20)$$

To specialise these expressions for SD-OCT and SS-OCT systems and to compare the resulting sensitivities with TD-OCT, assume that the A-scan length and acquisition time is identical for all three systems and have same instantaneous power in sample arm. For an SD-OCT system, the allowable power per spectral channel is decreased by the factor, M and the detection bandwidth, $B_{SD-OCT} = B_{TD-OCT}/M$, since signals from each channel is integrated over entire A-scan period. For an SS-OCT system, the allowable sample illumination power for each spectral channel is same as the total illumination power for TD-OCT. Also, detection bandwidth is limited by analog-to-digital sampling frequency and it is equal to the detection bandwidth of TD-OCT. Thus, SNR of SS-OCT and SD-OCT systems compared to TD-OCT can be written as:

$$SNR_{SD-OCT} = SNR_{SS-OCT} = \frac{\rho S_{TD-OCT} R_S}{4e B_{TD-OCT}} M = SNR_{TD-OCT} \cdot \frac{M}{2}$$

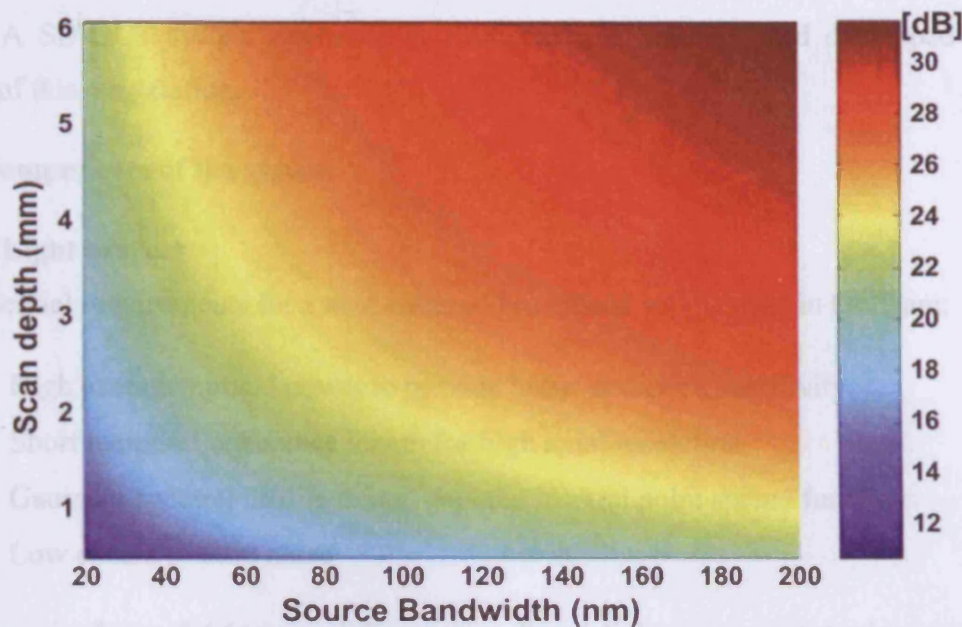


Figure 2.13: Sensitivity advantage ($\text{SNR}_{\text{FD-OCT}}/\text{SNR}_{\text{TD-OCT}}$) of FD-OCT over TD-OCT (Choma et al., 2003)

The improvement in SNR of both SD-OCT and SS-OCT over TD-OCT is due to the fact that both FD-OCT systems sample the entire depth all the time giving rise to a potential SNR improvement by a factor, M and this improvement is decreased by a factor of 2, since both these systems generate redundant data for positive and negative sample displacements relative to the reference position. Assuming that $M \approx 10^3$ for a realistic detector array or swept-source laser, FD-OCT systems are theoretically capable of upto 20 dB greater sensitivity than TD-OCT systems (Choma et al., 2003). The sensitivity advantage defined as $\text{SNR}_{\text{FD-OCT}}/\text{SNR}_{\text{TD-OCT}}$ expressed in dB is graphically represented in figure 2.13.

2.5 SD-OCT system at 1300 nm

A SD-OCT system operating at 1300 nm was designed and developed during the course of this dissertation.

2.5.1 Components of the system

2.5.1.1 Light sources

The essential requirements for a near-infrared broadband source used in OCT are:

- High average optical power to provide better detection sensitivity
- Short temporal coherence length for high axial resolution
- Gaussian spectral profile to prevent tails in axial point spread function
- Low excess photon noise

As shown in figure 2.14, three different broadband light sources centred around 1300 nm were used with this SD-OCT system: (1) a Ytterbium (Yb)-doped fibre laser (de Matos, Popov and Taylor, 2004), (2) a superluminescent diode (SLD) with 100 nm bandwidth (Thorlabs Inc., Newton, New Jersey) and (3) a SLED with 170 nm bandwidth (Praevium Inc., Santa Barbara, California).

2.5.1.1.1 Ytterbium-doped fibre laser

Supercontinuum generation using photonic crystal fibres have emerged as an important technique to produce broadband optical sources within the last few years. In the broadband laser employed with this OCT system, a fibre grating based commercial Yb-doped fibre laser (YDFL) was employed as the pump source. The continuous wave, 10 W YDFL (IPG Photonics, Oxford, Massachusetts) had a FWHM linewidth of around 0.8 nm and unpolarized output. The fibre output of the pump was directly spliced to a 100 m photonic crystal fibre to generate the continuum. The spectral output of the continuum at photonic crystal fibre output is brought close to Gaussian by using an optical fibre wavelength-division multiplexing coupler. The output power from the source was around 550 mW and FWHM bandwidth was around 140 nm centred at 1245 nm (de Matos et al., 2004).

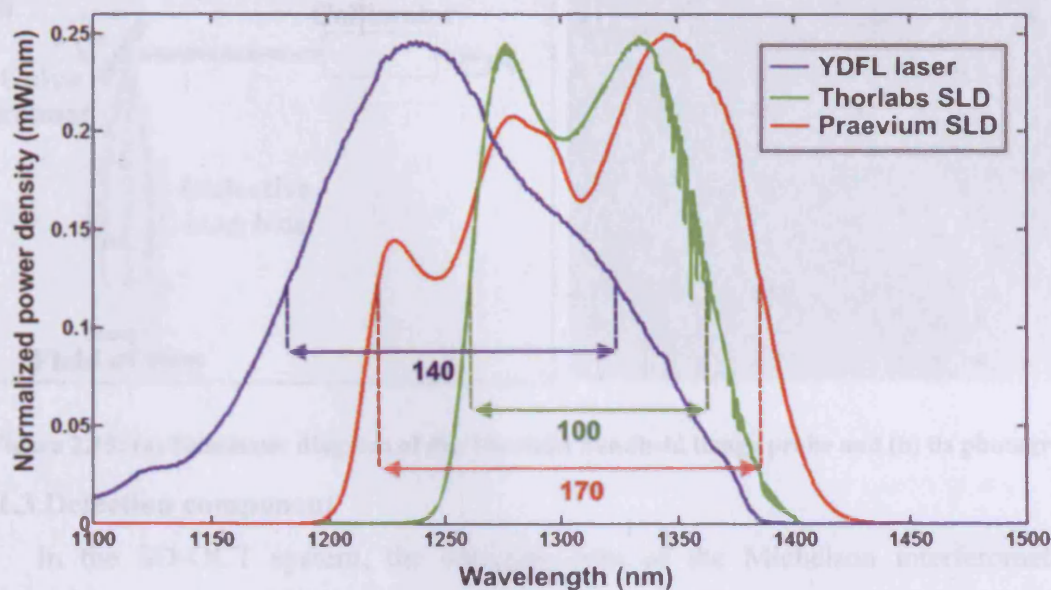


Figure 2.14: Spectra of the three different light sources used with the 1300 nm SD-OCT system

2.5.1.1.2 Superluminescent diodes

SLDs have always been attractive light sources for OCT due to their compactness, low cost, robustness and ease to operate. Until recently, the bandwidths and output powers of SLDs were relatively limited. However, significant advances have been made in SLD performance to provide broad bandwidths comparable to that of femtosecond laser sources (Schmitt et al., 1997; Ko et al., 2004; Wang, Jenkins and Rollins, 2008). In this SD-OCT system, two SLDs centred around 1300 nm with a FWHM bandwidth of 100 nm and 170 nm were used. The output power of the 100 nm and 170 nm SLEDs were 30 mW and 11 mW respectively. The noise was less for the SLEDs when compared to the Yb-doped fibre laser. However, the SNR of the OCT system was better while using the fibre laser due to its higher output power.

2.5.1.2 Imaging probe

The sample arm of the SD-OCT system was coupled to a handheld imaging probe (Thorlabs Inc., Newton, New Jersey) for obtaining 3D *in vivo* images [Figure 2.15]. It consisted of a collimator, two galvanometric mirrors for scanning in two dimensions and a focussing lens. The focussing lens was an achromatic doublet, which helped to reduce spherical and chromatic aberrations, as well as coupled back the backscattered light from the sample more efficiently. For imaging fixed specimens, the scanning head of the handheld probe was mounted onto a 2D translation stage.

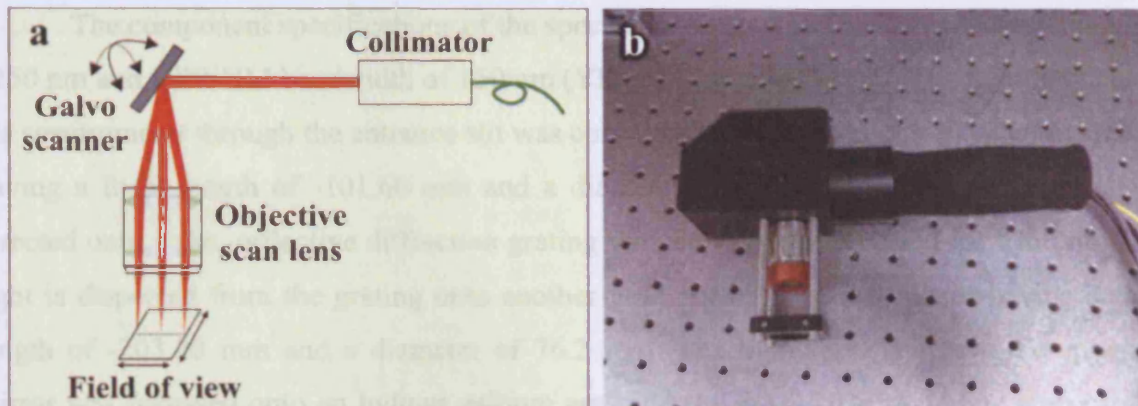


Figure 2.15: (a) Schematic diagram of the Thorlabs handheld image probe and (b) its photograph

2.5.1.3 Detection component

In the SD-OCT system, the detection arm of the Michelson interferometer was connected to a spectrometer. The all-reflective spectrometer in this system was based on a Czerny-Turner configuration (Shafer, Megill and Droppleman, 1964), which operated in a very compact geometry, maximizing mechanical stability and minimizing internal chromatic aberrations. In a Czerny-Turner spectrometer, coma aberrations induced by a spherical collimating mirror are partially compensated using a symmetrical, but oppositely oriented spherical focussing mirror. The ray-tracing diagram of a typical Czerny-Turner spectrometer is shown in figure 2.16. This spectrometer was optimized using the optical designing software known as ZEMAX (ZEMAX development corporation, Bellevue, Washington).

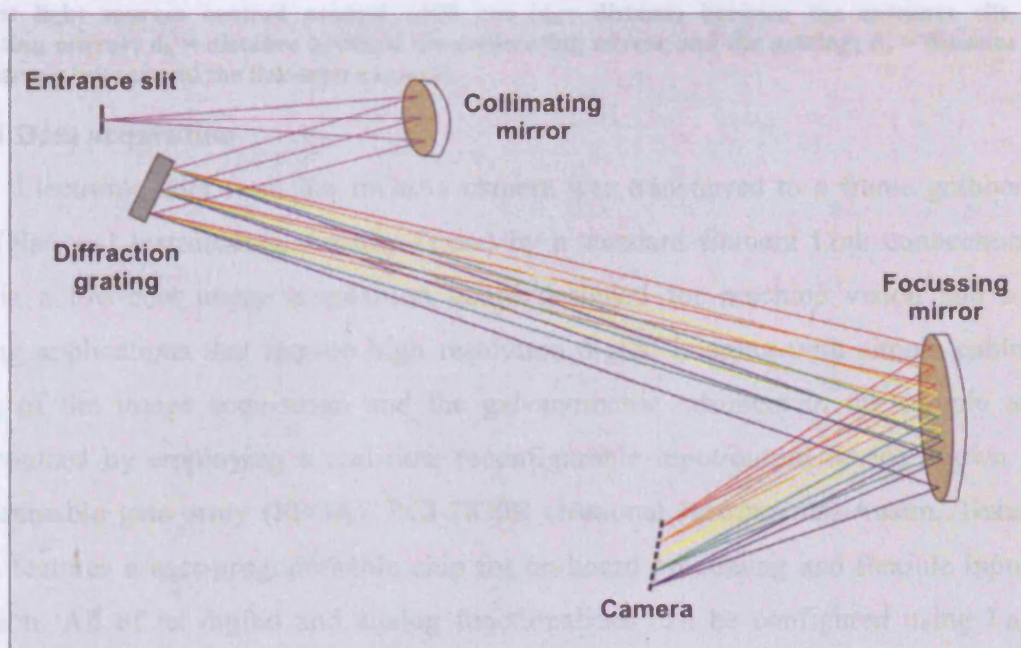


Figure 2.16: Ray tracing diagram of the Czerny-Turner spectrometer employed in this system

The component specifications of the spectrometer designed for a centre wavelength of 1250 nm and a FWHM bandwidth of 150 nm (YDFL) is detailed below. The light incident on the spectrometer through the entrance slit was collimated using a gold-coated spherical mirror having a focal length of -101.60 mm and a diameter of 25.4 mm. The collimated light is directed onto a flat, reflective diffraction grating with 600 lines/mm blazed for 1250 nm. The light is dispersed from the grating onto another gold-coated spherical mirror having a focal length of -203.20 mm and a diameter of 76.2 mm. The light reflected from the spherical mirror was focussed onto an Indium gallium arsenide (InGaAs) 1024 pixel line scan camera (Sensors Unlimited Inc., Princeton, New Jersey) with 25 μm pixel pitch. This high-speed near-infrared camera was capable of recording the spectrum (A-line) at a maximum rate of 47 kHz. Various modifications in the spectrometer design and components that were required to adapt the spectrometer for different light sources are given in table 2.1.

Light source	d_a (mm)	d_b (mm)	Grating (lines/mm)	d_c (mm)
Yb-doped fibre laser	118	100	600	145
100 nm SLD	116	101	830	147
170 nm SLD	107	100	600	188

Table 2.2: Comparison of the spectrometer specifications of the SD-OCT system, while employing different light sources centred around 1300 nm (d_a = distance between the entrance slit and the collimating mirror; d_b = distance between the collimating mirror and the grating; d_c = distance between the focussing mirror and the line-scan camera).

2.5.1.4 Data acquisition

Electronic data from the InGaAs camera was transferred to a frame grabber, PCIe-1427 (National Instruments, Austin, Texas) by a standard Camera Link connection. PCIe-1427 is a low-cost image acquisition board designed for machine vision and scientific imaging applications that require high resolution digital imaging with simple cabling. The timing of the image acquisition and the galvanometric scanners in the sample arm was synchronized by employing a real-time reconfigurable input/output device known as field programmable gate array (FPGA), PCI-7830R (National Instruments, Austin, Texas). This FPGA features a user-programmable chip for on-board processing and flexible input/output operation. All of its digital and analog functionalities can be configured using LabVIEW (National Instruments, Austin, Texas) graphical block diagrams and the FPGA module. The block diagram executes in the hardware, giving direct and immediate control over all

input/output signals to deliver high performance capabilities such as complete control over timing and triggering of signals, onboard decision making and individually configurable digital lines.

2.5.2 Implementation of the SD-OCT system

A fibre-optic coupler with an asymmetric splitting ratio was used to divide the light from the source into reference and sample arms. Previous studies have demonstrated improvements in SNR of an OCT system by obtaining higher signal feedback from the sample using asymmetric beam splitters. The ratio between the power back reflected from the attenuated reference arm and the sample arm has to be optimized with the dynamic range of the detector for obtaining the maximum SNR (Rollins and Izatt, 1999). Depending on the output power from the source, a fibre-optic coupler with a splitting ratio providing the maximum SNR was employed in this SD-OCT system.

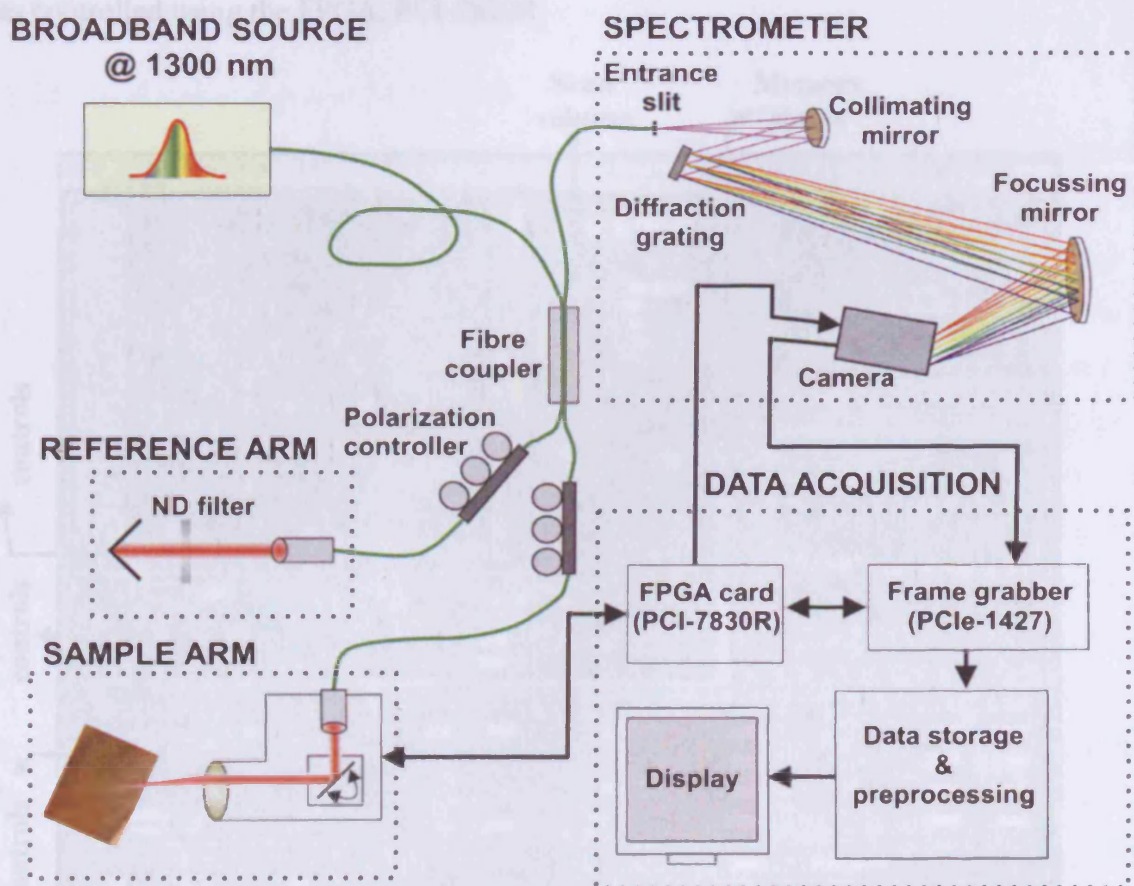


Figure 2.17: Schematic of the 1300 nm SD-OCT system

As shown in figure 2.17, the reference arm consisted of a free-space pathway with a variable neutral density filter for adjusting the reference arm power and a retroreflector

mounted on a translation stage for changing the relative path length, while the sample arm consisted of a handheld probe with two galvanometric mirrors for scanning in two dimensions. The base metal frame for setting up the reference arm was made of aluminium in the mill. Polarization controllers were used in both arms of the interferometer to adjust polarization mismatch and thus, to improve the SNR of the system.

The light returning from both arms was recombined in the coupler and was fed to the input of the spectrometer through the fourth arm of the fibre coupler. The spectrometer dispersed the signal across various constituent wavelengths using the diffraction grating and the interference spectrum was recorded using the InGaAs line scan camera. With 512 A-lines per B-scan, this camera was capable of recording more than 80 frames/second. The captured data was then transferred to the frame grabber, PCI-1427, by the Camera Link connection. The timing of image acquisition and the scanning of galvanometric mirrors in the sample arm was controlled using the FPGA, PCI-7830R.

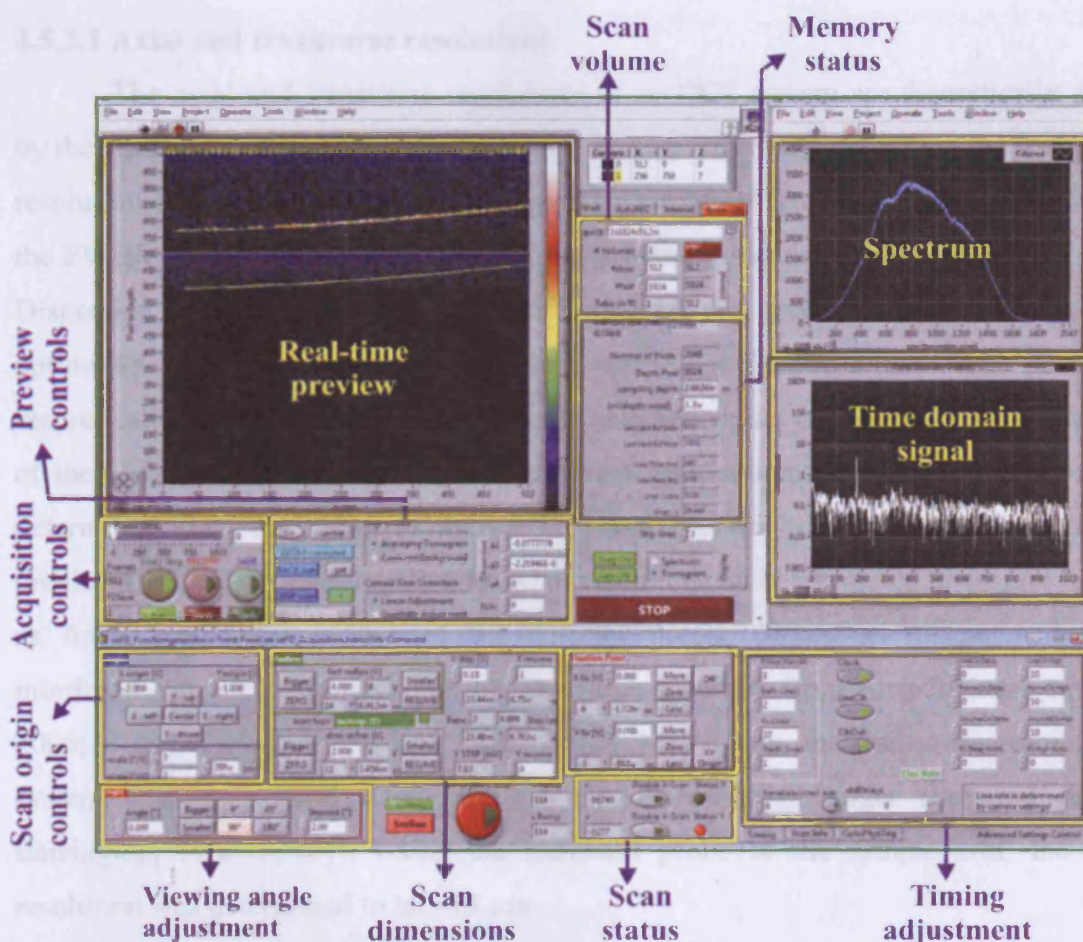


Figure 2.18: Front panel of LabVIEW image acquisition program displaying real-time image of a glass slide (Hofer, 2010)

Communications between these components of the image acquisition hardware were regulated by a LabVIEW programming interface. The LabVIEW program for OCT image acquisition was designed by Dr. Bernd Hofer, Biomedical Imaging Group, Cardiff University. The image acquisition program in LabVIEW performed several important functions such as controlling the scan dimensions; saving OCT data in a particular file format and processing a raw spectral data to generate a real-time preview of OCT image. The front panel of the LabVIEW image acquisition program that was used to manage OCT imaging sessions is shown in figure 2.18. The saved spectral data was inverse Fourier transformed and further processed in MATLAB (The MathWorks Inc., Natick, Massachusetts) to obtain actual image. The MATLAB program for OCT image processing was written and developed by Dr. Bernd Hofer and Dr. Boris Hermann, Biomedical Imaging Group, Cardiff University (Hofer, 2010).

2.5.3 Characterization of the SD-OCT system

2.5.3.1 Axial and transverse resolutions

The axial and transverse resolutions of an OCT system are theoretically determined by the equations 2.13 and 2.14 respectively. To experimentally determine the free-space axial resolution of the SD-OCT system, images of a single reflector like mirror was obtained and the FWHM of its signal peak (i.e., axial point spread function) provided the axial resolution. Dispersion mismatch between the two arms and the spectral shape of the source was optimized using software to achieve best possible axial resolution. Table 2.3 gives the theoretically determined and experimentally obtained values of the free-space axial resolution of the OCT system, when employing different light sources. However, the experimentally determined axial resolution of the OCT system was slightly lower than the theoretically predicted values. This degradation in axial resolution can be attributed to several factors such as finite spatial dimensions of the detector pixels, dispersion mismatch between the interferometer arms and deviation of the source spectrum from perfect Gaussian (Lu et al., 2006; Bousi, Charalambous and Pitris, 2010). Meanwhile, the transverse resolution of the system was determined using a 1951 USAF resolution target (Edmund optics Ltd., Barrington, New Jersey). Using the handheld probe in the sample arm, the transverse resolution was determined to be $\sim 15 \mu\text{m}$.

Light source	Axial resolution (μm)	
	Theoretical	Experimental
Yb-doped fibre laser	4.9	~ 5.4
100 nm SLD	7.7	~ 8.4
170 nm SLD	4.4	~ 5.0

Table 2.3: Comparison of theoretically calculated and experimentally determined axial resolution values for different light sources employed with the 1300 nm SD-OCT system.

2.5.3.2 Axial and transverse scaling

The actual spatial dimensions corresponding to each voxel had to be experimentally determined to ensure proper scaling of the OCT images. The scaling in axial direction was done using two or three glass cover slips of known thickness. The cover slips were arranged on top of each other in a fashion as shown in figure 2.19, with the middle one extending only in one half of the B-scan. OCT measures the optical thickness of the cover slip. Its refractive index is determined by comparing its optical thickness, t_{opt} to the corresponding thickness of air-filled gap, $t_{\text{air gap}}$. Since the actual physical thickness of the cover slip was known, the spatial dimension corresponding to a pixel along the depth in an OCT image could be determined accurately. Three cover slips with physical thickness of 0.19mm were used for axial scaling measurements.

The scaling in transverse directions was performed using a 1951 USAF resolution target [Figure 2.19]. Since the number of line pairs per mm for a particular element group in the resolution target was provided, the physical dimensions of a scan region for a given voltage can be calculated by scanning it across one of its element groups.

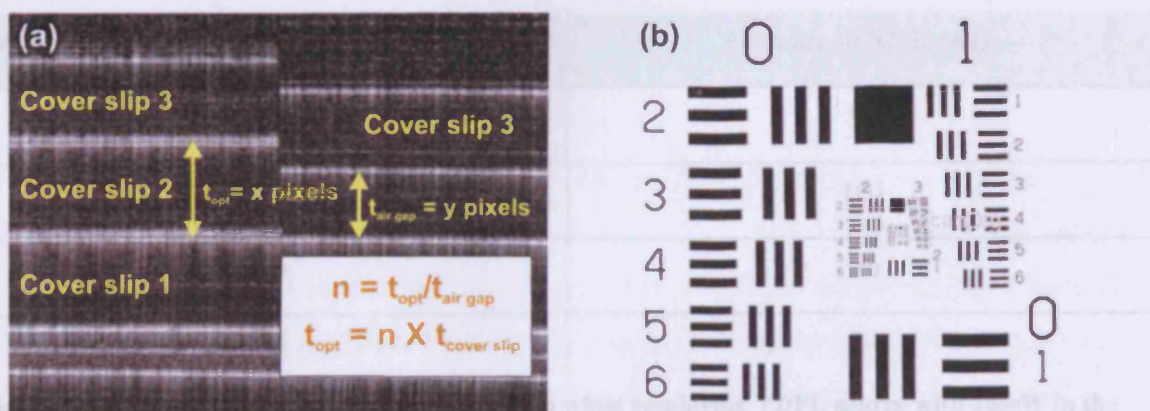


Figure 2.19: (a) Axial scaling set up using three glass slides of known thickness (t_{opt} = optical thickness of cover slip in pixels; $t_{\text{air gap}}$ = thickness of air gap in pixels; $t_{\text{cover slip}}$ = physical thickness of the cover slip in millimetres). (b) 1951 USAF resolution target used for transverse scaling

2.5.3.3 Detection sensitivity

SNR of this system was experimentally determined by taking the ratio of the signal peak from a plane mirror kept close to the zero delay and the noise floor. A neutral density filter of optical density, d , was inserted in front of the mirror in the sample arm to make the optical power returning to the detector comparable to the power backscattered from the biological tissue. Hence the total SNR of the system is given by,

$$SNR_{total} = 2 \times 10 \log \left(\frac{I}{I_0} \right) + 20 \log \left(\frac{S}{N} \right)$$

where I_0 = incident intensity at the sample arm, I = transmitted intensity by the neutral density filter, S = amplitude of the signal peak and N = amplitude of the noise floor. The factor, 2, in the first term on the right hand side of the equation accounts for the round trip attenuation produced by the neutral density filter.

In order to find the optimum splitting ratio of the fibre coupler, the SNR was measured employing fibre couplers of different splitting ratio. The output power of the YDFL was reduced using a fibre optic attenuator to a level that avoids saturation of the camera, but provides maximum SNR. Due to the higher available power of YDFL, an optimum SNR of ~ 101 dB at 20 mW in the sample arm was obtained using a 90/10 fibre coupler. Hence a 90/10 coupler was used for obtaining OCT images with the YDFL source. However, for the 100 nm SLD, the optimum SNR obtained using a 90/10 fibre coupler was ~ 94 dB with 3 mW in the sample arm. Meanwhile, for the 170 nm SLD, due to its lower output power and increased detection bandwidth, a maximum SNR of around ~ 90 dB was obtained using a 70/30 coupler with 2.5 mW in the sample arm.

Fibre coupling ratio (ref. arm : sample arm)	Measured SNR (dB)
94:6	98
90:10	101
70:30	96
50:50	94

Table 2.4: Comparison of the SNR of the OCT system while employing YDFL source with 20mW in the sample arm

In SD-OCT, signal sensitivity is strongly dependent on the depth within the image (Yun et al., 2003). The two important factors determining the signal fall off and maximum imaging depth in SD-OCT are the spectral resolution of the spectrometer and the spectral sampling interval respectively (Leitgeb et al., 2003). The sensitivity fall-off in SD-OCT is mainly due to the decrease in visibility of higher fringe frequencies corresponding to large sample depths. The sensitivity degradation of this system as a function of imaging depth was determined by attaching the spectrometer to a free space interferometer. The sample arm of the free space interferometer consisted of a retroreflector mounted on a motorized translation stage. Spectral interferograms were recorded from different positions separated by 200 μm across the entire imaging range of ~ 2.2 mm. As shown in figure 2.20, the peak signal dropped by 20 dB over the first 2 mm.

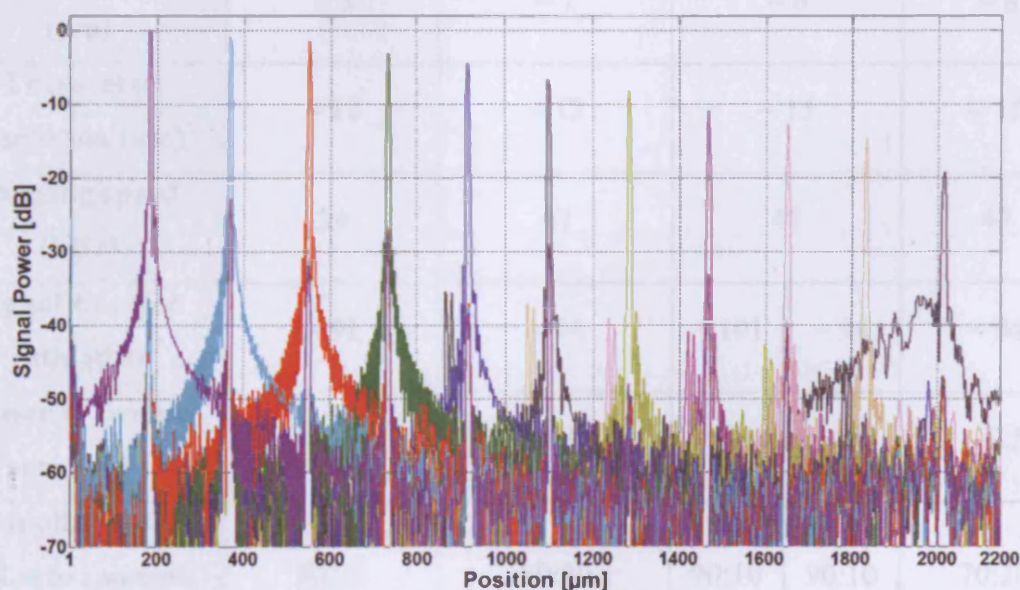


Figure 2.20: Sensitivity decay of the 1300 nm SD-OCT system

2.5.4 Comparison with other SD-OCT systems

The SD-OCT system operating at 1300 nm wavelength region was compared with two other SD-OCT systems operating at 800 nm and 1060 nm wavelength regions in terms of resolution, SNR and SNR roll-off with depth. An ultra-broadband coherent light source (Ti: Al_2O_3 laser) was used in the 800 nm OCT system; an amplified spontaneous emission (ASE) source was used in the 1060 nm OCT system; and a YDFL was used in 1300 nm OCT system. All three SD-OCT systems were designed in a similar manner. The 1300 nm and 1060 nm OCT systems were using all-reflective Czerny-Turner spectrometer configurations;

meanwhile the 800 nm spectrometer was making use of a spectrometer design based on a transmission grating. A comparison of main specifications of these three OCT systems is given in table 2.3.

	Ti: Sapphire laser	Amplified spontaneous emission source	Yb-doper fibre laser		Super luminescent diode
Centre wavelength (nm)	800	1050	1250		1320
Bandwidth (nm)	140	72	140		100
Axial resolution (μm)	~ 3	~ 7	~ 6		~ 8
Transverse resolution (μm)	~ 12	~ 12	~ 15		~ 15
Imaging speed (kHz)	20	47	47		47
Signal-to-noise ratio (dB)	~ 91	~ 94	~ 101	~ 94	~ 94
Power at sample arm (mW)	~ 4	~ 3	~ 20	~ 3	~ 2.5
Coupling ratio (ref.arm : sample arm)	80:20	80:20	90:10	90:10	70:30
6dB sensitivity roll off distance (mm)	~ 0.9	~ 1.2	~ 1.2	~ 1.2	~ 1.2

Table 2.5: Comparison of the specifications of the three OCT systems

The image acquisition rates were 20,000 A-scans/s for 800 nm system and 47,000 A-scans/s for both 1060 nm and 1300 nm systems. The optimum SNR for the 800 nm system was measured to be ~ 91 dB at 4 mW in the sample arm using a 90/10 coupler, whereas the optimum SNR for the 1060 nm system was ~ 93 dB at 3 mW in the sample arm using a 80/20 coupler. Thus, the SNR was highest for the 1300 nm system (~ 101 dB) due to its higher available power in the sample arm (~ 20 mW). The highest axial resolution was offered by

the 800 nm system, followed by the 1300 nm system and then the 1060 nm system. The same handheld probe was used along with all three systems. However, the wavelength-dependent components of the handheld probe such as the collimator and the objective lens were used appropriately for each system. The transverse resolution of these three systems was found to be comparable ($\sim 15 \mu\text{m}$).

3.1 Introduction

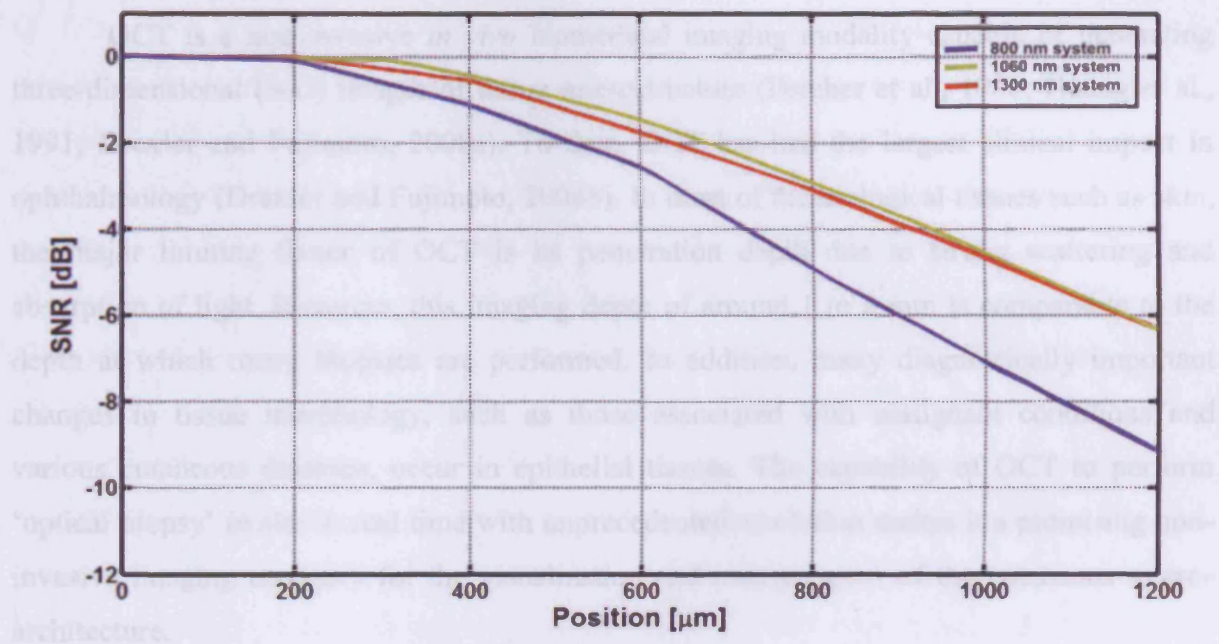


Figure 2.21: Comparison of the sensitivity degradation of the three SD-OCT systems

Figure 2.21 shows the comparison of normalized sensitivity fall-off with depth for the three systems. The maximum imaging depth of the 800 nm system was ~ 1.2 mm. The SNR degradation of the 1060 nm and 1300 nm systems were almost similar over this depth range. Their SNR dropped by 6 dB towards 1.2 mm. However, due to the ultrahigh resolution, i.e. higher spectral resolution (δk) of the 800 nm system, its 6 dB SNR fall-off distance was $\sim 900 \mu\text{m}$.

Chapter 3

Multispectral *in vivo* three dimensional OCT of human skin

3.1 Introduction

OCT is a non-invasive *in vivo* biomedical imaging modality capable of generating three-dimensional (3-D) images of tissue microstructure (Fercher et al., 1988; Huang et al., 1991; Drexler and Fujimoto, 2008a). To date, OCT has had the largest clinical impact in ophthalmology (Drexler and Fujimoto, 2008b). In most of the biological tissues such as skin, the major limiting factor of OCT is its penetration depth due to strong scattering and absorption of light. However, this imaging depth of around 1 to 2 mm is comparable to the depth at which many biopsies are performed. In addition, many diagnostically important changes in tissue morphology, such as those associated with malignant conditions and various cutaneous diseases, occur in epithelial tissues. The capability of OCT to perform ‘optical biopsy’ *in situ* in real time with unprecedented resolution makes it a promising non-invasive imaging modality for the visualization and interpretation of the cutaneous micro-architecture.

3.1.1 OCT in dermatology

Excisional biopsy and histology represent the ‘gold standard’ for morphological investigation of the human skin. The ultimate aim of non-invasive *in vivo* biomedical imaging modalities is to access the 3-D morphology of macroscopic volumes of thick areas ($>10 \times 10 \text{ mm}^2$), with a resolution similar to that of histology at speeds compatible to clinical requirements, i.e., within seconds or even real time, to reduce motion artifacts. In dermatology, several imaging methodologies including epiluminescence microscopy (ELM) (Steiner, Pehamberger and Wolff, 1987; Campos-do-Carmo and Ramos-e-Silva, 2008; Argenziano et al., 2009), confocal laser scanning microscopy (CLM) (Rajadhyaksha et al., 1995; Rajadhyaksha et al., 1999; Gerger et al., 2005; Nehal, Gareau and Rajadhyaksha, 2008), high-frequency ultrasound imaging (HFUS) (Hoffmann et al., 1992; Gammal et al., 1999; Schmid-Wendtner and Dill-Müller, 2008), multiphoton tomography (MPT) (König and Riemann, 2003; König, 2008; Dimitrow et al., 2009), magnetic resonance imaging (MRI) (Bittoun et al., 1990; Richard et al., 1993; Rodríguez et al., 2008) and OCT are being employed and investigated to realize this goal.

Since its introduction into dermatology in 1997, OCT has been utilized to obtain qualitative and quantitative information from human skin *in vivo* (Welzel et al., 1997; Welzel, 2001; Steiner, Kunzi-Rapp and Scharffetter-Kochanek, 2003; Gambichler et al., 2005; Welzel et al., 2008). In addition to the visualization of micro-morphological details of the normal skin, several explorative investigations have been conducted to study several inflammatory skin diseases such as contact dermatitis and psoriasis (Welzel, Bruhns and Wolff, 2003). OCT has been evolving as a promising diagnostic tool for the detection of tumours such as malignant melanoma (Gambichler et al., 2007b) and basal cell carcinoma (Gambichler et al., 2007a; Olmedo et al., 2007; Mogensen et al., 2009b). However, until now it remains difficult to delineate tumour margins and to detect deeper malignant lesions using OCT. Another application of dermal OCT is to monitor a variety of treatment effects *in vivo* such as effects of ointments and moisturizers, experimentally induced skin inflammation, effects of ultraviolet radiation, wound healing and tape strippings (Pagnoni et al., 1999; Welzel et al., 2004; Korde et al., 2007). Besides obtaining images of tissue microstructure based purely on the amplitude of the backscattered signals, information concerning tissue functionality may be extracted by considering the wave properties and polarization state of light. In skin, birefringent properties of the collagen bundles in the dermis changes the polarization state of the incoming light. Polarization-sensitive OCT (PS-OCT) allows these polarization effects to be quantified and related to the structural integrity of collagen scaffold to image thermally damaged skin and to assess burn depth (de Boer et al., 1998; Pierce et al., 2004). Regions of blood flow have been identified by both Doppler (Chen et al., 1997) and phase-resolved techniques (Zhao et al., 2000), enabling vessels and capillaries to be located and flow velocity determined. Spectroscopic OCT (SOCT) may be used to enhance image contrast, making it possible to detect spatially resolved functional and biochemical tissue information over the entire spectrum of the light source with a single measurement (Leitgeb et al., 2000; Morgner et al., 2000; Xu et al., 2004). A number of pathological processes such as oedema, fibrosis and calcification may alter elastic modulus of extracellular tissue matrix. OCT elastography can be used to assess the local variations of the stiffness inside a tissue non-invasively (Schmitt, 1998).

3.1.2 Anatomy of the human skin

The integumentary organ system, i.e. the outer covering of the human body, comprising the skin and its appendages, performs several essential functions such as:

- *Protection* – It acts as a barrier that prevents dehydration and protects against ultraviolet light, microorganisms, mechanical, chemical and thermal insults.
- *Sensation* – It contains various receptors for touch, pressure, pain and temperature.
- *Thermoregulation* – It insulates body from heat loss by the presence of hairs and subcutaneous adipose tissue. Conversely, heat loss is facilitated by evaporation of sweat from the skin surface and increased blood flow through dermis.
- *Excretion* – It functions in excretion through exocrine secretion of sweat, sebaceous and apocrine glands.
- *Metabolic functions* – It performs several metabolic functions such as synthesis of vitamin D and storage of energy in subcutaneous adipose tissue.

Skin is categorised as glabrous (thick) or hairy (thin) skin. The thickness of the skin varies over the surface of the body, from less than 1 mm to more than 5 mm. As shown in figure 3.1, skin has three main layers: epidermis (ED), dermis and hypodermis (HD).

3.1.2.1 Epidermis

The ED is mainly composed of stratified squamous epithelium and can be divided in five sub-layers. The deepest layer, **stratum basale** (SB), also called the stratum germinativum, form a single cell thick layer separated from the dermis by a basement membrane. The cuboidal cells of this layer are the stem cells of the ED. The layer above SB is called **stratum spinosum** (SS) because of numerous cytoplasmic ‘prickles’ bound by desmosomes to adjacent cells. Desmosomes are cell structures specialized for cell to cell adhesion mainly found in epithelial tissues. The thickness of the adjacent layer above, **stratum granulosum** (SG) varies from one to three cells. This layer contains numerous keratohyalin granules which are readily seen in routine histologic sections because of their intense basophilic staining. **stratum lucidum** (SL) is prominent only in the glabrous skin and pigment eleidin is found in this layer. The superficial layer, **stratum corneum** (SC) consists of dead and dying cells that are flattened and devoid of nuclei and other cytoplasmic organelles. These cells become filled almost entirely with keratin filaments. The thin air-filled layer comprising the dead cells that slough off on the skin surface is known as **stratum disjunctum**.

The cells of the ED consist of four different cell types:

- **Keratinocytes** – These are the predominant cell type of ED. They produce keratin, the major structural protein of ED and participate in formation of epidermal water barrier.
- **Melanocytes** – These cells are located in the basal layer of the ED. They are responsible for synthesis and release of melanin, which protects the body from damaging effects of ultraviolet radiation and determines the skin colour. Melanin is synthesised in membrane-bound oval granules called melanosomes and these melanosomes are transferred along cytoplasmic processes into neighbouring keratinocytes.
- **Langerhans cells** – These are dendritic-appearing, antigen-presenting cells in the ED. They are present in all layers of the ED, but are mostly seen in the SS. They are important components of the immune defence mechanism.
- **Merkel cells** – These are specialised touch receptors scattered very sparsely in the SB. They are abundant in skin where sensory perception is acute, such as the finger tips (Martin C. Mihm et al., 1976; Wheater, Heath and Young, 2000).

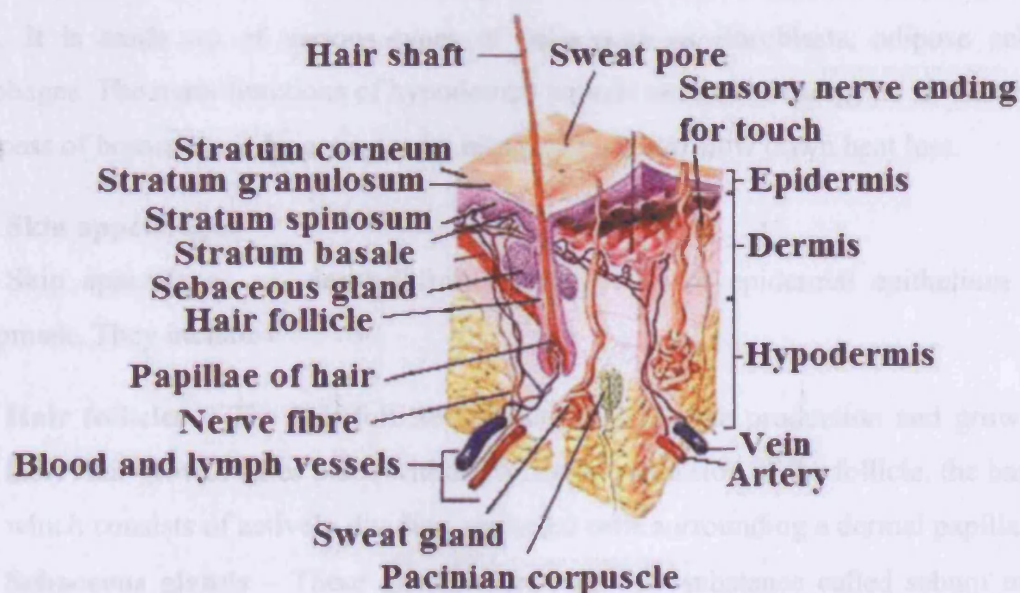


Figure 3.1: Schematic diagram depicting the anatomy of the human skin

3.1.2.2 Dermis

The dermis of the skin provides a flexible but robust base for the ED. It contains a generous vascular supply for the metabolic support of the avascular ED and for thermoregulation. The dermis is divided into two layers, the papillary dermis (PD) and the reticular dermis (RD). The PD is the superficial thin layer containing loose and fine interlacing collagen and elastic fibres. This layer possesses numerous connective tissue protrusions, known as dermal papillae, which project into the bottom surface of the ED. These papillae are complemented by similar epidermal protrusions, called rete ridges, that project into the dermis. The PD contains venules, arterioles and capillary loops, as well as lymphatic vessels and fine nerve twigs from the sensory nerve endings. The deeper and more extensive RD consists of long and thick collagen and elastic fibres. Besides fibroblasts, which are responsible for the production of collagen and elastin, lymphocytes, mast cells and tissue macrophages are the main cellular components present in the dermis. A network of small blood vessels, known as rete subpapillare (RS), runs along the border of the PD and the RD. The skin appendages and their ducts, larger blood vessels, nerves and some nerve endings also reside within the dermis (Ross, Kaye and Pawlina, 2002).

3.1.2.3 Hypodermis

HD, also known as subcutaneous layer, is the lowermost layer of the integumentary system. It is made up of various types of cells such as fibroblasts, adipose cells and macrophages. The main functions of hypodermis include storage of energy as fat and to aid in the process of homeostasis by acting as an insulating layer to slow down heat loss.

3.1.2.4 Skin appendages

Skin appendages are derived from downgrowths of epidermal epithelium during development. They include

- **Hair follicles** – The hair follicle is responsible for the production and growth of a hair. Hair growth takes place within a terminal expansion of the follicle, the hair bulb, which consists of actively dividing epithelial cells surrounding a dermal papilla.
- **Sebaceous glands** – These glands secrete an oily substance called sebum onto the hair surface in the upper part of the hair follicle. One or more sebaceous glands are associated with each hair follicle.
- **Sweat glands** - In most areas of skin, sweat glands are simple, coiled tubular glands which secrete a watery fluid onto the skin surface by the process of merocrine

secretion. Merocrine sweat glands are tubular structures without any association with the hair follicle. They play a significant role in regulating body temperature. In axilla and genital regions of humans, apocrine sweat glands are found. The viscid secretion that they produce by the apocrine process is discharged into the hair follicle rather than directly onto the surface.

- **Nails** – Nails are plates of keratinized cells containing hard keratin.

3.2 Motivation: Multi-spectral OCT of human skin

Most OCT systems operate in the wavelength region of 700 to 1300 nm, known as the ‘optical diagnostic window’, where light absorption by tissue components such as water, melanin and haemoglobin is relatively low. Meanwhile, the majority of OCT systems used for dermal imaging employ 1300 nm wavelength region. However, due to variation in tissue optical properties with wavelength, imaging parameters such as resolution, penetration depth and contrast depend on the central wavelength and bandwidth of the light source. Sainter *et al.* quantified the appropriateness of common OCT sources based on light-tissue interactions during light propagation through tissues with known optical properties and postulated that longer wavelength sources centred at 1300 nm would be capable of imaging deeper than those centred close to 800 nm (Sainter, King and Dickinson, 2004). Many comparative studies of OCT at different wavelength regions between 800 nm and 1800 nm have been performed to find an optimum wavelength region for dermal imaging (Schmitt *et al.*, 1994; Bouma *et al.*, 1998; Pan and Farkas, 1998). Recently, simultaneous detection of OCT images using two wavelength bands supplied by a single supercontinuum light source has been implemented, both in time and frequency domains (Spöler *et al.*, 2007; Kray *et al.*, 2009).

However, owing to variations in experimental conditions or due to differences in the purpose of study, no definite conclusions as to the optimum wavelength region employable for dermal OCT have been reached. Hence, this study aims for a systematic investigation comparing images of the human skin obtained *in vivo* from various locations using OCT systems operating at three different wavelength regions, each system optimized to be similar in terms of SNR, SNR roll-off with depth and transverse resolution.

3.3 Multispectral imaging of human skin

3.3.1 Subjects

During the course of this study, *in vivo* 3D OCT images of different dermal sites such as the skin above the proximal interphalangeal (PIP) joint of the middle finger and dorsal forearm were obtained from three subjects. As suggested by previous studies (Welzel et al., 2004), contact gel was topically applied to all these imaging sites as an index matching medium to decrease the superficial surface reflectivity and a tilted glass plate was placed above to avoid specular reflections. To determine the effect of skin pigmentation on OCT, normal subjects comprising skin types II (Caucasian), IV (Indian) and VI (African) according to Fitzpatrick scale (Fitzpatrick, 1975) participated in this study. In addition, OCT images of pigmented moles and scar tissue were obtained from two of these volunteers for analysis of the microstructural deformations in these tissues and also to observe the wavelength-dependent variations in visualization of minute morphological details.

3.3.2 Imaging systems

Three spectrometer-based frequency domain OCT systems operating at 800 nm, 1060 nm and 1300 nm wavelength regions respectively, were used to obtain images of the human skin *in vivo*. An ultra-broadband coherent light source (Ti: Al₂O₃ laser) was used in the 800 nm OCT system; an amplified spontaneous emission (ASE) source (NP Photonics, Tucson, Arizona) was used in the 1060 nm OCT system; and a Ytterbium (Yb)-doped fibre laser and a superluminescent light emitting diode source (Thorlabs Inc., Newton, New Jersey) were used in the 1300 nm OCT system. The design, implementation and the main specifications of these three OCT systems were previously described in detail in chapter 2. Typical surface dimensions of a scan region were approximately 8 X 8 mm², with 1024 transverse sampling points per B-scan. Sampling density was set to be just over the critical sampling limit. The wavelength-dependent components of the handheld probe such as the collimator and the objective lens were selected appropriately for each OCT system, so that they were comparable in terms of transverse resolution and depth of focus. All three OCT systems were found to be similar in terms of SNR, transverse resolution and sensitivity roll-off. However, the free-space axial resolution of the 800 nm system was measured to be better than the other two systems (refer table in chapter 2).

3.3.3 OCT image analysis

OCT images obtained at different wavelength bands from approximately same locations were compared in terms of resolution, contrast, penetration depth and dynamic range. To determine the variation in image penetration depth with wavelength, an average of 2 - 3 A-scans per B-scan was calculated from identical locations across a volume stack of 200 B-scans. The curve thus obtained showed the signal decay in depth along different dermal layers, rather than the signal depth profile itself. The signal decay curves were calculated from comparable locations of OCT images obtained at three wavelength regions. These depth decay profiles were normalized with respect to their maximum signal and they were fitted with suitable curves to extract signal decay coefficients for different wavelength regions.

Image contrast (C) is commonly defined as the quotient of the sample statistics for the median (M) and standard deviation (SD) (Duncan, Kirkpatrick and Wang, 2008). In the calculation of contrast in OCT images, median of the OCT signal intensity was used, instead of the mean signal, in order to reduce the effect of the speckle outliers in OCT images.

$$C = \frac{SD}{M} = \frac{\left(\frac{1}{n-1} \sum_{i=1}^n (x_i - \bar{x})^2\right)^{\frac{1}{2}}}{M} \quad \dots (3.1)$$

Where $\bar{x} = \frac{1}{n} \sum_{i=1}^n x_i$, x_i is the intensity values of each of the constituent pixel in the image and n is number of pixels in the image. M is the median value of the pixel intensities in the image.

For quantitative comparison of the contrast in OCT images, comparable volume stacks obtained at different wavelength regions were selected to analyse the variation of OCT signal within each *en face* section. The standard deviation of the OCT signal intensity in each *en face* section was divided by the median signal intensity of the respective section to obtain the contrast parameter. The contrast values thus calculated for each *en face* section were plotted along depth to determine the depth-dependent contrast variation.

3.3.4 Results

3.3.4.1 Glabrous skin

All three systems, with image acquisition rates of 20,000 A-scans/s (800 nm system) and 47,000 A-scans/s (both the 1060 nm and 1300 nm systems), demonstrated the tremendous potential of OCT to manifest micro-morphological information of the human

skin *in vivo*. Figure 3.2 depicts the capability of OCT to display the extracted information as cross-sectional images in orthogonal planes [Figs. 3.2(a) and 3.2(d)] and in 3D [Fig. 3.2(c)]. The 1300 nm system employing the fibre laser-based source could clearly visualize the morphology of several cutaneous layers such as ED, dermis and even the deeper layer of HD at the palmar side of the PIP joint of the middle finger.

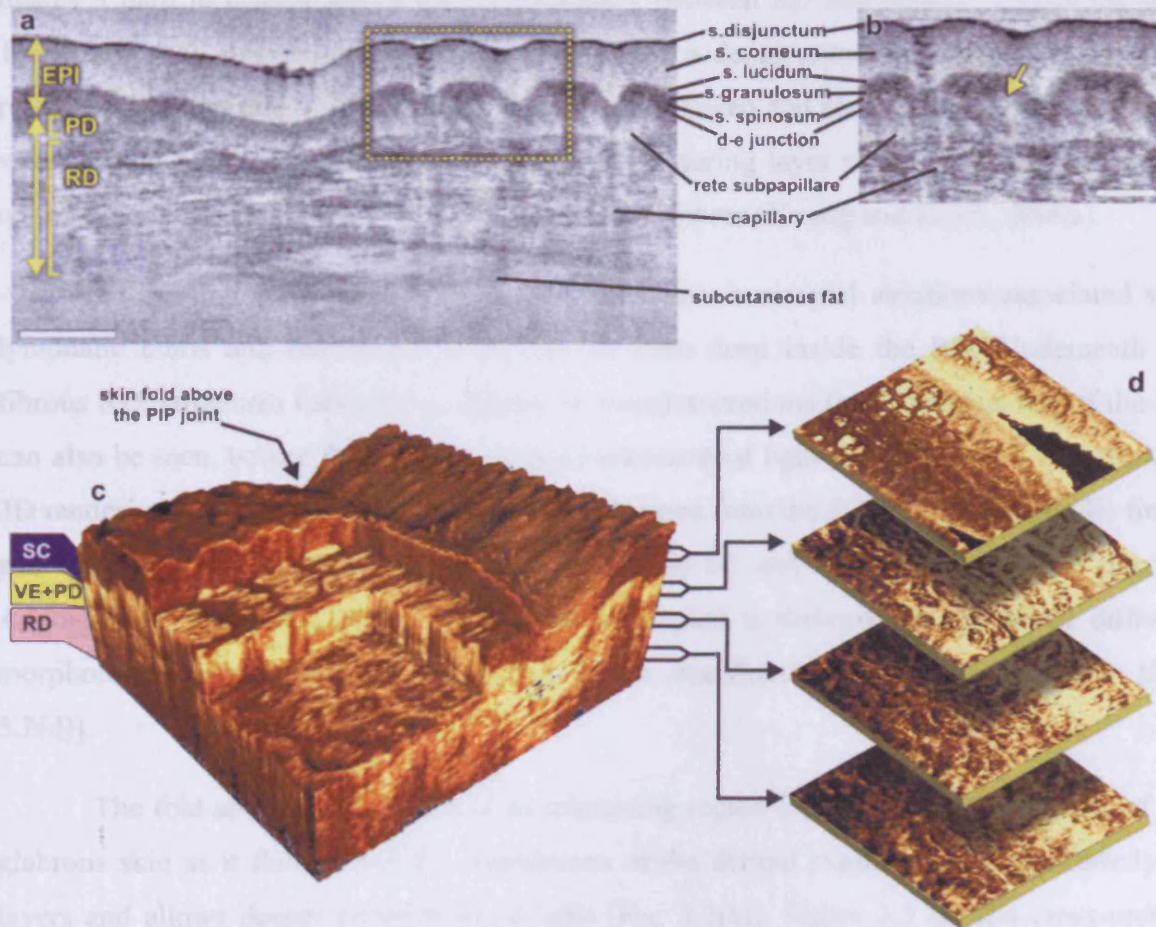


Figure 3.2: Different ways to display micro-morphological information obtained using OCT. (a) A B-scan obtained across the skin above the proximal interphalangeal joint of the middle finger obtained using the 1300 nm system. (b) Magnified view of different sub-layers of epidermis and dermis. The yellow arrow points toward the dermal-epidermal junction. (c) 3D rendering of the same region reconstructed from 1024 B-scans. (d) *En face* sections of the same region separated in depth by 360 μm . The scale bars in (a) denotes 500 μm and the scale bar in (b) denotes 200 μm .

Glabrous skin, as found on the palm, allows better discrimination of different layers in the OCT tomogram and their intensity pattern can be correlated to various anatomical structures. All major cutaneous layers, including different sub-layers [Figs. 3.2(a) and 3.2(b)], were well delineated due to pronounced differences in scattering. Above the thick and almost transparent SC, the stratum disjunctum can be clearly seen as a narrow region with increased scattering, caused by the mix of exfoliated corneal material and air. Higher concentration of

eleidin and the lack of intercellular bodies make the SL a homogenous, even less scattering layer between the SC and SG. As indicated by the yellow arrow in figure 3.2(b), beneath the highly reflecting SG and SS, the SB can be sometimes seen as a crisp, bright transition zone between highly scattering ED and less scattering PD. The absence of melanocytes in the basal layer of ED and the undulations of the dermal papillae at the dermal-epidermal junction makes it hard to clearly demarcate the boundary between ED and dermis in glabrous skin. The PD is well demarcated from RD by the RS, a dense network of capillaries at their relatively flat boundary. The PD, comprising fine collagen and elastin fibres and small blood vessels arising from the RS, seem to be a less scattering layer when compared to the RD, comprising large compact collagen and thick elastin fibres (Young and Heath, 2000a).

At the region of the fold above the PIP joint, horizontal striations associated with lymphatic clefts and microvasculature can be seen deep inside the RD. Underneath the fibrous RD, structures resembling adipose fat conglomerations (subcutaneous fat) of the HD can also be seen, before the intensity of the backscattered light drops. Figure 3.2(c) shows a 3D rendering constructed using 1024 B-scans obtained from the PIP joint of the middle finger and features a virtual dissection at the base of the SC and another one beneath the RS. Averaged *en face* views of the same volume sampled at different depths unveil different morphological structures more clearly due to the stratified nature of the human skin [Fig. 3.2(d)].

The fold above the PIP joint is an interesting region for obtaining OCT images of the glabrous skin as it flattens out the undulations of the dermal papillae, compacts underlying layers and allows deeper penetration of light [Fig. 3.2(a)]. Figure 3.3 depicts cross-section and *en face* images of the skin above the PIP joint obtained at three wavelengths. In this study, penetration depth appears to increase with wavelength at approximately identical locations [Figs. 3.3(a) – 3.3(c)], as demonstrated in many previous theoretical (Sainter et al., 2004) and experimental studies (Schmitt et al., 1994; Pan and Farkas, 1998). Interestingly, even at 800 nm, it was possible to see structures as deep as the RD. *En face* views of different cutaneous layers were constructed by averaging in depth across 1024 B-scans within the range indicated by markers in the corresponding cross-sections [Figs. 3.3(d) – 3.3(q)]. The number of *en face* sections averaged was based on the thickness of the respective dermal layer. *En face* projections obtained at the main dermal layers demonstrate the wavelength-dependent appearance of different anatomical features. In the SC [Figs. 3.3(d) - 3.3(f)],

parallel ridges formed by the underlying dermal papillae can be clearly distinguished, on top of which sweat ducts open. These are visible as bright spots [yellow arrow in fig. 3.3(d)]. The sweat ducts change their relative contrast and appear as dark spots inside the brighter islands formed by highly scattering viable epidermis (VE) [Figs. 3.3(g) – 3.3(i)] that is intersected by dark downward folds of thicker ED at the rete ridges. VE comprises all the sub-layers of ED except the SC. The PD [Figs. 3.3(j) – 3.3(l)] can be easily recognized by its honeycomb-like structure formed by fibrous stroma of the RD around the comparatively less scattering darker base of the dermal papillae. The RD [Figs. 3.3(m) – 3.3(q)] forms a high scattering layer with a rich supply of blood vessels, which can be easily identified as signal-poor regions.

The decay of signal intensity with depth on glabrous skin at different wavelength regions is compared in figure 3.4. Figure 3.4(a) shows the signal decay curves at different wavelength regions, which are normalised with respect to their entrance signal. These curves clearly showed that the signal attenuation was lower at 1300 nm wavelength region compared to other two wavelength regions. The transition between different dermal layers was demarcated by peaks along the signal decay curves at all wavelength regions. As depicted in figure 3.4(b), the attenuation was quite similar at 800 nm and 1060 nm wavelength regions within the dermal layers, the VE and the PD. The signal attenuation in these layers could be fitted using a linear function. The attenuation coefficients were obtained as $-0.001258 \mu\text{m}^{-1}$, $-0.00253 \mu\text{m}^{-1}$ and $-0.001977 \mu\text{m}^{-1}$ for 1300 nm, 1060 nm and 800 nm wavelength bands respectively. Within this layer, 1060 nm wavelength band was attenuated slightly more than the 800 nm region. The RD was strongly scattering layers as seen in the cross-sections [Figs. 3.3(a) - 3.3(c)]. The attenuation coefficients that were obtained from within the reticular dermis were $-0.001302 \mu\text{m}^{-1}$, $-0.0008569 \mu\text{m}^{-1}$ and $-0.0008053 \mu\text{m}^{-1}$ for 800 nm, 1060 nm and 1300 nm wavelength bands [Fig. 3.4(c)]. The measured attenuation coefficient at 800 nm was significantly higher in the RD than other wavelength regions and these values indicate the highly scattering nature of the RD. In figure 3.4(d), the contrast parameter extracted from the *en face* sections were plotted against depth. Since the contrast parameter was extracted from a volume stack, the shift in the position of different dermal layers is evident in this figure. The 1300 nm curve is shifted towards right compared to other two wavelength regions. The contrast obtained in the glabrous skin was quite comparable at 800 nm and 1060 nm wavelength regions.

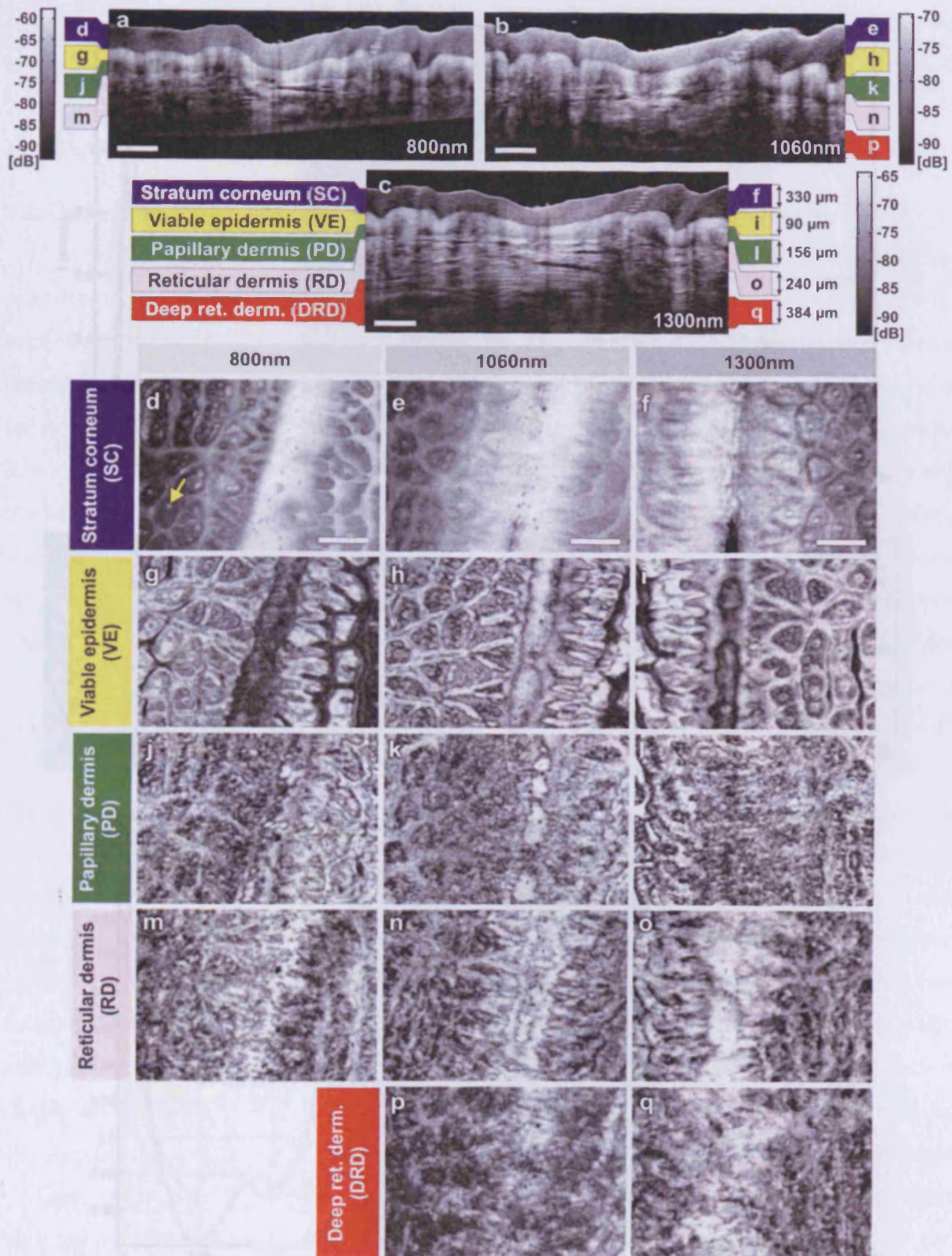


Figure 3.3: Images of glabrous skin located above the proximal interphalangeal joint of the middle finger obtained using three OCT systems. B-scans obtained using (a) 800 nm, (b) 1060 nm and (c) 1300 nm OCT systems. Dynamic ranges (dB) in these images are indicated using gray scales. *En face* images of various sub-surface layers from 800 nm (d, g, j, m), 1060 nm (e, h, k, n, p) and 1300 nm (f, i, l, o, q) OCT systems. The yellow arrow in (d) denotes a sweat duct. The scale bars denote 500 μm in (a, b, c) and 1mm in *en face* sections.

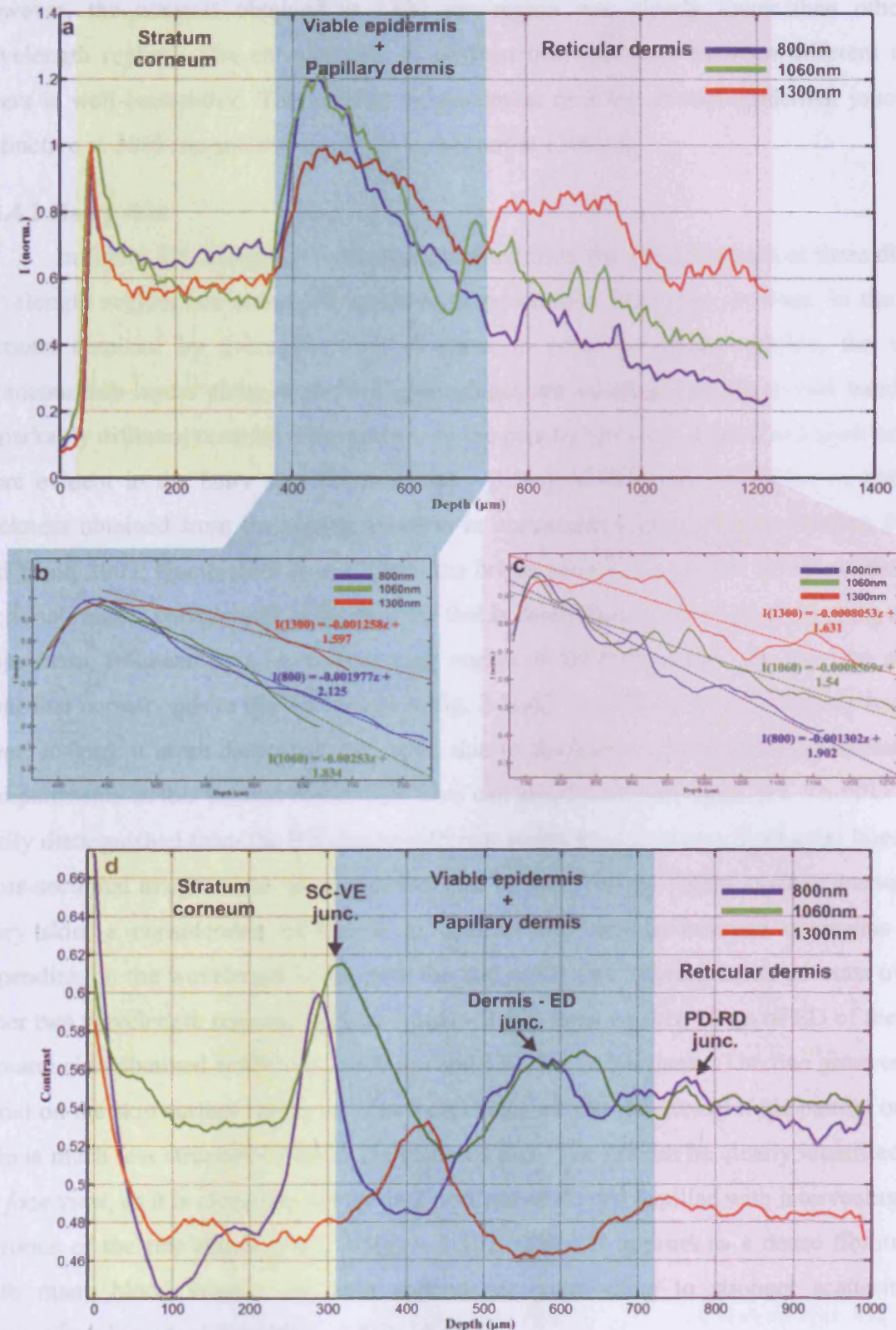


Figure 3.4: Analysis of OCT images obtained at three wavelength bands from glabrous skin located above the proximal interphalangeal joint of the middle finger. (a) OCT signal decay curves along depth. (b) Normalised OCT signal decay curves in the viable epidermis and the papillary dermis. (c) Normalised OCT signal decay curves in the reticular dermis. (d) Contrast variation along depth for different wavelength bands.

However, the contrast obtained at 1300 nm region was clearly lower than other two wavelength regions. The enhancement in contrast near junctions between different dermal layers is well-enunciated. The contrast enhancement near the dermal-epidermal junction is distinctive at 1060 nm and 800 nm regions, but not at 1300 nm.

3.3.4.2 Hairy skin

In figure 3.5, images of hairy skin obtained from the dorsal forearm at three different wavelength regions are compared in terms of penetration depth and contrast. In the cross-sections obtained by averaging three B-scans in order to reduce speckle, the various cutaneous sub-layers along with their appendages are visualized as horizontal bands with remarkably different contrast. The increase in the penetration depth with wavelength becomes more evident in the hairy skin [Figs. 3.5(a) – 3.5(c)]. Comparing the values of epidermal thickness obtained from the similar location in concurrent studies (Sandby-Møller, Poulsen and Wulf, 2003; Gambichler et al., 2006), the bright narrow line on the surface of the cross-sectional images corresponds to the thin SC that is dominated by the highly scattering stratum disjunctum, followed by a lower scattering region of the living epidermis and then a bright layer that corresponds to the SB [arrow in fig. 3.5(a)]. The SB appears as a highly scattering layer, making it more distinct in thin skin, due to the higher concentration of melanin-rich compartments in this portion of the ED. This can also be seen in figure 3.7. The PD can be easily distinguished from the RD due to different scattering properties. Dark axial lines in the cross-sectional images arise from shadows cast by hair. Due to higher average scattering in hairy skin, a considerable difference in contrast was noticed between cutaneous layers depending on the wavelength used, with the 800 nm region offering better contrast over the other two wavelength regions. Figures 3.5(d) – 3.5(f) show *en face* views of ED of the dorsal forearm skin obtained at 800 nm, 1060 nm and 1300 nm respectively. The fine grooves (sulci cutis) on the skin surface can be seen as a dark network and the dermal ridge pattern on hairy skin is much less structured than in the glabrous skin. The PD can be clearly identified in the *en face* view, as it is characterized by dark portions of dermal papillae with intervening bright portions of the rete ridges [Figs. 3.5(g) – 3.5(i)]. The RD appears as a dense fibrous layer with many blood vessels and skin appendages contributing to stronger scattering and absorption of incident light [Figs. 3.5(j) – 3.5(n)].

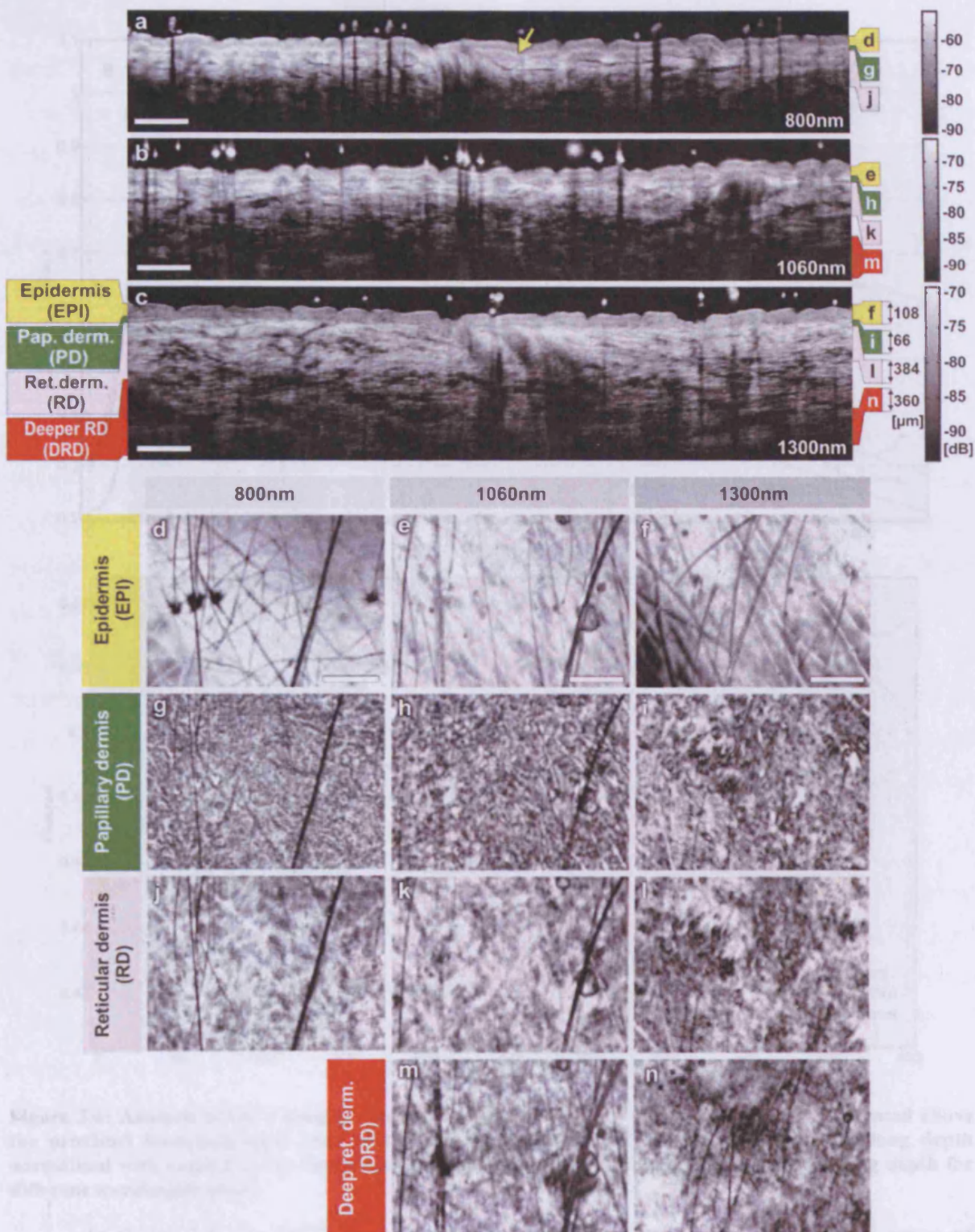


Figure 3.5: Images of skin at the dorsal forearm obtained using the three OCT systems operating at three different wavelength regions. B-scans obtained using (a) 800 nm, (b) 1060 nm and (c) 1300 nm OCT systems. Dynamic range (dB) in these images is indicated using gray scales. *En face* images of various sub-cutaneous layers obtained from 800 nm (d, g, j), 1060 nm (e, h, k, m) and 1300 nm (f, i, l, n) OCT systems. The scale bars denote 500 μ m in (a, b, c) and 1mm in *en face* sections.

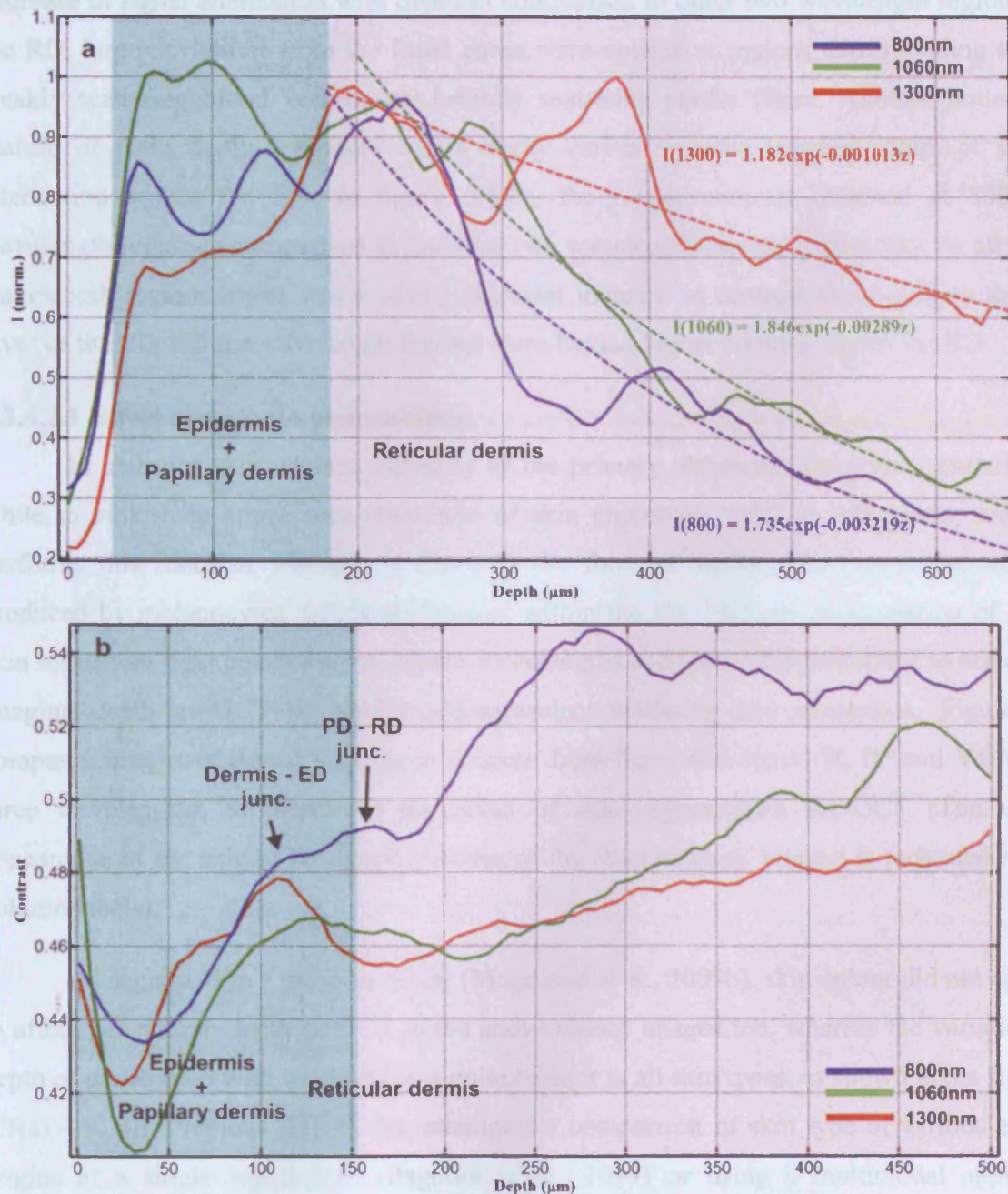


Figure 3.6: Analysis of OCT images obtained at three wavelength bands from hairy skin located above the proximal interphalangeal joint of the middle finger. (a) OCT signal decay curves along depth normalised with respect to the first peak in the reticular dermis. (b) Contrast variation along depth for different wavelength bands.

In figure 3.6, the OCT image data obtained from hairy skin is analysed in terms of penetration depth and contrast. As can be seen from figure 3.6(a), the variation in signal attenuation with wavelength was more distinctive in hairy skin compared to the glabrous skin. The attenuation coefficients obtained from the fitted curves were $-0.003219 \mu\text{m}^{-1}$, $-0.00289 \mu\text{m}^{-1}$ and $-0.001013 \mu\text{m}^{-1}$ for 800 nm, 1060 nm and 1300 nm wavelength regions respectively. As expected, OCT image obtained at 1300 nm displayed much more gradual

decrease in signal attenuation with depth in comparison to other two wavelength regions. In the RD, large deviations from the fitted curve were noticed at regions corresponding to the weakly scattering blood vessels and brightly scattering elastic fibres. Another noticeable feature of these depth-dependent signal decay curves was the varying nature of signal attenuation within the ED. In figure 3.6(b), the higher contrast obtained at 800 nm wavelength region in comparison to the other two wavelength regions is depicted. At all three wavelength regions, there was a very significant increase in contrast starting from the SB layer of the ED. All the wavelength regions were having higher contrast within the RD.

3.3.4.2.1 Effect of melanin pigmentation

In glabrous skin, eleidin functions as the primary ultraviolet-absorbent, rendering it white to pinkish in appearance regardless of skin phototype, while in hairy skin, melanin performs this function. Melanin is found in the form of highly scattering melanosomes, produced by melanocytes, which are located within the SB. Melanin pigmentation of hairy skin influences light penetration at shorter wavelengths and hence was postulated to affect the imaging depth of OCT by wavelength-dependent scattering and absorption. Figure 3.7 compares images of dorsal forearm skin taken from three skin types (II, IV and VI) at all three wavelengths, to determine the effect of skin pigmentation on OCT (The visual appearance of the skin at the dorsal forearm of the three subjects imaged is indicated in the column labels).

As suggested in a previous study (Mogensen et al., 2009b), skin colour did not appear to affect penetration depth of OCT in the above shown images too, whereas the variation in depth of penetration with wavelength is quite evident in all skin types, as shown in the figures 3.7(a) – 3.7(i). Previous studies that attempted a comparison of skin type of various ethnic origins at a single wavelength (Pagnoni et al., 1999) or using a multimodal approach (Querleux et al., 2009) concluded that the African-American skin (type VI) has more contrast at the dermal-epidermal junction and more prominent dermal papillae than Caucasian skin.

In order to obtain more information about the anatomical differences between these three skin types, *en face* views were generated across 1024 B-scans at the basal layer of ED [Figs. 3.7(j) – 3.7(r)]. The exact sampling location in depth of each *en face* section is indicated by yellow labelling boxes to the right of each of the cross-sectional images. In these *en face* sections, a higher concentration of bright ring-shaped structures, known as ‘edged papillae’, surrounding darker dermal papillae can be clearly seen in darker skin tones.

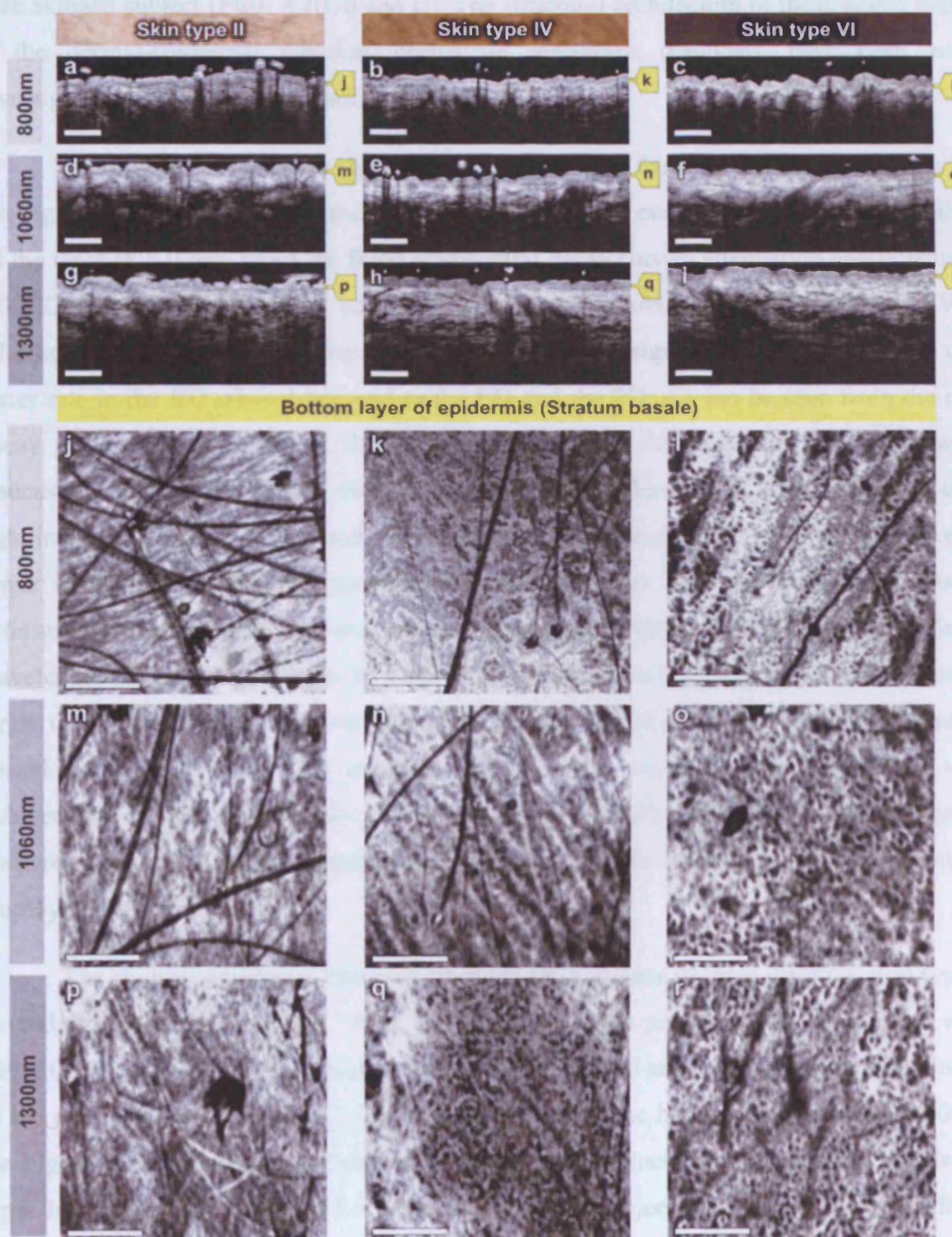


Figure 3.7: Images of dorsal forearm skin taken using the OCT systems operating at three different wavelength regions to show the effect of melanin pigmentation in OCT. B-scans of dorsal forearm skin comprising skin types II (Caucasian), IV (Indian) and VI (African) obtained using 800 nm (a, b, c), 1060 nm (d, e, f) and 1300 nm (g, h, i) OCT systems. *En face* images of the basal layer of the epidermis from these subjects obtained at 800 nm (j, k, l), 1060 nm (m, n, o) and 1300 nm (p, q, r). Edged papillae, comprising highly scattering melanin-rich keratinocytes, can be seen as bright rings surrounding the darker dermal papillae in the *en face* sections of the darker skin types (marked using yellow arrows in l, o and r). The scale bars denote 500 μ m in cross-sections and 1 mm in *en face* sections.

These structures are marked using yellow arrows in the en face sections obtained from the dark skinned subject [Figs. 3.7(l, o and r)]. The structural architecture of these edged papillae at the dermal-epidermal junction, critical in melanoma diagnosis, have been widely investigated using CLM (Pellacani et al., 2005).

Figure 3.8(a) depicts the signal decay over depth in these three skin types at the 1300 nm region. It can be seen from these curves that the signal attenuation was almost similar in all the three skin types. From the fitted exponential decay curves, attenuation coefficients of $-0.001224 \mu\text{m}^{-1}$, $-0.000968 \mu\text{m}^{-1}$ and $-0.001228 \mu\text{m}^{-1}$ were obtained for skin types II, IV and VI respectively. The depth decay profiles show that the signal began to decay at a much faster rate in the RD when compared to the ED and the PD. As can be seen from the depth decay profiles in figure 3.8(a), the OCT signal intensity first declined in the skin of the Caucasian subject, even though the African subject had a thicker ED. The attenuation of the light inside the tissue is influenced by both scattering and absorption, although latter is much lower in the near-infrared region (Tseng et al., 2009). A previous study carried out to determine the absorption and reduced scattering coefficients of the human skin in the wavelength range from 400 nm to 2000 nm concluded that the scattering at wavelengths larger than 600 nm originated from large Mie scatterers, such as collagen and elastin bundles (Bashkatov et al., 2005). This explains why the light penetration depth appeared to be independent of skin pigmentation, since the melanin, which behaves as a small Rayleigh scatterer, does not contribute significantly to the scattering of light in the wavelength regions employed for this study.

The contrast parameter obtained from the OCT images of three different skin types is plotted against depth in figure 3.8(b). As suggested in the previous studies (Pagnoni et al., 1999; Querleux et al., 2009), a higher contrast was observed at the dermal-epidermal junction of the subject with skin type VI [Fig. 3.8(b)]. Probably, the higher contrast could be due to the higher concentration of melanosomes and more prominent dermal papillae in this skin type. In addition, OCT signal from the dark-skinned subject (VI) had a relatively higher contrast in the RD, compared to the other two skin types (II and IV). The contrast variation in the OCT images obtained from skin types II and VI were quite similar along the entire depth of analysis.

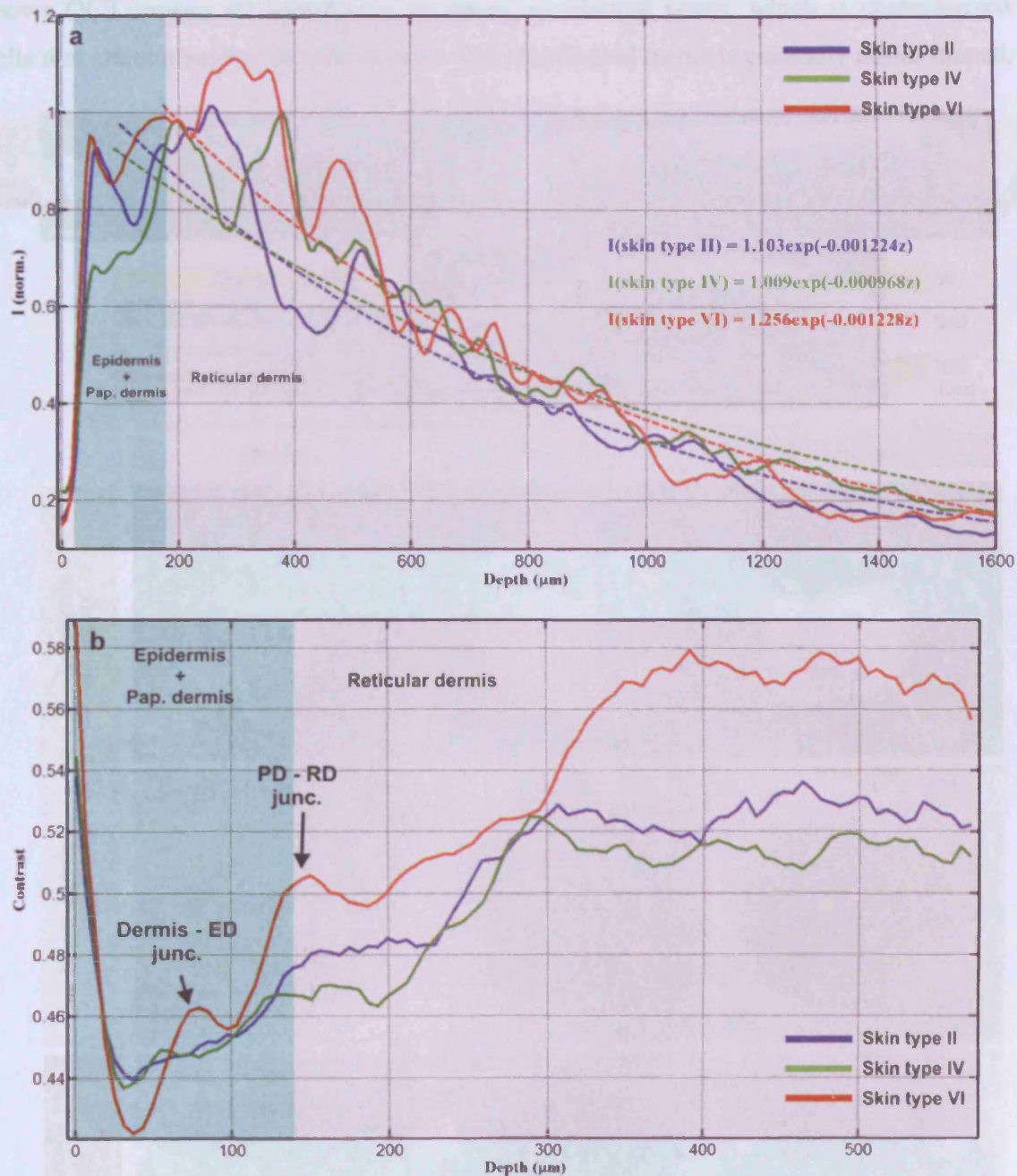


Figure 3.8: Effect of melanin pigmentation in OCT. (a) Depth-dependent drop in signal intensity on skin above dorsal forearm among skin types II (Caucasian), IV (Indian) and VI (African). These curves demonstrate that the skin pigmentation has little effect on light penetration. (b) Contrast variation over depth in different skin phototypes.

3.3.4.3 Nevi

In addition to normal skin, a range of nevi and scar tissue was investigated to determine the changes in the structural organization of different skin layers and also to analyse the performance of three wavelength regions on different types of tissues. Figure 3.9

shows OCT images of light-brown coloured intradermal nevus, which is characterized by cells that are confined within the dermis. The intradermal nevus is generally dome-shaped.

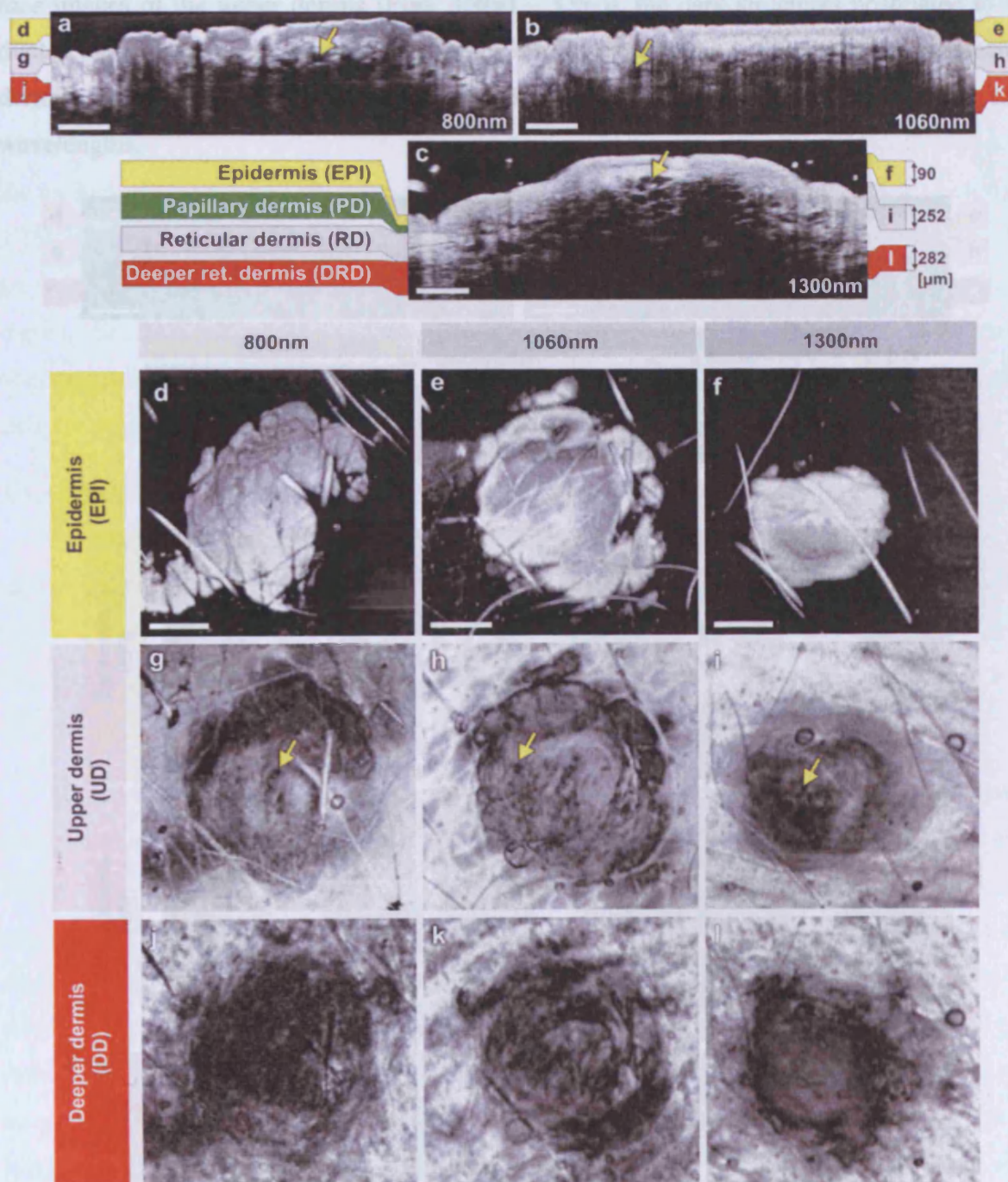


Figure 3.9: B-scan images of an intradermal nevus obtained using (a) 800 nm, (b) 1060 nm and (c) 1300 nm OCT systems. *En face* views of different layers of intradermal nevus obtained from 800 nm (d, g, j), 1060 nm (e, h, k) and 1300 nm (f, i, l) OCT systems. The dark structures marked by yellow arrows are postulated to be dilated blood vessels associated with the nevus. The scale bars denote 500 μ m in cross-sections and 1 mm in the *en face* views.

As a result of the slightly different force applied by the handheld probe on the surface of the nevus, its outer shape appears more or less flattened in B-mode scan cross-sections obtained

by the three OCT systems. As expected, the 1300 nm OCT system was capable of penetrating deeper into the nevus when compared to other two systems [Figs. 3.9(a) – 3.9(c)]. In the *en face* images of the upper dermis [Figs. 3.9(g) – 3.9(i)], the dark structures postulated to be dilated blood vessels, appear distinct from the brighter surroundings formed by the unaffected dermis. The 800 nm wavelength region provided a slightly better contrast over the other two wavelengths.

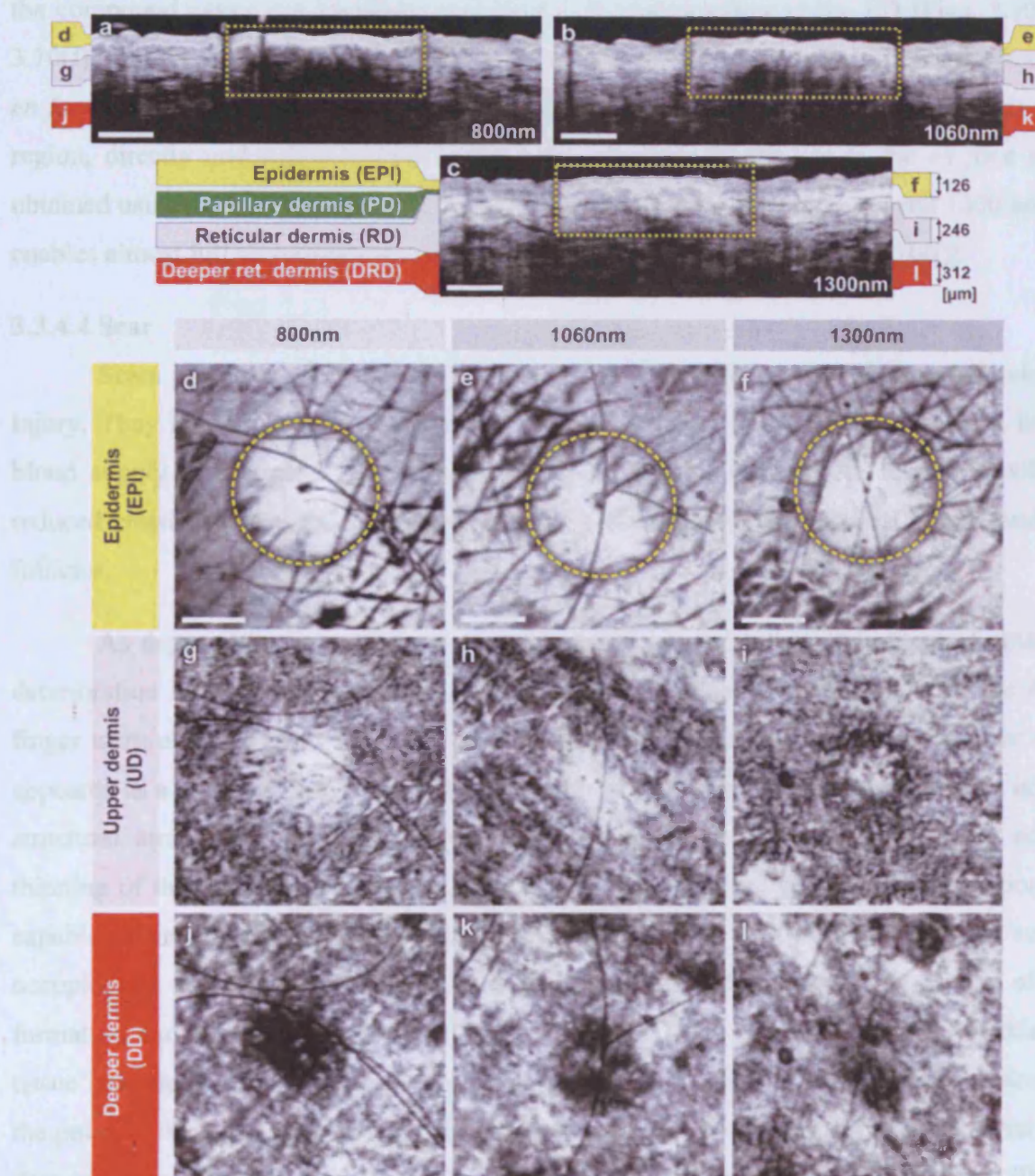


Figure 3.10: B-scan images of a compound nevus obtained using OCT at (a) 800 nm, (b) 1060 nm and (c) 1300 nm. *En face* views of different layers of compound nevus obtained from 800 nm (d, g, j), 1060 nm (e, h, k) and 1300 nm (f, i, l) OCT systems. The scale bars denote 500 μ m in cross-sections and 1 mm in *en face* sections.

OCT images of a black compound nevus, which is characterized by nevus cells present both in ED and dermis, are displayed in figure 3.10. The lower boundary of the nevus could be visualized only with the 1300 nm OCT system, as strong scattering by the densely packed nevus cells did not permit to penetrate deep enough with shorter wavelength systems [Figs. 3.10(a) – 3.10(c)]. However, the 800 nm system provided better contrast in the cross-sectional view and the image contrast diminished for higher wavelengths. The surface area of the compound nevus can be determined from the *en face* views of the ED [Figs. 3.10(d) – 3.10(f)] and the decrease in the strength of scattering with wavelength can be seen from the *en face* images of the upper dermis (UD) [Figs. 3.10(g) – 3.10(i)]. The deeper dermis (DD) region, directly underneath the nevus, becomes overcast by shadow in the *en face* image obtained using the 800 nm, while more information is found using 1060 nm and 1300 nm that enables almost full reconstruction of the tissue underneath [Figs. 3.10(j) – 3.10(l)].

3.3.4.4 Scar

Scars are areas of fibrous connective tissue that replace normal skin following an injury. They tend to be paler and denser than surrounding normal tissue due to a limited blood supply. Scar tissues in skin are inferior to healthy skin due to loss of flexibility, reduced resistance to ultraviolet radiation and incapability to grow sweat glands and hair follicles.

As depicted in figure 3.11, in order to determine the nature and extent of structural deterioration in scar tissues, OCT images of scar located above the PIP joint of the fourth finger were obtained using OCT operating in the three wavelength regions. The scar tissue appeared as a dense brightly scattering region due to higher collagen content. It lacks layered structural arrangement found in surrounding normal tissue as well as displays a notable thinning of the SC [boxes in figs. 3.11(a) – 3.11(c)]. The 1300 nm wavelength region was capable of penetrating deepest and allowed demarcation of the dimensions of the volume occupied by the scar tissue. *En face* views aided understanding of the pattern of scar formation and its variations in depth. The SC images [Figs. 3.11(d) – 3.11(f)] of this scar tissue indicate a different arrangement and density of sweat ducts, and the star-like shape of the putative fibrous collagen content forming the scar seems to consist of lifted material from deeper layers [Figs. 3.11(g) – 3.11(i)]. Again, images of deeper RD obtained at 1300 nm allow investigation of the fine structure of the fibrous component that forms a well-delineated

region of higher density and the deformation of reticular meshwork, which cannot be extracted by the systems operating at lower wavelengths.

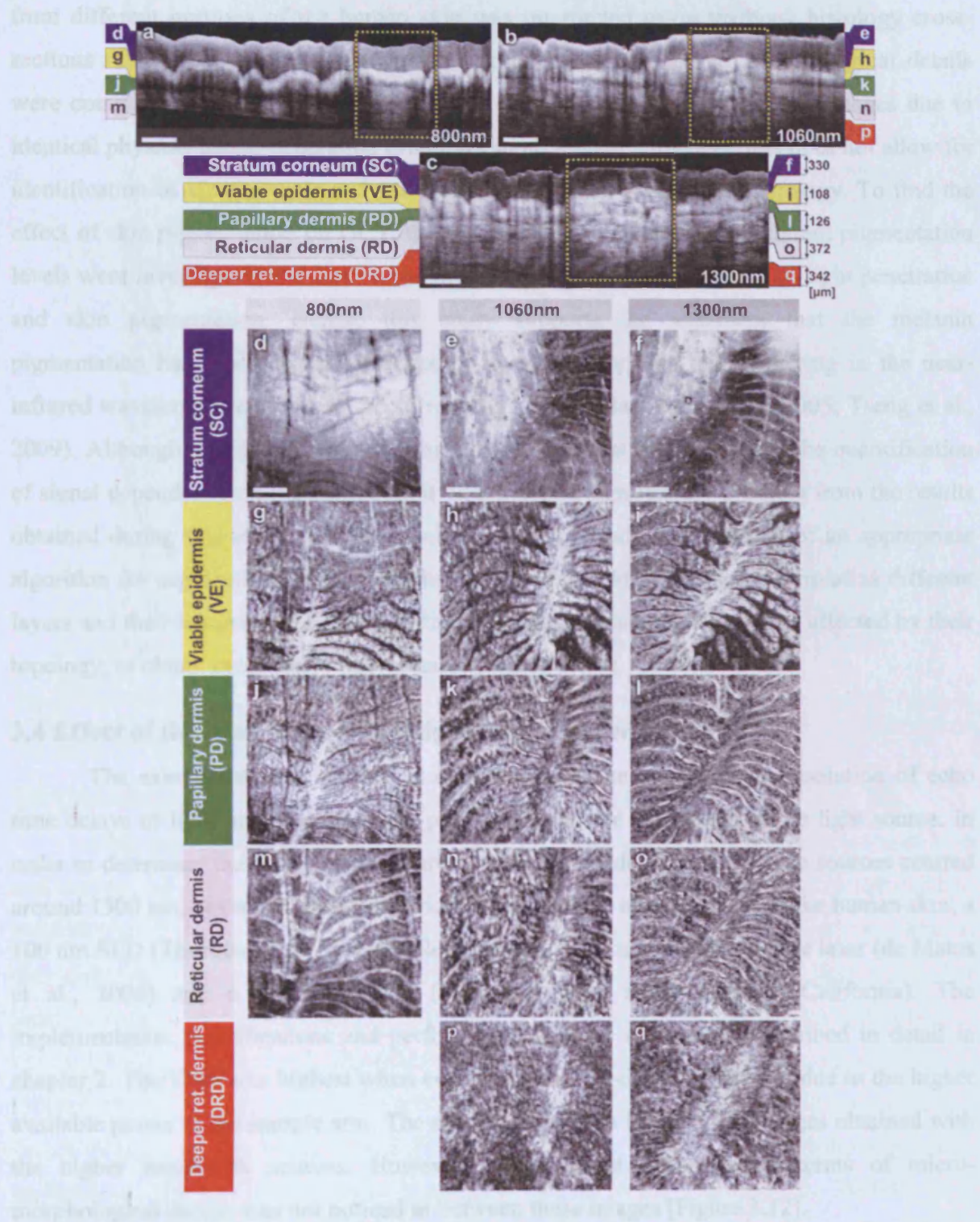


Figure 3.11: B-scan images of a scar tissue on the skin above proximal interphalangeal joint of the fourth finger obtained using (a) 800 nm, (b) 1060 nm and (c) 1300 nm OCT systems. *En face* views sampled across different dermal layers obtained at 800 nm (d, g, j, m), 1060 nm (e, h, k, n, p) and 1300 nm (f, i, l, o, q) illustrate increase in penetration depth with wavelength. The scale bars denote 500 μ m in cross-sections and 1 mm in *en face* sections.

3.3.5 Limitations of this study

In this preliminary study, microstructural information obtained *in vivo* using OCT from different portions of the human skin was interpreted using textbook histology cross-sections rather than the histology obtained from the excised tissue. Morphological details were compared between identical regions of OCT scans only. This has advantages due to identical physical image generation principles in all images. However, this does not allow for identification of all structures and 1:1 correlation with gold standard, histology. To find the effect of skin pigmentation on OCT, three subjects with distinctively different pigmentation levels were investigated and no correlation was found between the depth of light penetration and skin pigmentation. Hence, this study supports the statement that the melanin pigmentation has much lower influence on overall absorption and scattering in the near-infrared wavelength region than the surrounding tissue (Bashkatov et al., 2005; Tseng et al., 2009). Although a larger number of subjects and locations might improve the quantification of signal dependency on pigmentation, it would not be significantly different from the results obtained during this study. Another limitation of this study was the lack of an appropriate algorithm for segmenting different dermal layers. It should be possible to visualize different layers and their features much more distinctively through segmentation, less affected by their topology, to obtain more easily interpretable *en face* views.

3.4 Effect of the bandwidth of the light source in dermal OCT

The axial resolution in OCT is determined by the measurement resolution of echo time delays of light and it is inversely proportional to the bandwidth of the light source. In order to determine the effect of the source bandwidth in dermal OCT, three sources centred around 1300 nm, but of different bandwidths were used to obtain images of the human skin; a 100 nm SLD (Thorlabs, Inc., Newton, New Jersey), a 140 nm Yb-doped fibre laser (de Matos et al., 2004) and a 170 nm SLD (Praevium, Inc., Santa Barbara, California). The implementation, specifications and performance of these sources are described in detail in chapter 2. The SNR was highest when employing the Yb-doped fibre laser due to the higher available power at the sample arm. The speckle noise was lower in the images obtained with the higher bandwidth sources. However, a significant difference in terms of micro-morphological details was not noticed in between these images [Figure 3.12].

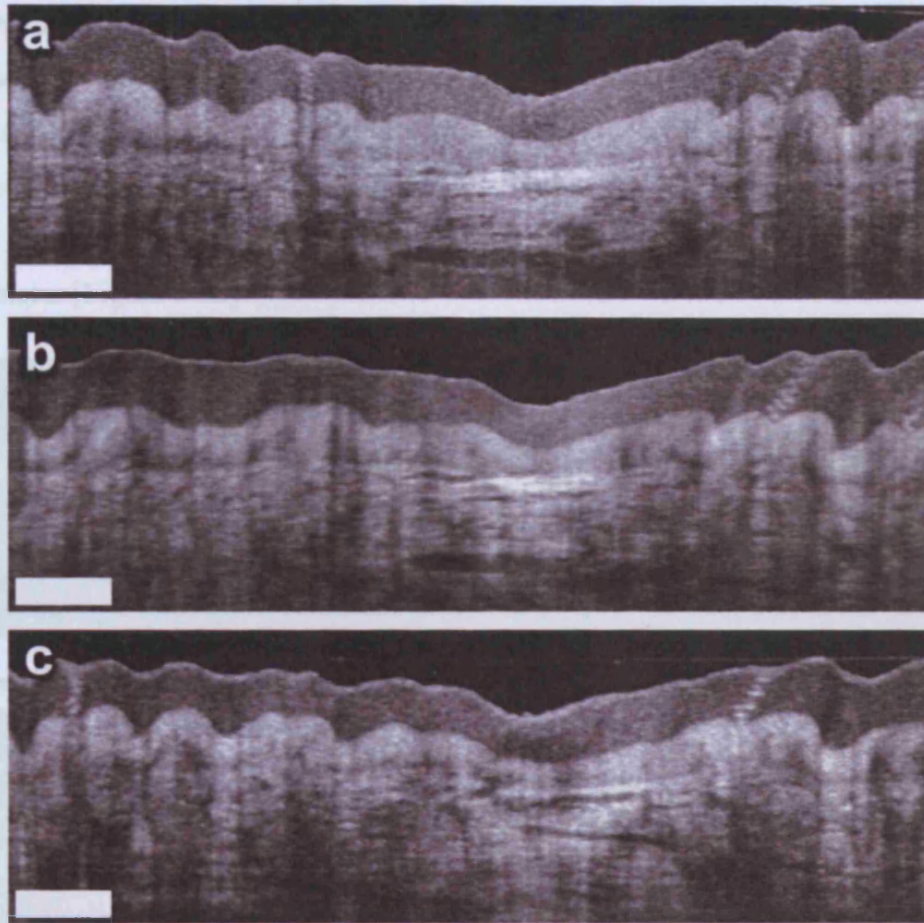


Figure 3.12: OCT images of human skin above the proximal interphalangeal joint of the middle finger at 1300 nm using sources of different bandwidths: (a) 170 nm SLD, (b) 140 nm Yb-doped fibre laser and (c) 100 nm SLD. The scale bars denote 500 μm .

3.5 Quantum-dot vs. amplified spontaneous emission SLD for OCT at 1 μm

1060 nm wavelength region seems to be a compromise when the high axial resolution and limited penetration obtained at 800 nm wavelength region is compared to the reduced resolution and enhanced penetration obtained at 1300 nm wavelength region. In addition, dispersion due to water, the main constituent of biological tissues such as skin (>70%), is nearly zero at 1 μm and this helps to eliminate the influence of depth-dependent dispersion in tissues (Wang et al., 2003b). The main limitation in this wavelength region for OCT is the reduced availability of ultra-broadband sources. Recently, a lot of research has been focussed on developing quantum-dot based SLDs for various medical and telecommunication applications, due to their naturally broad emission spectrum (Zhang et al., 2010b). OCT images of human skin above the PIP joint of the middle finger obtained using two broadband sources: an ASE source (NP Photonics, Tucson, Arizona) and a quantum-dot SLD (FP6 IST project, NANO-UB), both centred at 1.06 μm is compared. The main specifications and

system characteristics of the 1060 nm OCT system have been described in chapter 2. SNR, image resolution and penetration depth of these images were comparable as the output power and the bandwidth of these sources were almost identical. However, the OCT image obtained using the quantum-dot SLD displayed less speckle noise and was devoid of any ringing artifacts, arising due to the polarization mismatch between the arms of the Michelson interferometer [Figure 3.13].

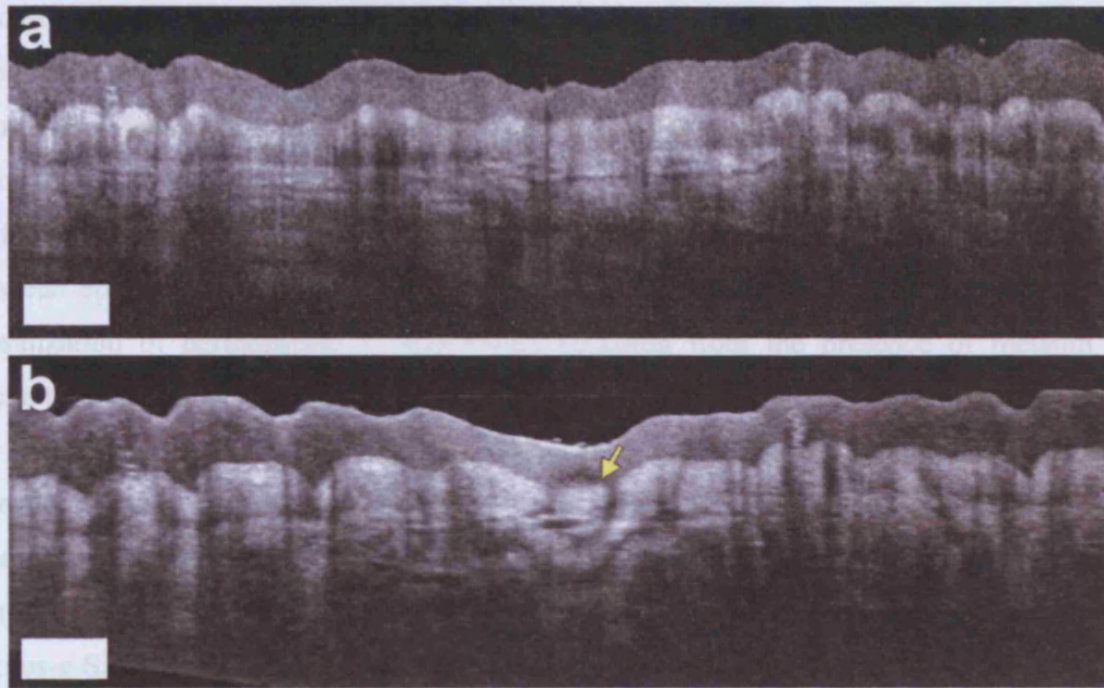


Figure 3.13: OCT images of human skin above the proximal interphalangeal joint of the middle finger obtained at 1060 nm using (a) quantum-dot SLD and (b) amplified spontaneous emission SLD. The yellow arrow in (b) points at the ringing artifact due to polarization mismatch. The scale bars denote 500 μm .

3.6 Comparison of dermal imaging modalities

The success of non-invasive treatment procedures using chemotherapeutic agents such as 5-fluororacil (Krawtchenko et al., 2007), imiquimod (Ulrich et al., 2006) and 5-aminolevulinic acid (McLoone et al., 2008) in basal cell carcinomas and actinic keratoses emphasizes the need for non-invasive imaging modalities with adequate resolution and penetration depth for monitoring disease progression. These non-invasive imaging techniques also help in delineating tumour margins, which is critical in surgery, photodynamic therapy and radiotherapy of skin cancers. Among various dermal imaging modalities, OCT appears to be a promising methodology for investigating micro-morphological and pathological features of the human skin. Multiple studies have been performed to demonstrate the potential of OCT as a non-invasive tool for imaging skin tumours (Barton et al., 2003; Gambichler et al.,

2007b; Mogensen et al., 2009b). Critically sampled 3D imaging capability, visualization of these volumes in arbitrary cross-sectional planes and comparatively larger field of view obtained using OCT helps in detecting tumour margins and other pathological conditions in lateral dimensions too.

A variety of non-invasive *in vivo* techniques showing promise as useful clinical tools in dermatology is currently being investigated. Imaging modalities with submicron-scale resolution, short acquisition time, sufficient contrast, adequate penetration depth and good applicability are of particular importance. ELM or dermoscopy is an imaging technique that allows the visualization of pigmented cutaneous lesion until the starting edge of the RD (Stolz et al., 1989). The dermatoscope generates a beam of light that falls on the cutaneous surface at an angle of 20° and a fluid (oil, water or glycerine) is placed at the interface between epidermis and the device's glass slide to eliminate light reflection, allowing the visualization of dermoscopic characteristics resulting from the presence of melanin and haemoglobin in the different skin layers. The dermatoscope, which allows superimposition of the skin layers, usually provides a 10-fold magnification, whereas a digital dermatoscope can provide a 70-fold magnification (Haenssle et al., 2006). Several studies have been performed to diagnose cutaneous melanoma and pigmented variant of basal cell carcinoma, which exhibit several characteristics which could be identified using ELM (Campos-do-Carmo and Ramos-e-Silva, 2008; Argenziano et al., 2009).

Skin structures down to a depth of 8 mm can be investigated using HFUS at 20 MHz, with a limited resolution of about 80 μm axially and 200 μm laterally (Schmid-Wendtner and Dill-Müller, 2008). However, various epidermal sub-layers could not be differentiated with this resolution. HFUS is used in pre-operative assessment and post-operative follow-up of skin tumours. To improve the resolution of sonographic images of the skin, ultrasound imaging units using up to 100 MHz transducers have been developed for experimental settings. This high centre frequency and bandwidth provides an axial resolution of 11 μm , a lateral resolution of 30 μm and a depth of penetration of 2 mm below the skin surface (Gammal et al., 1999). In general, malignant neoplasms appear as hypo-echoic focal lesions in HFUS images. Melanomas are usually visualized as hypo-echoic structures within the hyper-echoic dermis (Hoffmann et al., 1999).

The principle advantage of MRI over other imaging modalities is that it generates a map of water and lipid distribution in skin, without being degraded by the presence of dense

tissue. Unlike other techniques that have limitations in depth measurements, MRI gives direct tissue localization through slice selection in any depth of material and shows the spatial water distribution within the selected slice. Skin has a relatively short T2 compared to other soft biological tissues as most of its water molecules are in bound state with other macromolecules. Hence by increasing the gradient amplitude and/or duration, various skin layers such as ED, dermis, HD and even the SC can be visualized with a voxel size of the order of 20 μm (Song, Wehrli and Ma, 1997; Bittoun et al., 2006). With sufficient resolution, diagnosis of skin tumours is possible using MRI because the proton relaxation times T1 and T2 are significantly different among all skin layers and tumours. Magnetic resonance spectroscopy of the skin enables a better characterization of skin structures, providing information on skin metabolism. However, results obtained until now shows that the usefulness of MRI to differentiate malignant melanoma and benign melanocytic nevi is limited (Mäurer et al., 1995).

CLM is one of the prominent non-invasive *in vivo* imaging modalities, which could perform optical sectioning of human skin in the horizontal plane with a resolution comparable to that of histology. However, the depth of imaging is limited to $\sim 300\text{ }\mu\text{m}$ at 830 nm due to tissue-induced aberrations and scattering. This effect is also seen in the presented OCT images; however it has less influence on the OCT image formation. In CLM, imaging parameters such as field of view, axial and lateral resolutions are determined by the magnifying power and NA of the objective lens used. A routinely used objective lens with 30X magnification and 0.9 NA provides a field of view of 0.5 mm, a lateral resolution of 0.7 μm and an optical sectioning thickness of 3 μm at $\sim 30\text{ Hz}$ per individual cross section. To enable visualization of larger areas of tissue with varying magnification, a 2D sequence of images can be captured and software-stitched into a mosaic (Nehal et al., 2008). However, this procedure does require a time consuming repositioning of the focussing head. A comparative study using different illumination wavelengths (830 nm, 1064 nm and 1100 nm) demonstrated that the depth of imaging increased to $\sim 350\text{ }\mu\text{m}$ at 1064 nm (Rajadhyaksha et al., 1999). The pathological features and architectural disarray of premalignant and malignant lesions in skin can be identified using CLM. In a study conducted to differentiate benign nevi from malignant melanomas using CLM, melanocytes in benign nevi appeared as round to oval, bright and monomorphic cells, whereas melanomas tend to present polymorphic and irregularly shaped cells (Gerger et al., 2005). Recently, novel confocal line scanning

microscopes demonstrated imaging of nuclear and cellular morphology in human epidermis (Dwyer, DiMarzio and Rajadhyaksha, 2007).

MPT is another emerging non-invasive imaging technique in which intense pulsed near-infrared laser beams (700 to 1000 nm) are focussed onto a tiny excitation volume ($1\text{ }\mu\text{m}^3$) in order to realize non-linear, non-confocal high-resolution luminescence imaging. It enables 4D functional imaging of sub-cellular structures as deep as $\sim 200\text{ }\mu\text{m}$ by detecting the second harmonic signals, autofluorescence and spatially resolved fluorescent decay kinetics. Typically, MPT offers a resolution of 250 ps temporally, 0.4 to 0.6 μm laterally and 1.2 to 2 μm in the axial direction (König, 2008). Keratin in the SC, NAD(P)H in the SS, melanin in the SB, elastin in the dermis are the major fluorophores in the human skin. Collagen can be detected using second harmonic generation. The blue/green emitting co-enzyme NAD(P)H is one of the most interesting fluorophores that can provide information on the intracellular redox state and modifications of the cellular metabolism. Two-photon excitation using near-infrared pulses allows imaging of this co-enzyme in the mitochondria of cells in the basal layer of ED and even intradermal cells. Melanin shows a broad luminescence with a maximum in yellow/red spectral region, when excited with near-infrared femtosecond laser pulses. A variety of dermatological disorders such as psoriasis, skin allergies and cancer have been imaged using MPT. The characteristic symptoms of melanoma such as architectural disarray, pleomorphic cells, poorly defined keratinocyte cell borders and ascending melanocytes could be visualized using MPT (Dimitrow et al., 2009).

Although the resolution offered by OCT is superior to that of HFUS and MRI, it is inferior to that of MPT and CLM. Currently, the depth of imaging seems to be most limited for MPT and CLM ($< 300\text{ }\mu\text{m}$), followed by OCT (1 to 2 mm) and HFUS ($\sim 8\text{ mm}$ at 20 MHz) and the highest for MRI, among these dermal imaging techniques. All these imaging techniques are aiming to give access to huge data sets with the potential to give a complete representation of the morphology at the cellular level. For clinical applications, this raises the demand for automated detection of structural irregularities or more specific indicators typically based on spectroscopic information. While some of the competing techniques intrinsically deliver some kind of functional labelling, OCT in its current form is mainly limited to morphological imaging. Consequently, it emphasise the point that only a combination of multiple non-invasive technologies will be able to replace all aspects of invasive histology with its ability for chemically selective high resolution staining.

3.7 Conclusions and Outlook

In this chapter, *in vivo* 3D OCT images of human skin obtained at three different wavelength bands were compared in terms of resolution, penetration depth and contrast. As expected, the longer wavelengths were less affected by scattering losses and were capable of deeper penetration. All major sub-epidermal layers along with their appendages were clearly visible at different depths using all the wavelength regions employed. As can be seen from figure 3.5, highly scattering layers underneath the less scattering SC display a similar behaviour in hairy and glabrous skin. Interestingly, scattering in the SC itself seems to be strongly dependent on wavelength, which leads to a very different signal intensity profile at this region in the glabrous skin, especially in the 1060 nm wavelength region. The 800 nm system profits from the higher axial resolution and also delivers higher contrast in comparison to 1300 nm. This could be primarily due to the stronger scattering at smaller particles, but also can be influenced by absorption due to the endogenous chromophores such as melanin and haemoglobin. The SC is only $\sim 20\ \mu\text{m}$ thick in hairy skin, whereas it is $\sim 300\ \mu\text{m}$ thick in glabrous skin. Hence, this study emphasizes the need for high axial resolution systems to enable discrimination of thin layers such as the SC in hairy skin cross-sections, and also presents the advantage of high-speed imaging allowing high resolution en face sections at different depths and thus enabling the differentiation of minute morphological structures and abnormalities.

In agreement with previous studies (Mogensen et al., 2009b), the investigation of the normal subjects with different ethnic origins indicates that the skin pigmentation does not affect the depth of light penetration, but rather demonstrates that the main amount of scattering at infrared wavelengths occurs in the dermis. Bright ring-shaped structures associated with highly scattering melanin-rich keratinocytes surrounding dermal papillae in darker skin tones could be demarcated within the basal layer of the epidermis and were found to locally increase the contrast at the dermal-epidermal junction. The higher contrast observed at the dermal-epidermal junction of the dark-skinned subject was analytically verified. The investigation of moles and scar tissue during this study accentuated the need for employing longer wavelength sources to evoke information from deeper layers. Lower wavelength bands provided more contrast for superficial nevus nests in light-pigmented moles, while the nests of the thicker, highly pigmented moles were overcast by shadows, which could be suppressed by using longer wavelengths.

The dermal-epidermal junction, which is critical in early cancer diagnosis (Komitowski, 1982), could be well delineated using the 800 nm system and this wavelength is also best suited for pharmacological studies, which focus on the epidermal barrier function (Gfesser et al., 1997; Barai et al., 2007). Meanwhile, employment of the 1300 nm wavelength region becomes inevitable in applications such as detection of deeper tumour margins, assessment of larger skin pathologies and evaluation of treatment effects, which require information from deeper dermal layers. 1060 nm wavelength region is better suited than 800 nm and 1300 nm wavelength regions in terms of penetration depth and contrast, but is limited in axial resolution due to the reduced availability of ultra-broadband sources in this wavelength region.

The broad bandwidth of the light sources helped to obtain high quality OCT images of the human skin. However, slight differences in bandwidth did not have a large impact on the extent of microstructural details provided by the OCT images. The development of broadband quantum-dot SLDs around 1 μm wavelength region seems to be beneficial for dermal OCT. Among various optical imaging modalities, OCT appears to be a promising candidate having the essential requisites to visualize micro-morphology of skin as deep as 1-2 mm with a limited contrast. OCT systems that are capable of acquiring a gigavoxel image within ~ 10 s with micron-scale resolution to varying imaging depths have been demonstrated. Thus, this study manifests the potential of OCT as a high-speed, high-resolution non-invasive imaging technology for diagnostics and treatment monitoring in dermatology.

Chapter 4

***In vitro* tumour study in gastrointestinal tissues using 3-D OCT at multiple wavelengths**

4.1 Introduction

4.1.1 Anatomy of the oesophagus and the colon

The oesophagus and the colon are constituent parts of the gastrointestinal system of the human body, which is primarily involved in breaking down of food for absorption into the body. The oesophagus is a strong muscular tube which conveys food from the oropharynx to the stomach. Meanwhile, the colon is a section of large intestine, which helps to recover water and salt from the faeces, and propels increasingly solid faeces to the rectum prior to excretion. The colon is divided anatomically into ascending, transverse, descending and sigmoid segments. The arrangement of the major muscular components remains relatively constant in both the oesophagus and the colon, whereas its mucosa shows marked variations in both these regions. Both the oesophagus and the colon can be divided into four distinct functional layers.

- **Mucosa** – The mucosa is made up of three components: the epithelium, a supporting lamina propria (LP) and the muscularis mucosae (MM), a thin smooth muscle layer that produces local movement and folding of the mucosa.
- **Submucosa** – This layer of loose collagenous tissue supports the mucosa and contains the larger blood vessels, lymphatics and nerves.
- **Muscularis propria (MP)** – This muscular wall consists of smooth muscles, which is usually arranged as an inner circular layer and an outer longitudinal layer.
- **Adventitia (oesophagus)/Serosa (colon)** – This outer layer comprises loose supporting tissue conducting the major vessels, lymphatics and nerves (Young and Heath, 2000b).

4.1.1.1 Oesophageal mucosa

The oesophagus is lined by squamous epithelium except for a small segment at its lower end, which consists of mucin-secreting columnar epithelium. The squamous-lined

mucosa is $\sim 500 - 800 \mu\text{m}$ thick and is composed of non-keratinizing stratified squamous epithelium with subjacent LP, which rests on the underlying MM, as shown in figure 4.1. The squamous epithelium has a basal zone consisting of several layers of cuboidal cells with dark nuclei and it accounts for 10 – 15% of the thickness of the normal epithelium (Day et al., 2003a). Above the basal zone, the epithelial cells are larger and become progressively flattened, but retain their nuclei even on the surface. The lower border of the squamous epithelium is irregular because of the presence of numerous vascular papillae of connective tissue, which project upwards from the LP to as far as two-third of the way into the total thickness of the epithelium.

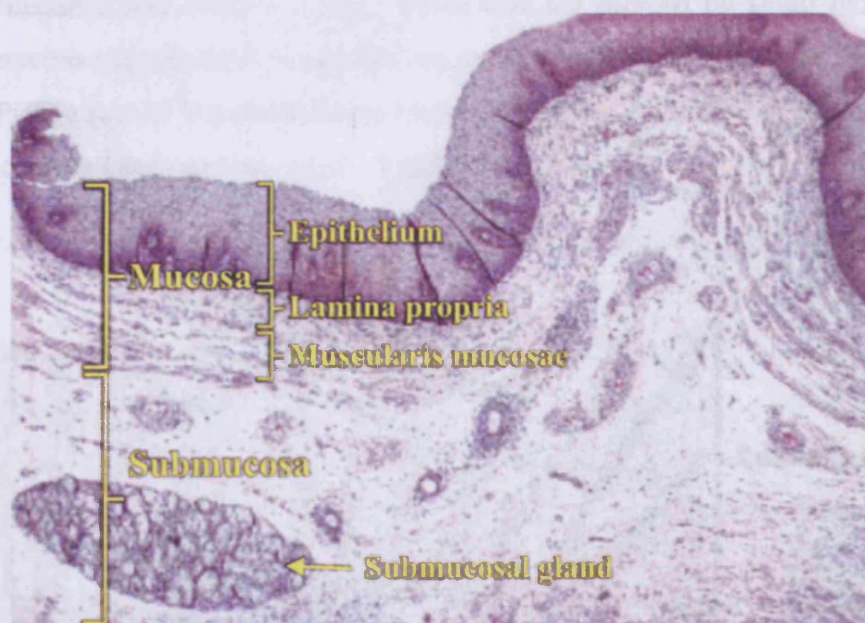


Figure 4.1: Normal oesophageal mucosa (Forbes et al., 2005a)

The LP consists of loose connective tissue in which there are a sprinkling of lymphocytes, plasma cells and eosinophils. The MM has a variable pattern. In the upper part, it commonly consists of isolated or irregularly arranged muscle bundles rather than forming a continuous sheet. However, in the middle and lower portions, it forms a continuum of longitudinal and transverse fibres. The thick submucosa contains deeper oesophageal glands and a spread out lymphatic plexus in a loose connective tissue network, which accounts for the early and extensive submucosal spread of oesophageal carcinoma.

4.1.1.2 Colon mucosa

Colonic mucosa comprises parallel rows of epithelial tubules or crypts, surrounded by the connective tissue framework of the LP and resting on the MM (Figure 4.2). The four main

cell types represented within the colonic crypt and surface epithelium are columnar cells, goblet cells, paneth cells and endocrine cells, which are derived from common stem cells that reside at or near the crypt base. The structure and function of columnar cells are altered as it leaves the crypt to occupy the one cell thick surface epithelium. Crypt columnar cells are primarily secretory cells, whereas surface columnar cells function as absorptive units and are characterized by their well-developed microvillous brush border. The bases of the crypts are predominantly occupied by small and condensed goblet cells, which secrete various mucins. The LP of colonic mucosa is composed of a stroma of argyrophilic fibres containing fibroblasts, lymphocytes, plasma cells, mast cells and macrophages. The MM consists of longitudinal, transverse and oblique muscle fibres that are pierced by small blood vessels supplying the mucous membrane. Lymphatics are mostly found within the MM, but very few pass into the LP. The foci of lymphoid tissue interfere with the continuity of the MM causing its fibres to become splayed out (Day et al., 2003b).

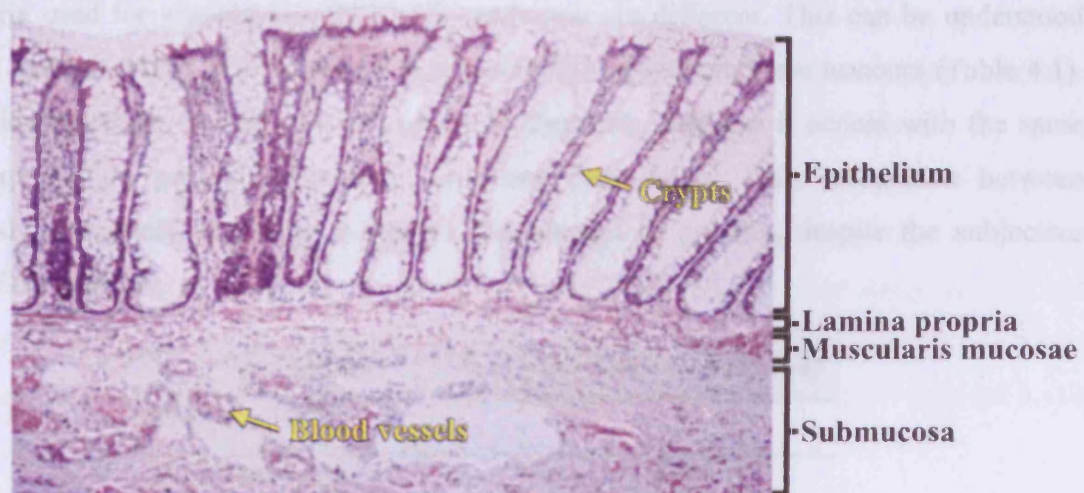


Figure 4.2: Normal colonic mucosa (Forbes et al., 2005b)

4.1.2 Tumour classification of the oesophagus and the colon

A general classification of a tumour tissue is depicted in figure 4.3. A tumour is a neoplasm or solid lesion formed by abnormal growth of cells. It can be benign, pre-malignant or malignant. In the oesophagus and the colon, carcinomas (malignant epithelial tumours) are mainly of squamous or glandular origin. Dysplasia refers to an abnormality in the development of a cell. It is typically used when the cellular abnormality is restricted to the originating tissue, but may transform into a malignant version.

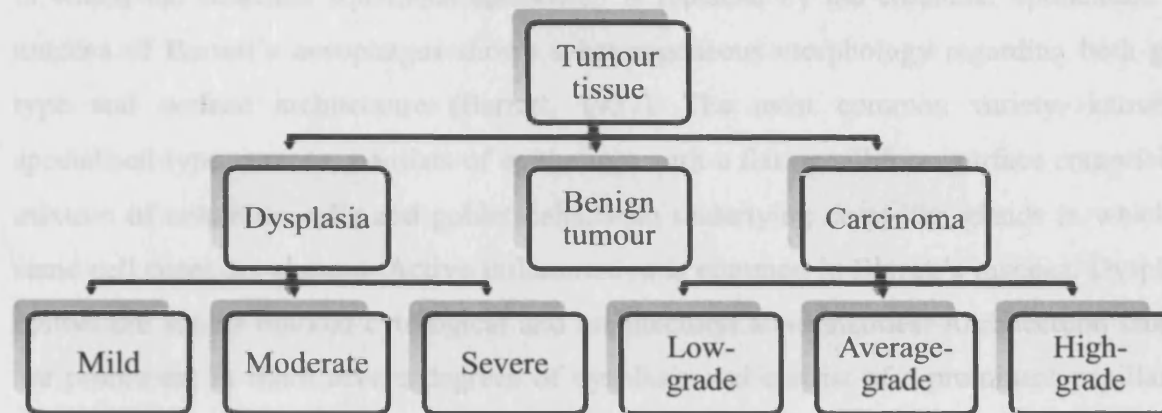


Figure 4.3: General tumour classification

The most reliable feature for assessing the grade of dysplasia and carcinoma are tissue architecture, nuclear changes and cytoplasmic differentiation. Dysplasia is graded as mild, moderate or severe. Meanwhile, carcinoma is graded as well-differentiated (low-grade), moderately-differentiated (average-grade) and poorly-differentiated (high-grade). However, the criteria used for grading dysplasia and carcinoma are different. This can be understood from the analysis of the distribution of aneuploid DNA content in these tumours (Table 4.1). Aneuploidy increases in step with the grade of dysplasia, whereas it occurs with the same high frequency in graded carcinomas (Goh and Jass, 1986). This association between aneuploidy and grade of tumour validates the concept of grading, despite the subjective nature of the exercise.

Grade	DNA aneuploidy (%)
Mild dysplasia	4
Moderate dysplasia	18
Severe dysplasia	36
Low-grade carcinoma	63
Average-grade carcinoma	64
High-grade carcinoma	63

Table 4.1: Percentage variation in DNA aneuploidy for various grades of tumour (Goh and Jass, 1986)

4.1.2.1 Oesophageal epithelial tumours

A large majority of the oesophageal and colonic tumours originate from the epithelial tissues. These tumours can be classified into several categories on the basis of tumour progression and other characteristic features. Barrett's oesophagus is a pathologic condition

in which the stratified squamous epithelium is replaced by the columnar epithelium. The mucosa of Barrett's oesophagus shows a heterogeneous morphology regarding both gland type and surface architecture (Barrett, 1957). The most common variety, known as specialised-type mucosa, consists of epithelium with a flat or villiform surface comprising a mixture of columnar cells and goblet cells, with underlying crypt-like glands in which the same cell types are present. Active inflammation is common in Barrett's mucosa. Dysplastic epithelium shows marked cytological and architectural abnormalities. Architectural changes are prominent in more severe degrees of dysplasia and consist of a prominent papillary or villous configuration of the surface and branching, complex budding and a back-to-back arrangement of glands. There are two types of epithelial dysplasia: In type 1, the changes resemble those seen in adenomatous epithelium with enlarged, elongated, hyperchromatic nuclei showing crowding or stratification. Meanwhile in type 2, there are rounded or pleomorphic vesicular nuclei without crowding or stratification (Schmidt et al., 1985). The two forms are frequently found together. Based on the severity, epithelial dysplasia can be subdivided into mild, moderate and severe dysplasia (Riddell et al., 1983).

The epithelial tumours can be benign or malignant. Squamous cell papillomas are benign multi-lobulated tumours with a granular or warty surface and a firm consistency. They have a papillary architecture with central cores of vascular connective tissue covered by thickened stratified squamous epithelium which lacks atypia and shows normal differentiation from the basal to the surface layer. Meanwhile, inflammatory polyps are another type of benign structures, which have a relatively smooth surface. They show basal cell hyperplasia with varying erosion of the epithelium and usually have a marked acute inflammatory cell infiltrate of the LP (Parnell et al., 1978).

Malignant oesophageal tumours are mainly two types: squamous cell carcinomas (SCC) and adenocarcinomas, which usually arise from Barrett's oesophagus (Vizcaino et al., 2002). In superficial oesophageal cancer, the tumour is confined to the mucosa or has not spread further than the submucosa, with or without lymph node metastasis. It has been found that the presence of an elevated component in superficial oesophageal cancer is an important macroscopic feature suggesting submucosal invasion and a high probability of lymph node involvement (Sugimachi et al., 1988). SCC appear as exophytic, ulcerating or infiltrating lesions or a combination of these and often result in a stricture which is usually irregular, friable and haemorrhagic. Sometimes, an oesophageal carcinoma is surrounded by satellite

nodules due to submucosal extension. These tumours show all grades of differentiation, from keratinizing squamous carcinomas with well-formed cell nests to undifferentiated growths without recognizable keratin, which are difficult to identify as squamous (Kuwano et al., 1985). Infiltration of the submucosa is often a conspicuous microscopic feature of squamous cell carcinoma. Three uncommon variants of SCC are verrucous SCC, carcinosarcoma and basaloid-squamous carcinoma. Adenocarcinomas are flat, ulcerating, infiltrative lesions, frequently associated with stenosis of oesophageal lumen. They have a tubular or papillary pattern and severe dysplasia is common in adjacent epithelium. Lymph node metastases are more frequently seen in adenocarcinomas (Thompson, Zinsser and Enterline, 1983). There are also other uncommon aggressive oesophageal tumours such as adenosquamous carcinoma, small cell carcinoma, choriocarcinoma and malignant melanoma.

4.1.2.2 Colonic epithelial tumours

Inflammatory disorders such as ulcerative colitis and Crohn's disease are common in colon. Inflammatory polyps are result of full-thickness ulceration of the mucosa with undermining of adjacent intact mucosa, which is relatively raised up so that it projects into lumen. Benign inflammatory polyps rarely become dysplastic. Adenoma is a benign tumour of glandular origin and most of the colonic adenomas are present as a protuberant mass or polyp. They are benign neoplasms, but have malignant potential. Adenoma has been considered as the most important type of epithelial polyp in the colon. Small adenomas are usually sessile and slightly redder than surrounding mucosa. With increasing size, adenomas usually become pedunculated, their head become dark red and are broken into lobules with intercommunicating clefts. This darkening is due to a combination of increased vascularity and different light scattering properties of the neoplastic epithelium. The stalk of the pedunculated adenoma is composed of normal mucosa and submucosa (Day et al., 2003c).

Based on their microscopic appearance, adenomas are classified as tubular, tubulovillous and villous. Tubular adenoma consists of closely packed, branching tubules, separated by varying amounts of LP. These tubules may be relatively regular or show considerable irregularity with much branching, budding and infolding. Tubules may show focal cystic dilation, leading to secondary infection and haemorrhage in the substance of tumour. In villous adenoma, each folium consists of a core of LP covered by a sheet of epithelial cells. Between the folia, the epithelium rests upon the MM (Thompson and Enterline, 1981). Adenomas show abnormalities in architecture, cytology and differentiation

that are encompassed by the term dysplasia. All adenomas are, by definition, dysplastic. In mild dysplasia, nuclei are slightly enlarged, elongated, hyperchromatic, crowded and pseudostratified, but cellular polarity is well preserved. The tubules will be regular, though closely apposed and show branching. In moderate dysplasia, nuclei are further enlarged, less elongated and show focal loss of polarity. While in severe dysplasia, nuclear polarity is just lost, nuclei are greatly enlarged, round and contain prominent nucleoli. Cytoplasm is undifferentiated. Tubules show irregular or complex branching and budding (Konishi and Morson, 1982). It has been observed that the frequency of severe dysplasia increases with the size of the adenoma and is highest in villous adenoma. Serrated adenoma is another type of serrated polyp that contains dysplastic epithelium. However, the criteria for diagnosing serrated adenoma remain imprecise.

Several studies have shown that the malignant potential is increased in large adenomas compared to smaller ones (Enterline et al., 1962; Silverberg, 1970). The prevalence of cancer in adenomas less than 1 cm in size is only about 1%; in those between 1 and 2 cm in diameter is about 10%; whereas in those over 2 cm in diameter, there is nearly 50% malignancy rate. The malignant potential of adenomas has also been calculated on the basis of their size and histological type. It has been shown that very common tubular adenoma, less than 1 cm in diameter, has a very low malignant potential (1%), whereas the small villous tumour has a 10% malignancy rate. Tubulovillous adenomas of this size have a malignant potential of about 4%. In those tumours between 1 and 2 cm in diameter, there is no significant variation in the malignancy rate with histological type, but in polyps over 2 cm in diameter the malignant potential is significantly greater for tumours with a villous component than for tubular adenomas. The grading of adenomas into mild, moderate or severe dysplasia has shown that, irrespective of histological growth pattern, their malignancy potential increases with increasing degrees of dysplasia (Muto, Bussey and Morson, 1975). However, the malignancy rate in large adenomas (> 2 cm) shows little relation to the degree of dysplasia.

Colorectal cancer is the fourth most common cancer in males and the third most common cancer in females worldwide (Parkin et al., 2005). The main type of colon cancer falls under the category of adenocarcinomas. The pathologic condition is referred to as adenocarcinoma, when the neoplastic cells invade across the mucosa into deeper regions. Once growth extends into the MP, there is ~ 12% risk of lymph node metastasis. Tubular

differentiation can be easily discerned in adenocarcinomas. The grade of differentiation is gauged mainly on architectural features. Low-grade or well-differentiated tumours are composed of regular tubules lined by columnar epithelium. Nuclei are uniform in size and shape, and cellular polarity is easily noticed. This resembles adenomatous epithelium. In average-grade or moderately differentiated cases, tubules are regular or slightly irregular and cellular polarity is just discerned. Meanwhile in high-grade or poorly-differentiated tumours, tubules are highly irregular or absent altogether. In place of tubules are single cells, small clumps or large sheets of undifferentiated cells (Jass et al., 1986). Besides adenocarcinomas, other types of tumours such as endocrine cell tumours, SCC and adenosquamous carcinomas are also found in the colon.

4.1.3 Motivation: *In vitro* gastrointestinal tumour imaging using multispectral OCT

Since 1970's, the incidence rate of adenocarcinoma in the oesophagus and the colon has increased dramatically. The incidence of oesophageal cancers has been rising by 4 – 10% annually and this increasing trend is still continuing (Devesa, Blot and Fraumeni, 1998; Ferlay et al., 2008). Oesophageal cancer has a very poor survival rate: 16% of the cases in the United States of America and 10% of the cases in Europe survive at least five years (Sant et al., 2003; Altekruse et al., 2009). The most recognized risk factor of the oesophageal cancer is Barrett's oesophagus. Colorectal cancer is the second most common cause of cancer-related deaths in the United States of America and a recent study has shown an increase in incidence rate of colorectal cancer in patients aged < 40 years (Meyer et al., 2010). Colorectal cancers usually originate from hyperplastic or dysplastic polyps. The steady rise in cancer incidence rates among the general population and poor survival rates of patients, point towards the urgent importance of effective, low-cost, non-invasive and repeatable cancer diagnostic imaging methods.

OCT is a promising non-invasive *in vivo* 3-D imaging modality capable of delivering ultrahigh resolution images of biological tissues with a penetration depth of 1 – 2 mm (Drexler and Fujimoto, 2008a). It is capable of detecting microstructural changes in the tissue architecture with high sensitivity and its image contrast is based on the inherent optical scattering. The imaging speed of OCT has significantly increased during the past two decades and the high-speed image acquisition makes this technique less prone to motion artifacts. OCT is a relatively simple optical imaging technique, which does not require any contact medium and it is easily compatible to catheter endoscopes. These factors make OCT a

potential candidate for gastrointestinal imaging applications. Majority of gastrointestinal tumours are of epithelial origin. Hence, the penetration depth achieved using OCT will be adequate for detecting the malignant changes occurring in gastrointestinal tissues. Several *in vitro* and *in vivo* studies have been performed on gastrointestinal tissues using OCT (Qi.X, Jr. and Rollins, 2008).

However, more systematic studies are needed to realize the advantages and limitations of OCT in diagnosing gastrointestinal pathologies. In this study, *in vitro* samples of the oesophagus and the colon at various stages of tumour progression is imaged using OCT at multiple wavelengths. This *in vitro* study attempts to find the capability of OCT for diagnosing malignant changes in tissues. Moreover, this investigation will help to determine the optimal wavelength region for tumour studies using OCT, through the comparison of these images in terms of resolution, penetration depth and contrast.

4.2 Materials and methods

4.2.1 Specimens

In vitro tumour samples of oesophagus and colon were imaged using OCT at three different wavelengths. The specimens were obtained from our research collaborators, Mr. Bob Bonwick, Histology technician; Dr. Catherine Kendall, Post-doctoral research fellow and Prof. Nicholas Stone, Head of Biophotonics group in Gloucestershire Hospitals NHS Foundation Trust, Gloucester, UK. All necessary risk assessment procedures for imaging, storing and transporting the tumour samples had been followed and ethical approval had been obtained from the responsible authorities for carrying out this collaborative study (Ethical approval no. 03/142G, 02/58G). To study various micro-morphological changes taking place during malignant transformations, samples were selected to comprise different grades of dysplasia and carcinoma. The specimens employed for this study were snap frozen samples maintained at -80°C following surgical resection. This cryopreservation helped to preserve the structural organization of these samples intact over a long period of time. In addition to oesophagus and colon, a few other samples from prostate, stomach and larynx were also imaged. The tumour samples were removed from the freezer and brought to room temperature prior to OCT imaging.

4.2.2 OCT imaging

Three spectrometer-based frequency domain OCT systems operating at 800 nm, 1060 nm and 1300 nm wavelength regions respectively, were used to obtain images of the tumour samples *in vitro*. An ultra-broadband coherent light source (Ti: Al₂O₃ laser) was used in the 800 nm OCT system; an amplified spontaneous emission (ASE) source (NP Photonics, Tucson, Arizona) was used in the 1060 nm OCT system and a superluminescent light emitting diode source (Thorlabs Inc., Newton, New Jersey) were used in the 1300 nm OCT system. The design, implementation and the main specifications of these three OCT systems have been described in detail in chapter 2. Surface dimensions of the scan region were selected appropriately depending on the size of the specimen, with 1024 transverse sampling points per B-scan. The wavelength-dependent components of the handheld probe such as the collimator and the objective lens were selected appropriately for each OCT system, so that they were comparable in terms of transverse resolution and depth of focus. The handheld probe was mounted vertically onto a translational stage to set the focus on the sample surface. The specimens were immersed in saline solution and covered from above with a tilted glass plate for refractive index matching. This helped to maximise the backscattered signal collected from the sample. All three OCT systems were found to be similar in terms of SNR, transverse resolution and sensitivity roll-off. However, the free-space axial resolution of the 800 nm system was found to be better than the other two systems (refer table in chapter 2). Images obtained from these specimens at three wavelengths were compared in terms of resolution, contrast and penetration depth.

4.2.3 Tissue marking and fixing

The tumour specimens were placed on marked dishes for OCT imaging and these marks were aligned with the OCT imaging axis. After OCT images were obtained from the three systems, the tissues were marked on both ends of the scan axis using a tissue marking dye, Biomark Blue (Biostain Ready Reagents Ltd., Manchester, UK). Prior to marking, the surface of the specimens was dehydrated using methylated spirit, in order to prevent spreading of the marking dye. Then the specimens were fixed using the standard tissue preservative, 10% neutral buffered formalin.

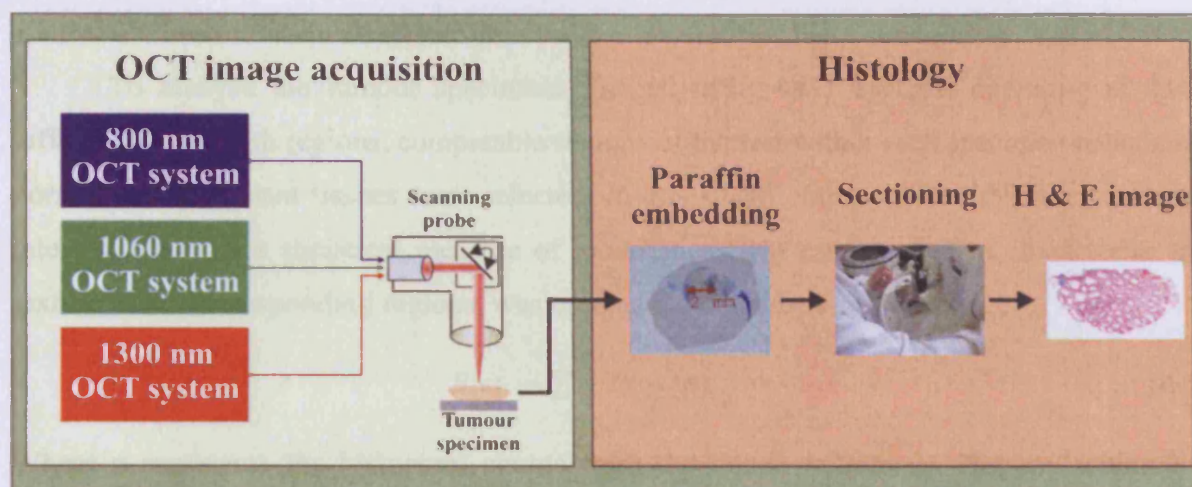


Figure 4.4: Schematic diagram depicting the OCT systems and the histology procedures followed

4.2.4 Histology

The formalin fixed samples were sent over to our collaborators for histology. Biological tissues had to be supported in a hard matrix in order to allow sufficiently thin sections to be cut. For this purpose, the samples were completely dehydrated by transferring them through baths of progressively more concentrated industrial methylated spirits (IMS). At first 70% IMS was used to avoid tissue brittleness and to prevent chattering during its sectioning. Then these tissues were processed in 100% IMS three times to ensure complete dehydration. After this processing, the hydrophobic clearing agent, Xylene, was used to remove the alcohol from the specimens. Subsequently, molten paraffin wax was impregnated into these specimens using reduced pressure at a temperature of 62°C. This wax impregnation process is repeated four times. Once the specimens had been properly processed, they were embedded into a wax block, which provides external support during microscopy. The embedding medium fills all the spaces within the specimen and resists any kind of distortion while sectioning. A microtome was used to cut the paraffin blocks containing the specimens into 10 µm thick sections. The sectioning was performed vertically perpendicular to the surface of the tissues. Then these sections were stained using Mayer's haematoxylin and eosin yellowish. Haematoxylin, a basic dye, stains cell nuclei blue-back; whereas, eosin, an acidic dye, stains cell cytoplasm and connective tissue fibres in varying shades of pink, orange and red (Bancroft and Gamble, 2008). Thus these stains together could demonstrate the general histological architecture of a tissue. Finally, these sections were washed in the weak alkaline solution of lithium carbonate to improve the visualization of cell nuclei, which helps to identify regions with increased mitoses.

4.2.5 OCT tumour data analysis

To analyse the tumour specimens imaged using OCT systems operating at three different wavelength regions, comparable regions of interest within each specimen containing normal and malignant tissues were selected. In this study, entropy (E) within the region of interest, which is a statistical measure of randomness that can be used to characterise the texture of the corresponding regions, was used as the diagnostic parameter.

$$E = -\sum p \cdot \log_2(p) \quad \dots (4.1)$$

Where p represents the histogram counts from the region of interest. Entropy within the cross-sectional images was calculated and was plotted across the regions of interest. This approach helped to determine the variation of entropy along the tumour margins and was found to be useful in determining the optimum wavelength region that could be employed for OCT imaging to demarcate tumour regions.

4.3 Results

4.3.1 Oesophageal specimens

OCT images of an oesophageal sample having Barrett's oesophagus on its extreme right side were obtained at three wavelength regions [Figure 4.5]. The mucosa of columnar-lined oesophagus showed a heterogeneous morphology regarding gland type and surface architectures in the histological section. In OCT sections, the glandular inflammation and structural disarray could be observed in the extreme right side of the specimen. The structural contrast was least for the OCT image obtained at 1300 nm.

Figures 4.5(e - g) shows the comparable regions that were used for data analysis and the direction in which the entropy data was plotted. In figure 4.5(h), the entropy obtained over depth from each cross-section is plotted against the region showing transition from the normal oesophagus to Barrett's oesophagus. It can be seen from this figure that the entropy shows an increasing trend as it approaches the Barrett's oesophagus region. The boundary between the normal and Barrett's oesophagus was marked by sudden increase in entropy at all three wavelength regions. It is observed that the entropy variation towards Barrett's oesophagus were quite similar at all three wavelength regions.

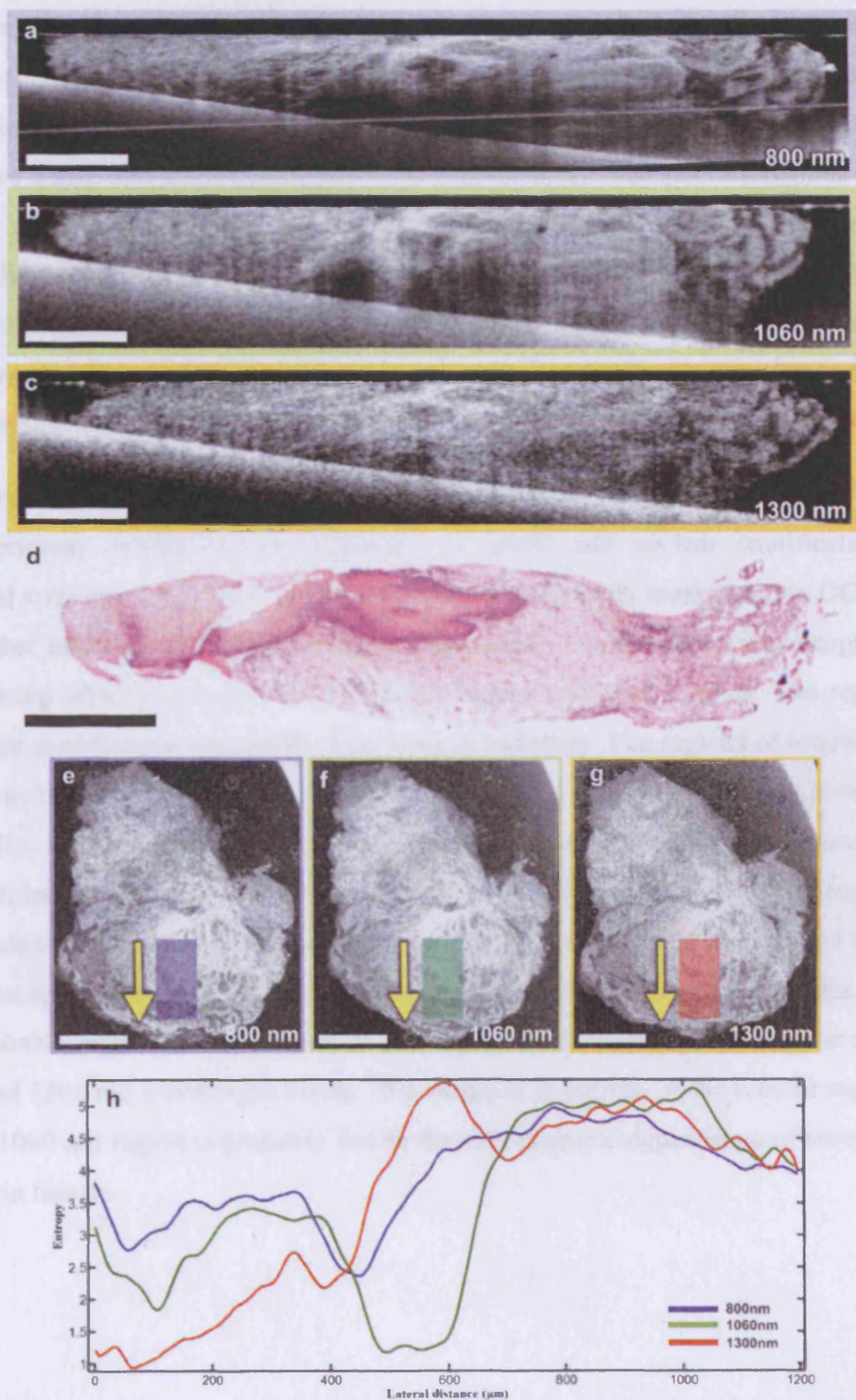


Figure 4.5: An oesophageal sample showing normal (left) and Barrett's oesophagus (extreme right side). OCT images obtained at 800 nm (a), 1060 nm (b), 1300 nm (c) and its corresponding histology (d). *En face* sections showing the selected regions of interest at 800 nm (e), 1060 nm (f) and 1300 nm (g). The yellow arrows denote the direction of entropy evaluation. Entropy variation at the three wavelength regions plotted along the lateral distance (h). The scale bars denote 500 μm in cross-sections (a-c) and 1 mm in *en face* sections (e-g).

In a dysplastic epithelium of oesophagus, architectural changes were present more frequently (Figures 4.6 and 4.7). Figure 4.6 shows OCT images from a Barrett's oesophageal specimen having mild dysplasia. It is evident from the histology that the Barrett's islands tend to have denser nucleation and higher structural disarray. The selected regions of interest containing dysplastic tissues on the left side and normal tissues towards the right side is shown in the *en face* sections [Figs. 4.6(e-g)]. As can be seen from figure 4.6(h), the entropy in the cross-sections decrease towards the normal tissues. The images obtained using 1300 nm OCT system shows a sharper decline in entropy, compared to images obtained using the other two systems.

However, these changes become more prominent in more severe degrees of dysplasia. These specimens exhibit increased density of nuclei and nuclear stratification in the histological sections. The higher density of nuclei can be clearly marked out in OCT sections due to higher backscattering in this region [Figs. 4.7(a - c)]. For lower wavelength regions, the shadowing effect is prominent beneath the highly scattering regions. The regions with high nuclear proliferation are readily detectable in histology. The regions of interest used for data analysis is marked in the *en face* sections [Figs. 4.7(e - g)]. In the entropy plots shown in figure 4.7(h), the curves form a deep valley in the tumour regions at 800 nm and 1300 nm wavelength bands. However, the effect was just the opposite at 1060 nm wavelength region. As the grade of the tumour increases, it leads to poor structural differentiation and the tumour masses appears as strongly scattering homogenous structures in OCT images. This may be the probable reason for the decline of entropy in the tumour regions that were visible at 800 nm and 1300 nm wavelength bands. The variation in entropy at the tumour region that is visible at 1060 nm region is probably due to the spectroscopic dependence of absorption and scattering in tissues.

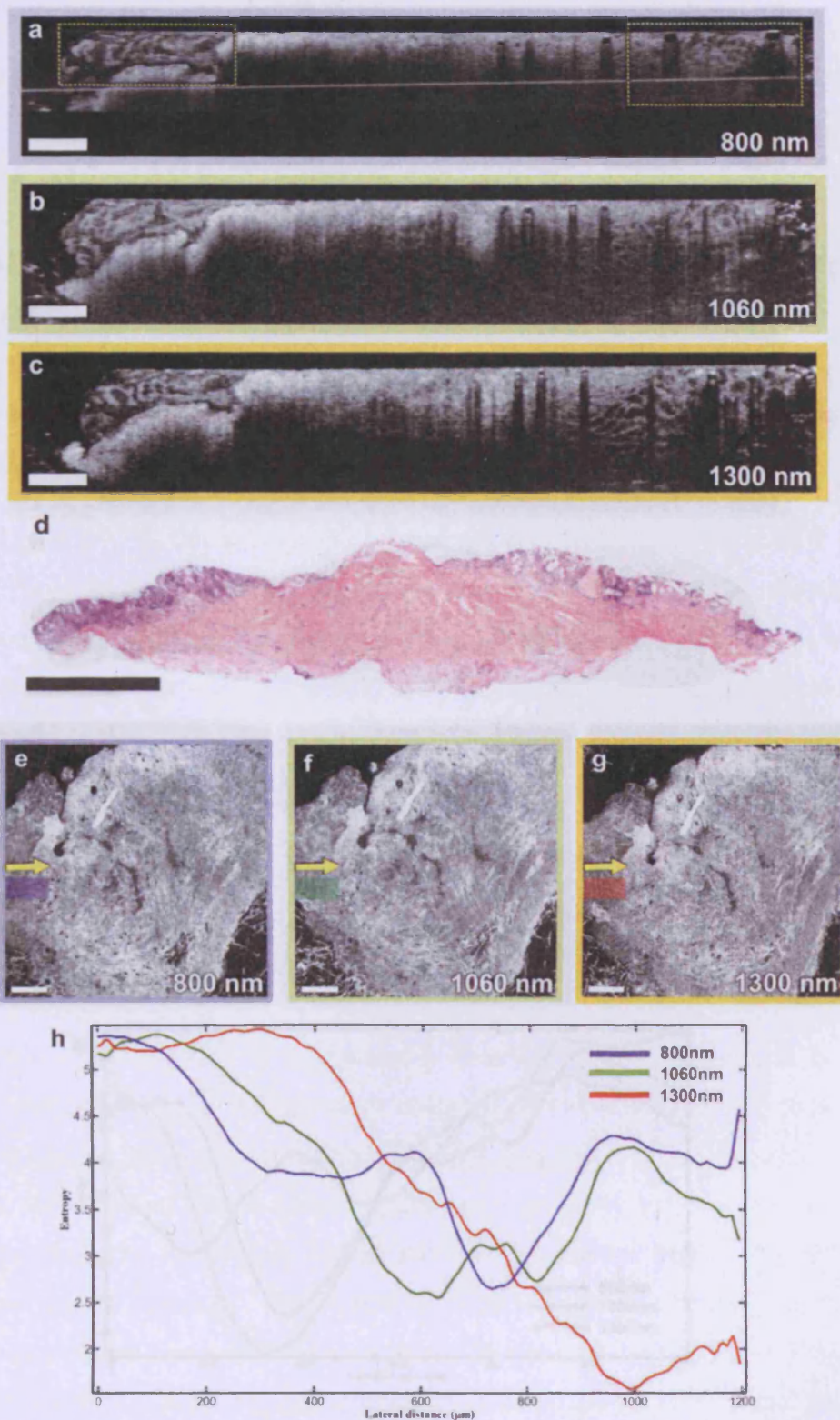


Figure 4.6: A Barrett's oesophageal specimen showing mild dysplasia. OCT images obtained at 800 nm (a), 1060 nm (b), 1300 nm (c) and its Corresponding histology (d). *En face* sections showing the selected regions of interest at 800 nm (e), 1060 nm (f) and 1300 nm (g). The yellow arrows denote the direction of entropy evaluation. Entropy variation at the three wavelength regions plotted along the lateral distance (h). The scale bars denote 500 μm in cross-sections (a-c) and 1 mm in *en face* sections (e-g).

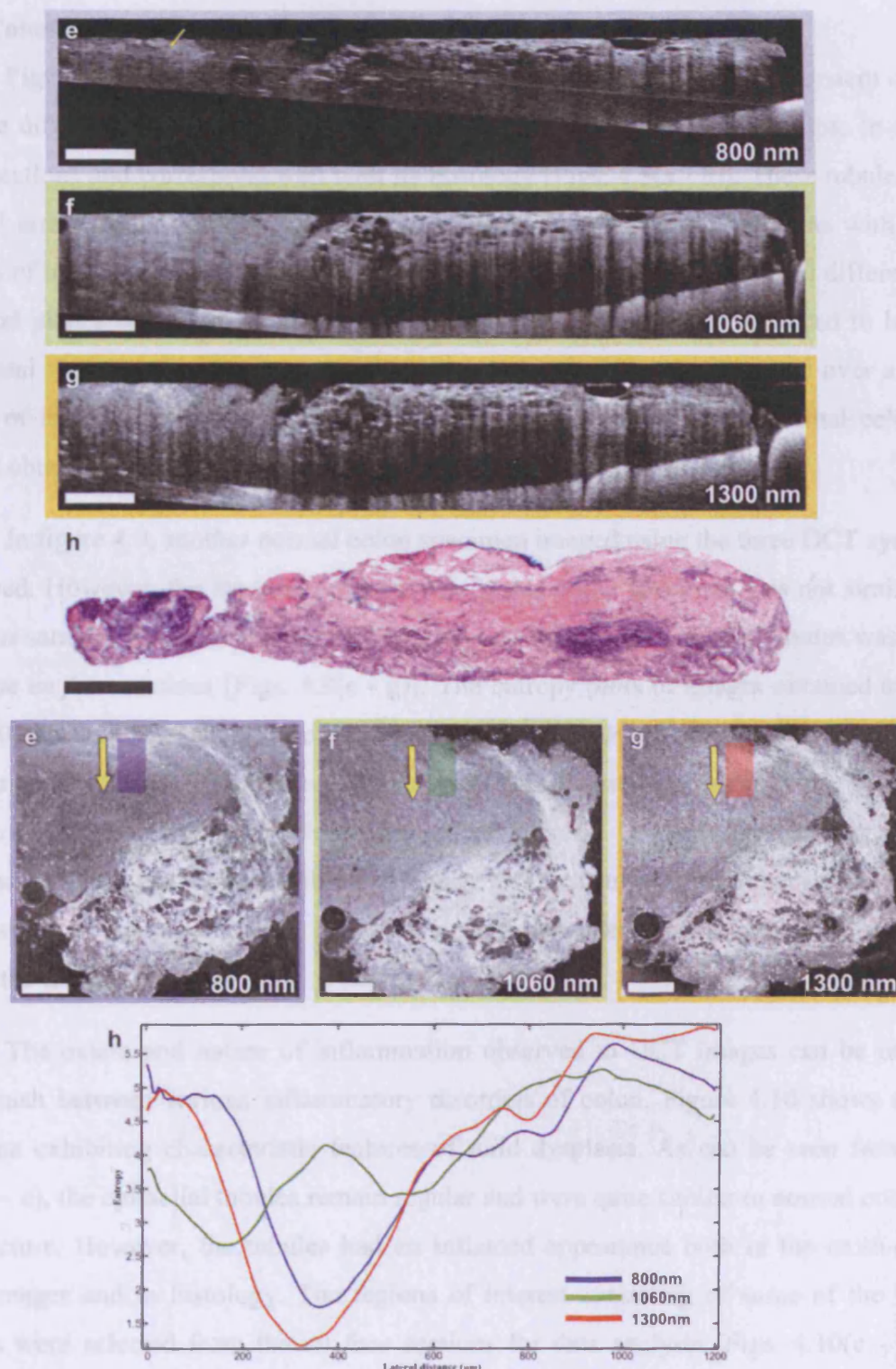


Figure 4.7: A Barrett's oesophageal specimen showing high grade dysplasia. OCT images obtained at 800 nm (a), 1060 nm (b), 1300 nm (c) and its corresponding histology (d). *En face* sections showing the selected regions of interest at 800 nm (e), 1060 nm (f) and 1300 nm (g). The yellow arrows denote the direction of entropy evaluation. Entropy variation at the three wavelength regions plotted along the lateral distance (h). The scale bars denote 500 µm in cross-sections (a-c) and 1 mm in *en face* sections (e-g).

4.3.2 Colonic specimens

Figure 4.8 shows the OCT images of a normal polyp obtained using system operating at three different wavelength regions. The epithelial tubules are clearly visible in the OCT cross-sections and correspond well with its histology [Figs. 4.8(a - d)]. These tubules show a parallel arrangement and are devoid of any branching. The en face sections with selected regions of interest are displayed in figs. 4.8(e - g). The entropy obtained from different cross-sectional planes was plotted against the lateral distance. The curves appeared to be almost horizontal showing that the entropy within the cross-sections was the same over a selected region of interest for normal colon tissues. The entropy curves of the normal colon tissue images obtained at all three wavelength regions were quite similar.

In figure 4.9, another normal colon specimen imaged using the three OCT systems are displayed. However, the structural appearance of this colon specimen was not similar to the previous sample. A region containing both muscle tissues and epithelial tubules was selected from the *en face* sections [Figs. 4.9(e - g)]. The entropy plots of images obtained at 800 nm and 1300 nm had a negative slope. However, the entropy plot of images obtained at 1300 nm was almost horizontal. This difference in slopes of the curves was probably due to difference in ratio of constituents in the selected region of interests. It shows that entropy in images obtained at 1300 nm wavelength region was less sensitive to the changes in structural composition of the target tissue, instead it mainly dependent on the structural organization within the tissue.

The extent and nature of inflammation observed in OCT images can be utilized to distinguish between various inflammatory disorders of colon. Figure 4.10 shows a tubular adenoma exhibiting characteristic features of mild dysplasia. As can be seen from figures 4.10(a - c), the epithelial tubules remain regular and were quite similar to normal colon tissue architecture. However, the tubules had an inflamed appearance both in the cross-sectional OCT images and in histology. The regions of interest consisting of some of the inflamed tubules were selected from the *en face* sections for data analysis [Figs. 4.10(e - g)]. The entropy calculated from these regions of interest decreased towards the normal region (on the right side of the regions of interest), which were devoid of the inflamed tubules. The drop in entropy was slightly different in images obtained using 800 nm OCT system [Figure 4.10(h)].

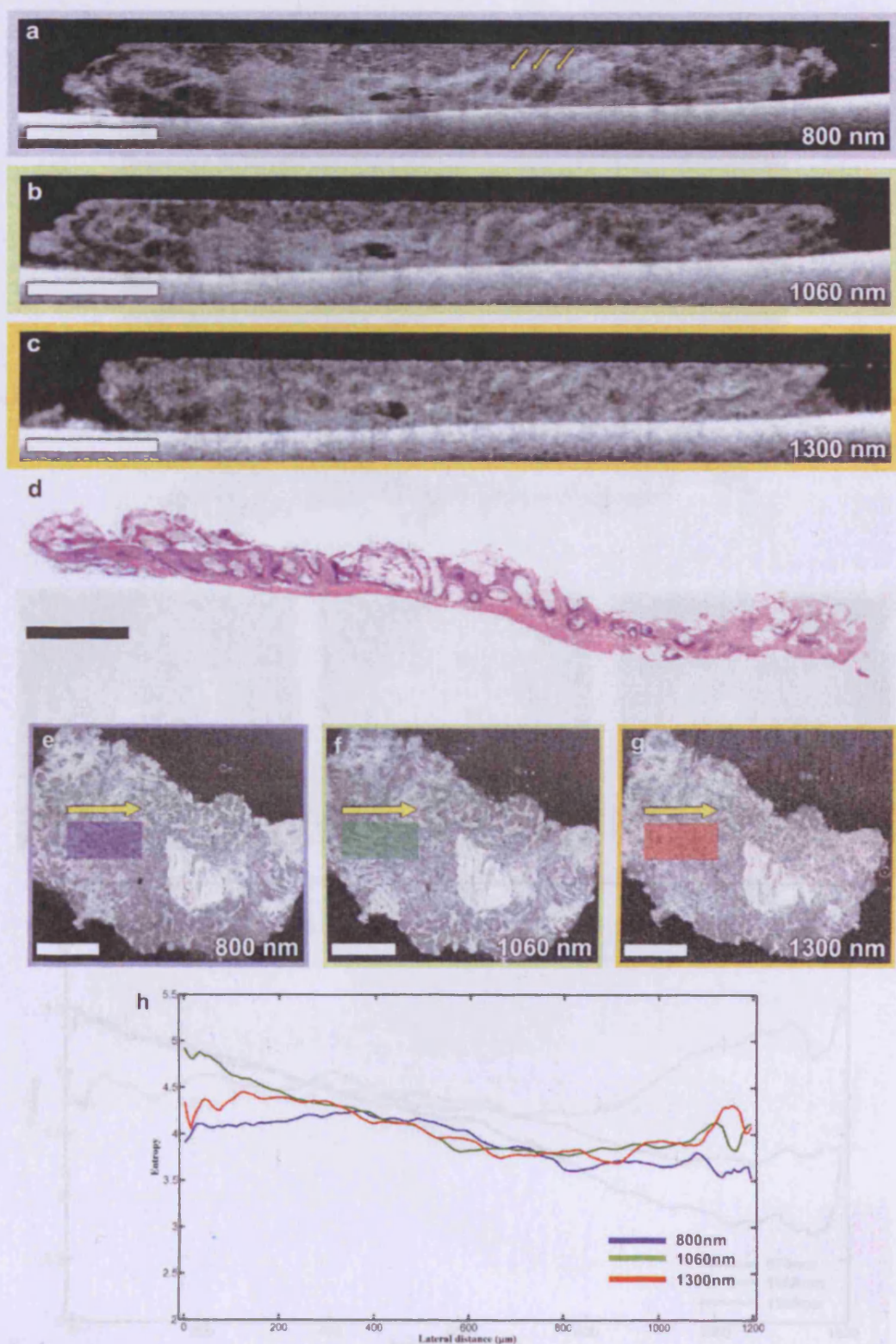


Figure 4.8: Images of normal colonic polyp specimen. OCT images obtained at 800 nm (a), 1060 nm (b), 1300 nm (c) and its corresponding histology (d). *En face* sections showing the selected regions of interest at 800 nm (e), 1060 nm (f) and 1300 nm (g). The yellow arrows denote the direction of entropy evaluation. Entropy variation at the three wavelength regions plotted along the lateral distance (h). The scale bars denote 500 μm in cross-sections (a-d) and 1 mm in *en face* sections (e-g).

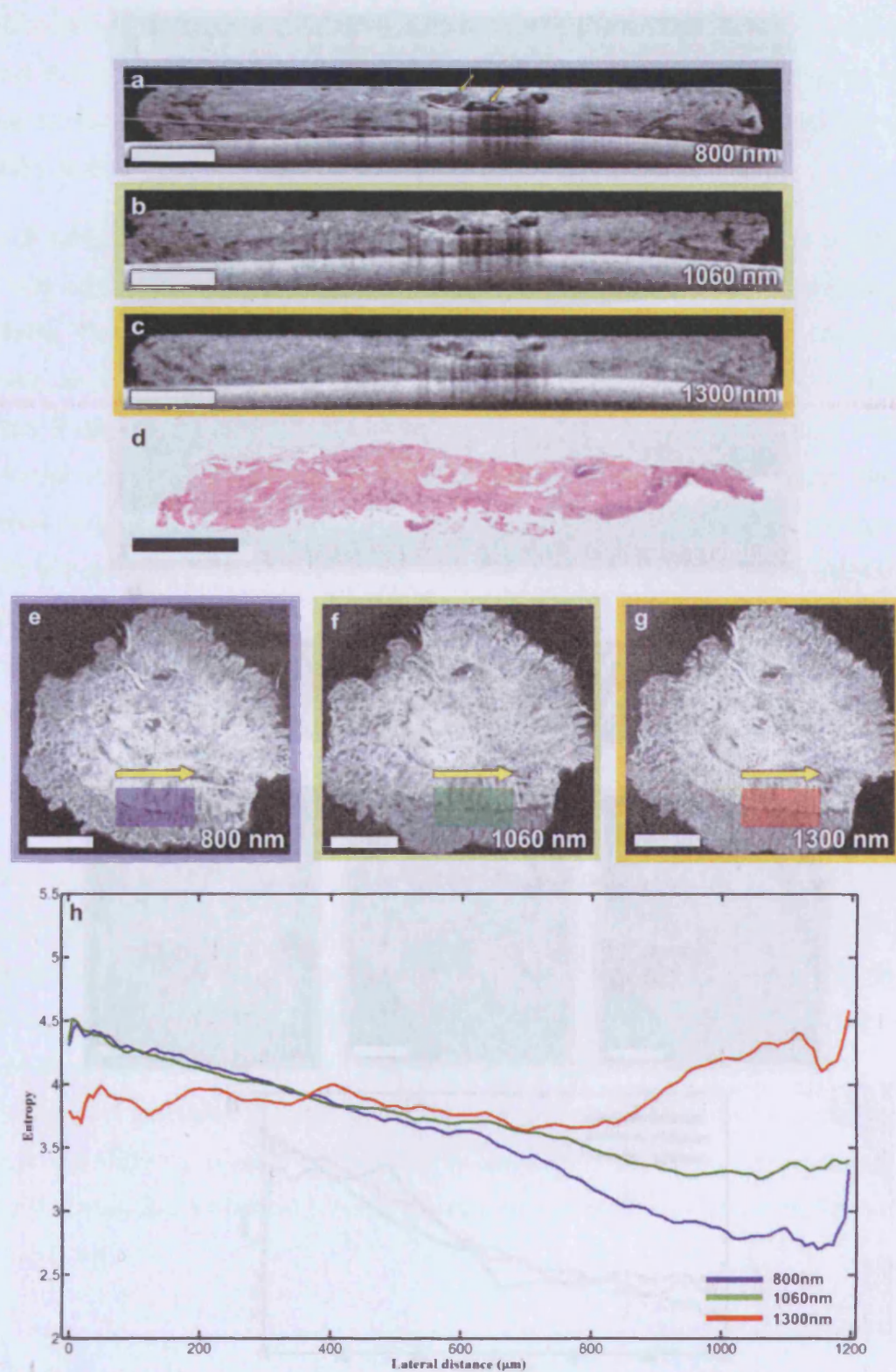


Figure 4.9: Images of a normal colonic specimen. OCT images obtained at 800 nm (a), 1060 nm (b), 1300 nm (c) and its corresponding histology (d). *En face* sections showing the selected regions of interest at 800 nm (e), 1060 nm (f) and 1300 nm (g). The yellow arrows denote the direction of entropy evaluation. Entropy variation at the three wavelength regions plotted along the lateral distance (h). The scale bars denote 500 μm in cross-sections (a-d) and 1 mm in *en face* sections (e-g).

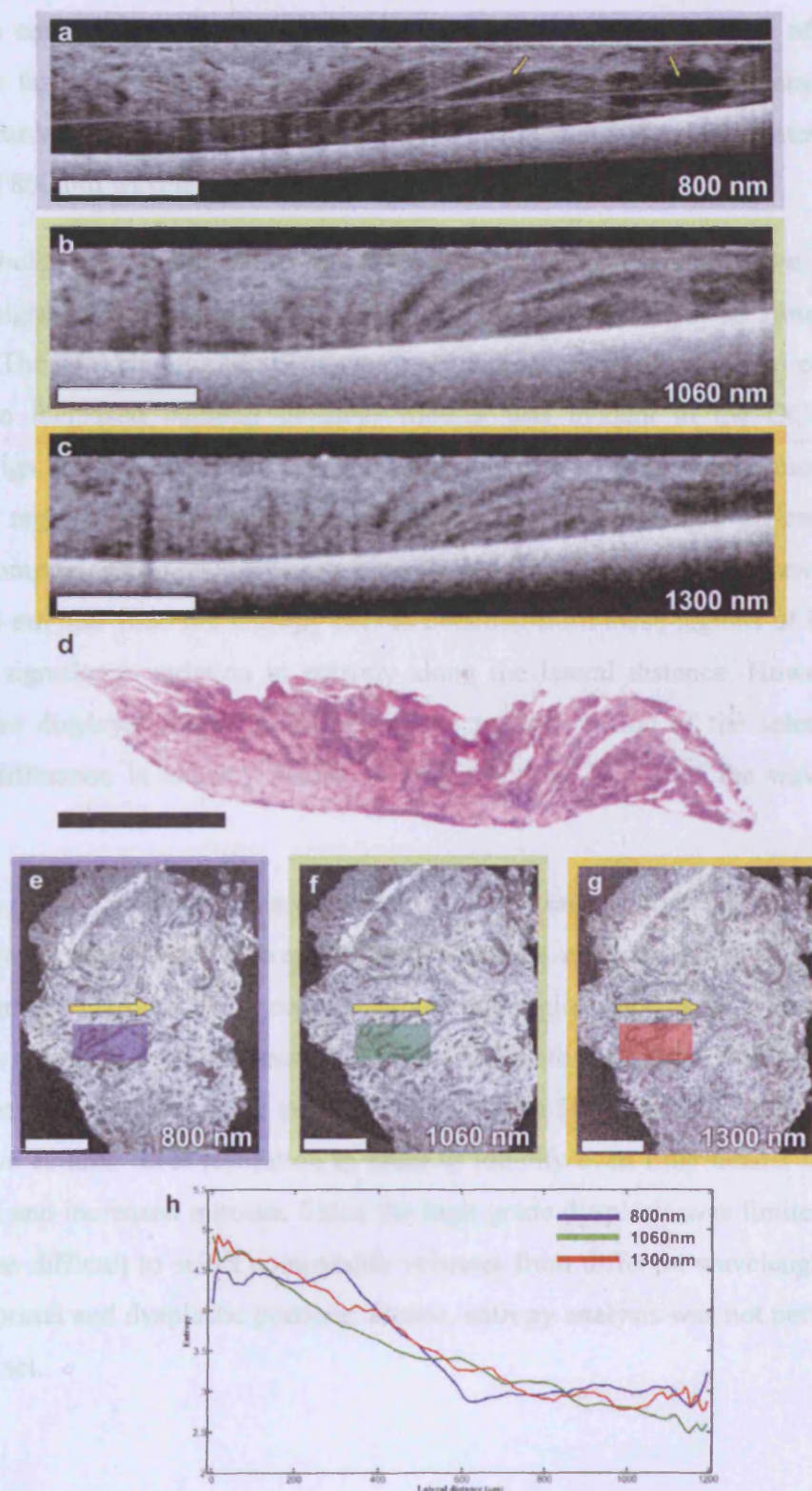


Figure 4.10: Images of a colonic specimen having mild dysplasia. OCT images obtained at 800 nm (a), 1060 nm (b), 1300 nm (c) and its corresponding histology (d). *En face* sections showing the selected regions of interest at 800 nm (e), 1060 nm (f) and 1300 nm (g). The yellow arrows denote the direction of entropy evaluation. Entropy variation at the three wavelength regions plotted along the lateral distance (h). The scale bars denote 500 μ m in cross-sections (a-d) and 1 mm in *en face* sections (e-g).

The 800 nm entropy curve stayed horizontal at the left side of the region of interest, later declined at a faster rate than the other two wavelength regions and then again stayed almost constant towards its right side. This entropy curve obtained at 800 nm illustrates the enhanced capability of 800 nm wavelength region for delineating boundaries.

A tubular adenoma specimen exhibiting moderate dysplasia is shown in figure 4.11. There was higher average backscattering due to higher density of nuclei along the edges of the tubules. The epithelial tubules displayed a structure similar to the normal colonic tubules. However, an increased budding of these tubules was evident in the OCT images and histology [Figs. 4.11(a – d)]. Due to the larger thickness of this sample, more information from deeper regions was obtained while employing higher wavelength regions. The regions of interest comprising complex tubules were selected from the *en face* sections [Figs. 4.11(e – g)]. The 800 nm and 1060 nm entropy curves obtained from these regions of interest did not exhibit any significant variation in entropy along the lateral distance. However, 1300 nm entropy curve displayed slight deviations at the middle portion of the selected region. A significant difference in entropy values were not noticed in any of the wavelength bands employed.

High grade dysplasia is characterised by greatly enlarged nuclei and undifferentiated crypt-like structures. These features are evident in the extreme left side of the histology image in figure 4.12(d). In OCT cross-sections, this region appears as a brightly scattering homogenous region due to high density of nuclei and epithelial crypts were hardly noticeable in this region in contrast to other parts of the specimen [Figs. 4.12(a – c)]. However, OCT needs to have cellular-level resolution in order to identify even finer details such as nuclear enlargement and increased mitoses. Since the high grade dysplasia was limited a very small region, it was difficult to select comparable volumes from different wavelength regions that contained normal and dysplastic portions. Hence, entropy analysis was not performed on this sample data set.

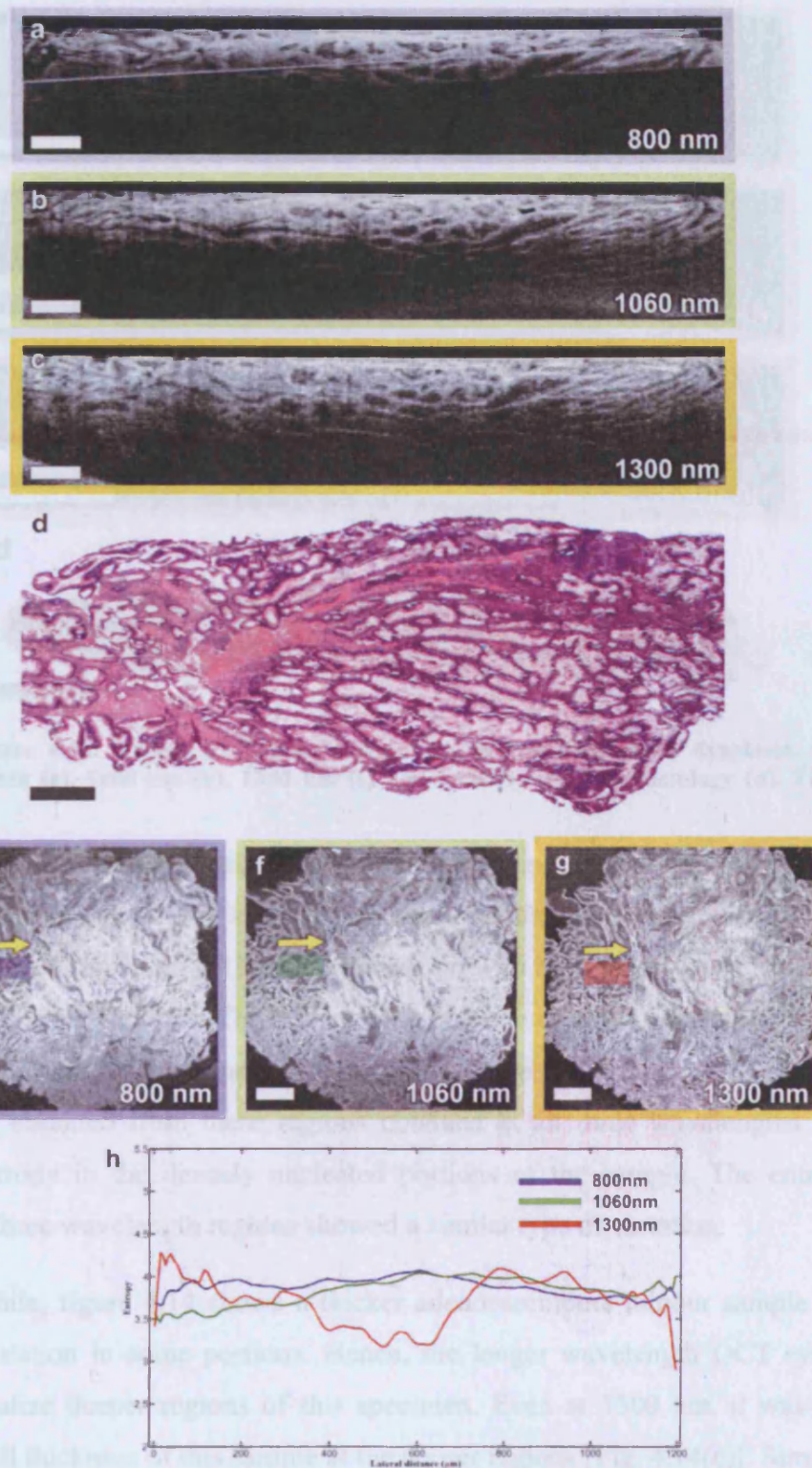


Figure 4.11: Images of a colonic specimen having moderate dysplasia. OCT images obtained at 800 nm (a), 1060 nm (b), 1300 nm (c) and its corresponding histology (d). *En face* sections showing the selected regions of interest at 800 nm (e), 1060 nm (f) and 1300 nm (g). The yellow arrows denote the direction of entropy evaluation. Entropy variation at the three wavelength regions plotted along the lateral distance (h). The scale bars denote 500 μ m in cross-sections (a-d) and 1 mm in *en face* sections (e-g).

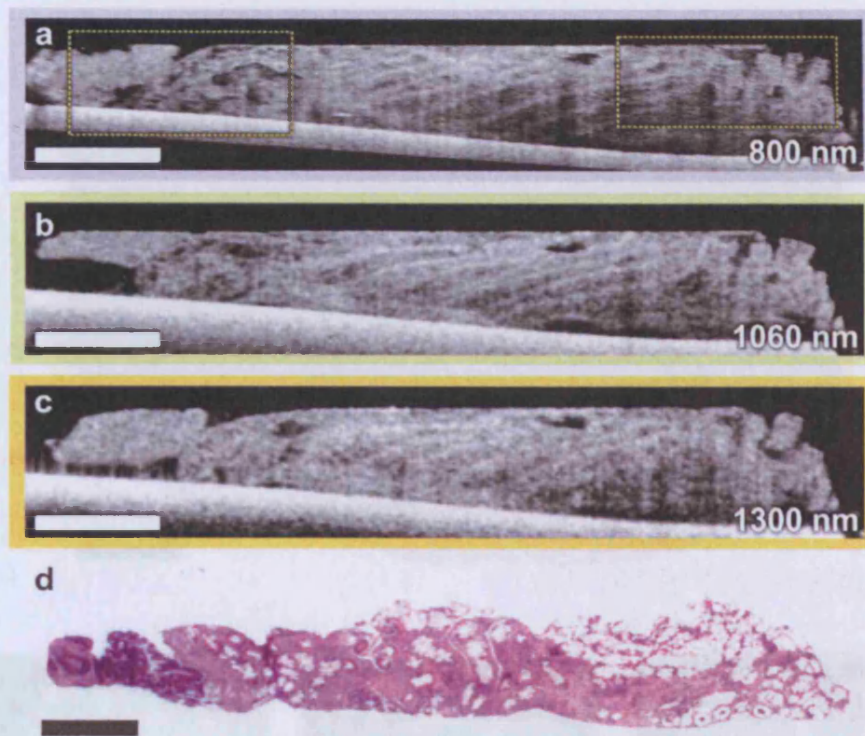


Figure 4.12: Images of a colonic specimen having high grade dysplasia. OCT images obtained at 800 nm (a), 1060 nm (b), 1300 nm (c) and its corresponding histology (d). The scale bars denote 500 μm .

In the adenocarcinoma specimens shown in figures 4.13 and 4.14, both OCT images and histology did not exhibit any kind of structural organization. Both these specimens were poorly differentiated. In figure 4.13(a - c), the region with high density of nuclei appeared as a bright region in OCT sections. The regions with dense nucleation surrounded by the normal sample were selected for data analysis from the *en face* sections [Figs. 4.13(e - g)]. The entropy curves obtained from these regions obtained at all three wavelengths exhibited a decrease in entropy in the densely nucleated portions of the sample. The entropy curves obtained at all three wavelength regions showed a similar type of variation.

Meanwhile, figure 4.14 shows a thicker adenocarcinoma tumour sample with dense nuclear accumulation in some portions. Hence, the longer wavelength OCT systems were needed to visualize deeper regions of this specimen. Even at 1300 nm, it was difficult to penetrate the full thickness of this sample at the denser regions [Fig. 4.14(c)]. Similar to other advanced tumour samples, the entropy plots obtained from this sample also showed a dip at regions of denser nucleation [Fig. 4.14(h)]. The decrease in entropy was more prominent in 800 nm and 1060 nm wavelength regions. The 1300 nm entropy curve was influenced less by denser nucleation, probably due to the lower scattering at this wavelength region.

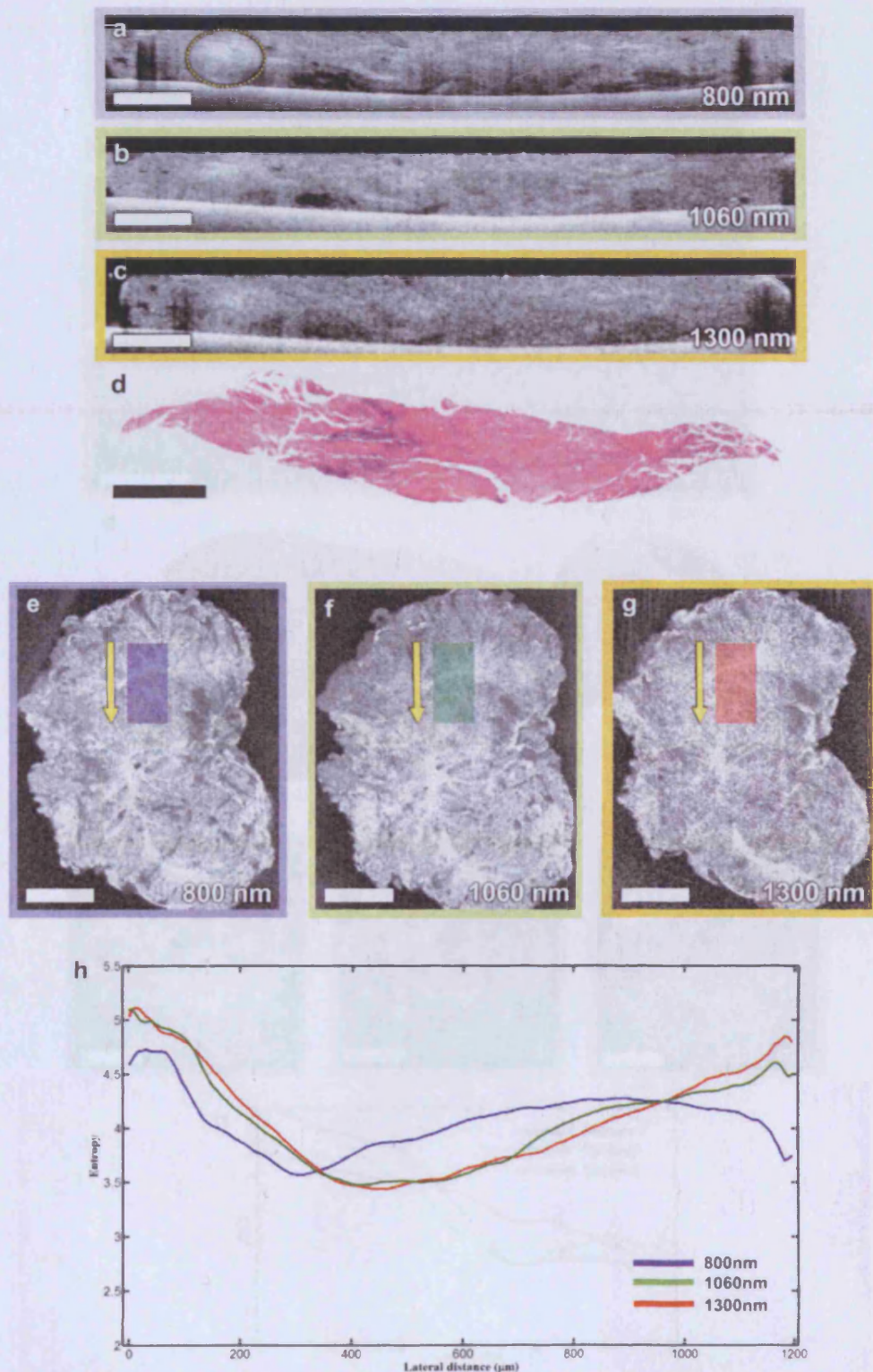


Figure 4.13: Images of a colonic specimen having adenocarcinoma. OCT images obtained at 800 nm (a), 1060 nm (b), 1300 nm (c) and its corresponding histology (d). *En face* sections showing the selected regions of interest at 800 nm (e), 1060 nm (f) and 1300 nm (g). The yellow arrows denote the direction of entropy evaluation. Entropy variation at the three wavelength regions plotted along the lateral distance (h). The scale bars denote 500 μm in cross-sections (a-d) and 1 mm in *en face* sections (e-g).

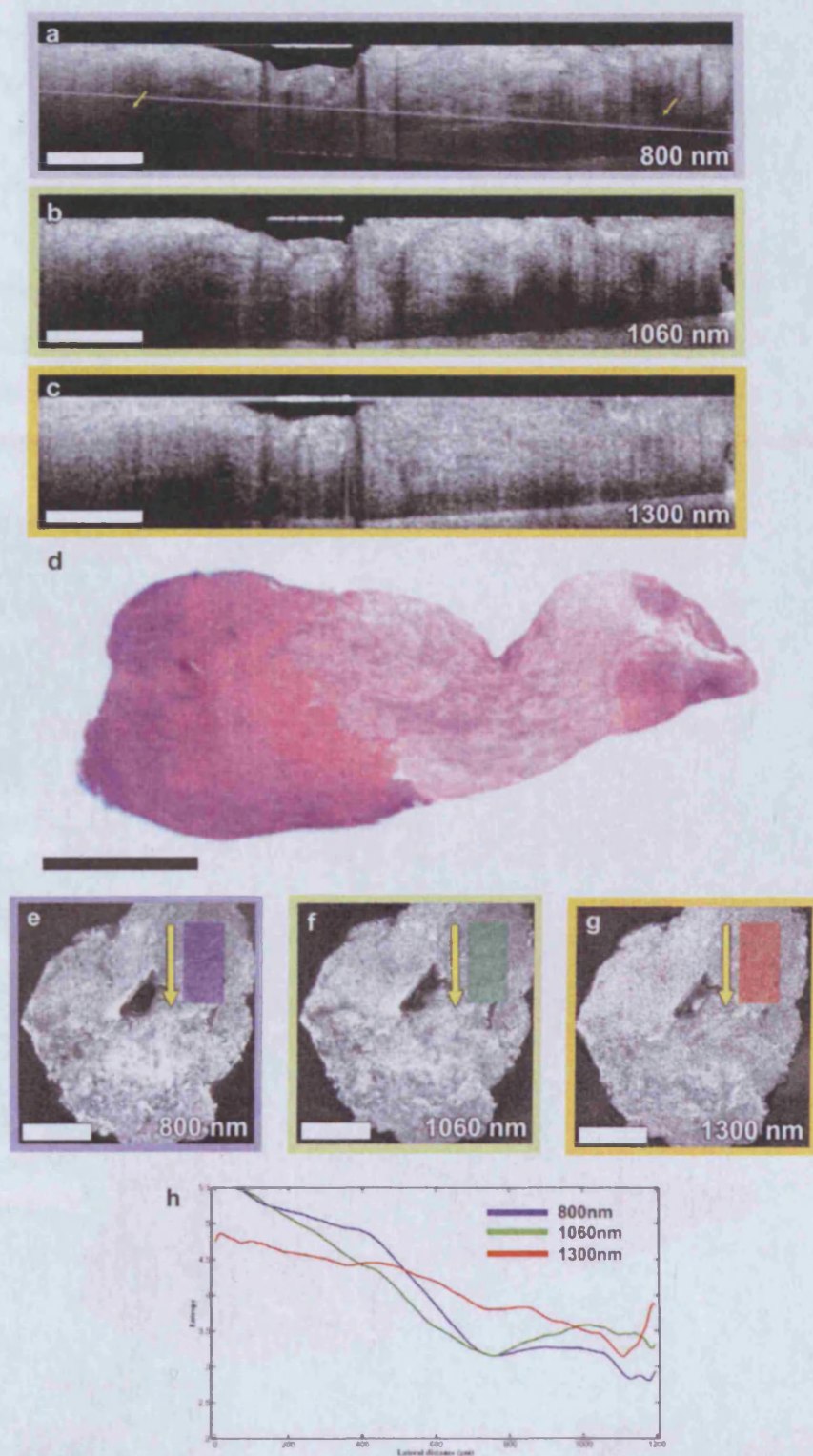


Figure 4.14: Images of a colonic specimen having adenocarcinoma. OCT images obtained at 800 nm (a), 1060 nm (b), 1300 nm (c) and its corresponding histology (d). *En face* sections showing the selected regions of interest at 800 nm (e), 1060 nm (f) and 1300 nm (g). The yellow arrows denote the direction of entropy evaluation. Entropy variation at the three wavelength regions plotted along the lateral distance (h). The scale bars denote 500 μ m in cross-sections (a-d) and 1 mm in *en face* sections (e-g).

4.3.3 Other specimens

Figure 4.15 shows the OCT images of a prostate specimen obtained at three different wavelength regions. The light could not penetrate much deeper in prostate mucosa and it appeared to be a homogenous layer devoid of any distinctive structural features. Figure 4.16 shows OCT images of a normal stomach biopsy obtained using the three OCT systems. The tubule-like structures lined by mucus-secreting cells could be well delineated from the rest of the tissue in both cross-sectional and *en face* images. In pharyngeal mucosa, bright band-like structures were evident at all the wavelengths (Figure 4.17). Histology needs to be performed on these tissues to confirm the anatomical regions corresponding to these bright structures.

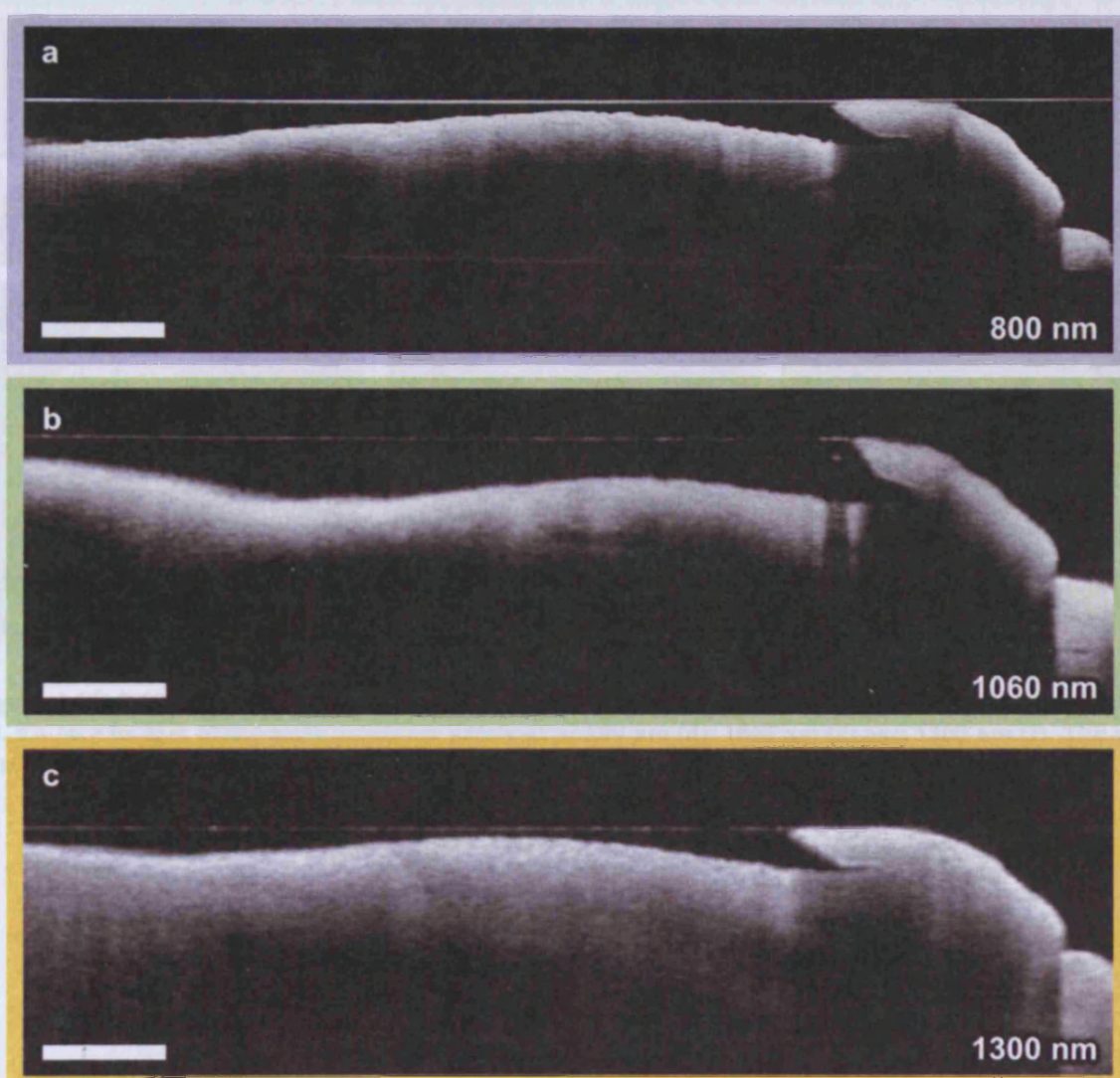


Figure 4.15: OCT images of a prostate specimen obtained at 800 nm (a), 1060 nm (b) and 1300 nm (c). The scale bars denote 500 μm .

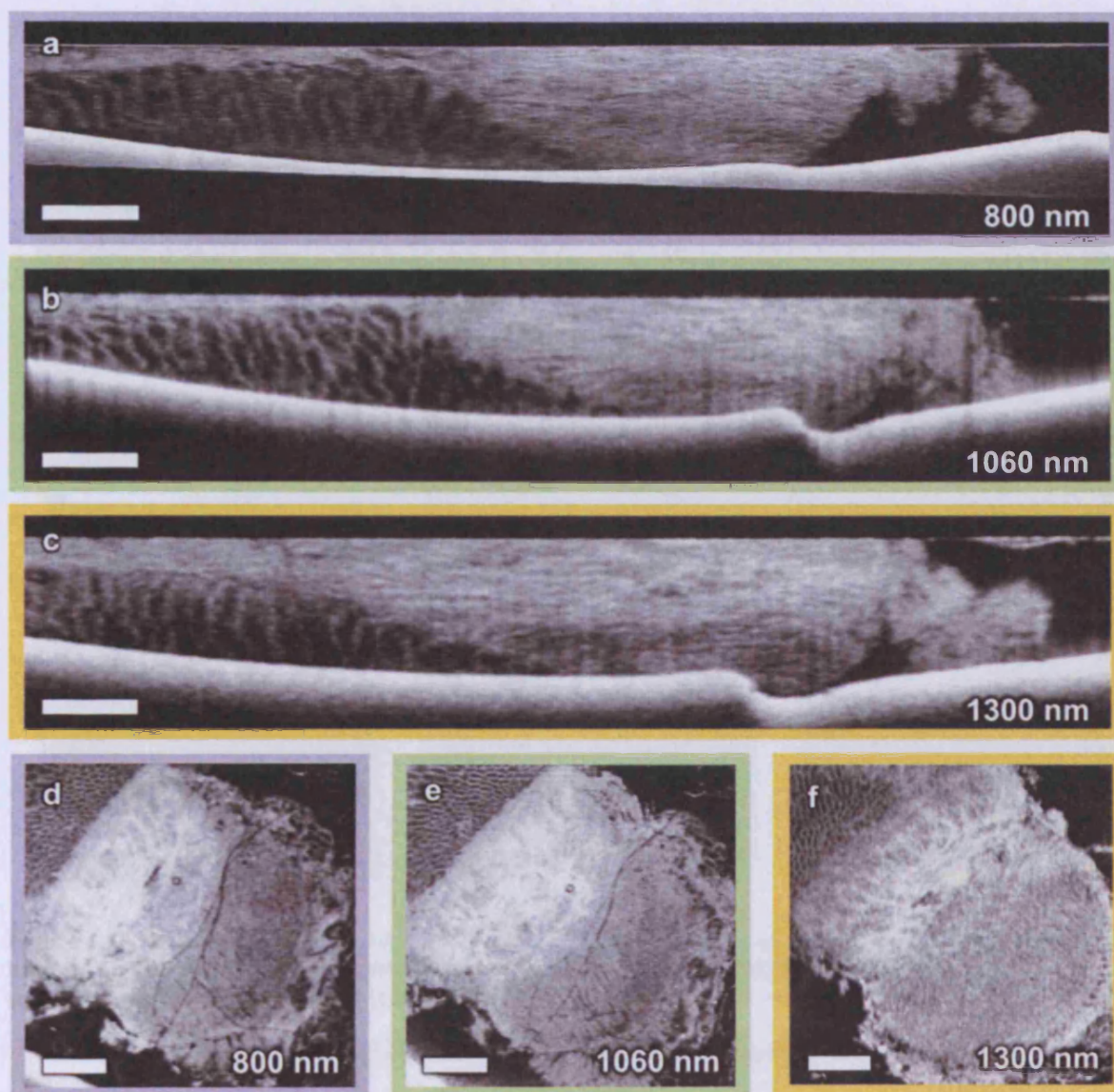


Figure 4.16: OCT B-scan images of a stomach specimen obtained at 800 nm (a), 1060 nm (b) and 1300 nm (c). En face images of the same specimen obtained at 800 nm (d), 1060 nm (e) and 1300 nm (f). The scale bars denote 500 μm in (a, b, c) and 1 mm in (d, e, f).

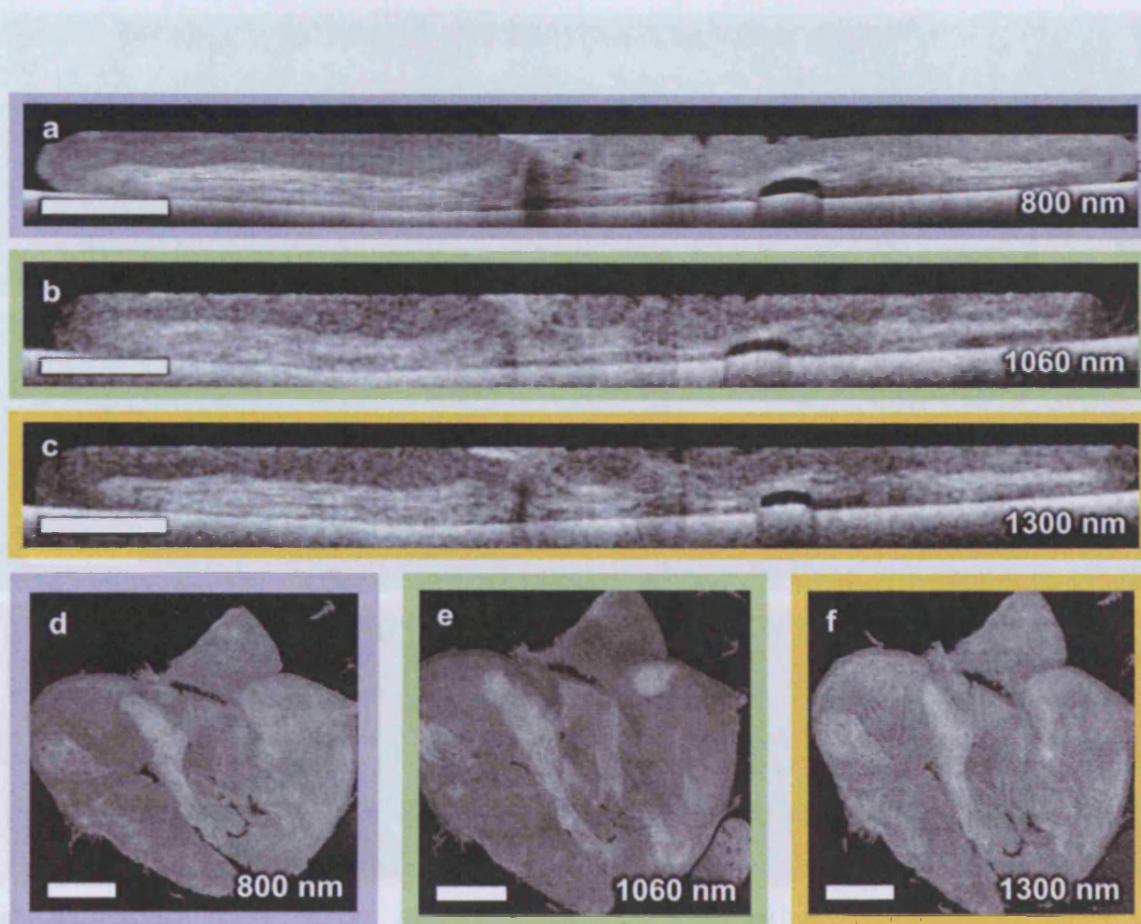


Figure 4.17: OCT B-scan images of a pharyngeal specimen obtained at 800 nm (a), 1060 nm (b) and 1300 nm (c). En face images of the same specimen obtained at 800 nm (d), 1060 nm (e) and 1300 nm (f). The scale bars denote 500 μm in (a, b, c) and 1 mm in (d, e, f).

Pyriform fossa is a pear-shaped recess in the hypopharynx region of the human body. Figure 4.18 shows OCT images obtained from the tumour-infected mucosa of a left pyriform fossa. Many lobular structures can be seen in this specimen in both cross-sectional and *en face* views. OCT images obtained from a laryngeal polyp are shown in figure 4.19. The mucosal epithelium appears as bright layer and can be clearly demarcated from the underlying LP.

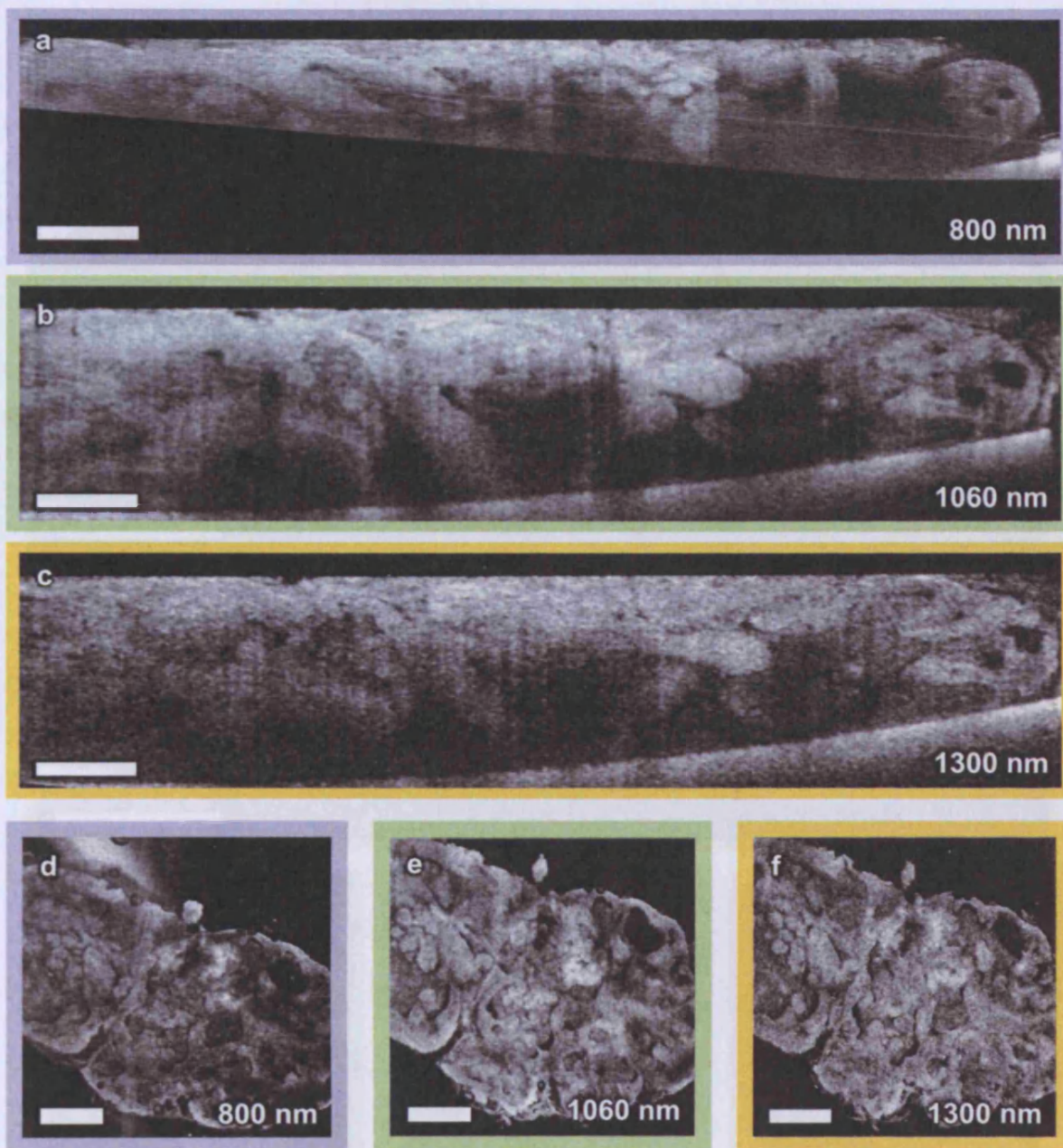


Figure 4.18: B-scans of a pyriform fossa specimen obtained at 800 nm (a), 1060 nm (b) and 1300 nm (c). En face images of the same specimen obtained at 800 nm (d), 1060 nm (e) and 1300 nm (f). The scale bars denote 500 μm in (a, b, c) and 1 mm in (d, e, f).

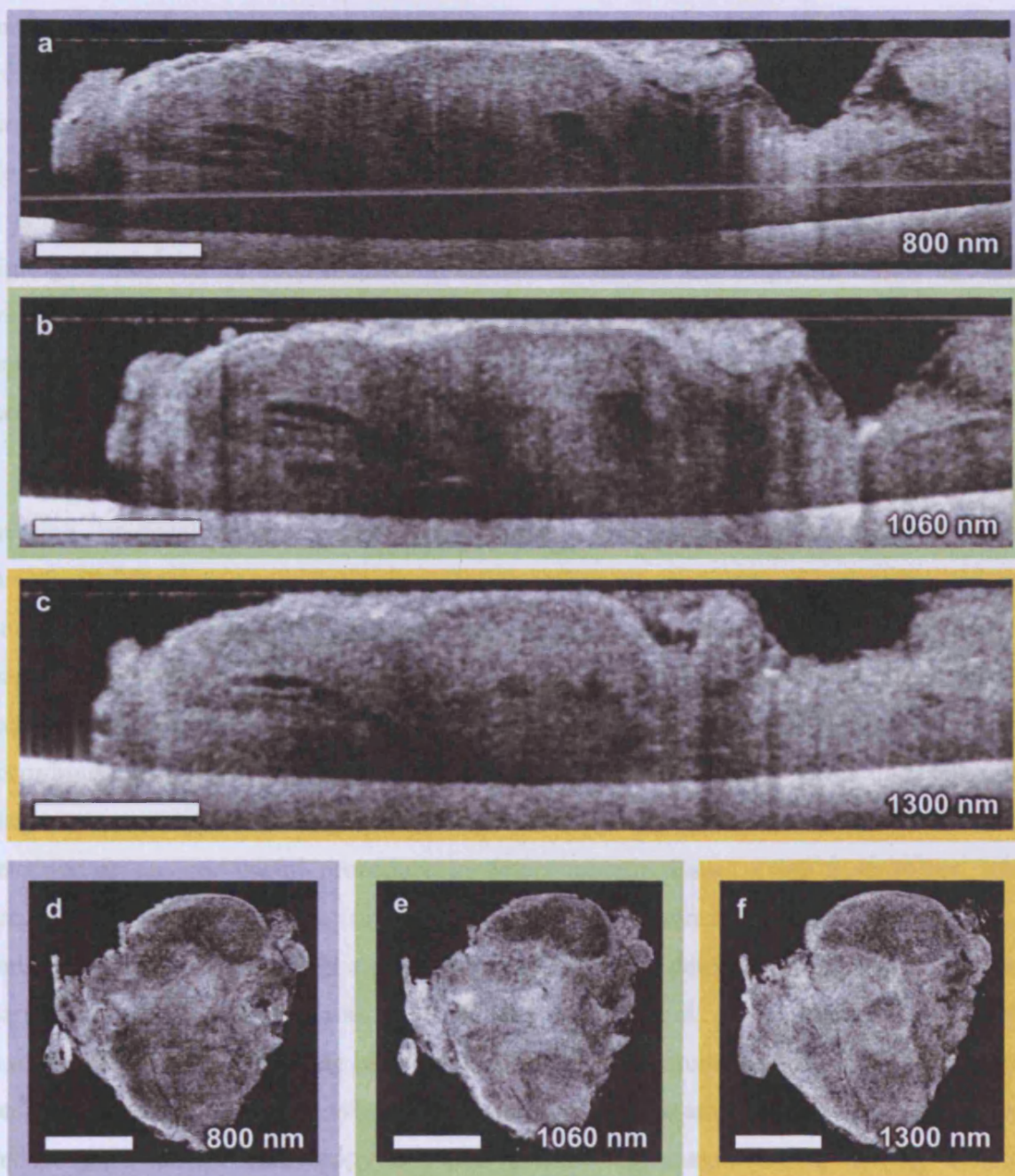


Figure 4.19: B-scans of a laryngeal polyp specimen obtained at 800 nm (a), 1060 nm (b) and 1300 nm (c). En face images of the same specimen obtained at 800 nm (d), 1060 nm (e) and 1300 nm (f). The scale bars denote 500 μm in (a, b, c) and 1 mm in (d, e, f).

4.4 Discussion

Conventional gastrointestinal endoscopic diagnosis is predicated on the gross architectural characteristics of mucosal and submucosal abnormalities. Hence, endoscopic diagnosis is less successful in detecting premalignant changes such as Barrett's oesophagus and dysplasia, where the architectural abnormalities are microscopic in nature. Thus, the only

endoscopic method of surveillance for detecting precancerous conditions is to obtain biopsies from the target tissues in a random or predetermined pattern. Nevertheless, these random biopsies are associated with an inevitable sampling error. Moreover, when a single tumour is discovered, the entire organ must be examined to exclude presence of synchronous tumours. It is common to find residual dysplasia beneath the resected portion of the tumour. This highlights the need for deep biopsies to access the changes and long term follow-up studies are needed to investigate behaviour of the tissues in these regions concerned. All these aspects necessitate the need for an *in vivo* non-invasive biomedical imaging modality for monitoring premalignant changes.

There are several non-invasive endoscopic imaging modalities such as ultrasound imaging, confocal microscopy, optical coherence tomography and fluorescence imaging investigated for their applicability in detecting malignant conditions of gastrointestinal tract. Endoscopic ultrasound imaging has so far been the most successful imaging modality in staging carcinomas in gastrointestinal tract (Falk et al., 1994; Scotinotis et al., 2001). This technique has been used to detect the depth of invasion and thus is capable of staging cancer accordingly. However, endoscopic ultrasound imaging is limited in terms of resolution to diagnose premalignant changes occurring within the mucosa. Endoscopic fluorescence detection is another useful procedure to detect tumour tissues using a sensitizer, which accumulates selectively in tumours. Endoscopic fluorescence detection using 5-aminolaevulinic acid has been a promising method in the detection of dysplastic lesions in Barrett's oesophagus (Panjehpour et al., 1996; Endlicher et al., 2001). However, this method is more effective in diagnosing high grade dysplasia and carcinomas. Its sensitivity depends mainly on the sensitizer dose, whose administration on large amounts may cause side effects. Endoscopic confocal microscopy is a non-invasive high-magnification imaging technique that produces *en face* images with sub-micron scale resolution comparable to that of histology (Evans and Nishioka, 2005). This technique has yielded promising results in identifying and characterising neoplasia in colon specimens (Sakashita et al., 2003). However, confocal microscopy is limited to a penetration depth of $\sim 250 \mu\text{m}$ in gastrointestinal tissues. OCT has provided encouraging results in distinguishing gastrointestinal abnormalities both *in vitro* and *in vivo*. Even though it is limited in penetration depth to $\sim 1 - 2 \text{ mm}$, the combined thickness of mucosa and submucosa is less than $700 \mu\text{m}$ in gastrointestinal tissues (Bouma et al., 2000). In addition, most of the

neoplasms do not have the potential for lymph node metastasis until they have invaded across MM into submucosa. When compared to other non-invasive technologies, OCT can be easily coupled with endoscopes, does not need any contrast agents or contact medium and can image larger areas of tissue in real-time. These factors make OCT a suitable candidate for performing optical biopsy of the gastrointestinal tissues to diagnose any premalignant transformations.

Several studies have been performed to demonstrate the feasibility of OCT to obtain high resolution images of the gastrointestinal tissues. In an *in vitro* study using surgically excised human tissues, Izatt *et al.* demonstrated that OCT can clearly delineate sub-layers of the mucosa from the submucosa in specimens of the stomach and colon (Izatt *et al.*, 1996). Additionally, OCT demonstrated obvious differences between normal and malignant tissue, specifically a loss of tissue architecture and differences in backscattering properties. Tearney *et al.* obtained micro-detailed endoscopic OCT images of the oesophagus *in vivo* using an animal model (Tearney *et al.*, 1997). The MM is an important structure in respect to accurate evaluation of malignancy invasiveness. Two time-domain OCT systems using 800 nm and 1275 nm light sources were employed to obtain images of the oesophagus *in vitro* and were compared to corresponding histology (Çilesiz *et al.*, 2002). Both systems proved to be capable of delineating the MM of oesophageal mucosa as a separate layer. Following these studies, endoscopic OCT was used to visualize different regions of gastrointestinal tract and to diagnose different pathological conditions (Bouma *et al.*, 2000; Li *et al.*, 2000; Pitris *et al.*, 2000; Pfau *et al.*, 2003; Tumlinson *et al.*, 2006). Endoscopic OCT provided a diagnostic accuracy of 78% for detection of dysplasia in patients with Barrett's oesophagus (Isenberg and Sivak, 2003). Endoscopic OCT images showed precise correlation with the histological structure of the mucosa and the submucosa of the gastrointestinal tract (Westphal *et al.*, 2005). *In vivo* 3-D endoscopic OCT images of normal and pathologic regions of the colon and the rectum demonstrated the potential role of 3D-OCT in assessing malignant conditions and guiding endoscopic therapies (Adler *et al.*, 2009). Thus, endoscopic OCT has been shown to have a strong potential to become a promising tool to investigate various gastrointestinal pathologies. However, to our knowledge, there has been a lack of systematic studies conducted to compare OCT images obtained from normal and abnormal gastrointestinal tissues at different wavelengths, in order to determine the pros and cons of each wavelength region.

This *in vitro* study demonstrates the capability of OCT to extract microstructural information pertaining to premalignant transformation in oesophagus, colon and other tissues. OCT could distinguish architectural disorders and variations in backscattering properties of tissues associated with various pathological conditions. In both oesophageal and colonic specimens, the degree of architectural disarray was related to the degree of dysplasia. This was confirmed by comparing with corresponding histologies. In advanced stages of carcinoma, the specimen appeared to be completely devoid of any of its characteristic structural features. Since majority of the specimens were thin pathological samples collected during endoscopic resection, the difference in depth of penetration was not noticed at different wavelength regions. However, the effect of wavelength on penetration depth was prominent in the thicker samples, as well as in samples with higher nuclear density and absorbing components. 800 nm wavelength region gave better contrast over the other two wavelength regions, which helped to identify the structural components much more clearly. In addition, the higher resolution offered by this wavelength region aided in revealing finer micro-morphological details. In thicker samples, the higher scattering and absorption cast shadows on deeper regions of the specimens. This was overcome to some extent by employing longer wavelength regions. However, dense nucleation and strong absorption limited the penetration depth of light in a few samples, even at 1300 nm.

The specimens employed in this study were snap frozen and extreme care was taken to preserve the tissues in the best possible manner. However, the freezing prior to the storage and thawing prior to OCT imaging may have caused subtle changes in the architectural arrangement of these specimens. Moreover, the preservation of these tissues in 10% neutral buffered formalin after the imaging session could have caused shrinkage of tissues. This is quite evident in the histological images of some of the specimens. Another limitation of this study is its *in vitro* nature. The scattering and absorptive properties of tissues will be slightly different *in vivo*. Even though, this *in vitro* study proves the capability of OCT to discern abnormal structural variations across different stages of tumour progression. In addition, all the experimental conditions such as system sensitivity, sensitivity roll-off and transverse resolution were made identical, in order to ensure a true comparison of OCT images obtained at three wavelength regions.

4.5 Conclusions

The capability of OCT to display the modifications in micro-architectural arrangement across various stages of tumour non-invasively has been demonstrated in this *in vitro* study. All three wavelength regions employed in this study could visualize different characteristic structural features of the tumour samples. The 800 nm system offered a better contrast and resolution over the other two wavelength regions. At 800 nm, penetration as deep as submucosa was achieved in majority of the specimens. As expected, the depth of penetration was highest for 1300 nm system. 1060 nm system was a compromise between the other two systems in terms of resolution, contrast and penetration depth. The degree of dysplasia in the tumour specimen could be identified by noticing the micro-morphological variations and comparing them with the normal specimens. From the entropy plots, the entropy of the image appeared to increase with the degree of dysplasia. However, the entropy was found to be reduced in advanced stages carcinoma. Hence, entropy could be a useful parameter in measuring the extent and nature of structural disarray. The malignant regions also displayed significant differences in light backscattering properties. The employment of longer wavelength regions helped to visualize deeper in thicker and denser samples. However, densely packed poorly differentiated cells in adenocarcinomas cast shadows in the deeper portions of the specimens at all three wavelength regions.

In summary, OCT is capable of becoming one of the most useful non-invasive imaging modalities that could be used for diagnosing precancerous conditions in gastrointestinal tissues. However, further improvements in resolution offered by OCT are needed to precisely demarcate the nature and extent of a tumour. In addition, enhancement of imaging speed will help to reduce motion artifacts during *in vivo* applications. With these improvements in technology, OCT could be employed as a non-invasive imaging tool for gastrointestinal clinical studies such as guidance of endoscopic therapies, diagnosis of premalignant lesions and long term follow up of tumour progression.

Chapter 5

Multimodal optical coherence/photoacoustic tomography

5.1 Introduction to photoacoustic imaging

Multimodal imaging paves the way to combine the advantages of different contrast mechanisms to provide comprehensive structural and functional information of biological tissues. Recently, there has been an increasing trend in biomedical research to integrate multiple complementary imaging modalities into a single platform for simultaneous acquisition of physiological information. Multimodal approaches such as PET/CT, SPECT/CT and PET/MRI are already established clinical imaging modalities, which have made possible the integration of nuclear medicine techniques devoted to functional imaging with anatomical imaging modalities (Beyer et al., 2000; Chowdhury and Scarsbrook, 2008; Judenhofer et al., 2008; Papathanassiou and Liehn, 2008).

Photoacoustic (PA) imaging is a non-invasive optical imaging modality for visualizing the structure and function of soft tissues (Xu and Wang, 2006). It combines optical-absorption contrast with ultrasonic spatial resolution for deep imaging of biological tissues in the optical quasi-diffusive or diffusive regime (Wang and Wu, 2007). Ultrasonic generation using light was first reported in 1880 by Alexander Graham Bell (Bell, 1880). PA imaging relies upon irradiating the tissue surface with low energy nanosecond pulses of visible or near-infrared light [Figure 5.1]. The absorption of light by sub-surface anatomical features such as blood vessels leads to impulsive heating accompanied by rapid thermo-elastic expansion. This subsequently leads to the generation of broadband ultrasonic pulses (tens of MHz), which propagate towards the surface and are detected at multiple points using either an array of ultrasound transducers or a mechanically scanned single element receiver (Sun and Diebold, 1992; Xu and Wang, 2006). By determining the time of arrival of the acoustic pulses over the tissue surface and knowing the speed of sound in the tissue, a volumetric image of the internally absorbed optical energy distribution can be reconstructed by back-projecting the acoustic signals in 3-D. PA imaging provides better spatial resolution than pure optical imaging when the imaging depth is beyond the mean free path of one

optical transport (~ 1 mm in scattering tissues), because ultrasonic scattering is two to three orders of magnitude weaker than optical scattering in biological tissue (Duck, 1990).

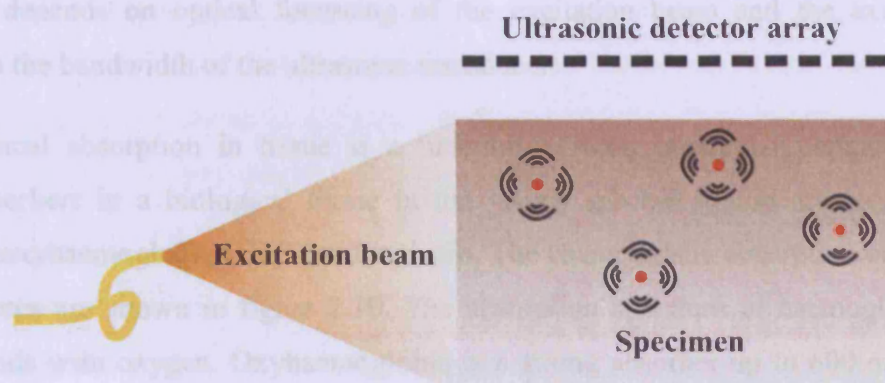


Figure 5.1: Photoacoustic imaging principle

PA imaging currently has three major forms of implementation.

- PA tomography (PAT): employs a scanning unfocussed ultrasonic transducer or an array of unfocussed ultrasonic transducers in combination with a reconstruction algorithm to form an image (Wang et al., 2003a).
- PA microscopy (PAM): based on a scanning focussed ultrasonic transducer operating in confocal reflection mode, which is used to detect photoacoustic signals produced by a weakly focussed donut-shaped excitation beam (Maslov, Stoica and Wang, 2005).
- Optical resolution PAM (OR-PAM): uses focussed illumination for photoacoustic excitation, which is detected using a scanning focussed ultrasonic transducer (Maslov et al., 2008).

Spatial resolutions of PA imaging depends on the ultrasonic parameters. In-plane resolution of PAT, which operates in orthogonal mode, is derived from the reconstruction accuracy that depends on the bandwidth of the transducer and its out-of-plane resolution is determined from the aperture effect or cylindrical focussing of the ultrasonic transducer. Whereas, in PAM, lateral resolution is determined by the focal diameter of the ultrasonic transducer at its centre frequency and axial resolution is inversely related to the bandwidth of the transducer. Hence, a large numerical aperture, a high centre frequency and a wide bandwidth is needed to achieve high spatial resolutions in PAM. However, ultrasonic penetration limit is inversely proportional to its frequency. As a result, both the spatial

resolutions and maximum imaging depth of PA imaging are scalable with ultrasonic parameters within the reach of excitation photons (Wang, 2008b). In OR-PAM, the lateral resolution depends on optical focussing of the excitation beam and the axial resolution depends on the bandwidth of the ultrasonic transducer.

Optical absorption in tissue is a function of their molecular composition. Major optical absorbers in a biological tissue in the visible spectral region are oxyhaemoglobin (HbO_2), deoxyhaemoglobin (HbR) and melanin. The characteristic absorption curves of these chromophores are shown in figure 2.10. The absorption spectrum of haemoglobin changes when it binds with oxygen. Oxyhaemoglobin is a strong absorber up to 600 nm at which it drops off steeply, by almost two orders of magnitude and remains low. However, the absorption spectrum of deoxyhaemoglobin does not drop dramatically; it stays relatively high, although it decreases with increasing wavelengths. The isosbestic point, where the absorption spectra of these two chromophores intersect, occurs at about 800 nm (Mobley and Vo-Dinh, 2003). The strong optical absorption of these chromophores and the spectroscopic dependence on their oxygenation status makes the PA imaging technique particularly well-suited for visualizing the structure and function of the vasculature. The parameters such as concentration of haemoglobin and its oxygen saturation are related to angiogenesis and hypermetabolism, which are considered as the hallmarks of cancer. Applications that exploit this capability include the clinical assessment of the breast and skin tumours (Manohar et al., 2005; Oh et al., 2006), dermal vascular lesions and soft tissue damages such as burns (Zhang et al., 2006b) and other abnormalities characterized by changes in the local tissue perfusion and oxygenation status.

Most photoacoustic imaging instruments employ piezoelectric receivers as ultrasonic transducers to detect photoacoustic signals. However, these suffer from two major limitations, particularly for superficial imaging applications. The PA imaging device has to be operated in backward or reflection mode for imaging highly superficial features such as skin microvasculature, where the photoacoustic signals are detected only on the irradiated side of the tissue. In this case, delivery of the excitation laser light without being obscured by the detectors becomes difficult. Vertically offsetting the detector array helps in delivering the excitation beam obliquely to the tissue surface. However, this reduces the SNR and the measurement aperture of the PA system. The second limitation of the piezoelectric detectors is that their sensitivity falls off with decreasing element size. Most of the image

reconstruction algorithms require the detector size to be very small compared to the acoustic wavelength, so that it can be approximated to a point receiver (Zhang et al., 2006a). When imaging superficial anatomy, the photoacoustic signal is only weakly band-limited by the frequency dependent attenuation characteristics of soft tissues and hence can be extremely broadband extending tens of megahertz. As a consequence, piezoelectric receivers with element dimensions of a few tens of micrometres are required.

5.1.1 Optical ultrasound detection

Optical ultrasound detection techniques offer the prospect to overcome these limitations. Several optical methods based on a variety of transduction mechanisms have been investigated (Hamilton and O'Donnell, 1998; Köstli et al., 2001; Payne et al., 2003). A promising category of interferometric techniques is based upon the detection of acoustically-induced changes in optical thickness of a solid planar Fabry-Perot interferometer (FPI) (Beard, Perennes and Mills, 1999). As shown in figure 5.2, FPI is fabricated by sandwiching a polymer spacer between a pair of mirrors formed by the deposition of optically reflective coatings. This type of sensors can provide broadband frequency response, small element size and high sensitivity. Furthermore, the sensor can be made transparent to the excitation laser wavelength, but highly reflective at other wavelengths for enabling backward mode detection by using dichroic dielectric coatings to form the FPI mirrors (Beard, Zhang and Cox, 2004). A focussed laser beam is scanned across the surface of the FPI sensor at a wavelength at which the FPI mirrors are highly reflective. The spatial-temporal distribution of the incident PA waves can be mapped in 2-D by recording the time-varying reflected optical power modulation at each point of the scan. The detected PA signals are then input to a k-space acoustic back-propagation algorithm in order to reconstruct a 3-D image of the initial pressure distribution, which forms the PA image.

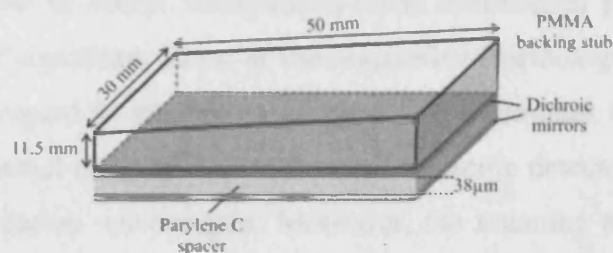


Figure 5.2: Schematic of an optical ultrasound detector based on a Fabry-Perot interferometer (Zhang, Laufer and Beard, 2008).

5.2 Motivation for this study: OCT/PAT multimodal imaging

Most of the optical imaging systems retrieve structural and functional information based on the interactions of light within biological tissue through processes such as scattering, absorption, phase changes and fluorescence. OCT is a non-invasive imaging technique capable of visualizing three-dimensional microstructures of tissue in real-time with high spatial resolutions. OCT has already proven its ability to obtain qualitative and quantitative information from human skin *in vivo* (Welzel et al., 1997). However, the intrinsic contrast in OCT images is based on the differences in localized backscattering of the sample. Hence, OCT is sensitive to any kind of tissue and lacks the ability to select specific regions based on their chemical content.

PA imaging is a non-invasive *in vivo* imaging modality capable of visualizing structural and functional information of soft tissues based on its optical absorption properties. Melanin and haemoglobin are the most important sources of naturally occurring contrast for PA imaging technique. This makes PA imaging technique particularly well-suited for visualizing the structure and function of the dermal vasculature. OCT offers micrometre-scale axial and transverse resolutions with a penetration depth of about 1 – 2 mm. Meanwhile, PAT offers a spatial resolution of the order of tens of micrometres with a penetration depth of several millimetres. Hence, OCT and PAT are complementary imaging techniques that can provide micro-structural and functional information of skin simultaneously with enhanced penetration and high spatial resolution. OCT provides micro-morphological information of biological tissues based on the optical scattering and PAT provides metabolic or functional information based on optical absorption. Thus, an OCT/PAT multimodal imaging system can have profound applications in diagnosing skin tumours, dermal vascular lesions and other similar abnormalities. Besides detecting minute structural abnormalities with improved sensitivity, an OCT/PAT system employing proper contrast agents or multi-wavelength illumination will be able to obtain molecular-specific information pertaining to the target tissue, which can be of significant value in the diagnosis of pathological conditions. One of the major issues with regard to integration of these two techniques for superficial imaging applications such as dermal imaging was to find an ultrasonic detector that is transparent to both OCT and PA excitation wavelengths. Moreover, the scanning mechanisms need to be compatible for both these techniques. With the advent of ultrasonic detection using planar dichroic FPI mirrors, the prospect of developing a multimodal OCT/PAT imaging system

became much simpler. This FPI sensor permits *in vivo* multimodal imaging of skin to be performed in an identical fashion without any further complications.

5.3 Materials and methods

This study was a collaborative project between Biomedical Imaging group, School of Optometry and Vision Sciences, Cardiff University and Photoacoustic imaging and optical ultrasound sensing research group, Department of medical physics and bioengineering, University College London, UK. Mr. Aneesh Alex, Dr. Boris Považay and Prof. Wolfgang Drexler participated in the study from the Biomedical imaging group and Dr. Edward Zhang, Dr. Jan Laufer and Prof. Paul Beard took part in the study from the Photoacoustic imaging and optical ultrasound sensing research group. The photoacoustic imaging system used for this study were developed by our collaborators and the tumour-infected mouse for demonstrating the capability of this multimodal imaging system were also provided by our collaborators. The small animal imaging experiments were performed under the supervision of a licensed staff and all necessary ethical procedures were strictly followed.

5.3.1 Subjects

The multimodal OCT/PAT imaging system was used to obtain *in vivo* images of human skin from the palmar region. OCT and PAT images were acquired sequentially and the imaging times were ~ 10 s and 4 minutes respectively. In addition, multimodal images were obtained *in vivo* from the skin of a 5 weeks old female hairless mouse.

5.3.2 OCT/PAT imaging system

An amplified spontaneous emission source (NP Photonics, Tucson, USA) centred at 1050 nm and having a bandwidth of 72 nm was employed in the spectrometer-based frequency domain OCT system (Povazay et al., 2007). The design of this OCT system is similar to the 1300 nm OCT system described in chapter 2 and specifications of this OCT system has been given in table 2.3. The axial resolution of the OCT system was ~7 μm . Its signal-to-noise ratio was measured to be ~93 dB and was capable of acquiring depth-scans at a rate of 47 kHz.

The photoacoustic imaging system used a solid planar FPI sensor and operated in backward mode (Zhang et al., 2008). The excitation source was a tuneable optical parametric oscillator laser system (410–1200 nm) with 50 Hz pulse repetition frequency, 8 ns pulse duration and maximum pulse output energy of 55 mJ. A schematic of the multimodal OCT/PAT imaging

system used in this study is shown in figure 5.3. PA excitation wavelength was set at 670 nm. The dielectric coatings of the FPI sensor were highly transparent in the region 590 – 1200 nm (>80% transmission). However, these coatings exhibited high reflectivity in the region between 1500 nm and 1600 nm (>95% reflectivity). Hence, a 10 mW fibre-coupled tunable cw external cavity laser (Thorlabs ECL5000DT) operating at 1550 nm was used to provide the sensor interrogation beam. This beam was focused onto the surface of the FPI sensor and scanned across to measure the time-varying reflected optical power modulation at each point of the scan. The beam reflected from the sensor was directed via an optical fiber circulator onto a 50 MHz InGaAs photodiode. The average acquisition time achieved in this study was limited to 20 ms per scan step. The axial resolution of the PAT system was measured to be $\sim 20 \mu\text{m}$ and a lateral resolution was measured to be $\sim 100 \mu\text{m}$.

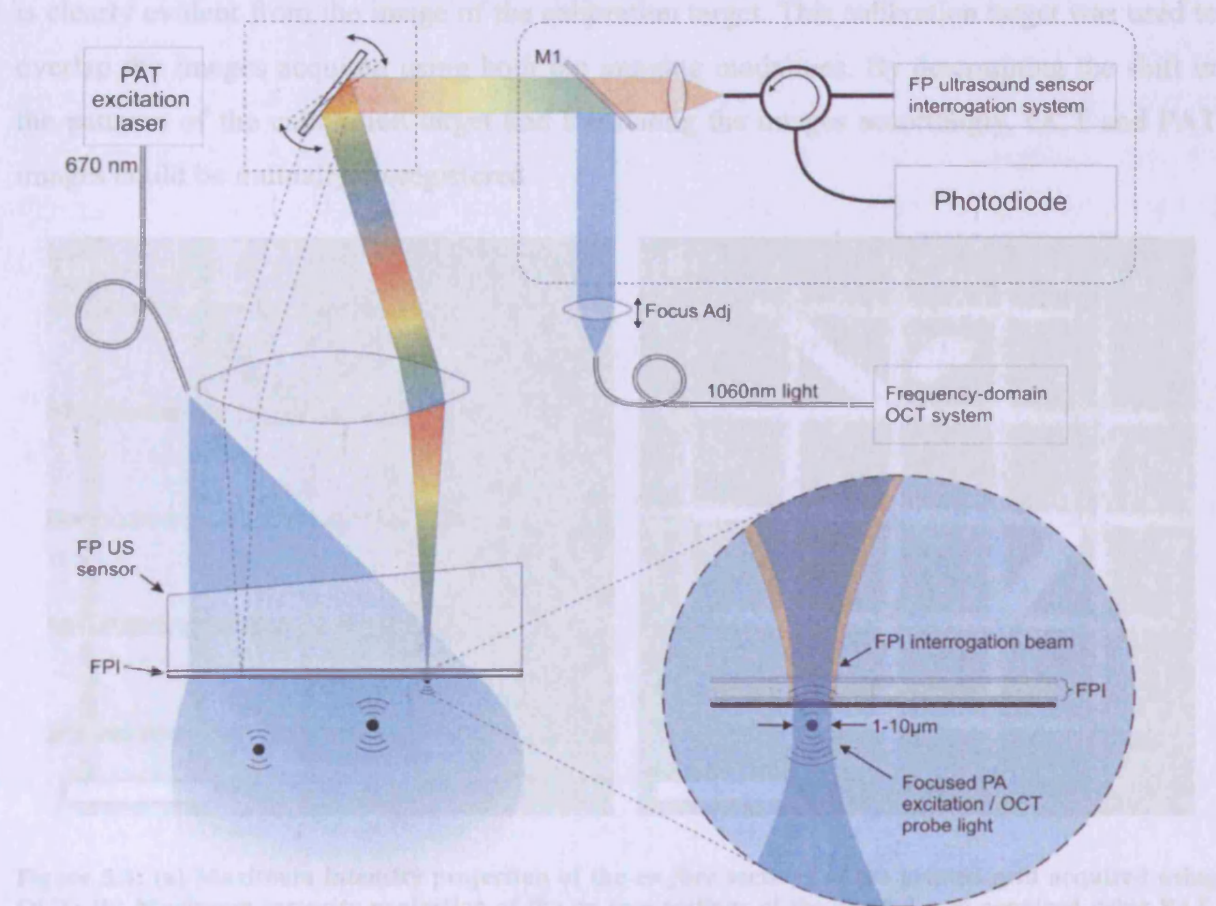


Figure 5.3: Schematic of the OCT/PAT multimodal imaging system used in this study. This diagram has been adapted from reference, (Zhang et al., 2010a).

The sample arm of the 1060 nm OCT system was combined with the PAT system using a dichroic mirror inserted into the path of the 1550 nm sensor interrogation beam as

shown in figure 5.3. During OCT imaging, an optical wedge was inserted in between the FPI sensor and the focusing lens to remove unwanted reflections at 1060 nm from the FPI sensor. Both these beams were collinearly aligned to maximize the intrinsic overlap of OCT and PAT images.

5.3.3 Calibration target

OCT and PAT images of a plastic sheet imprinted with a grid pattern formed of black lines was recorded sequentially before each imaging session. As shown in the figure 5.4, the black lines appeared as dark lines in the OCT image, whereas it appeared as bright lines in the PAT image. The black lines in the calibration target were regions devoid of any backscattering in OCT. On the contrary, those black lines turned out to be highly absorptive regions in PA imaging. Thus, the complementary behaviour of both these imaging modalities is clearly evident from the image of the calibration target. This calibration target was used to overlap the images acquired using both the imaging modalities. By determining the shift in the patterns of the calibration target and translating the images accordingly, OCT and PAT images could be mutually co-registered.

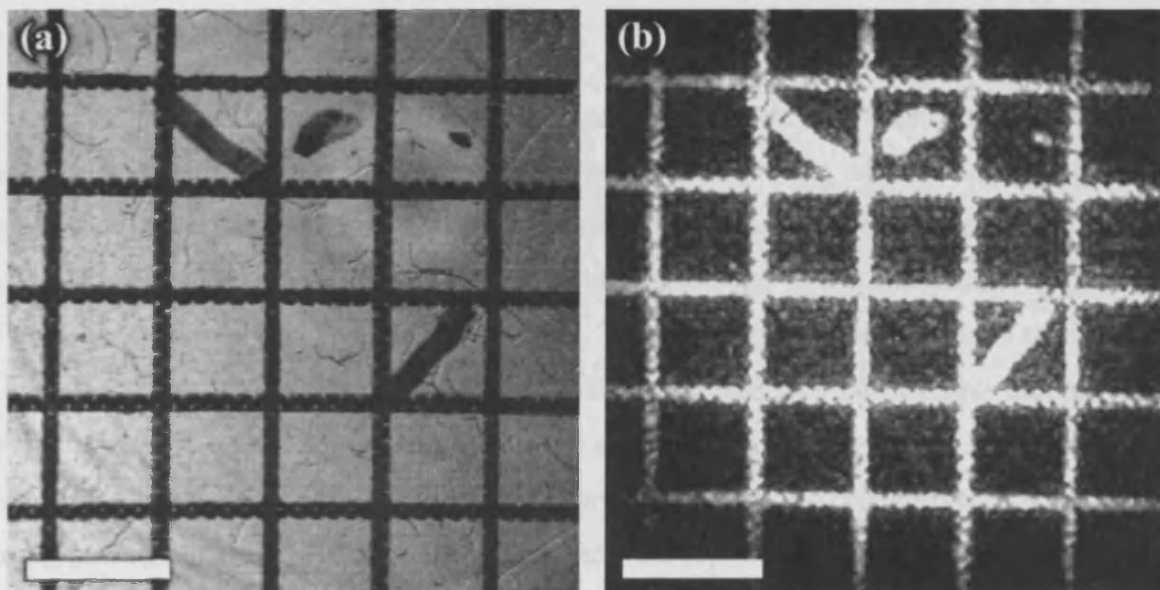


Figure 5.4: (a) Maximum intensity projection of the *en face* sections of the printed grid acquired using OCT; (b) Maximum intensity projection of the *en face* sections of the printed grid acquired using PAT. The scale bars denote a distance of 3 mm.

5.4 Results and Discussions

In vivo images of human and mouse skin were obtained using OCT and PAT systems sequentially with high spatial resolutions, revealing microstructural and vascular information upto a depth of ~ 2 mm. Figure 5.5 shows co-registered OCT/PAT images from the palmar region of a Caucasian subject. OCT revealed micro-morphological information as deep as 1 mm, meanwhile the vascular network down to a depth of ~ 2 mm can be visualized in the PA image [Figure 5.5(a)]. The thick SC, the PD and the RD can be well-demarcated from the OCT image. The distribution of small capillaries supplying blood to the upper dermis and the bigger blood vessels lying underneath in the deeper dermis can be clearly seen in the PAT image. Figure 5.5(b, c) shows *en face* views of the co-registered images from different depths: the upper dermis and the deeper dermis. As can be seen from the *en face* views, there is little morphological information available in the deep regions of dermis. However, the vascular network could be well delineated, even at these deeper dermal regions. Different views of the 3D cut through sections are shown in figure 5.5(d, e, f, g). The planar structure seen on the top of the tissue is the surface of the FPI sensor. These 3D models demonstrate the capability of this multimodal imaging modality to obtain complementary information and to visualize this data from various angles.

Figure 5.6 shows the *in vivo* skin images of a 5 weeks old female mouse. As can be seen from figure 5.6(a), the different cutaneous sub-layers of mouse skin could be demarcated from the OCT image and the blood vessels running through these structures are visible from the PA image. There are noticeable differences in the backscattering properties of various cutaneous sub-layers of mouse skin. The dermal-epidermal junctions and the lower boundary of dermis could be clearly seen. Hypodermis layer constituting adipose tissue conglomerations was a low scattering layer, compared to the upper layers, with a grainy appearance. The blood vessels distribution unveiled by the PA imaging technique showed strong correspondence with the dark dermal features seen in the OCT section. *En face* views of the co-registered images from the upper dermis and hypodermis is shown in figure 5.6(b, c). The branching patterns of blood vessels are clearly visible from both cross sectional and *en face* images. Figure 5.6(d, e, f, g) shows 3D views of OCT/PAT images of mouse skin from various angles. These 3D reconstructions illustrate the potential of this multimodal imaging technique to cut through a tissue to extract micro-morphological as well as functional information.

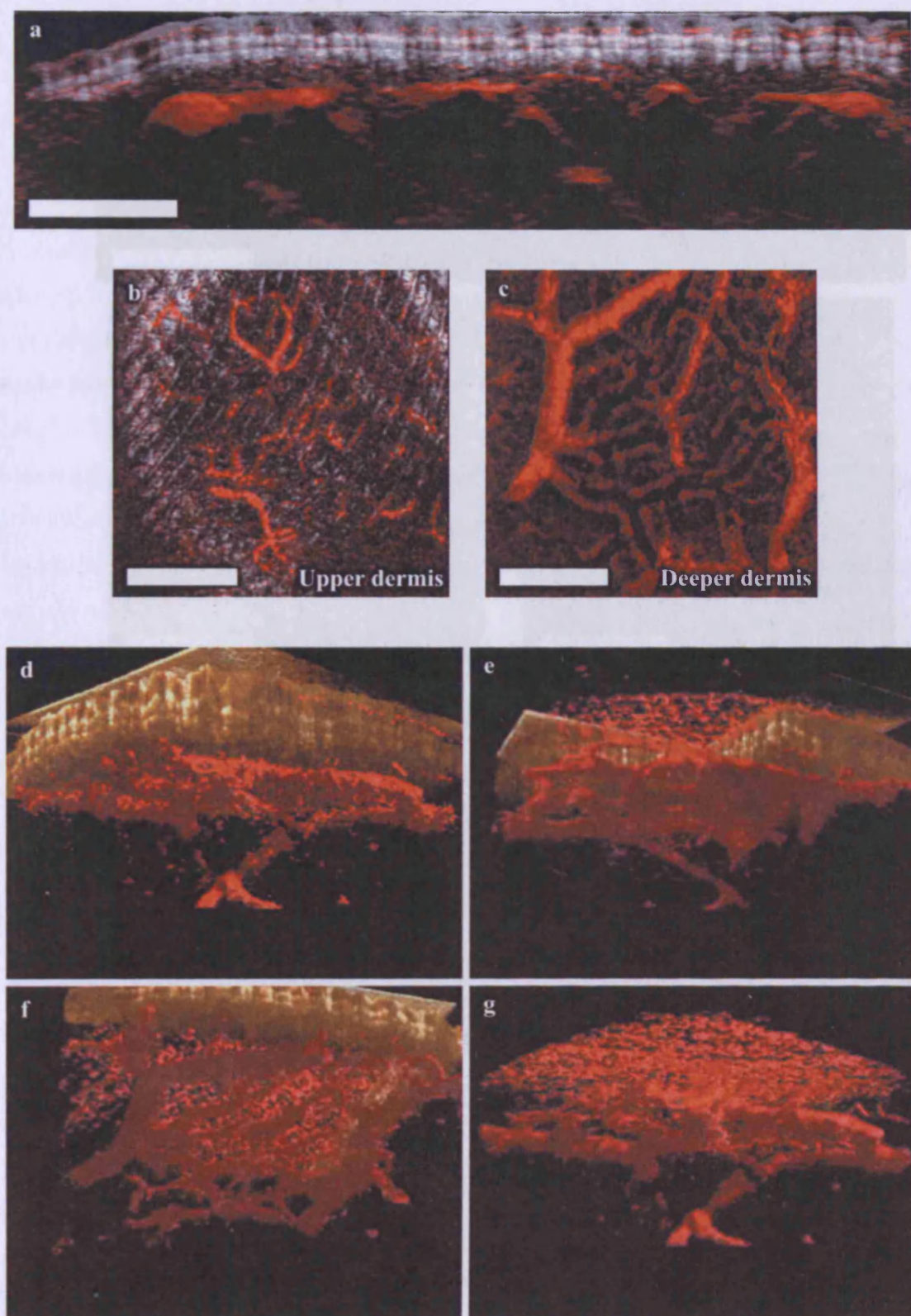


Figure 5.5: Combined OCT/PAT images obtained from the palmar region of the human skin. (a) Cross-section of the co-registered OCT/PAT image. (b, c) *En face* views of the co-registered images from upper dermis and deeper dermis respectively. (d, e, f, g) Different views of the 3D reconstruction of the co-registered volume. The scale bars denote a distance of 2 mm.

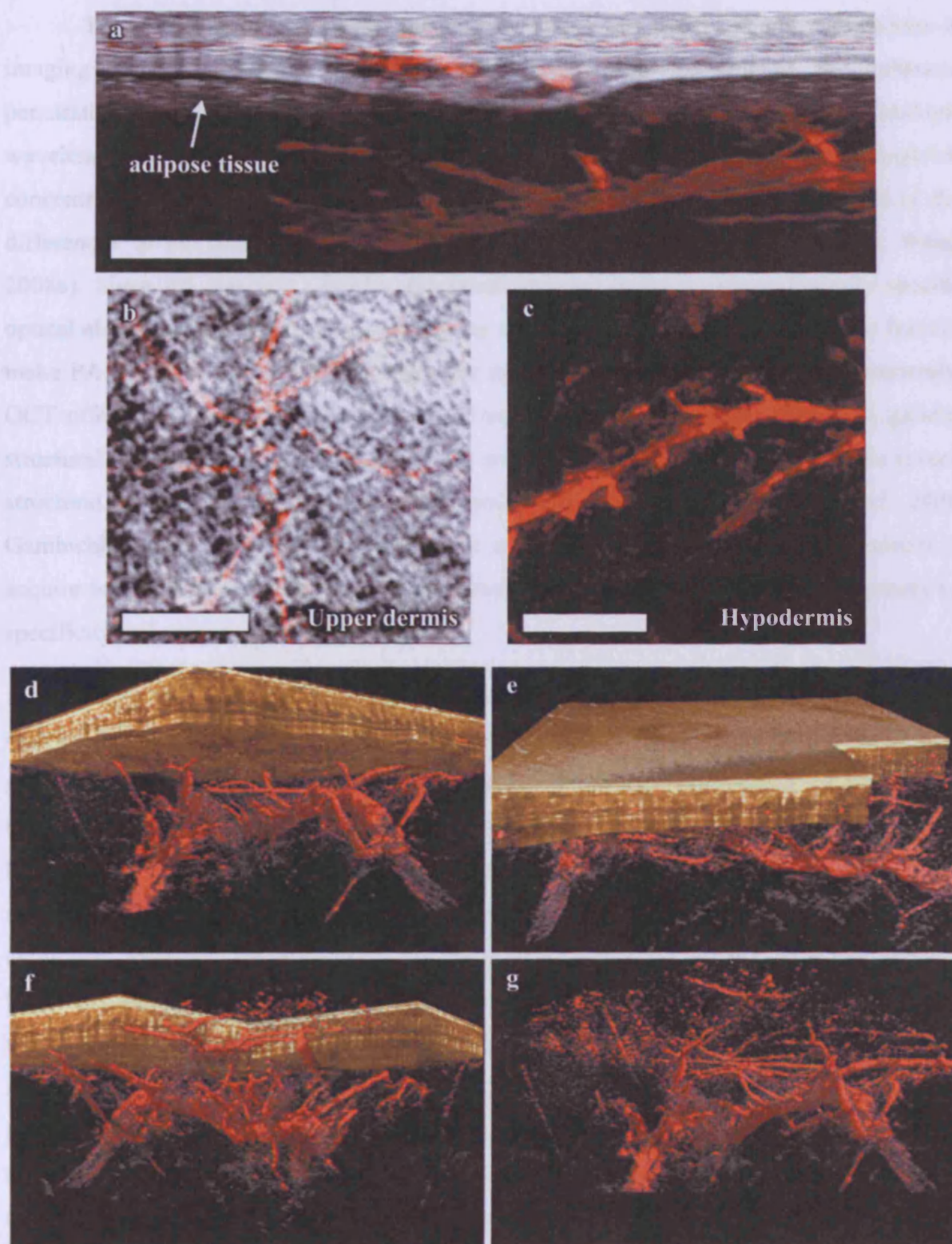


Figure 5.6: Combined OCT/PAT images obtained *in vivo* from the skin of a 5 weeks old hairless female mouse. (a) Cross-section of the co-registered OCT/PAT image. (b, c) *En face* views of the co-registered images from upper dermis and hypodermis respectively. (d, e, f, g) Different views of the 3D reconstruction of the co-registered volume. The scale bars denote a distance of 1 mm in cross-section and 2 mm in *en face* views.

Thus, multimodal OCT/PAT imaging technique can find profound applications in imaging several pathological processes, which need increased contrast and enhanced penetration. In addition to providing information on microcirculation, PA imaging at multiple wavelengths can provide information on several diagnostic factors such as total haemoglobin concentration, haemoglobin oxygen saturation and melanin concentration, because of the differences in the absorption spectra of these components (Zhang et al., 2006a; Wang, 2008a). Since PA imaging provides functional imaging based on physiologically specific optical absorption contrasts, it is devoid of any speckle and background noise. These features make PA imaging a well-suited modality for imaging vascular abnormalities. Concurrently, OCT offers micro-morphological images of tissues at micrometer-scale resolution, gaining structural contrast from variations in optical scattering. It has been shown to diagnose several structural abnormalities associated with various pathological conditions (Welzel, 2001; Gambichler et al., 2005). Thus, combination of these 3D real-time imaging techniques to acquire images based on complementary contrasts can significantly improve the sensitivity, specificity and accuracy of disease diagnosis.

Some *in vivo* dermal imaging studies have already been demonstrated using multimodal OCT/PAM technique (Jiao et al., 2009; Li et al., 2009). Both studies combined a spectral domain OCT system operating at 800 nm wavelength region with a PAM system. One of those studies used the PA system in OR-PAM mode, while the other study used it in PAM mode. Both studies were able to visualize the micro-morphology as well as the microvasculature in a mouse ear at high spatial resolutions. However, both these studies employed ultrasonic piezoelectric transducers for detecting PA signals. When operated in backward mode, piezoelectric transducers have limitations such as strong entrance signal from sample surface and reduced spatial resolution for *in vivo* imaging of superficial dermal structures. Meanwhile, it would not be possible to image thick specimens in forward mode. Hence, based on our results, backward mode operation using an optically-transparent FPI sensor has been proven to be an effective method for multimodal *in vivo* imaging of superficial dermal structures. It allows the OCT beam to pass through without any interference and provides higher sensitivity for detecting PA signals generated by superficial structures (Zhang et al., 2009).

This OCT/PAT study was a preliminary demonstration of the capability of this multimodal approach to extract complementary information from biological tissues. Further

modifications of this multimodal system are needed to improve the quality of both OCT and PAT images. A possible variation is to operate the PAT system in OR-PAM mode to increase the spatial resolution of PA imaging system. An OCT system employing longer wavelengths can be used to improve the penetration depth of OCT system. The image acquisition speed of the PAT system has to be improved further in order to make it a convenient *in vivo* imaging technique. Further studies need to be performed on normal and malignant specimens using this multimodal system to determine its sensitivity and effectiveness for diagnosing pathologic conditions. Moreover, multispectral studies capable of measuring the haemoglobin concentration, haemoglobin oxygenation level and blood flow are required to determine the true potential of this multimodal imaging modality for detecting tumours and other similar abnormalities.

5.5 Conclusions

OCT and PAT are promising non-invasive *in vivo* optical imaging techniques with tremendous potential in dermatology. However, the intrinsic contrast in OCT images by refractive index variations alone is not capable of differentiating various microstructures with similar scattering properties. PA imaging provides highly localized spectroscopic contrast based on optical absorption properties of tissue without any background signals and speckle noise. As compatible non-invasive *in vivo* optical imaging modalities, OCT/PAT multimodal imaging approach seems to have tremendous potential in dermatology. This preliminary study demonstrated the capability of a multimodal OCT/PAT imaging system to extract micro-morphological and functional information of biological tissues from deeper depths with increased contrast. It helped to delineate vascular structures from other micro-morphological features observed in OCT and provided vascular information from deeper regions (~ 2 mm) of mouse and human skin. The employment of the planar, optically-transparent FPI sensor facilitated backward mode PA scanning, which is essential for superficial imaging applications and permitted OCT imaging without any further modifications.

PAT images can be obtained at multiple illumination wavelengths in order to obtain functional information on haemoglobin concentration and its oxygenation status. Quantitative information on these biomarkers obtained via PAT, along with OCT or optical Doppler tomographic images that provide a structural background can significantly increase the sensitivity, specificity and accuracy of diagnosing precancerous lesions. PAT system can be

operated in optical resolution mode (OR-PAM) in order to increase its spatial resolutions. In summary, OCT/PA multimodal imaging technique is a promising approach with tremendous potential in various dermatological applications such as early diagnosis of skin cancer, assessment of dermal lesions and various other pathological conditions.

Chapter 6

Summary & Outlook

6.1 Summary

Among various non-invasive *in vivo* biomedical imaging modalities, OCT is one of the most promising imaging modality capable of performing high resolution, 3D imaging of the internal microstructure in biological tissues by measuring echoes of backscattered light. In the past two decades, development of ultra-broadband light sources, fibre optics technology and introduction of frequency domain techniques have led to tremendous improvements in resolution, SNR and imaging speed, without degrading the image quality. FD-OCT techniques are capable of providing a sensitivity improvement of 20 - 30 dB compared to an equivalent TD-OCT system (Choma et al., 2003; de Boer et al., 2003; Leitgeb et al., 2003).

6.1.1 Design and development of 1300 nm SD-OCT system

During the course of this dissertation, an SD-OCT system centred at 1300 nm wavelength region was designed and developed. The fibre-based OCT system consisted of an asymmetric fibre coupler, reference arm, sample arm and a spectrometer based on Czerny-Turner configuration. This system was compared with similar SD-OCT systems operating at 800 nm and 1060 nm wavelength regions in terms of axial and transverse resolutions, SNR, depth-dependent SNR degradation, image contrast and achievable depth of penetration. The spectrometer of the 1300 nm SD-OCT system was re-designed to be used with light sources of different bandwidths: 100 nm SLD, 140 nm YDFL and 170 nm SLD. The images obtained with these sources were compared to demonstrate the effect of source bandwidth on axial resolution in OCT.

6.1.2 Optimal wavelength region for dermal OCT

The capability of OCT to perform optical biopsy *in situ* in real time with micrometre-scale resolution makes it a versatile imaging modality for visualization and interpretation of microstructural information of biological tissue. Since its introduction in 1997, OCT has been utilized in obtaining qualitative and quantitative information from human skin *in vivo* (Welzel

et al., 2008). Due to variations in optical properties of tissues with wavelength, imaging parameters such as resolution, contrast and penetration depth depends on the centre wavelength and the bandwidth of the light source used. A systematic investigation was conducted to determine optimal wavelength region for dermal OCT. Images of the human skin obtained *in vivo* from different locations using similar OCT systems operating at 800 nm, 1060 nm and 1300 nm respectively was compared in terms of resolution, penetration depth and contrast. Moreover, OCT images were obtained from subjects with different ethnic origins (skin types II, IV and VI) in order to find the effect on melanin pigmentation on OCT. The 800 nm OCT system offered better contrast over other two wavelength regions, making this wavelength region more suitable for investigating structural abnormalities down to dermal-epidermal junction, which is critical in cancer diagnosis. However, 1300 nm OCT system was required to obtain information from deeper dermal regions and pigmented lesions. The 1060 nm system was a compromise between 800 nm and 1300 nm wavelength regions in terms of resolution and contrast (Alex et al., 2010).

6.1.3 *In vitro* tumour study using multispectral OCT

In vitro oesophageal and colonic tumour samples were imaged at three different wavelength regions to verify the capability of OCT to identify architectural abnormalities in various stages of tumour progression. Subsequently, these specimens were analysed using histological methods to confirm the pathological condition. It was found that the extent of architectural disarray observed in OCT sections corresponded well to the degree of dysplasia. The loss of structural features in advanced stages of tumour progression was evident in all wavelength bands. The better contrast offered by 800 nm wavelength region helped to reveal finer micro-morphological changes in tumour samples. However, this wavelength region could not penetrate deep in thicker samples. Employment of longer wavelengths helped to visualize deeper structural details. However, dense nucleation in some of the carcinoma samples prevented the light from penetrating its entire thickness, even at 1300 nm. The entropy analysis of the OCT data obtained from the tumour regions showed a dependence on the extent of structural disorganization. The entropy was found to increase with the degree of dysplasia. However, it appeared to decline at advanced stages of carcinoma. This tumour study demonstrated the potential of OCT to be used as a non-invasive imaging tool for diagnosing precancerous conditions in gastrointestinal tissue.

6.1.4 Multimodal OCT/PAT imaging approach

The inherent contrast in OCT depends on the differences in the backscattering properties of the target tissue, whereas the inherent contrast in PA imaging is derived from the optical absorption properties of the tissue. Hence, these complementary imaging modalities were combined to acquire structural and functional information of skin simultaneously from deeper depths with enhanced contrast. A planar, dichroic FPI sensor was used for ultrasonic detection of PA signals and this detector was transparent to both OCT and PA excitation wavelengths. The multimodal OCT/PAT system was used to obtain *in vivo* images of the mouse and human skin. It helped to delineate vascular structures from other microstructural features observed in OCT and provided vascular information from as deep as 2 mm. Thus, this preliminary study showed OCT/PAT multimodal imaging technique as a promising approach with wide applications in the field of dermatology.

6.2 Future prospects of this research

6.2.1 Pharmacological applications

Topical application of medicinal formulations, such as creams and ointments, is a non-invasive and patient-friendly method of drug delivery. This has been found effective in treatment of several dermal inflammatory diseases, such as psoriasis and eczema. Majority of these dermal disorders are characterized by changes in epidermal thickness and other structural abnormalities. Conventional diagnostic method for these disorders is to perform invasive histological studies. For both research and clinical applications, OCT can be a promising non-invasive imaging tool that can monitor these changes with high precision in real-time (Welzel et al., 2003). Hence, a study was conducted to assess the potential of OCT to determine the variations in epidermal thickness of a mutant mouse on application of different anti-psoriatic agents such as betamethasone dipropionate (BD) and fish oil (FO). This study was carried out in collaboration with Pharmaceutical Biology Research Group, Welsh School of Pharmacy, Cardiff University, UK. The mutant mouse models and treatment formulations were obtained from our collaborators. A commercial swept source OCT system (Thorlabs Inc., Newton, New Jersey) operating at a centre wavelength of 1325 nm and having a sweep width of 100 nm was used in this study to obtain OCT images. The epidermal thickness variation was quantified for each mouse model by dividing the optical thickness of the epidermis, which were measured from the OCT cross-sections, with an average refractive index of 1.4. Following 10 days of topical treatment with BD, the average epidermal

thickness in mice reduced by 38.8%. Conversely, the average epidermal thickness increased by 105% in mice treated with FO. A noticeable change in the average epidermal thickness was absent in mice that were treated with a mixed formulation, containing both BD and FO [Figure 6.1]. These epidermal thickness values obtained using OCT were validated by histology and the results from this study suggests the potential applications of OCT in monitoring effects of topical pharmacologic treatments.

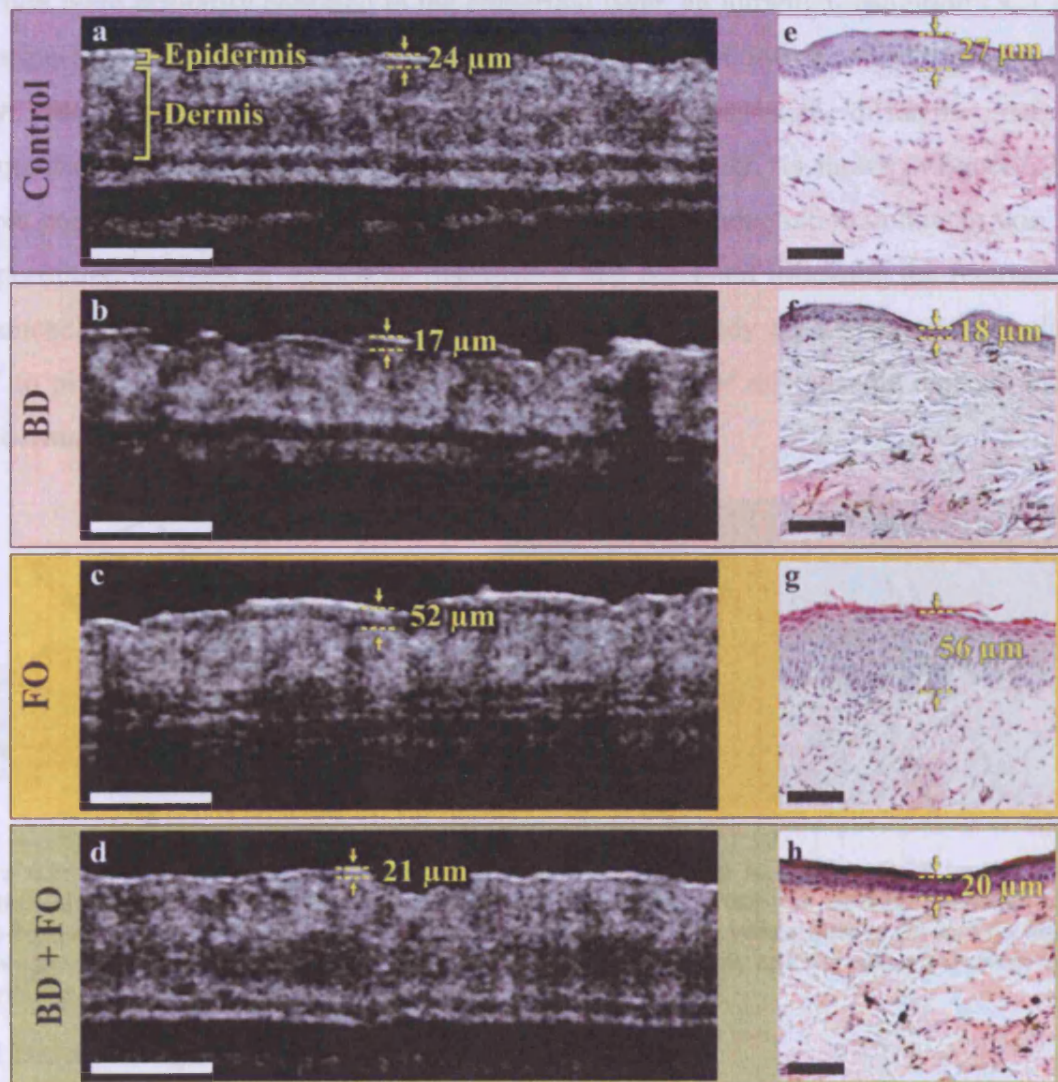


Figure 6.1: OCT cross-sectional images obtained using the 1300 nm swept source OCT system (a-d) and corresponding histology slices (e-h). OCT and corresponding histology sections of a control mouse (a, e), a mouse treated with betamethasone dipropionate (b, f), a mouse treated with fish oil (c, g) and a mouse treated with a mixture of both betamethasone dipropionate and fish oil (d, h). The scale bars denote 250 μm in (a, b, c, d) and 50 μm in (e, f, g, h).

However, the number of drug candidates that can be topically delivered is restricted due to the barrier properties of the outermost skin layer, the SC. One of the proposed methods

to overcome the skin barrier is to create conduits using microneedles (Henry et al., 1998). In contrast to hypodermic needles, microneedles can be used for localized drug delivery to the viable epidermis with minimal disruption to the tissue architecture. A systematic investigation was performed, in collaboration with Gene Delivery Research Group, Welsh School of Pharmacy, Cardiff University, UK, to obtain *in situ* images of microneedle-treated human skin *in vivo* using OCT. As the microchannels created as a result of microneedle insertion were primarily confined to the epidermal layer, an ultrahigh-resolution OCT system operating at 800 nm wavelength region with a bandwidth of 140 nm was employed for this study. Steel, silicon and polymer microneedle devices, with different microneedle arrangements and morphologies were applied during this study. As shown in figure 6.2, OCT images provided representative illustrations of microneedle penetration in human skin *in vivo* and permitted analysis of epidermal disruptions that remained following the removal of the microneedle devices (Coulman et al., 2010). Thus, this study demonstrates the aptitude of OCT to play a highly influential role in the development of microneedle devices and other transdermal drug delivery systems.

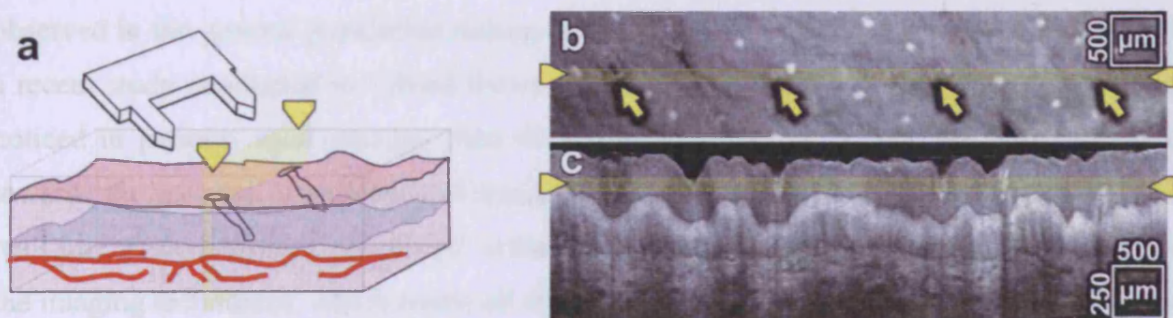


Figure 6.2: (a) Schematic of the experimental procedure followed to capture OCT images following insertion of the microneedle. (b) *En face* image obtained from within the stratum corneum layer. (c) Cross-sectional image showing stratified nature of palmar skin. The yellow lines in (b) and (c) denote the relative locations of the cross-sectional and *en face* images respectively and the yellow arrows in (b) point towards the minute microneedle insertion points.

6.2.2 Dermal diagnostic applications

Based on the conclusions from Chapter 3, 800 nm wavelength region appears to be the preferred wavelength region for superficial imaging applications confined to the epidermal layer, which requires higher resolution and contrast. Meanwhile, longer wavelength regions are inevitable for obtaining morphological details from deeper dermal layers and strongly scattering tissue. The visible appearance of normal healthy skin in OCT is variable, depending on the location. OCT can be employed for diagnosis of skin diseases

such as epithelial tumours and inflammatory diseases, by comparing the microstructural features of infected regions with that of normal skin. OCT is capable of visualizing changes of the epidermis like ulceration, crusts and atrophy associated with malignant transformation. Several studies have demonstrated the capability of OCT to diagnose skin tumours and other abnormalities (Gambichler et al., 2007a; Welzel et al., 2008; Mogensen et al., 2009a). However, improvements in resolution and contrast offered by OCT are needed to differentiate grades of tumour and to detect tumour boundaries with higher precision. Further systematic studies on various skin diseases that could depict associated microstructural modifications have to be conducted using OCT, in order to establish OCT as a clinical dermal imaging modality.

6.2.3 Gastrointestinal endoscopic applications

The incidence of oesophageal and colorectal cancers has increased dramatically in the past few decades. The most recognized risk factor for oesophageal cancer is Barrett's oesophagus, which increases the risk of malignant transformation by 30-125 fold (Solaymani-Dodaran et al., 2004). A linear increase in incidence of Barrett's oesophagus has been observed in the general population during the period 1997 – 2002 (van Soest et al., 2005). In a recent study conducted in United States, an increase in the incidence of rectal cancer was noticed in patients aged younger than 40 years (Meyer et al., 2010). All these data point towards the growing significance of access to effective non-invasive, portable, low-cost and real-time gastrointestinal endoscopic screening techniques for all age groups. OCT is one of the imaging techniques, which meets all these prerequisites and can be easily integrated to an endoscope. Several *in vitro* and *in vivo* trials have been performed using OCT to diagnose gastrointestinal pathologies (Pfau et al., 2003; Westphal et al., 2005). However, further improvements in technology and more clinical studies that can demonstrate the diagnostic efficacy of endoscopic OCT need to be carried out in gastrointestinal tissues.

6.2.4 Potential applications of multimodal OCT/PAT approach in dermatology

The complimentary scattering and absorption contrasts obtained using a multimodal OCT/PAT imaging system can present a huge potential for a wide variety of dermal imaging applications. This multimodal approach is still in its preliminary stage, with a few proof-of-principle studies demonstrated in normal skin (Qi.X et al., 2008; Jiao et al., 2009; Li et al., 2009). A lot of research studies with various modifications to the multimodal OCT/PAT system are needed to explore its true potential in dermatology. PAT employing multiple

excitation wavelengths together with optical Doppler tomography can be used to extract critical structural and functional information concerning tumour angiogenesis and hypermetabolism. Alternatively, PA images can be obtained using a focussed excitation beam (OR-PAM) to obtain highly resolved functional images with a penetration depth comparable to that of OCT. In addition to dermatological studies, modified OCT/PAT systems can be extended into other areas such as cerebral microcirculation studies, ophthalmology and cardiology (Jiao et al., 2010).

Bibliography

Adler D C, Zhou C, Tsai T-H, Schmitt J, Huang Q, Mashimo H, and Fujimoto J G (2009) Three-dimensional endomicroscopy of the human colon using optical coherence tomography. *Optics Express* 17: 784-796.

Alex A, Povazay B, Hofer B, Popov S, Glittenberg C, Binder S, and Drexler W (2010) Multispectral in vivo three-dimensional optical coherence tomography of human skin. *Journal of Biomedical Optics* 15: 026025-026015.

Altekruse S F, Kosary C L, Krapcho M, Neyman N, Aminou R, Waldron W, Ruhl J et al. (2009) SEER cancer statistics review, 1975 - 2007. In: Institute N C [ed.] Bethesda, Maryland.

Argenziano G, Ferrara G, Francione S, Nola K D, Martino A, and Zalaudek I (2009) Dermoscopy - The Ultimate Tool for Melanoma Diagnosis. *Seminars in Cutaneous Medicine and Surgery* 28: 142-148.

Bach P B, Kelley M J, Tate R C, and McCrory D C (2003) Screening for Lung Cancer. *Chest* 123: 72S-82S.

Bancroft J D, and Gamble M (2008) Chapter 9: The hematoxylin and eosin. *Theory and Practice of Histological Techniques*. (6 edn.) London: Churchill Livingstone.

Barad Y, Eisenberg H, Horowitz M, and Silberberg Y (1997) Nonlinear scanning laser microscopy by third harmonic generation. *Applied Physics Letters* 70: 922-922.

Barai N D, Supp A P, Kasting G B, Visscher M O, and Boyce S T (2007) Improvement of Epidermal Barrier Properties in Cultured Skin Substitutes after Grafting onto Athymic Mice. *Skin Pharmacology and Physiology* 20: 21-28.

Barrett N R (1957) The lower esophagus lined by columnar epithelium. *Surgery* 41: 881-894.

Barton J K, Gossage K W, Xu W, Ranger-Moore J R, Saboda K, Brooks C A, Duckett L D et al. (2003) Investigating sun-damaged skin and actinic keratosis with optical coherence tomography: a pilot study. *Technology in Cancer Research & Treatment* 2: 525-535.

Barton J K, Guzman F, and Tumlinson A (2004) Dual modality instrument for simultaneous optical coherence tomography imaging and fluorescence spectroscopy. *Journal of Biomedical Optics* 9: 618-623.

Bashkatov A N, Genina E A, Kochubey V I, and Tuchin V V (2005) Optical properties of human skin, subcutaneous and mucous tissues in the wavelength range from 400 to 2000 nm. *Journal of Physics D: Applied Physics* 38: 2543-2555.

Beard P C, Perennes F, and Mills T N (1999) Transduction mechanisms of the Fabry-Perot polymer film sensing concept for wideband ultrasound detection. *Ultrasonics, Ferroelectrics and Frequency Control, IEEE Transactions on* 46: 1575-1582.

Beard P C, Zhang E Z, and Cox B T [eds.] (2004) *Transparent Fabry-Perot polymer film ultrasound array for backward-mode photoacoustic imaging*. Proceedings of SPIE. San Jose, CA, USA.

Becerra L, Harris W, Grant M, George E, Boas D, and Borsook D (2009) Diffuse Optical Tomography Activation in the Somatosensory Cortex: Specific Activation by Painful vs. Non-Painful Thermal Stimuli. *PLoS ONE* 4: e8016-e8016.

Bell A G (1880) On the production and reproduction of sound by light: the photophone. *American Journal of Science* 20: 305 - 324.

Beyer T, Townsend D W, Brun T, Kinahan P E, Charron M, Roddy R, Jerin J et al. (2000) A Combined PET/CT Scanner for Clinical Oncology. *Journal of Nuclear Medicine* 41: 1369-1379.

Bhatia V (2010) Endoscopic ultrasound: imaging techniques and applications in the mediastinum. *Tropical Gastroenterology* 30: S4-19-S14-19.

Bishop J F, and Bishop P B [eds.] (1999) *Cancer facts: A concise oncology text*. London: Informa health care.

Bittoun J, Querleux B, and Darrasse L (2006) Advances in MR imaging of the skin. *NMR in Biomedicine* 19: 723-730.

Bittoun J, Saint-Jalmes H, Querleux B G, Darrasse L, Jolivet O, Idy-Peretti I, Wartski M et al. (1990) In vivo high-resolution MR imaging of the skin in a whole-body system at 1.5 T. *Radiology* 176: 457-460.

Blankenberg F G, and Strauss H W (2002) Nuclear Medicine Applications in Molecular Imaging. *Journal of Magnetic Resonance Imaging* 16: 352-361.

Bloch F, Hansen W W, and Packard M (1946) Nuclear Induction. *Physical Review* 69: 127-127.

Boas D A, Brooks D H, Miller E L, Dimarzio C A, Kilmer M, Gaudette R J, and Zhang Q (2001) *Imaging the body with Diffuse Optical Tomography*. IEEE Signal Processing Magazine. pp. 57 - 75.

Bouma B E, Nelson L E, Tearney G J, Jones D J, Brezinski M E, and Fujimoto J G (1998) Optical Coherence Tomographic Imaging of Human Tissue at 1.55 μm and 1.81 μm Using Er- and Tm-Doped Fiber Sources. *Journal of Biomedical Optics* 3: 76-79.

Bouma B E, Tearney G J, Compton C C, and Nishioka N S (2000) High-resolution imaging of the human esophagus and stomach in vivo using optical coherence tomography. *Gastrointestinal Endoscopy* 51: 467-474.

Bousi E, Charalambous I, and Pitris C (2010) Optical coherence tomography axial resolution improvement by step-frequency encoding. *Optics Express* 18: 11877-11890.

Campagnola P J, Wei M D, Lewis A, and Loew L M (1999) High-resolution nonlinear optical imaging of live cells by second harmonic generation. *Biophysical Journal* 77: 3341-3349.

Campos-do-Carmo G, and Ramos-e-Silva M (2008) Dermoscopy: basic concepts. *International Journal of Dermatology* 47: 712-719.

Caspers P J, Lucassen G W, and Puppels G J (2003) Combined In Vivo Confocal Raman Spectroscopy and Confocal Microscopy of Human Skin. *Biophysical Journal* 85: 572-580.

Cense B, Nassif N, Chen T C, Pierce M C, Yun S H, Park B H, Bouma B E et al. (2004) Ultrahigh-resolution high speed retinal imaging using spectral domain optical coherence tomography. *Optics Express* 12: 2435-2447.

Chen Z, Milner T E, Srinivas S, Wang X, Malekafzali A, van Gemert M J C, and Nelson J S (1997) Noninvasive imaging of in vivo blood flow velocity using optical Doppler tomography. *Optics Letters* 22: 1119-1121.

Cheng J-X (2007) Coherent Anti-Stokes Raman Scattering Microscopy. *Applied spectroscopy* 61: 197-208.

Chinn S R, Swanson E A, and Fujimoto J G (1997) Optical coherence tomography using a frequency-tunable optical source. *Optics Letters* 22: 340-342.

Choe R (2009) Diffuse optical tomography & spectroscopy in breast cancer characterization & therapy monitoring at UPENN. *Conference Proceedings: Annual International Conference of the IEEE Engineering in Medicine and Biology Society. IEEE Engineering in Medicine and Biology Society. Conference 2009*: 6335-6337.

Choma M A, Sarunic M V, Yang C, and Izatt J A (2003) Sensitivity advantage of swept source and Fourier domain optical coherence tomography. *Optics Express* 11: 2183-2189.

Chowdhury F U, and Scarsbrook A F (2008) The role of hybrid SPECT-CT in oncology: current and emerging clinical applications. *Clinical Radiology* 63: 241-251.

Çilesiz I, Fockens P, Kerindongo R, Faber D, Tytgat G, ten Kate F, and van Leeuwen T (2002) Comparative optical coherence tomography imaging of human esophagus: How accurate is localization of the muscularis mucosae? *Gastrointestinal Endoscopy* 56: 852-857.

Coulman S A, Birchall J C, Alex A, Pearton M, Hofer B, O'Mahony C, Drexler W et al. (2010) In Vivo, In Situ Imaging of Microneedle Insertion into the Skin of Human Volunteers Using Optical Coherence Tomography. *Pharmaceutical Research* 28: 66-81.

Cox I J (1996) Development and applications of *in vivo* clinical magnetic resonance spectroscopy. *Prog. Biol. molec Biol.* 65: 45 - 82.

Cutler M (1929) Transillumination as an aid in the diagnosis of breast lesions. *Surgery, Gynecology and Obstetrics* 48: 721-729.

Day D W, Jass J R, Price A B, Shepherd N A, Sloan J M, Talbot I C, Williams G T et al. (2003a) Chapter 4: Normal oesophagus. *Morson and Dawson's gastrointestinal pathology*. (4 edn.) Massachusetts: Blackwell, pp. 21 - 25.

Day D W, Jass J R, Price A B, Shepherd N A, Sloan J M, Talbot I C, Williams G T et al. (2003b) Chapter 33: Normal large intestine. *Morson and Dawson's gastrointestinal pathology*. (4 edn.) Massachusetts: Blackwell, pp. 435-444.

Day D W, Jass J R, Price A B, Shepherd N A, Sloan J M, Talbot I C, Williams G T et al. (2003c) Chapter 38: Epithelial tumours of the large intestine. *Morson and Dawson's gastrointestinal pathology*. (4 edn.) Massachusetts: Blackwell, pp. 551-609.

de Boer J, Srinivas S, Malekafzali A, Chen Z, and Nelson J (1998) Imaging thermally damaged tissue by Polarization Sensitive Optical Coherence Tomography. *Optics Express* 3: 212-218.

de Boer J F, Cense B, Park B H, Pierce M C, Tearney G J, and Bouma B E (2003) Improved Signal-to-noise ratio in spectral-domain compared to time-domain optical coherence tomography. *Optics Letters* 28: 2067-2069.

de Matos C J S, Popov S V, and Taylor J R (2004) Temporal and noise characteristics of continuous-wave-pumped continuum generation in holey fibers around 1300nm. *Applied Physics Letters* 85: 2706-2708.

Deans S (1992) *The Radon Transform and Some of Its Applications*. 1 ed. Malabar, Florida: Krieger Publishing Company.

Denk W, Strickler J H, and Webb W W (1990) Two-photon laser scanning fluorescence microscopy. *Science* 248: 73-76.

Devesa S S, Blot W J, and Fraumeni J F (1998) Changing patterns in the incidence of esophageal and gastric carcinoma in the United States. *Cancer* 83: 2049-2053.

Dimitrow E, Ziemer M, Koehler M J, Norgauer J, Konig K, Elsner P, and Kaatz M (2009) Sensitivity and Specificity of Multiphoton Laser Tomography for In Vivo and Ex Vivo Diagnosis of Malignant Melanoma. *Journal of Investigative Dermatology* 129: 1752-1758.

Ding Z, Ren H, Zhao Y, Nelson J S, and Chen Z (2002) High-resolution optical coherence tomography over a large depth range with an axicon lens. *Optics Letters* 27: 243 - 245.

Drexler W, Chen Y, Aguirre A, Považay B, Unterhuber A, and Fujimoto J G (2008) Chapter 8: Ultrahigh resolution optical coherence tomography. In: Drexler W, and Fujimoto J G [eds.] *Optical Coherence Tomography: Technology and Applications*. (1 edn.) Berlin: Springer, pp. 239 - 279.

Drexler W, and Fujimoto J G (2008a) *Optical Coherence Tomography: Technology and Applications*. Berlin: Springer.

Drexler W, and Fujimoto J G (2008b) State-of-the-art retinal optical coherence tomography. *Progress in Retinal and Eye Research* 27: 45-88.

Drexler W, Morgner U, Kartner F X, Pitris C, Boppart S A, Li X D, Ippen E P et al. (1999) In vivo ultrahigh-resolution optical coherence tomography. *Optics Letters* 24: 1221-1223.

Drezek R A, Richards-Kortum R, Brewer M A, Feld M S, Pitris C, Ferenczy A, Faupel M L et al. (2003) Optical imaging of the cervix. *Cancer* 98: 2015-2027.

Duck F A (1990) *Physical Properties of Tissue*. London: Academic Press Inc.

Duguay M A, and Mattick A T (1971) Ultrahigh Speed Photography of Picosecond Light Pulses and Echoes. *Applied Optics* 10: 2162 -2169.

Duncan D D, Kirkpatrick S J, and Wang R K (2008) Statistics of local speckle contrast. *Journal of the Optical Society of America A* 25: 9-15.

Dwyer P J, DiMarzio C A, and Rajadhyaksha M (2007) Confocal theta line-scanning microscope for imaging human tissues. *Applied Optics* 46: 1843-1851.

Efimov I R, Nikolski V P, and Salama G (2004) Optical Imaging of the Heart. *Circulation Research* 95: 13.

Ehman R L, Hendee W R, Welch M J, Dunnick N R, Bresolin L B, Arenson R L, Baum S et al. (2007) Blueprint for imaging in biomedical research. *Radiology* 244: 12 -27.

Endlicher E, Knuechel R, Hauser T, Szeimies R M, Schölmerich J, and Messmann H (2001) Endoscopic fluorescence detection of low and high grade dysplasia in Barrett's oesophagus using systemic or local 5-aminolaevulinic acid sensitisation. *Gut* 48: 314-319.

Enterline H T, Evans G W, Mercado-Lugo R, Miller L, and Fitts W T (1962) Malignant Potential of Adenomas of Colon and Rectum. *JAMA* 179: 322-330.

Evans C L, Potma E O, Puoris'haag M, Côté D, Lin C P, and Xie X S (2005) Chemical imaging of tissue in vivo with video-rate coherent anti-Stokes Raman scattering microscopy. *Proceedings of the National Academy of Sciences of the United States of America* 102: 16807-16812.

Evans J A, and Nishioka N S (2005) Endoscopic confocal microscopy. *Current Opinion in Gastroenterology* 21: 578-584.

Falk G W, Catalano M F, Sivak M V, Rice T W, and Van Dam J (1994) Endosonography in the evaluation of patients with Barrett's esophagus and high-grade dysplasia. *Gastrointestinal Endoscopy* 40: 207-212.

Fasola G, Belvedere O, Aita M, Zanin T, Follador A, Cassetti P, Meduri S et al. (2007) Low-Dose Computed Tomography Screening for Lung Cancer and Pleural Mesothelioma in an Asbestos-Exposed Population: Baseline Results of a Prospective, Nonrandomized Feasibility

Trial An Alpe-Adria Thoracic Oncology Multidisciplinary Group Study (ATOM 002). *Oncologist* 12: 1215-1224.

Fass L (2008) Imaging and cancer: A review. *Molecular Oncology* 2: 115 - 152.

Fenster A, and Downey D B (2000) Three-dimensional ultrasound imaging. *Annual Review of Biomedical Engineering* 2: 457 - 475.

Fercher A F, Hitzenberger C K, Drexler W, Kamp G, and Sattmann H (1993) *In vivo* Optical Coherence Tomography. *American Journal of Ophthalmology* 116: 113 - 115.

Fercher A F, Hitzenberger C K, Kamp G, and El-zaiat s Y (1995) Measurement of Intraocular distances by backscattering speckle interferometry. *Optics communications* 117: 43-48.

Fercher A F, Mengdoht K, and Werner W (1988) Eye length measurements by interferometry with partially coherent light. *Optics Letters* 13: 186 -188.

Ferlay J, Shin H R, Bray F, Forman D, Matthers C, and Parkin D M (2008) GLOBOCAN 2008: Cancer incidence and mortality worldwide. In: International Agency for Research on Cancer W H O [ed.] Lyon, France.

Fitzpatrick T B (1975) Soleil et peau. *Journal of Medical Esthetics* 2: 33-34.

Forbes A, Misiewicz. J J, Compton C C, Levine M S, Rubesin S E, Thuluvath P J, and Quraishy S (2005a) Chapter 1: The Oesophagus. *Atlas of clinical gastroenterology*. (3 edn.) Philadelphia: Elsevier Mosby, p. 4.

Forbes A, Misiewicz. J J, Compton C C, Levine M S, Rubesin S E, Thuluvath P J, and Quraishy S (2005b) Chapter 6: Colon I. *Atlas of clinical gastroenterology*. (3 edn.) Philadelphia: Elsevier Mosby, p. 137.

Fujimoto J, and Drexler W (2008) Chapter 1: Introduction to optical coherence tomography. In: Drexler W, and Fujimoto J G [eds.] *Optical Coherence Tomography: Technology and Applications*. (1 edn.) Berlin: Springer, pp. 1 - 45.

Fujimoto J G, Silvestri S D, Ippen E P, Puliafito C A, Margolis R, and Oseroff A (1986) Femtosecond optical ranging in biological systems. *Optics Letters* 11: 150 -152.

Gambichler T, Matip R, Moussa G, Altmeyer P, and Hoffmann K (2006) In vivo data of epidermal thickness evaluated by optical coherence tomography: Effects of age, gender, skin type, and anatomic site. *Journal of Dermatological Science* 44: 145-152.

Gambichler T, Moussa G, Sand M, Sand D, Altmeyer P, and Hoffmann K (2005) Applications of optical coherence tomography in dermatology. *Journal of Dermatological Science* 40: 85-94.

Gambichler T, Orlikov A, Vasa R, Moussa G, Hoffmann K, Stücker M, Altmeyer P et al. (2007a) In vivo optical coherence tomography of basal cell carcinoma. *Journal of Dermatological Science* 45: 167-173.

Gambichler T, Regeniter P, Bechara F G, Orlikov A, Vasa R, Moussa G, Stücker M et al. (2007b) Characterization of benign and malignant melanocytic skin lesions using optical coherence tomography in vivo. *Journal of the American Academy of Dermatology* 57: 629-637.

Gammal S E, Gammal C E, Kaspar K, Pieck C, Altmeyer P, Vogt M, and Ermert H (1999) Sonography of the Skin at 100 MHz Enables In Vivo Visualization of Stratum Corneum and Viable Epidermis in Palmar Skin and Psoriatic Plaques. *Journal of Investigative Dermatology* 113: 821-829.

Garvey C J, and Hanlon R (2002) Computed tomography in clinical practice. *British Medical Journal* 324: 1077-1080.

Gerger A, Koller S, Kern T, Massone C, Steiger K, Richtig E, Kerl H et al. (2005) Diagnostic Applicability of In Vivo Confocal Laser Scanning Microscopy in Melanocytic Skin Tumors. *Journal of Investigative Dermatology* 124: 493-498.

Gfesser M, Abeck D, Rügemer J, Schreiner V, Stäb F, Disch R, and Ring J (1997) The early phase of epidermal barrier regeneration is faster in patients with atopic eczema. *Dermatology (Basel, Switzerland)* 195: 332-336.

Goh H S, and Jass J R (1986) DNA content and the adenoma-carcinoma sequence in the colorectum. *Journal of Clinical Pathology* 39: 387-392.

Göppert-Mayer M (1931) Über Elementarakte mit zwei Quantensprüngen. *Annalen der Physik* 401: 273-294.

Hadani M, Bruk B, Ram Z, Knoller N, Spiegelmann R, and Segal E (1999) Application of transcranial Doppler ultrasonography for the diagnosis of brain death. *Intensive Care Medicine* 25: 822-828.

Haenssle H A, Krueger U, Vente C, Thoms K-M, Bertsch H P, Zutt M, Rosenberger A et al. (2006) Results from an Observational Trial: Digital Epiluminescence Microscopy Follow-Up of Atypical Nevi Increases the Sensitivity and the Chance of Success of Conventional Dermoscopy in Detecting Melanoma. *Journal of Investigative Dermatology* 126: 980-985.

Hagmann P, Jonasson L, Maeder P, Thiran J P, Wedeen V J, and Meuli R (2006) Understanding Diffusion MR Imaging Techniques: From Scalar Diffusion-weighted Imaging to Diffusion Tensor Imaging and Beyond1. *Radiographics* 26: S205-S223.

Hamblin M R [ed.] (2006) *Mechanisms of low level light therapy*. Proceedings of SPIE. San Jose, CA, USA.

Hamilton J D, and O'Donnell M (1998) High frequency ultrasound imaging with optical arrays. *IEEE Transactions on Ultrasonics, Ferroelectrics, and Frequency Control* 45: 216-235.

Hartl I, Li X D, Chudoba C, Ghanta R K, Ko T H, Fujimoto J G, Ranka J K et al. (2001) Ultrahigh-resolution optical coherence tomography using continuum generation in an ar-silica microstructure optical fiber. *Optics Letters* 26: 608-610.

Harvey C J, Pilcher J M, Eckersley R J, Blomley M J K, and Cosgrove D O (2002) Advances in Ultrasound. *Clinical Radiology* 57: 157 -177.

Häusler G, Herrmann J M, Kummer R, and Lindner M W (1996) Observation of light propagation in volume scatterers with 1011-fold slow motion. *Optics Letters* 21: 1087-1089.

He Y X, and Guo Q Y (2008) Clinical applications and advances of positron emission tomography with fluorine-18-fluorodeoxyglucose (18F-FDG) in the diagnosis of liver neoplasms. *Postgraduate Medical Journal* 84: 246 - 251.

Hebden J C, Arridge S R, and Delphy D T (1997) Optical imaging in medicine: I. Experimental techniques. *Physics in Medicine and Biology* 42: 825 - 840.

Hellwarth R, and Christensen P (1974) Nonlinear optical microscopic examination of structure in polycrystalline ZnSe. *Optics Communications* 12: 318-322.

Henry S, McAllister D V, Allen M G, and Prausnitz M R (1998) Microfabricated microneedles: a novel approach to transdermal drug delivery. *Journal of Pharmaceutical Sciences* 87: 922-925.

Hirano T, Otake H, Yoshida I, and Endo K (1995) Primary Lung Cancer SPECT Imaging with Pentavalent Technetium-99m-DMSA. *Journal of Nuclear medicine* 36: 202-207.

Hofer B (2010) *Advanced signal acquisition and processing for frequency domain optical coherence tomography*. Medical University Vienna.

Hoffmann K, Happe M, Schüller S, Stücker M, Wiesner M, Gottlöber P, Schwarz M et al. (1999) Ranking of 20 MHz sonography of malignant melanoma and pigmented lesions in routine diagnosis. *Ultraschall in Der Medizin (Stuttgart, Germany: 1980)* 20: 104-109.

Hoffmann K, Jung J, Gammal S E, and Altmeyer P (1992) Malignant melanoma in 20-MHz B scan sonography. *Dermatology (Basel, Switzerland)* 185: 49-55.

Hounsfield G N (1973) Computerized transverse axial scanning (tomography): Part 1. Description of system. *Br J Radiol* 46: 1016-1022.

Hu X, and Norris D G (2004) Advances in high-field magnetic resonance imaging. *Annual Review of Biomedical Engineering* 6: 157-184.

Huang D, Swanson E A, Lin C P, Schuman J S, Stinson W J, Chang W, Hee M R et al. (1991) Optical coherence tomography. *Science* 254: 1178 -1181.

Huber R, Wojtkowski M, and Fujimoto J G (2006) Fourier Domain Mode Locking (FDML): A new laser operating regime and applications for optical coherence tomography. *Optics Express* 14: 3225-3237.

Huzjan R, Sala E, and Hricak H (2005) Magnetic resonance imaging and magnetic resonance spectroscopic imaging of prostate cancer. *Nature Clinical Practice Urology* 2: 434-442.

Isenberg G, and Sivak, Jr. (2003) Gastrointestinal optical coherence tomography. *Techniques in Gastrointestinal Endoscopy* 5: 94-101.

Isles M G, McConkey C, and Mehanna H M (2008) A systematic review and meta-analysis of the role of positron emission tomography in the follow up of head and neck squamous cell carcinoma following radiotherapy or chemoradiotherapy. *Clinical Otolaryngology* 33: 210 - 222.

Izatt J A, and Choma M A (2008) Chapter 2: Theory of Optical coherence tomography. In: Drexler W, and Fujimoto J G [eds.] *Optical Coherence Tomography: Technology and Applications*. (1 edn.) Berlin: Springer, pp. 48 - 72.

Izatt J A, Kulkarni M D, Hsing-Wen W, Kobayashi K, and Sivak M V (1996) Optical coherence tomography and microscopy in gastrointestinal tissues. *IEEE Journal of Selected Topics in Quantum Electronics* 2: 1017-1028.

Jansen J F A, Backes W H, Nicolay K, and Kooi M E (2006) ^1H MR Spectroscopy of the Brain: Absolute Quantification of Metabolites¹. *Radiology* 240: 318-332.

Jass J R, Atkin W S, Cuzick J, Bussey H J, Morson B C, Northover J M, and Todd I P (1986) The grading of rectal cancer: historical perspectives and a multivariate analysis of 447 cases. *Histopathology* 10: 437-459.

Jiao S, Jiang M, Hu J, Fawzi A, Zhou Q, Shung K K, Puliafito C A et al. (2010) Photoacoustic ophthalmoscopy for in vivo retinal imaging. *Optics Express* 18: 3967-3972.

Jiao S, Xie Z, Zhang H F, and Puliafito C A (2009) Simultaneous multimodal imaging with integrated photoacoustic microscopy and optical coherence tomography. *Optics Letters* 34: 2961-2963.

Jones C W, Smolinski D, Keogh A, Kirk T B, and Zheng M H (2005) Confocal laser scanning microscopy in orthopaedic research. *Progress in Histochemistry and Cytochemistry* 40: 1 -70.

Judenhofer M S, Wehrl H F, Newport D F, Catana C, Siegel S B, Becker M, Thielscher A et al. (2008) Simultaneous PET-MRI: a new approach for functional and morphological imaging. *Nature medicine* 14: 459-465.

Jung W, Zhang J, Chung J, Wilder-Smith P, Brenner M, Nelson J S, and Chen Z (2005) Advances in Oral Cancer Detection Using Optical Coherence Tomography. *IEEE Journal of Selected Topics in Quantum Electronics* 11: 811 - 817.

Kaiser W, and Garrett C G B (1961) Two-Photon Excitation in CaF_2 : Eu^{2+} . *Physical Review Letters* 7: 229-229.

Kalender W A (2006) X-ray computed tomography. *Physics in Medicine and Biology* 51: R29-43.

Kasparov S, Teschemacher A G, and Paton J F (2002) Dynamic confocal imaging in acute brain slices and organotypic slice cultures using a spectral confocal microscope with single photon excitation. *Experimental Physiology* 87: 715-724.

Kim K T, Black K L, Marciano D, Mazziotta J C, Guze B H, Grafton S, Hawkins R A et al. (1990) Thallium-201 SPECT Imaging of Brain Tumors: Methods and Results. *J Nucl Med* 31: 965-969.

Knesaurek K, and Machac J (2006) Comparison of 18F SPECT with PET in myocardial imaging: A realistic thorax-cardiac phantom study. *BMC Nuclear Medicine* 6: 5-5.

Ko T, Adler D, Fujimoto J, Mamedov D, Prokhorov V, Shidlovski V, and Yakubovich S (2004) Ultrahigh resolution optical coherence tomography imaging with a broadband superluminescent diode light source. *Optics Express* 12: 2112-2119.

Kolkman R G M, Hondebrink E, Steenbergen W, and de Mul F F M (2003) In vivo photoacoustic imaging of blood vessels using an extreme-narrow aperture sensor. *IEEE Journal of Selected Topics in Quantum Electronics* 9: 343-346.

Komitowski D (1982) Epidermal-dermal Junction during Experimental Skin Carcinogenesis and Cocarcinogenesis as Revealed by Scanning Electron Microscopy. *Journal of Investigative Dermatology* 78: 395-401.

König K (2008) Clinical multiphoton tomography. *Journal of Biophotonics* 1: 13-23.

König K, and Riemann I (2003) High-resolution multiphoton tomography of human skin with subcellular spatial resolution and picosecond time resolution. *Journal of Biomedical Optics* 8: 432-439.

König K, Speicher M, Bückle R, Reckfort J, McKenzie G, Welzel J, Koehler M J et al. (2009) Clinical optical coherence tomography combined with multiphoton tomography of patients with skin diseases. *Journal of Biophotonics* 2: 389-397.

Konishi F, and Morson B C (1982) Pathology of colorectal adenomas: a colonoscopic survey. *Journal of Clinical Pathology* 35: 830-841.

Korde V R, Bonnema G T, Xu W, Krishnamurthy C, Ranger-Moore J, Saboda K, Slayton L D et al. (2007) Using optical coherence tomography to evaluate skin sun damage and precancer. *Lasers in Surgery and Medicine* 39: 687-695.

Köstli K P, Frenz M, Weber H P, Paltauf G, and Schmidt-Kloiber H (2001) Optoacoustic tomography: time-gated measurement of pressure distributions and image reconstruction. *Applied Optics* 40: 3800-3809.

Krawtchenko N, Roewert-Huber J, Ulrich M, Mann I, Sterry W, and Stockfleth E (2007) A randomised study of topical 5% imiquimod vs. topical 5-fluorouracil vs. cryosurgery in immunocompetent patients with actinic keratoses: a comparison of clinical and histological outcomes including 1-year follow-up. *The British Journal of Dermatology* 157 Suppl 2: 34-40.

Kray S, Spöler F, Först M, and Kurz H (2009) High-resolution simultaneous dual-band spectral domain optical coherence tomography. *Optics Letters* 34: 1970-1972.

Kruger R A, Reinecke D R, and Kruger G A (1999) Thermoacoustic computed tomography--technical considerations. *Medical Physics* 26: 1832-1832.

Ku G, Fornage B D, Jin X, Xu M, Hunt K K, and Wang L V (2005) Thermoacoustic and photoacoustic tomography of thick biological tissues toward breast imaging. *Technology in Cancer Research & Treatment* 4: 559-566.

Kuwano H, Ueo H, Sugimachi K, Inokuchi K, Toyoshima S, and Enjoji M (1985) Glandular or mucus-secreting components in squamous cell carcinoma of the esophagus. *Cancer* 56: 514-518.

Kwock L, Smith J K, Castillo M, Ewend M G, Collichio F, Morris D E, Bouldin T W et al. (2006) Clinical role of proton magnetic resonance spectroscopy in oncology: brain, breast, and prostate cancer. *The Lancet Oncology* 7: 859-868.

Lauterbur P C (1973) Image Formation by Induced Local Interactions: Examples Employing Nuclear Magnetic Resonance. *Nature* 242: 190-191.

Leber A W, Johnson T, Becker A, von Ziegler F, Tittus J, Nikolaou K, Reiser M et al. (2007) Diagnostic accuracy of dual-source multi-slice CT-coronary angiography in patients with an intermediate pretest likelihood for coronary artery disease. *European Heart Journal* 28: 2354-2360.

Leitgeb R, Drexler W, Unterhuber A, Hermann B, Bajraszewski T, Le T, Stingl A et al. (2004) Ultrahigh resolution Fourier domain optical coherence tomography. *Optics Express* 12: 2156 - 2165.

Leitgeb R, Hitzengerger C K, and Fercher A F (2003) Performance of Fourier domain vs. time domain optical coherence tomography. *Optics Express* 11: 889 - 894.

Leitgeb R, Wojtkowski M, Kowalczyk A, Hitzengerger C K, Sticker M, and Fercher A F (2000) Spectral measurement of absorption by spectroscopic frequency-domain optical coherence tomography. *Optics Letters* 25: 820-822.

Levi H (1976) George Hevesy and his concept of radioactive indicators-In retrospect. *European Journal of Nuclear Medicine* 1: 3-10.

Li L, Maslov K, Ku G, and Wang L V (2009) Three-dimensional combined photoacoustic and optical coherence microscopy for in vivo microcirculation studies. *Optics Express* 17: 16450-16455.

Li X D, Boppart S A, Van Dam J, Mashimo H, Mutinga M, Drexler W, Klein M et al. (2000) Optical coherence tomography: advanced technology for the endoscopic imaging of Barrett's esophagus. *Endoscopy* 32: 921-930.

Lu C-w, Tsai M-t, Wang Y-m, Kiang Y-w, and Yang C C (2006) Resolution Improvement in Optical Coherence Tomography with Segmented Spectrum Management. *Optical and Quantum Electronics* 37: 1165-1173.

Ludwig G D, and Struthers F W (1949) *Considerations underlying the use of ultrasound to detect gallstones and foreign bodies in tissue*. Report No.4, Project NM 004:001, Naval Research Laboratory, Washington.

Luker G D, and Luker K E (2008) Optical Imaging: Current Applications and Future Directions. *Journal of Nuclear medicine* 49: 1 - 4.

Manohar S, Kharine A, Hespen J C G v, Steenbergen W, and Leeuwen T G v (2005) The Twente Photoacoustic Mammoscope: system overview and performance. *Physics in Medicine and Biology* 50: 2543-2557.

Martin C, Mihm J, Soter N A, Dvorak H F, and Austen K F (1976) The Structure of normal skin and the morphology of atopic eczema. *The Journal of Investigative Dermatology* 67: 305-342.

Maslov K, Stoica G, and Wang L V (2005) In vivo dark-field reflection-mode photoacoustic microscopy. *Optics Letters* 30: 625-627.

Maslov K, Zhang H F, Hu S, and Wang L V (2008) Optical-resolution photoacoustic microscopy for in vivo imaging of single capillaries. *Optics Letters* 33: 929-931.

Masters B R, So P T, and Gratton E (1997) Multiphoton excitation fluorescence microscopy and spectroscopy of in vivo human skin. *Biophysical Journal* 72: 2405-2412.

Mäurer J, Knollmann F D, Schlums D, Garbe C, Vogl T J, Bier J, and Felix R (1995) Role of high-resolution magnetic resonance imaging for differentiating melanin-containing skin tumors. *Investigative Radiology* 30: 638-643.

McDonald D M, and Choyke P L (2003) Imaging of angiogenesis: from microscope to clinic. *Nature Medicine* 9: 713-725.

McLoone N, Donnelly R F, Walsh M, Dolan O M, McLoone S, McKenna K, and McCarron P A (2008) Aminolaevulinic acid diffusion characteristics in 'in vitro' normal human skin and actinic keratosis: implications for topical photodynamic therapy. *Photodermatology, Photoimmunology & Photomedicine* 24: 183-190.

Mettler F A J, and Guiberteau M J (2005) *Essentials of Nuclear Medicine Imaging*. 5 ed. Philadelphia: Saunders Elsevier.

Meyer J E, Narang T, Schnoll-Sussman F H, Pochapin M B, Christos P J, and Sherr D L (2010) Increasing incidence of rectal cancer in patients aged younger than 40 years. *Cancer*: 4354 -4359.

Minsky M (1988) Memoir on Inventing the Confocal Scanning Microscope. *Scanning* 10: 128-138.

Mobley J, and Vo-Dinh T (2003) Chapter 2: Biomedical Photonics Handbook. In: Vo-Dinh T [ed.] Boca Raton, Florida: CRC Press, pp. 2.1 - 2.7.

Mogensen M, Lars T, Thomas M J r, Peter E A, and Gregor B E J (2009a) OCT imaging of skin cancer and other dermatological diseases. *Journal of Biophotonics* 2: 442 - 451.

Mogensen M, Nürnberg B M, Forman J L, Thomsen J B, Thrane L, and Jemec G B E (2009b) In vivo thickness measurement of basal cell carcinoma and actinic keratosis with optical coherence tomography and 20-MHz ultrasound. *British Journal of Dermatology* 160: 1026-1033.

Montet X, Ntziachristos V, Grimm J, and Weissleder R (2005) Tomographic Fluorescence Mapping of Tumor Targets. *Cancer Research* 65: 6330 - 6335.

Morgner U, Drexler W, Kärtner F X, Li X D, Pitris C, Ippen E P, and Fujimoto J G (2000) Spectroscopic optical coherence tomography. *Optics Letters* 25: 111-113.

Muehllehner G, and Karp J S (2006) Positron emission tomography. *Physics in Medicine and Biology* 51: R117-R137.

Müller, Squier, Wilson, and Brakenhoff (1998) 3D microscopy of transparent objects using third-harmonic generation. *Journal of Microscopy* 191: 266-274.

Muto T, Bussey H J, and Morson B C (1975) The evolution of cancer of the colon and rectum. *Cancer* 36: 2251-2270.

Natt O, and Frahm J (2005) *In vivo* magnetic resonance imaging: insights into structure and function of the central nervous system. *Measurement Science and Technology* 16: 17 -36.

Nehal K S, Gareau D, and Rajadhyaksha M (2008) Skin Imaging With Reflectance Confocal Microscopy. *Seminars in Cutaneous Medicine and Surgery* 27: 37-43.

Newman P G, and Rozycki G S (1998) The history of ultrasound. *Surgical Clinics of North America* 78: 179-195.

Ntziachristos V (2006) Fluorescence molecular imaging. *Annual Review of Biomedical Engineering* 8: 1-33.

Ogawa S, Lee T M, Kay A R, and Tank D W (1990) Brain magnetic resonance imaging with contrast dependent on blood oxygenation. *Proceedings of the National Academy of Sciences of the United States of America* 87: 9868-9872.

Oh J-T, Li M-L, Zhang H F, Maslov K, Stoica G, and Wang L V (2006) Three-dimensional imaging of skin melanoma in vivo by dual-wavelength photoacoustic microscopy. *Journal of Biomedical Optics* 11: 34032-34032.

Olmedo J M, Karen E W, Joseph M S, and David L S (2007) Correlation of Thickness of Basal Cell Carcinoma by Optical Coherence Tomography In Vivo and Routine Histologic Findings: A Pilot Study. *Dermatologic Surgery* 33: 421-426.

Olmedo J M, Warschaw K E, Schmitt J M, and Swanson D L (2006) Optical coherence tomography for the characterization of basal cell carcinoma in vivo: A pilot study. *Journal of American Academy of Dermatology* 55: 408 - 412.

Pagnoni A, Knuettel A, Welker P, Rist M, Stoudemayer T, Kolbe L, Sadiq I et al. (1999) Optical coherence tomography in dermatology. *Skin Research and Technology* 5: 83-87.

Pan Y, and Farkas D L (1998) Noninvasive Imaging of Living Human Skin with Dual-Wavelength Optical Coherence Tomography in Two and Three Dimensions. *Journal of Biomedical Optics* 3: 446-455.

Panjehpour M, Overholt B F, Vo-Dinh T, Haggitt R C, Edwards D H, and Buckley F P (1996) Endoscopic fluorescence detection of high-grade dysplasia in Barrett's esophagus. *Gastroenterology* 111: 93-101.

Papathanassiou D, and Liehn J-C (2008) The growing development of multimodality imaging in oncology. *Critical Reviews in Oncology/Hematology* 68: 60-65.

Parkin D M, Bray F, Ferlay J, and Pisani P (2005) Global Cancer Statistics, 2002. *CA* 55: 74-108.

Parnell S A, Peppercorn M A, Antonioli D A, Cohen M A, and Joffe N (1978) Squamous cell papilloma of the esophagus. Report of a case after peptic esophagitis and repeated bougienage with review of the literature. *Gastroenterology* 74: 910-913.

Patil C A, Bosschaart N, Keller M D, van Leeuwen T G, and Mahadevan-Jansen A (2008) Combined Raman spectroscopy and optical coherence tomography device for tissue characterization. *Optics Letters* 33: 1135-1137.

Payne B P, Venugopalan V, Mikić B B, and Nishioka N S (2003) Optoacoustic tomography using time-resolved interferometric detection of surface displacement. *Journal of Biomedical Optics* 8: 273-280.

Pellacani G, Cesinaro A M, Longo C, Grana C, and Seidenari S (2005) Microscopic In Vivo Description of Cellular Architecture of Dermoscopic Pigment Network in Nevi and Melanomas. *Archives of Dermatology* 141: 147-154.

Pfau P R, Sivak, Jr., Chak A, Kinnard M, Wong R C K, Isenberg G A, Izatt J A et al. (2003) Criteria for the diagnosis of dysplasia by endoscopic optical coherence tomography. *Gastrointestinal Endoscopy* 58: 196-202.

Pierce M C, Strasswimmer J, Park B H, Cense B, and de Boer J F (2004) Birefringence measurements in human skin using polarization-sensitive optical coherence tomography. *Journal of Biomedical Optics* 9: 287-291.

Pilleul F, Penigaud M, Milot L, Saurin J-C, Chayvialle J-A, and Valette P-J (2006) Possible Small-Bowel Neoplasms: Contrast-enhanced and Water-enhanced Multidetector CT Enteroclysis. *Radiology* 241: 796-801.

Pitris C, Jesser C, Boppart S A, Stamper D, Brezinski M E, and Fujimoto J G (2000) Feasibility of optical coherence tomography for high-resolution imaging of human gastrointestinal tract malignancies. *Journal of Gastroenterology* 35: 87-92.

Podoleanu A G, Dobre G M, and Jackson D A (1998) En-face coherence imaging using galvanometer scanner modulation. *Optics Letters* 23: 147-149.

Podoleanu A G, Dobre G M, Webb D J, and Jackson D A (1996) Coherence imaging by use of a Newton rings sampling function. *Optics Letters* 21: 1789-1791.

Podoleanu A G, Rogers J A, and Jackson D A (2000) Three dimensional OCT images from retina and skin. *Optics Express* 7: 292 - 297.

Potsaid B, Gorczynska I, Srinivasan V J, Chen Y, Jiang J, Cable A, and Fujimoto J G (2008) Ultrahigh speed Spectral / Fourierdomain OCT ophthalmic imaging at 70,000 to 312,500 axial scans per second. *Optics Express* 16: 15149-15169.

Povazay B, Hermann B, Unterhuber A, Sattmann H, Hofer B, Zeiler F, Morgan J et al. (2007) Spatially encoded frequency domain optical coherence tomography system for volumetric in vivo imaging at 1050nm. In: *Photonics West 2007*. San Jose, United States.

Purcell E M, Torrey H C, and Pound R V (1946) Resonance Absorption by Nuclear Magnetic Moments in a Solid. *Physical Review* 69: 37-38.

Qi.X, Jr. M V S, and Rollins A M (2008) Chapter 33: Optical coherence tomography for gastrointestinal endoscopy. In: Drexler W, and Fujimoto J G [eds.] *Optical Coherence Tomography: Technology and Applications*. (1 edn.) Berlin: Springer, pp. 1047 - 1081.

Querleux B (2004) Magnetic resonance imaging and spectroscopy of skin and subcutis. *Journal of Cosmetic Dermatology* 3: 156-161.

Querleux B, Thérèse B, Stéphane D, Jean de R, Etienne H, Frédéric L, and Victoria Holloway B (2009) Skin from various ethnic origins and aging: an in vivo cross-sectional multimodality imaging study. *Skin Research and Technology* 15: 306-313.

Rajadhyaksha M, González S, Zavislan J M, Anderson R R, and Webb R H (1999) In vivo confocal scanning laser microscopy of human skin II: Advances in instrumentation and comparison with histology. *Journal of Investigative Dermatology* 113: 293-303.

Rajadhyaksha M, Grossman M, Esterowitz D, Webb R H, and Anderson R R (1995) In Vivo Confocal Scanning Laser Microscopy of Human Skin: Melanin Provides Strong Contrast. *Journal of Investigative Dermatology* 104: 946-952.

Rembielak A, Cullen J, Saleem A, and Price P (2007) Imaging in cancer. *Medicine* 36: 5 - 8.

Richard S, Querleux B, Bittoun J, Jolivet O, Idy-Peretti I, de Lacharriere O, and Leveque J-L (1993) Characterization of the Skin In Vivo by High Resolution Magnetic Resonance Imaging: Water Behavior and Age-Related Effects. *Journal of Investigative Dermatology* 100: 705-709.

Riddell R H, Goldman H, Ransohoff D F, Appelman H D, Fenoglio C M, Haggitt R C, Ahren C et al. (1983) Dysplasia in inflammatory bowel disease: standardized classification with provisional clinical applications. *Human Pathology* 14: 931-968.

Rodríguez I, Pérez-Rial S, González-Jimenez J, Pérez-Sánchez J M, Herranz F, Beckmann N, and Ruíz-Cabello J (2008) Magnetic resonance methods and applications in pharmaceutical research. *Journal of Pharmaceutical Sciences* 97: 3637-3665.

Roentgen W C (1896) On a new kind of rays. *Nature* 53: 274-277.

Rollins A M, and Izatt J A (1999) Optimal interferometer designs for optical coherence tomography. *Optics Letters* 24: 1484 - 1486.

Rollins A M, Kulkarni M D, Yazdanfar S, Ung-arunyawee R, and Izatt J A (1998) *In vivo* video rate optical coherence tomography. *Optics Express* 3: 219 - 228.

Rosa C C, Rogers J, and Podoleanu A G (2005) Fast scanning transmissive delay line for optical coherence tomography. *Optics Letters* 30: 3263-3265.

Ross M H, Kaye G I, and Pawlina W (2002) Chapter 14: Integumentary system. In: Scogna K H, and Cady B [eds.] *Histology: A text and atlas*. (4 edn.) Philadelphia: Lippincott Williams & Wilkins, pp. 400 - 432.

Ryu S Y, Choi H Y, Na J, Choi E S, and Lee B H (2008) Combined system of optical coherence tomography and fluorescence spectroscopy based on double-cladding fiber. *Optics Letters* 33: 2347-2349.

Sainter A W, King T A, and Dickinson M R (2004) Effect of target biological tissue and choice of light source on penetration depth and resolution in optical coherence tomography. *Journal of Biomedical Optics* 9: 193-199.

Sakashita M, Inoue H, Kashida H, Tanaka J, Cho J Y, Satodate H, Hidaka E et al. (2003) Virtual histology of colorectal lesions using laser-scanning confocal microscopy. *Endoscopy* 35: 1033-1038.

Sandby-Møller J, Poulsen T, and Wulf H C (2003) Epidermal thickness at different body sites: relationship to age, gender, pigmentation, blood content, skin type and smoking habits. *Acta Dermato-Venereologica* 83: 410-413.

Sant M, Aareleid T, Berrino F, Bielska Lasota M, Carli P M, Faivre J, Grosclaude P et al. (2003) EUROCARE-3: survival of cancer patients diagnosed 1990-94--results and commentary. *Annals of Oncology* 14 Suppl 5: v61-118.

Schmid-Wendtner M H, and Dill-Müller D (2008) Ultrasound Technology in Dermatology. *Seminars in Cutaneous Medicine and Surgery* 27: 44-51.

Schmidt H G, Riddell R H, Walther B, Skinner D B, and Riemann J F (1985) Dysplasia in Barrett's esophagus. *Journal of Cancer Research and Clinical Oncology* 110: 145-152.

Schmitt J (1998) OCT elastography: imaging microscopic deformation and strain of tissue. *Optics Express* 3: 199-211.

Schmitt J M (1999) Optical Coherence Tomography (OCT): A Review. *IEEE Journal of Selected Topics in Quantum Electronics* 5: 1205 -1214.

Schmitt J M, Knuttel A, Yadlowsky M, and Eckhaus M A (1994) Optical-coherence tomography of a dense tissue: statistics of attenuation and backscattering. *Physics in Medicine and Biology* 39: 1705-1720.

Schmitt J M, Lee S L, and Yung K M (1997) An optical coherence microscope with enhanced resolving power in thick tissue. *Optics Communications* 142: 203 -207.

Schoder H, Larson S M, and Yeung H W D (2004) PET/CT in Oncology: Integration into Clinical Management of Lymphoma, Melanoma, and Gastrointestinal Malignancies. *Journal of Nuclear Medicine* 45: S72-81.

Scotiniotis I A, Kochman M L, Lewis J D, Furth E E, Rosato E F, and Ginsberg G G (2001) Accuracy of EUS in the evaluation of Barrett's esophagus and high-grade dysplasia or intramucosal carcinoma. *Gastrointestinal Endoscopy* 54: 689-696.

Seo Y, Mari C, and Hasegawa B H (2008) Technological Development and Advances in Single-Photon Emission Computed Tomography/Computed Tomography. *Seminars in Nuclear Medicine* 38: 177-197.

Shafer A B, Megill L R, and Droppleman L (1964) Optimization of the Czerny-Turner Spectrometer. *Journal of the Optical Society of America* 54: 879-886.

Silverberg S G (1970) Focally malignant adenomatous polyps of the colon and rectum. *Surgery, Gynecology & Obstetrics* 131: 103-114.

Solaymani-Dodaran M, Logan R F A, West J, Card T, and Coupland C (2004) Risk of oesophageal cancer in Barrett's oesophagus and gastro-oesophageal reflux. *Gut* 53: 1070-1074.

Song H K, Wehrli F W, and Ma J (1997) In vivo MR microscopy of the human skin. *Magnetic Resonance in Medicine* 37: 185-191.

Spöler F, Kray S, Grychtol P, Hermes B, Bornemann J, Först M, and Kurz H (2007) Simultaneous dual-band ultra-high resolution optical coherence tomography. *Optics Express* 15: 10832-10841.

Steiner A, Pehamberger H, and Wolff K (1987) Improvement of the diagnostic accuracy in pigmented skin lesions by epiluminescent light microscopy. *Anticancer Research* 7: 433-434.

Steiner R, Kunzi-Rapp K, and Scharffetter-Kochanek K (2003) Optical Coherence Tomography: Clinical Applications in Dermatology. *Medical Laser Application* 18: 249-259.

Stolz W, Bilek P, Landthaler M, Merkle T, and Braun-Falco O (1989) Skin surface microscopy. *Lancet* 2: 864-865.

Sugimachi K, Ohno S, Matsuda H, Mori M, and Kuwano H (1988) Lugol-combined endoscopic detection of minute malignant lesions of the thoracic esophagus. *Annals of Surgery* 208: 179-183.

Sun T, and Diebold G J (1992) Generation of ultrasonic waves from a layered photoacoustic source. *Nature* 355: 806-808.

Swanson E A, Izatt J A, Hee M R, Huang D, Lin C P, Schuman J S, Puliavito C A et al. (1993) In vivo retinal imaging by optical coherence tomography. *Optics Letters* 18: 1864 - 1866.

Tearney G J, Brezinski M E, Bouma B E, Boppart S A, Pitris C, Southern J F, and Fujimoto J G (1997) In Vivo Endoscopic Optical Biopsy with Optical Coherence Tomography. *Science* 276: 2037-2039.

Tervo T, and Moilanen J (2003) In vivo confocal microscopy for evaluation of wound healing following corneal refractive surgery. *Progress in Retinal and Eye Research* 22: 339-358.

Thompson J J, and Enterline H T (1981) The macroscopic appearance of colorectal polyps. *Cancer* 48: 151-160.

Thompson J J, Zinsser K R, and Enterline H T (1983) Barrett's metaplasia and adenocarcinoma of the esophagus and gastroesophageal junction. *Human Pathology* 14: 42-61.

Thorne S H, and Contag C H (2005) Using in Vivo Bioluminescence Imaging to Shed Light on Cancer Biology. *Proceedings of the IEEE* 93: 750-762.

Townsend D W (2001) A combined PET/CT scanner: the choices. *Journal of Nuclear Medicine* 42: 533-534.

Tseng S-H, Bargo P, Durkin A, and Kollias N (2009) Chromophore concentrations, absorption and scattering properties of human skin in-vivo. *Optics Express* 17: 14599-14617.

Tumlinson A R, Barton J K, Povazay B, Sattman H, Unterhuber A, Leitgeb R A, and Drexler W (2006) Endoscope-tip interferometer for ultrahigh resolution frequency domain optical coherence tomography in mouse colon. *Optics Express* 14: 1878-1887.

Tumlinson A R, Hariri L P, Utzinger U, and Barton J K (2004) Miniature endoscope for simultaneous optical coherence tomography and laser-induced fluorescence measurement. *Applied Optics* 43: 113-121.

Ulrich C, Busch J O, Meyer T, Nindl I, Schmook T, Sterry W, and Stockfleth E (2006) Successful treatment of multiple actinic keratoses in organ transplant patients with topical 5% imiquimod: a report of six cases. *British Journal of Dermatology* 155: 451-454.

Unterhuber A, Považay B, Hermann B, Sattmann H, Drexler W, Yakovlev V, Tempea G et al. (2003) Compact, low-cost Ti:Al₂O₃ laser for *in vivo* ultrahigh-resolution optical coherence tomography. *Optics Letters* 28: 905-907.

van Soest E M, Dieleman J P, Siersema P D, Sturkenboom M C J M, and Kuipers E J (2005) Increasing incidence of Barrett's oesophagus in the general population. *Gut* 54: 1062-1066.

Vizcaino A P, Moreno V, Lambert R, and Parkin D M (2002) Time trends incidence of both major histologic types of esophageal carcinomas in selected countries, 1973-1995. *International Journal of Cancer* 99: 860-868.

Wagner H N (2006) Chapter 12: History of the role of nuclear medicine in the thyroid gland and its diseases: A personal perspective. In: Wartofsky L, and Nostrand D V [eds.] *Thyroid cancer*. Totowa: Humana Press, pp. 117-128.

Wang H, Jenkins M, and Rollins A (2008) A combined multiple-SLED broadband light source at 1300nm for high resolution optical coherence tomography. *Optics Communications* 281: 1896-1900.

Wang L, Jackson W C, Steinbach P A, and Tsien R Y (2004) Evolution of new nonantibody proteins via iterative somatic hypermutation. *Proceedings of the National Academy of Sciences of the United States of America* 101: 16745-16749.

Wang L V (2008a) Prospects of photoacoustic tomography. *Medical Physics* 35: 5758-5767.

Wang L V (2008b) Tutorial on Photoacoustic Microscopy and Computed Tomography. *IEEE Journal of Selected Topics in Quantum Electronics* 14: 171-179.

Wang L V, and Wu H-i (2007) *Biomedical optics: principles and imaging*. New Jersey: Wiley-Interscience.

Wang X, Pang Y, Ku G, Xie X, Stoica G, and Wang L V (2003a) Noninvasive laser-induced photoacoustic tomography for structural and functional in vivo imaging of the brain. *Nature biotechnology* 21: 803-806.

Wang Y, Nelson J, Chen Z, Reiser B, Chuck R, and Windeler R (2003b) Optimal wavelength for ultrahigh-resolution optical coherence tomography. *Optics Express* 11: 1411-1417.

Welzel J (2001) Optical coherence tomography in dermatology: a review. *Skin Research and Technology* 7: 1-9.

Welzel J, Bruhns M, and Wolff H H (2003) Optical coherence tomography in contact dermatitis and psoriasis. *Archives of Dermatological Research* 295: 50-55.

Welzel J, Lankenau E, Birngruber R, and Engelhardt R (1997) Optical coherence tomography of the human skin. *Journal of the American Academy of Dermatology* 37: 958-963.

Welzel J, Lankenau E, Huttmann G, and Birngruber R (2008) Chapter 35: OCT in Dermatology. In: Drexler W, and Fujimoto J G [eds.] *Optical Coherence Tomography: Technology and Applications*. (1 edn.) Berlin: Springer, pp. 1103 - 1121.

Welzel J, Reinhardt C, Lankenau E, Winter C, and Wolff H H (2004) Changes in function and morphology of normal human skin: evaluation using optical coherence tomography. *British Journal of Dermatology* 150: 220-225.

Wernick M N, and Aarsvold J N [eds.] (2004) *Emission Tomography: The fundamentals of PET and SPECT*. (1 edn.) San Diego: Elsevier Academic Press.

Westbrook C, Roth C K, and Talbot J (2005) *MRI in Practice*. 3 ed. Oxford: Wiley-Blackwell.

Westphal V, Rollins A M, Willis J, Sivak Jr M V, and Izatt J A (2005) Correlation of endoscopic optical coherence tomography with histology in the lower-GI tract. *Gastrointestinal Endoscopy* 61: 537-546.

Wheater P R, Heath J W, and Young B (2000) Skin. *Wheater's Functional Histology: A Text and Colour Atlas*. (4 edn.) London: Churchill Livingstone, pp. 157-171.

Wild J J (1950) The use of ultrasonic pulses for the measurement of biologic tissues and the detection of tissue density changes. *Surgery* 27: 183-188.

Wojtkowski M, Leitgeb R, Kowalczyk A, Bajraszewski T, and Fercher A F (2002) In vivo human retinal imaging by Fourier domain optical coherence tomography. *Journal of Biomedical Optics* 7: 457 - 462.

Wojtkowski M, Srinivasan V J, Ko T H, Fujimoto J G, Kowalczyk A, and Duker J S (2004) Ultrahigh-resolution, high-speed, Fourier domain optical coherence tomography and methods for dispersion compensation. *Optics Express* 12: 2404 - 2422.

Wolf R L, and Detre J A (2007) Clinical Neuroimaging Using Arterial Spin-Labeled Perfusion MRI. *Neurotherapeutics* 4: 346-359.

Woodward R M, Wallace V P, Pye R J, Cole B E, Arnone D D, Linfield E H, and Pepper M (2003) Terahertz Pulse Imaging of ex vivo Basal Cell Carcinoma. *Journal of Investigative Dermatology* 120: 72-78.

Xu C, Marks D, Do M, and Boppart S (2004) Separation of absorption and scattering profiles in spectroscopic optical coherence tomography using a least-squares algorithm. *Optics Express* 12: 4790-4803.

Xu M, and Wang L V (2006) Photoacoustic imaging in biomedicine. *Review of Scientific Instruments* 77: 041101-041101.

Young B, and Heath J W (2000a) Chapter 9: Skin. In: Home T [ed.] *Wheater's Functional Histology: A Text and Colour Atlas*. (4 edn.) London: Churchill Livingstone, pp. 157-171.

Young B, and Heath J W (2000b) Chapter 14: Gastrointestinal tract. In: Home T [ed.] *Wheater's Functional Histology: A Text and Colour Atlas*. (4 edn.) London: Churchill Livingstone, pp. 249-273.

Yun S H, Tearney G J, Bouma B E, Park B H, and Boer J F d (2003) High-speed spectral-domain optical coherence tomography at 1.3 micron wavelength. *Optics Express* 11: 3598 - 3604.

Zhang E, Laufer J, and Beard P (2008) Backward-mode multiwavelength photoacoustic scanner using a planar Fabry-Perot polymer film ultrasound sensor for high-resolution three-dimensional imaging of biological tissues. *Applied Optics* 47: 561-577.

Zhang E Z, Laufer J, Povazay B, Alex A, Hofer B, Drexler W, and Beard P [eds.] (2010a) *Multimodal simultaneous photoacoustic tomography, optical resolution microscopy, and OCT system*. Photons Plus Ultrasound: Imaging and Sensing 2010. San Francisco, California, USA. SPIE.

Zhang E Z, Laufer J G, Pedley R B, and Beard P C (2009) In vivo high-resolution 3D photoacoustic imaging of superficial vascular anatomy. *Physics in Medicine and Biology* 54: 1035-1046.

Zhang H F, Maslov K, Stoica G, and Wang L V (2006a) Functional photoacoustic microscopy for high-resolution and noninvasive in vivo imaging. *Nature biotechnology* 24: 848-851.

Zhang H F, Maslov K, Stoica G, and Wang L V (2006b) Imaging acute thermal burns by photoacoustic microscopy. *Journal of Biomedical Optics* 11: 054033-054033.

Zhang Z Y, Hogg R A, Lv X Q, and Wang Z G (2010b) Self-assembled quantum-dot superluminescent light-emitting diodes. *Advances in Optics and Photonics* 2: 201-228.

Zhao Y, Chen Z, Saxer C, Xiang S, de Boer J F, and Nelson J S (2000) Phase-resolved optical coherence tomography and optical Doppler tomography for imaging blood flow in human skin with fast scanning speed and high velocity sensitivity. *Optics Letters* 25: 114-116.

Zipfel W R, Williams R M, Christie R, Nikitin A Y, Hyman B T, and Webb W W (2003a) Live tissue intrinsic emission microscopy using multiphoton-excited native fluorescence and second harmonic generation. *Proceedings of the National Academy of Sciences of the United States of America* 100: 7075-7080.

Zipfel W R, Williams R M, and Web W W (2003b) Nonlinear magic: multiphoton microscopy in the biosciences. *Nature biotechnology* 21: 1369 -1376.

List of Abbreviations

BCC	Basal cell carcinoma
BD	Betamethasone dipropionate
BLI	Bioluminescence imaging
CARS	Coherent anti-stokes Raman scattering
CLSM	Confocal laser scanning microscopy
CT	Computed tomography
DOT	Diffuse optical tomography
ED	Epidermis
ELM	Epiluminescence microscopy
FD-OCT	Frequency domain optical coherence tomography
fMRI	Functional magnetic resonance imaging
FMT	Fluorescence molecular tomography
FO	Fish oil
FPI	Fabry-Perot interferometer
FWHM	Full width at half maximum
HD	Hypodermis
HFUS	High frequency ultrasound
LP	Lamina propria
MM	Muscularis mucosae
MP	Muscularis propria
MPT	Multiphoton tomography
MRI	Magnetic resonance imaging
OCM	Optical coherence microscopy
OCT	Optical coherence tomography
ORPAM	Optical resolution photoacoustic microscopy
PAM	Photoacoustic microscopy
PAT	Photoacoustic tomography
PD	Papillary dermis
PET	Positron emission tomography
PIP	Proximal interphalangeal
RD	Reticular dermis
RS	Raman spectroscopy
RS	Rete subpapillare
SB	Stratum basale
SC	Stratum corneum
SCC	Squamous cell carcinoma
SD-OCT	Spectral domain optical coherence tomography
SG	Stratum granulosum
SL	Stratum lucidum
SLED	Superluminescent light emitting diode
SNR	Signal to noise ratio
SPECT	Single photon emission computed tomography
SS	Stratum spinosum
SS-OCT	Swept source optical coherence tomography
TAT	Thermoacoustic tomography
TD-OCT	Time domain optical coherence tomography
TPI	Terahertz pulse imaging
YDFL	Ytterbium-doped fibre laser